



**HAL**  
open science

# Spectroscopie de fluorescence : application pour la caractérisation d'interactions entre macromolécules d'intérêt biologiques et l'étude enzymologique de l'activité hélicase

Na Li

► **To cite this version:**

Na Li. Spectroscopie de fluorescence : application pour la caractérisation d'interactions entre macromolécules d'intérêt biologiques et l'étude enzymologique de l'activité hélicase. Sciences du Vivant [q-bio]. École normale supérieure de Cachan - ENS Cachan, 2009. Français. NNT: . tel-00468571

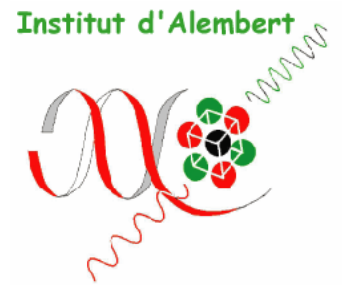
**HAL Id: tel-00468571**

**<https://theses.hal.science/tel-00468571>**

Submitted on 31 Mar 2010

**HAL** is a multi-disciplinary open access archive for the deposit and dissemination of scientific research documents, whether they are published or not. The documents may come from teaching and research institutions in France or abroad, or from public or private research centers.

L'archive ouverte pluridisciplinaire **HAL**, est destinée au dépôt et à la diffusion de documents scientifiques de niveau recherche, publiés ou non, émanant des établissements d'enseignement et de recherche français ou étrangers, des laboratoires publics ou privés.



**THESE DE DOCTORAT  
DE L'ECOLE NORMALE SUPERIEURE DE CACHAN**

Présentée par  
Mademoiselle Na LI

**Pour obtenir le grade de  
DOCTEUR DE L'ECOLE NORMALE SUPERIEURE DE CACHAN**

Sujet de la thèse :

**Spectroscopie de fluorescence : application pour la caractérisation  
d'interactions entre macromolécules d'intérêt biologiques et l'étude  
enzymologique de l'activité hélicase**

Thèse présentée et soutenue à Bâtiment IDA à ENS-Cachan le 20 octobre 2009 à 14h30  
devant le jury composé de :

Yves Mely	Professeur, Université de Strasbourg	Rapporteur
Anny Slama-Schwok	Chargée de Recherche HDR, INSERM	Rapporteur
Jean-Claude Brochon	Directeur de Recherche, CNRS	Co-Directeur de thèse
Yun-Long Zhao	Professeur, ECNU Université, Shanghai	Co-Directeur de thèse
Eric Deprez	Chargé de Recherche HDR, CNRS	Examineur
Xu-Guang Xi	Directeur de Recherche, CNRS	Examineur

*Laboratoire de Biologie et Pharmacologie Appliquées  
(CNRS UMR 8113)  
61, avenue du Président Wilson, 94235 Cachan CEDEX (France)*



## **REMERCIEMENTS**

J'ai effectuée ce travail de thèse dans l'équipe Biophotonique des interactions moléculaires au Laboratoire de Biologie et Pharmacologie Appliquées, UMR 8113 du CNRS. Je voudrais d'abord remercier Christian AUCLAIR et Jean-François MOUSCADET, qui ont assurée successivement la direction du laboratoire au cours de ces trois années, pour m'avoir accueillie au sein de leur unité de recherche et m'avoir permis de travailler dans un environnement scientifique aussi exceptionnel.

Je suis très sensible à l'honneur que m'ont fait les membres du jury de thèse en acceptant de lire et d'évaluer ce travail. Je les remercie d'avoir apporté un intérêt à mon travail. Ce mémoire a beaucoup bénéficié des commentaires qu'ils ont tous effectués.

Je tiens également à exprimer toute ma gratitude à Jean-Claude BROCHON pour la confiance qu'il m'a témoignée en me proposant d'effectuer ma thèse sous sa direction quand j'étais encore en Chine en M2 de toxicologie. Ses connaissances scientifiques, sa réceptivité, et son enthousiasme face aux évolutions de l'expérience m'ont toujours impressionné et ont contribué à la réussite de ma thèse. En fait, après la toxicologie, je pensais que les techniques de fluorescence constitueraient un sujet d'étude totalement nouveau pour moi. C'est lui qui m'a beaucoup encouragée et m'a introduite dans le domaine de fluorescence magnifique. Je lui suis très reconnaissante pour le soutien et la confiance qu'il m'a témoignés notamment lors de certaines démarches administratives et procédures concernant mon avenir professionnel.

Mes premiers remerciements sont aussi adressés à Eric DEPRez, Responsable d'équipe, qui m'a encadrée au cours de ces trois années de thèse. Son dynamisme, sa simplicité, son efficacité exceptionnelle à réfléchir et à résoudre les problèmes scientifiques, sa sympathie ont été très appréciables et m'ont évitée les soucis dont je pouvais parfois m'encombrer l'esprit. J'ai appris à tirer le maximum d'informations selon les datas et à gérer mon temps efficacement auprès de Eric. Je le remercie particulièrement pour toutes les discussions favorables et sa capacité à toujours me trouver une place dans son agenda bien remplis. Merci Eric de m'avoir guidée et soutenue tout au long de ce travail.

Je tiens, d'autre part à remercier le Professeur Yun-long ZHAO, directeur du département zoologie à l'East China Normal University, qui m'a accueillie au sein de son labo en Chine. Malgré ses grandes responsabilités au laboratoire puis au ministère de la recherche, il est toujours très actif et réceptif. Son enthousiasme face aux résolutions des problèmes scientifiques m'ont toujours impressionné et m'ont beaucoup encouragé. Je le remercie pour son aide lorsque j'ai rencontré des problèmes administratifs en Chine et surtout pour toutes les discussions concernant mon avenir professionnel.

C'est encadrée de tous mes collègues passés et présents de cette équipe que j'ai eu la chance d'apprivoiser la voûte céleste de la fluorescence et ses applications dans le domaine de la biologie. Merci à Patrick, Etienne, Elvire pour leur aide en mécanique et électronique ; à Françoise et Kévin pour leur soutien au début de ma thèse. Leurs constantes bienveillances, leur aide technique, leur amitié, et toutes les discussions efficaces sur les expériences m'ont beaucoup apporté. Merci aussi au sympathique stagiaire de M2, Mani Naresh, avec qui j'ai eu grand plaisir à travailler et à discuter.

Je remercie également tous les membres du LBPA pour les temps inoubliables que j'ai passés en votre compagnie. En particulier, je souhaite remercier Janine et Anne-Marie pour leur aide à résoudre les problèmes administratifs pendant mes trois années de thèse en France et pour mes commandes au labo. Merci à toutes les deux pour leur gentillesse et leur patience. Merci également à Martine pour les autoclaves. Ta disponibilité et ta gentillesse m'ont beaucoup frappée.

Je n'oublierai pas non plus mes collègues au LBPA : Marie-Christine, Françoise, Christine, Marie-Alix, Olivier, Gladys, Aurélie, Stéphanie, Barbara, Alexandra, Bernie, Laurent, Houcine, Bianca, Hervé, Philippe, Malcolm, Sylvie... Merci pour toutes les discussions scientifiques ainsi que pour les bons moments que nous avons pu partager. Un merci tout particulier à Marc: ton amitié, tes conseils, ton soutien pour les diverses corrections de mes expressions françaises m'ont beaucoup bénéficiée. Merci à tous pour m'avoir installée dans une ambiance amicable et pour toute la confiance dont vous avez fait preuve au cours de ces trois ans.

Un grand merci également à l'équipe de Xu-Guang XI de l'Institut Curie à Orsay qui s'est impliquée dans nos études en milieu biochimie et nous a fourni les différentes protéines Hélicase avec les quelles j'ai travaillées.

Je souhaite aussi remercier le programme de coopération entre l'GENS (Groupes des Ecoles Normales Supérieurs) et l'ECNU (East China Normal University), qui m'offre une formation complète et véritablement professionnelle. Merci à Madame Bogdana NEUVILLE, Christine ROSE et Brigitte VITALE à l'ENSC pour leur aide pour résoudre les problèmes administratifs et dans la vie quotidienne en France. Mes grands mercis également à Madame Yun-Hua QIAN, Monsieur Hai-sheng LI à l'ECNU pour leur aide concernant les affaires administratives en Chine.

Je tiens à mentionner mes collègues chinoises au labo : Yingying, Xiao-Ju, Huahua, et Rong-Bin, qui m'ont soutenue et supportée lors des moments difficiles au long de ma thèse et qui sont devenues mes amies très proches. Elles ont, chacune à leur manière, contribué à l'ambiance familiale au labo, je ne l'oublierai pas.

Enfin, merci à tous mes amis en France (Fan, Wu E, Zhou Ge, Tingting, Jingjing, Lili, Jiangjiang, Tongtong, Sun Zhe, Ding-wei, Elisa, Binbin, Géraldine, Yi Hua, Zhang Min, Haibin, Zhou Liang, Zhu Min-xuan, LI Chun, Gong Yan-chun, Irynka, Lulu...) pour leur humour, leur gentillesse, leur amitié, leurs conseils et soutiens de chaque instant lors des moments difficiles. Vous allez vraiment me manquer lorsque je retournerai en Chine.

Mon grand et même le plus important merci est pour toi: Jie. Ton amour, ton soutien et ta compréhension m'ont toujours accompagné pendant les 10 ans où tu as été à mes cotés. C'est toi qui m'as rappelé qu'il y a une vie hors de la science, et que c'est même souvent là qu'elle commence. Grâce à toi, je n'ai jamais peur face aux difficultés, parce que je sais que tu seras toujours là pour me soutenir et me supporter. Merci d'avoir eu confiance en mes choix et je suis convaincu que notre avenir sera plus beau.

Mes principaux remerciements s'adressent finalement à mes parents. Je vous remercie pour votre confiance que vous m'avez témoignée durant ce long parcours d'études. Merci de m'avoir donné la vie assez belle, de m'avoir aidée à croire en moi pendant toutes ces années d'études, et de m'avoir toujours bien soutenue sur le plan du moral et matériellement. Si j'ai eu une réussite là, c'est grâce à vous deux. Je vous dédie cette thèse.

*A ma famille ...*

# TABLE AND MATERIALS

REMERCIEMENTS .....	1
TABLE AND MATERIALS .....	4
TABLE OF FIGURES .....	6
ABREVIATIONS .....	6
摘要.....	10
PREFACE .....	18
INTRODUCTION ON FLUORESCENCE .....	22
I.1 General Definitions: Characteristics of fluorescence and the fluorescence microscope .....	24
I.1.1 <i>Photoluminescence process</i> .....	24
I.1.2 <i>Steady-state characteristics of fluorescence emission</i> .....	27
I.1.3 <i>Time - resolved characteristics of fluorescence emission, fluorescence lifetime</i> .....	37
I.2 Fluorescence anisotropy and instrumental considerations.....	39
I.2.1 <i>Steady-state fluorescence anisotropy: definition and principle</i> .....	39
I.2.2 <i>Time-resolved fluorescence anisotropy: definition and principle</i> .....	42
I.2.3 <i>Instrumentation and design of pulse fluorometers</i> .....	43
I.2.4 <i>Examples of application of fluorescence anisotropy in the field of biology</i> .....	46
I.3 Fluorescence correlation spectroscopy .....	48
I.3.1 <i>Fluorescence correlation spectroscopy: definition</i> .....	49
I.3.2 <i>Conceptual basis of Fluorescence correlation spectroscopy and determination of diffusion constant</i> .....	52
I.3.3 <i>Fluorescence cross-correlation spectroscopy: definition and conceptual basis</i> .....	53
I.3.4 <i>Instrumentations and methods of FCS and FCCS</i> .....	55
I.3.5 <i>Example of application of FCS and FCCS in the field of biology</i> .....	61
MOTIVATION AND OBJECTIVE .....	64
MATERIAL AND METHODES.....	67
II.1 Reagents and buffers .....	68
II.1.1 <i>HIV integrase related buffers</i> .....	68
II.1.2 <i>RecQ helicase related buffers</i> .....	69
II.2 Protein and oligonucleotides purification.....	70
II.2.1 <i>HIV integrase purification</i> .....	70
II.2.2 <i>RecQ helicase purification</i> .....	71
II.2.3 <i>Oligonucleotides purification and preparation</i> .....	72
II.3 Enzymatic activity measurements .....	73
II.3.1 <i>Steady-state fluorescence based activity measurements</i> .....	73
II.3.2 <i>Fluorescence cross-correlation measurements</i> .....	74
II.3.3 <i>Quantified maximum entropy method of time-resolved fluorescence data (MEM)</i> .....	77
APPLICATION OF FCCS TO STUDY THE ENZYMATIC KINETICS OF RECQ HELICASE .....	78
III.1 General introduction to the relationship between DNA and helicases.....	79
III.1.1 <i>Structure and function of DNA</i> .....	79
III.1.2 <i>The function of helicase in cellular processes involved with DNA</i> .....	81
III.1.3 <i>Helicase characteristics and helicase deficiency diseases</i> .....	84

III.2 E.Coli RecQ Helicase Unwinding Activity as Monitored by Dual Color Fluorescence Correlation Spectroscopy .....	91
<i>III.2.1 Introduction</i> .....	91
<i>III.2.2 Manuscript</i> .....	92
<i>III.2.3 Conclusion</i> .....	117
III.3 Human RecQ5 $\beta$ Unwinding and Strand-Annealing Activity as Monitored by Dual Color Fluorescence Correlation Spectroscopy .....	120
<i>III.3.1 INTRODUCTION</i> .....	120
<i>III.3.2 MATERIALS AND METHODS</i> .....	121
<i>III.3.3 RESULTS</i> .....	122
<i>III.3.4 DISCUSSION</i> .....	126
<i>III.3.5 PROSPECTIVE</i> .....	129
<i>III.3.6 FIGURES AND LEGENDS</i> .....	130
APPLICATION OF FLUORESCENCE ANISOTROPY TO STUDY ENZYMATIC KINETICS OF HIV-IN .....	138
IV.1 The basic biology of retroviruses .....	139
<i>IV.1.1 Structural taxonomic for the family of retroviruses</i> .....	139
<i>IV.1.2 Replication cycle and pathology of HIV-virus</i> .....	141
<i>IV.1.3 Introduction to anti-retroviral treatments</i> .....	144
<i>IV.1.4 Structure and function of HIV-integrase</i> .....	147
IV.2 The G140S mutation in HIV integrases from raltegravir-resistant patients rescues catalytic defect due to the resistance Q148H mutation .....	153
<i>IV.2.1 Introduction</i> .....	153
<i>IV.2.2 Manuscript</i> .....	154
<i>IV.2.3 Conclusion</i> .....	164
APPLICATION OF PHOTOLUMINESCENCE DECAY TO CHARACTERIZE QDS FLUORESCENCE PROPERTIES .....	166
V.1 General introduction to the semiconductor nanoparticles .....	167
<i>V.1.1 Definition of quantum dots</i> .....	167
<i>V.1.2 Spectral properties of quantum dots</i> .....	170
<i>V.1.3 Solubilization and biological applications of quantum dots</i> .....	171
V.2 Multi-exponential Photoluminescence Decay of CdTe Quantum Dots upon One and Two Photon Excitation .....	178
<i>V.2.1 INTRODUCTION</i> .....	178
<i>V.2.2 MATERIALS AND METHODS</i> .....	179
<i>V.2.3 RESULTS</i> .....	183
<i>V.2.4 DISCUSSION AND CONCLUSION</i> .....	186
<i>V.2.5 PROSPECTIVE</i> .....	188
<i>V.2.6 FIGURES AND LEGENDS</i> .....	188
GENERAL CONCLUSION .....	197
REFERENCES .....	202

# **TABLE OF FIGURES**

## ***INTRODUCTION ON FLUORESCENCE***

Figure 1 : Definition of Biophotonics. ....	19
Figure 2 : Illustration the multidisciplinary scope of biophotonics. ....	20
Figure 3 : Illustration of Perrin-Jablonski diagram. ....	25
Figure 4 : Illustration the Stokes shift. ....	28
Figure 5 : Illustration of principle of photoselection process. ....	32
Figure 6 : Relationship between anisotropy and the angle of emission. ....	35
Figure 7 : Configuration of the excitation and emission polarizers for observing a signal proportional to the total fluorescence intensity. ....	41
Figure 8 : Configuration of the time-resolved anisotropy when excited the sample with pulsed laser. ....	43
Figure 9 : Schematic diagram of a single-photon timing fluorometer. ....	45
Figure 10 : Instrumentation of anisotropy fluorometer. ....	45
Figure 11 : The principle of FCS measurements. ....	51
Figure 12 : Illustrations of the fluctuation about an average fluorescence count at given time. ....	51
Figure 13 : Principles of dual-color cross-correlation fluorescence spectroscopy. ....	55
Figure 14 : Schematic of two-photon excitation compared to one-photon excitation. ....	57
Figure 15 : Illustrations of two-photon excitation compared to one-photon excitation. ....	57
Figure 16 : Instrumentation of two-photon FCS. ....	60
Figure 17 : Schematic setup of two-photon FCCS. ....	60

## ***APPLICATION OF FCCS TO STUDY THE ENZYMATIC KINETICS OF RECQ HELICASE***

Figure 18 : DNA and its building blocks. ....	80
Figure 19 : Schematic of DNA replication process. ....	84
Figure 20 : Schematic illustration of E.Coli RecQ helicase structure. ....	86
Figure 21 : Two potential mechanisms for RhlB-activated degradation of structure RNA by the degradosome. ....	88

## ***APPLICATION OF FLUOROSCENCE ANISOTROPY TO STUDY ENZYMATIC KINETICS OF HIV-IN***

Figure 22 : Illustration of genomorganization of HIV. ....	140
Figure 23 : Schematic of phylogenetic tree of retrovirus. ....	140
Figure 24 : Replication cycle of HIV-1. ....	143
Figure 25 : IN catalysed reactions in vivo: 3'-OH terminal is in red and the 5' terminal is in green. ....	149
Figure 26 : Domains structure of HIV-IN. ....	150
Figure 27 : Structure of strand transfer inhibitor (INSTI). ....	152

## ***APPLICATION OF FLUROSCENCE DECAY TO STUDY THE PROPERTIES OF NANOCRYSTALS QDS***

Figure 28 : Emission maxima and size of QDs of different composition. ....	168
Figure 29 : Schematic of a core-shell QDs with a biologically compatible surface. ....	169
Figure 30 : Illustration of fluorescence decay. ....	169

## ABBREVIATIONS

3TC	lamivudine
A	Adenine
ACF	Auto-Correlation Function
AIDS	Acquired Immune Deficiency Syndrome
ALT	Alternative Lengthening of Telomeres
APD	Avalanche Photodiode
AZT	Zidovudine
BLM	Bloom Protein
BS	Bloom's Syndrome
C	Cytosine
CdSe	Cadmium Selenide
D4T	Stavudine
ddc	zalcitabin
ddI	Didanosine
dHJ	double Holiday Junction
DKAs	$\beta$ -Diketo Acids
DLV	Delavirdine
EFV	Efavirenz
EGF	Epidermal Growth Factor
FCCS	Fluorescence Cross-Correlation Spectroscopy
FA	Fluorescence anisotropy
FD	Frequency Domain
FDA	Food and Drug Administration
FIV	Feline Immunodeficiency Virus
FRET	Fluorescence Resonance Energy Transfer
FTC	Emtricitabine
G	Guanine
G4	G-quadruplex

HAART	Highly Active Anti-Retroviral therapy
HIV	Human Immunodeficiency Virus
HJ	Holiday Junction
HR	Homologous Recombination
IC <sub>50</sub>	50% Inhibitory Concentration
IN	Integrase
INBI	Integrase Binding Inhibitor
INSTI	Integrase Strand Transfer Inhibitor
Kb	Kilobases
Kd	Dissociation Constant
LADH	Liver Alcohol Dehydrogenase
MCA	Multi-Channel Analyzer
MLCK	Myosin Light-Chain Kinase
MMC	Mitomycin C
MMS	Methyl Methane Sulfonate
MPA	Mercaptopropionic Acid
MPE	Multi-Photon Excitation
NNRTI	Non-Nucleoside and nucleotide Reverse Transcriptase Inhibitors
nRTI	Nucleoside and Nucleotide Reverse Transcriptase Inhibitors
NSOM	Near-field Scanning Optical Microscopy
NVP	Nevirapine
OH	Hydroxyl
P	Phosphate
PBMCs	Peripheral Blood Mononuclear Cells
PIC	Pre-integration Complex
PIs	Protease Inhibitors
PL	Photoluminescence
QDs	Quantum Dots
QE	Quantum Efficiency
RAI	Raltegravir
RT	Reverse transcriptase

RTS	Rothmund-Thomson Syndrome
SCEs	Sister Chromatid Exchanges
SFs	Super Families
SMD	Single-Molecular Detection
SPT	Single Photon Timing
SSB	Single-Strand Binding Protein
T	Thynine
T20	Enfuvirtide
TAC	Time-to-Amplitude Converter
TCSPC	Time Correlated Single Photon Counting
TD	Time-Domain
TDF	Tenofovir
Tm	Melting Temperature
UV	Ultraviolet
WHO	World Health organization
WRN	Werner Protein
WS	Werner Syndrome
ZnS	Zinc Sulfide

---

# 摘要

---

当前，以基因工程、细胞工程、酶工程为代表的现代生物技术迅猛发展，人类基因组计划等重大技术也相继取得突破。生物医药产业化进程明显加快，现代生物技术在医学诊疗方面得到了广泛的应用。然而，功能性生物大分子在体内相互作用机制的研究仍有待发展。近年来，随着交叉学科的不断兴起，生物分子间相互作用的研究进入了更高的阶段，特别是一些光学方法和荧光标记的引入，使得体外生物分子间相互作用的研究由离体转入活体细胞（Lacowicz, 2006）。生命科学的发展对分析检测技术的灵敏度要求越来越高。本研究选取当前生物学领域中广泛采用的荧光光谱检测技术（如：荧光交联相关光谱技术，FCCS；荧光偏振检测技术，Fluorescence anisotropy 以及荧光强度衰退检测技术，Photoluminescence decay）并深入开展其在生物大分子相互作用机制中的应用研究，以期阐明生物系统内蛋白质-蛋白质、蛋白质-核酸以及核酸-核酸之间的相互作用机理。这不仅在理论上完善了荧光光谱检测技术在生命科学领域中应用的可行性，同时该研究为酶动力学参数计算，核酸分析，化学扩散常数计算，活细胞分析，肿瘤早期诊断以及高通量药物筛选等研究提供了数据支持。研究结果与结论如下：

### 一. 荧光交联相关光谱技术及其在 RecQ 解旋酶活性作用研究中的应用

荧光交联相关光谱（Fluorescence Cross-Correlation Spectroscopy, FCCS）是一种统计小样本中荧光分子的荧光强度波动的相关分析方法（Schwille, 2001）。在这种方法的经典模式中（Schwille et al., 1997），样本体积被聚焦激光束和共聚焦小孔所限定，样本发出的荧光被高数值孔径的显微镜物镜所收集，然后被灵敏的单光子技术其所监测。被探测到的荧光是随时间波动的，且这些时间函数是自相关的。归一化的荧光波动自相关函数提供了两类信息，函数的大小反比于所观测的荧光分子的平均数量，时间衰退的速率和形态反映了所观测的荧光分子的动力学特征。

荧光交联相关光谱的工作原理基于物质的荧光强度与其浓度（即荧光分子数）成正比的理论。在照射微区内由于布朗运动或化学反应使进入或离开微区的分子数目总是在其平衡值处发生变化，从而产生荧光涨落现象，它是时间的函数  $F(t)$ 。微区内的荧光分子数在任一时间  $t$  的变化导致荧光强度的涨落值为  $\delta F(t)$ ，它反映了分子在微区内的运动轨迹。用归一化自相关函数 (Normalized autocorrelation function)， $G_{ij}(\tau)$  可将荧光的涨落与延迟时间  $\tau$  相关：

$$G_{ij}(\tau) = \frac{\langle \delta F_i(t) \delta F_j(t + \tau) \rangle}{\langle F_i(t) \rangle \langle F_j(t) \rangle}$$

其中  $\langle \rangle$  代表时间平均值， $\delta F(t)$  表示在任一时间  $t$  时的荧光涨落， $\delta F(t + \tau)$  代表经延迟时间  $t$  后的荧光涨落。上式经过一系列数学推导后转换为：

$$G_{ij}(\tau) = \frac{1}{N} \cdot \frac{1}{(1 + \tau/\tau_D)} \cdot \frac{1}{1 + (\omega_0/z_0)^2 \cdot \tau/\tau_D}$$

其中  $N$  为照射区内双光子标记的物质分子数， $\tau_D$  为荧光分子的特征扩散时间常数， $\omega_0$  和  $z_0$  分别为微区的径向和轴向半径。该式包含了丰富的单分子动力学和热力学方面的信息。

本研究利用实验室自组装的荧光交联相关光谱仪器（仪器构造见 Figure 17），测定了 *E.Coli* RecQ 解旋酶蛋白对双链 DNA 的解链活性以及人类 RecQ5 $\beta$  解旋酶蛋白对序列互补单链 DNA 的链退火活性。该仪器采用远红外“飞秒”激光作为激发光源，基于激光共焦构型，构建了一套具有高灵敏度和高稳定性的荧光相关光谱单分子检测系统。系统采用高数值孔径物镜使激光束高度聚焦，并用同一物镜收集样品的荧光，单光子计数器用于实时记录荧光信号。实验选用双荧光标记互补链小片断寡聚核苷酸链作为研究底物，利用 FCCS 荧光检测技术实时监控大肠杆菌 RecQ 以及人类 RecQ5 $\beta$  解旋酶蛋白的酶促反应活性。

### 1) 应用 FCCS 技术监测 *E.Coli* RecQ 解旋酶蛋白的双链 DNA 解链活性

本实验选取高度保守的大肠杆菌 *E.Coli* RecQ 解旋酶（Xu et al., 2003）作为研究对象，并采用 FCCS 技术作为检测手段，监测 *E.Coli* RecQ 蛋白的酶促反应活性。实验基本原理如下：同时标记有 Alexas488 以及 TexasRed 的双色荧光生色团的双链 DNA 在 *E.Coli* RecQ 解旋酶作用下逐渐解开双链，最终生成两条独立的单链 DNA。FCCS 荧光检测表明，荧光交联相关曲线的振幅随 DNA 双链解链程度的增强而呈逐渐降低的趋势，至双链完全解旋，荧光交联相关曲线的振幅降至最低点，具体原理见章节 III.2.2 中 Figure 1 以及章节 III.2.2 中 Figure 2。实验分别在一级反应（酶浓度大于底物浓度）以及多级反应（底物浓度大于酶浓度）条件下监测 *E.Coli* RecQ 解旋酶酶促反应活性，研究结果表明：在一级反应条件下，*E.Coli* RecQ 蛋白对底物的作用方式具有温度依赖性；在 37 度孵育温度下 *E.Coli* RecQ 蛋白酶促反应活性要显著大于 25 度孵育温度的酶反应活性（见章节 III.2.2 中 Figure 3C），该现象主要归因于温度可显著影响蛋白对 DNA 底物的协同作用程度（见章节 III.2.2 中 Figure 4）。此外，DNA 底物核苷酸链的长度也会影响蛋白对底物的协同作用程度，进而引发酶促反应活性的显著差异。为了消除反应体系中自发的链“退火”现象对酶促反应常数的影响，本试验进而研究了与解链 DNA 互补的单链寡聚核苷酸片断对 *E.Coli* RecQ 蛋白酶促反应活性的影响，并比较了该效应与单链 DNA 结合蛋白（SSB）对 *E.Coli* RecQ 蛋白酶促反应活性的影响程度（见章节 III.2.2 中 Figure 7 与 Figure 8）。结果表明在反应体系中加入适当浓度（ $K_m$  值附近）的短链互补单链 DNA 片断（<10b）可显著提高 *E.Coli* RecQ 蛋白酶促反应活性。长片断互补单链 DNA（32b；45b）会抑制 *E.Coli* RecQ 蛋白酶促反应活性，该结果印证了长链 DNA 对解旋酶蛋白具有更强的亲和力，进而非特异性的结合反应体系中的酶蛋白，

从而抑制其蛋白酶促反应效率。在多级反应条件下，DNA 底物链长度不会影响酶蛋白对底物协同作用效应，主要由于反应体系中底物浓度远远大于酶蛋白浓度，该结果再次印证了一级反应条件下蛋白酶促活性的差异是由于酶蛋白对底物协同作用效应差异而引起的。

## 2) 应用 FCCS 技术监测 RecQ5 $\beta$ 解旋酶蛋白的互补单链 DNA 链“退火”活性

RecQ 家族解旋酶对保持遗传稳定性起着重要的作用。在人体细胞内，至少有 5 种 RecQ 解旋酶，其中 BLM, RecQ4 和 WRN 解旋酶的缺失或变异分别会导致 Bloom, Rothmund-Thomson 以及 Werner 综合症 (Wang et al., 2003)。当前，有报道关于人类 RecQ5 $\beta$  解旋酶蛋白具有互补单链 DNA 链“退火”活性，然而关于 RecQ5 $\beta$  解旋酶蛋白引发互补单链 DNA 链“退火”现象的具体原因尚不清楚。本研究采用 FCCS 技术作为检测手段，监测人类 RecQ5 $\beta$  解旋酶蛋白的酶促反应活性。实验基本原理如下：分别标记有 Alexas488 以及 TexasRed 的荧光生色团的互补单链 DNA 在 RecQ5 $\beta$  解旋酶蛋白作用下逐渐杂交形成双链，最终生成一条稳定的双链 DNA。FCCS 荧光检测表明，荧光交联相关曲线的振幅随 DNA 双链“退火”程度的增强而呈逐渐增加的趋势，至双链完全形成，荧光交联相关曲线的振幅增加至最高点，具体原理见章节 III.3.6 中 Figure 1A。为了更好的证明双链 DNA 的形成是由于 RecQ5 $\beta$  酶蛋白的酶促反应活性，而并非仅仅由于酶蛋白同时与两条互补单链 DNA 结合，拉近了两条互补链的距离，从而增加了互补单链自发“退火”的几率，本研究比较了不同温度下互补单链 DNA 自发链“退火”程度（无 RecQ5 $\beta$  酶蛋白），以及在添加 RecQ5 $\beta$  酶蛋白条件下互补单链 DNA 链“退火”程度。研究结果表明 RecQ5 $\beta$  酶蛋白能够引发互补单链 DNA 链“退火”反应，且该反应活性与 DNA 底物链长度无关（见章节 III.3.6 中 Figure 3A. B.）。同时在较高温度下互补单链 DNA 链“退火”程度较高，虽然互补单链 DNA 自发链“退火”程度也有温度依赖性，但程度远远低于添加 RecQ5 $\beta$  酶蛋白的反应体系（见章节 III.3.6 中 Figure 5）。通过研究 RecQ5 $\beta$  酶蛋白在不同孵育温度下对 DNA 的底物亲和力，结果表明 RecQ5 $\beta$  酶蛋白对底物 DNA 结合能力不受孵育温度的影响，进而印证了较高温度下较强的互补单链 DNA 链“退火”程度归因为 RecQ5 $\beta$  酶蛋白自身具有的酶促反应活性（见章节 III.3.6 中 Figure 2）。该研究还检测了反应体系中镁离子浓度对互补单链 DNA 链“退火”程度的影响，结果表明人类 RecQ5 $\beta$  解旋酶蛋白的互补单链 DNA 链“退火”活性不具有镁离子依赖性。

综合上述 *E.Coli* RecQ 解旋酶蛋白对双链 DNA 的解链活性以及人类 RecQ5 $\beta$  解旋酶蛋白对序列互补单链 DNA 的链退火活性研究情况，结果表明荧光交联相关光谱技术 FCCS

适用于实时监测 RecQ 解旋酶蛋白的酶促反应活性。且该检测体系具有较高的灵敏性与稳定性。

## 二. 稳态荧光偏振检测技术在 HIV 病毒整合酶蛋白酶促反应活性研究中的应用

用偏振光去激发一个荧光系统，可以产生偏振荧光（Fluorescence Polarisation）。通过对偏振光的分析可确定分子的大小，形状和流动性等性质。因此偏振荧光分析在生物研究中是一种有力的手段（Lacowicz, 2006）。

荧光偏振测量原理如 Figure 8 所示：假设沿 z 轴震动的平面偏振光由 x 轴入射原点。原点处的荧光分子受激发后发射偏振荧光，在 y 轴收集偏振荧光，令  $I_H$  为沿 z 轴震动的偏振荧光，令  $I_V$  为沿 x 轴震动的偏振荧光，则荧光各向异性 a 可被定义为：

$$a = \frac{I_H - I_V}{I_H + 2I_V}$$

在溶液中的分子其分布是随机的，而且从吸收到发射的时间之内，分子本身已经产生了转动。因此荧光各向异性可以反映分子在朝向无规律且分子不能自由运动溶液中的分子特性。当采用恒定的激发光源时，荧光各向异性被称为稳态荧光不对称性，即 Steady-State Fluorescence Anisotropy。

本研究采用稳态荧光偏振检测仪 Beacon 2000 (PanVera, Madison, WI) 来实时监控 HIV 病毒整合酶蛋白与底物 DNA 结合过程中稳态偏振荧光数值的变化。实验选用具有 HIV 病毒序列特异性的 DNA 底物 (5'-GTGTGGAAAATCTCTAGCAGT-3')，其中 3'端的-GT 序列是 HIV 病毒整合酶活性作用过程中特异性的酶切位点。该序列 3'端被特异性标记了荧光素分子，利于观测病毒整合酶的作用活性。HIV 病毒整合酶对病毒特异性底物的活性作用分两个步骤：1) 整合酶稳定的结合到特异性 DNA 底物上。该步骤的酶促反应一般在 25 度孵育温度下完成。孵育过程中形成的整合酶-DNA 复合体数量 (Y) 可以通过下式计算：

$$Y = \frac{r - r_{ODN}}{r_{max} - r_{ODN}} \times 100$$

式中  $r_{max}$  与  $r_{ODN}$  分别表示整合酶-DNA 复合体以及单独 DNA 底物条件下的荧光偏振值。2) HIV 病毒整合酶对 DNA 底物 3'端 -GT 序列切割过程。该过程可以反映病毒整合酶将病毒 DNA 整合到宿主 DNA 过程中的酶促反应动力学参数。3'端 -GT 序列切割过程在 37 度孵育温度下完成，该步骤酶促反应活性可以通过稳态荧光偏振值的降低程度来衡量。常用的量化方法分以下两种：a) 采用 0.25% 终浓度的 SDS 在规定的反应时间内中止反应。此时在该反应体系中含有两类荧光标记物，分别为未被整合酶处理的寡聚核苷酸以及在整合酶

3'端切割过程中产生的荧光素标记的-GT 序列。这里被释放的双核苷酸数量 ( $F_{\text{dinu}} = [\text{GT}]/[\text{DNA}]_{\text{total}}$ ) 可以通过下式计算:

$$F_{\text{dinu}} = \frac{r_{\text{NP}} - r}{r_{\text{NP}} - r_{\text{dinu}}}$$

式中  $r_{\text{NP}}$  及  $r_{\text{dinu}}$  分别表示未被整合酶处理前双链寡聚核苷酸的荧光偏振值以及被整合酶处理后-GT 双核苷酸的荧光偏振值。本研究采用 Eurogentec 公司商业合成的 5'-GT-3'F 双核苷酸来确定荧光偏振值  $r_{\text{dinu}}$ 。b) 在实时动态监测过程中, 反应体系中除却未被整合酶处理的寡聚核苷酸以及在整合酶 3'端切割过程中产生的荧光素标记的-GT 序列外还存在整合酶-DNA 复合体荧光物质。此时,  $F_{\text{dinu}}$  采用下式计算:

$$F_{\text{dinu}} = \frac{r_{t=0} - r}{r_{\text{max}} - r_{\text{dinu}}}$$

式中  $r_{\text{max}}$  表示最大反应活性下的特征荧光偏振值,  $r_{t=0}$  表示整合酶 3' 处理活性作用前的荧光偏振值。在一级反应的条件下, 表观酶动力学参数可以通过下式获得:

$$\ln(1 - F_{\text{dinu}}) = -k_{\text{obs}} \times t$$

且

$$k_{\text{obs}} = K_{\text{chemistry}} / ((k_{\text{d,app}} / [I]_0) + 1)$$

式中  $k_{\text{chemistry}}$  表示一级反应的反应级数,  $K_{\text{d,app}}$  表示表观解离常数。

基于上述反应原理, 本试验研究了两类主要的针对 HIV 病毒复制以及重组 HIV 整合酶蛋白催化特性的遗传抑制通路 (N155H 以及 G140S/Q148H)。该研究采用稳态荧光偏振检测技术, 成功实时监测了野生型以及突变型 HIV 整合酶蛋白的 DNA 结合活性以及 3'端处理活性。结果表明 N155H, G140S, Q148H 以及 G140S/Q148H 每种整合酶遗传突变体都会对整合酶蛋白活性产生抑制作用, 然而抑制程度依据突变类型的不同存在不同程度的差异。其中 Q148H 突变在单独存在的情况下对抗病毒药物 RAL 具有最强的抗药性; G140S 则表现出较弱的抗药性; 然而 G140S/Q148H 双重突变体却表现出极强的抗药性, 且此时病毒复制水平类似于野生型 HIV 病毒。但是研究表明 Q148H 突变不仅抑制了重组病毒整合酶的催化活性, 同时该突变体也严重抑制了病毒的复制能力。尽管 G140S 未表现出强烈的抗药性, 但该突变可以帮助 Q148H 突变体恢复病毒复制能力。这与体外试验研究结果一致: 即 G140S/Q148H 双重突变体能够恢复至野生型病毒整合酶的活性, 但 Q148H 单突变体不具备该能力。该结果很好的诠释了为何艾滋病患者在服用 RAL 抗病毒

药物后体内会很快形成 G140S/Q148H 双重突变整合酶。本研究还表明较之 N155H 突变体，Q148H 突变体具有更强的抗 RAL 抗药性，进而解释了为何艾滋病患者在服用 RAL 抗病毒药物后体内的 N155 代谢通路会很快转变为 Q148H 代谢通路。

### 三. 荧光强度衰减检测技术在 纳米量子点荧光特性研究中的应用

荧光强度衰减 (Photoluminescence decay) 检测技术是与荧光寿命相关的高效、灵敏分析手段。荧光寿命通常被定义为荧光分析再回到基态之前驻留在激发态的时间。检测荧光寿命将直接指示反应环境与反应物状态的变化，在监测生化和生物反应进程作用中具有广泛的应用前景。

荧光寿命测定的原理基于一种被称作时间关联的单光子计数技术( Time-Correlated Single Photon Counting, TCSPC)，试验过程采用一个脉冲激光器重复激发样品，调节激发脉冲的强度，使得对于任何一个脉冲，在探测器上只有一个光子被计数。按照测量的激光脉冲和探测器感应之间的这段时间，将计数值引入已用荧光计数和时间绘制的柱状图。该基本试验的千万分之一的重复的数据积分会产生一个平滑的曲线，这条曲线代表的就是一条荧光衰减曲线。为了确保单光子计数模式，试验中采用的计数速率相当于激发速率的 1%。Mai-Tai 远红外激发光源的激发速率为 25-100 纳秒产生一次脉冲，从而使得使用者在不到一秒中能够在探测器上收集到一千万个重复计数。因此，在荧光寿命检测和标准检测模式之间的最主要技术差别是它避免了时间平均化，可对分子进行动态观测，从这个角度讲该法则也被称作“时间显微术”。对于衰减曲线性状的描述主要依据曲线本身。特征越少，越容易描述。通常一条单阶衰减曲线的形状很容易用一个单一的参数定义，该参数即为单阶的时间寿命。而在一个复对数的曲线上，时间寿命则等同于曲线斜率的倒数。对于具有不同时间寿命的物质所构成的一个样品所衍生的衰减曲线，则需要更复杂的描述。本试验选用描述二阶模式的二阶衰减曲线的方法，是产生四个参数。包含两个时间寿命 ( $\tau_1, \tau_2$ ) 和对应的两个振幅 ( $\alpha_1, \alpha_2$ )。利用公式

$$\langle \tau \rangle = (\alpha_1 \cdot \tau_1 \cdot \tau_1 + \alpha_2 \cdot \tau_2 \cdot \tau_2) / (\alpha_1 \cdot \tau_1 + \alpha_2 \cdot \tau_2)$$

可以得到一个值，将其定义为平均时间寿命。平均时间寿命类似用单阶曲线归一化相同数据即可得到荧光寿命的值。

本试验采用荧光衰减检测技术以及常用的光谱技术来研究实验室合成的具有 MPA 外壳 CdTe 纳米量子点荧光特性。分析了量子点体积依赖性和温度依赖性相关的时间相关荧光衰减特征曲线，结果表明：最小体积纳米量子点（直径约为 2 纳米）的激发光谱在较长的波长处具有一个小峰值。CdTe 量子点的荧光寿命峰值分布在 0.1ns, 1-3ns, 10-20ns 以及 40-50 ns。类似的分析结果曾被 Fernandez-Aguelles 采用荧光共振能量转移技术在 CdSe 纳米

量子点特性研究中报道过(Fernandez-Agüelles et al., 2007)。此外, 研究结果表明量子点体积越大, 其荧光寿命衰减越慢。且荧光寿命的数值在单光子激发与双光子激发情况下无显著差异。温度梯度研究结果表明, 在较高温度下, 纳米量子点的荧光衰减寿命越慢。上述研究结果表明纳米量子点的荧光光谱特性相当复杂, 且与量子点的体积大小密切相关。因而量子点在荧光共振能量转移研究技术中的应用需要多阶分析函数模型的辅助。纳米量子点表面电荷对其荧光衰减特性影响的研究仍有待发展。

综上所述, 随着生命科学的发展, 荧光光谱技术的日趋完善以及商品化专用仪器的问世, 荧光光谱检测方法在生命科学中的应用也会越来越广, 特别在生物分子相互作用、活细胞分析、疾病早期诊断、蛋白、肽以及酶研究及高通量筛选方面有巨大的研究潜力。本论文成功将多种现代荧光相关光谱检测技术用于酶动力学参数监测以及化学合成纳米量子点荧光特性的研究当中, 并阐明了该检测手法较之传统微量元素检测技术的优越性以及该检测手法的生物适应性。荧光检测技术与微分离技术(如: 毛细管电泳, 微流控芯片)联用会更进一步推动该技术的发展, 同时如何将该技术拓展到纳米材料、环境科学等领域的研究将具有更广阔的应用前景。

---

# **PREFACE**

---

Currently, we live in an era of technological revolutions which are among the most important things that happen to humanity and would continue to impact our lives. During the past century, many technological breakthroughs, such as emergence of new materials, the developments in telecommunications...have constantly redefined the activities of our social interactions. One of the most significant technological breakthroughs among them is photonics. Since the demonstration of the first laser in 1960, the photonics has been greatly revolutionized.

Meanwhile, the life science began to show its tremendous impacts to our modern world. The words like *gene manipulation*, *cloning*, *genetic engineering*, etc. have stumbled our daily newspapers and have drawn the attentions to the exact biological systems. However, many biological mechanisms are barely known to exist, let alone fully understood. Therefore, the primary goals of current biological research are not only the identification, but also the precise physico-chemical characterization of elementary processes at the level of individual proteins and nucleic acids. To address these real-time quantifications in life systems, a new extension of photonics which involves a fusion of photonics and biology has been proposed. It is termed as BIOPHOTONICS.

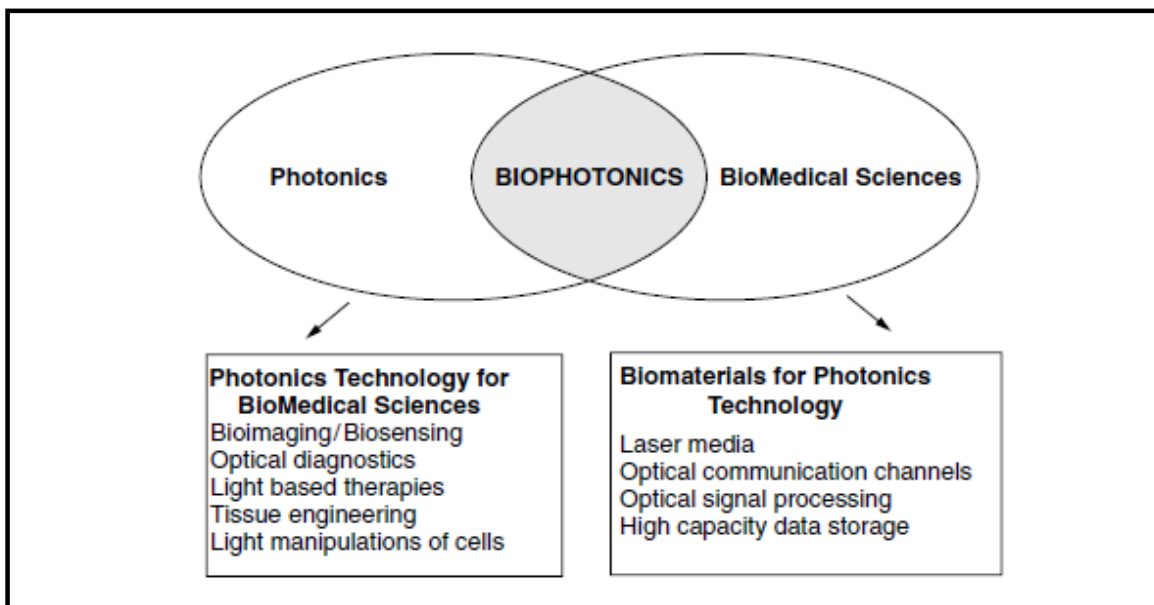


**Figure 1 : Definition of Biophotonics.**

The biophotonics has been defined as the fusion of photonics and biomedical sciences. The two broad aspects of biophotonics are also identified. *From (Prasad, 2003).*

Biophotonics is the exciting marriage of photonics and biology (Prasad, 2003). It deals with interactions between light and biological matter. A general introduction to biophotonics is illustrated in Figure 1. Research in field of biophotonic is addressing important issues in many disciplines, such as life, medical and pharmaceutical sciences. Key fields of biophotonics include optical diagnostics and therapy, photobiology and biophotonic materials.

New frontiers have been reached in this newly emerged interdisciplinary, which integrated four major technologies: lasers, photonics, nanotechnology, and biotechnology. Fusion of these technologies truly offers a new dimension for both diagnostics and therapy. An overview of biophotonics for health care applications is presented in Figure 2. It illustrates the scope of biophotonics through multidisciplinary comprehensive research and development possibilities, and could offer tremendous opportunities for both biotechnology development and fundamental research.

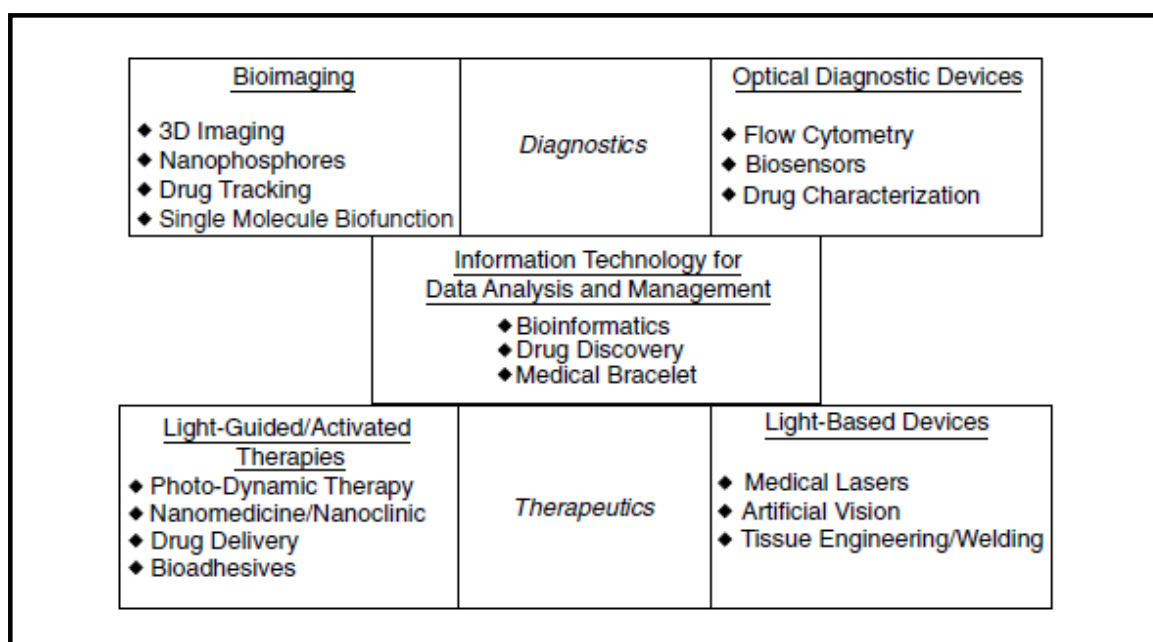


**Figure 2 : Illustration the multidisciplinary scope of biophotonics.**

The comprehensive multidisciplinary scope of biophotonics for health care has been illustrated. From (Prasad, 2003).

In this case, biophotonics offers challenging opportunities for biomedical researches. Our present study aims at understanding the fundamental principles of the light activation of biomolecules, bioassemblies, and the subsequent photoinduced processes. Meanwhile, the understanding of multiphoton processes by use of ultrashort laser pulses is a necessity to evaluate time-resolved processes in living biological systems. This thesis encompasses the fundamentals and various applications involving the integration of light, photonics and biology into biophotonics. The description of future directions of research and development is also provided.

---

# **INTRODUCTION ON FLUORESCENCE**

---

In the early 19th century, biologists strove to characterize molecular interactions directly in the intracellular environment (Bacia *et.al.*, 2006). Biological macromolecules are inherently heterogeneous, exhibiting different folded states, distinct conformations or varying stages during typical biological process. Microscopy techniques using visible light are applicable to living entities but are intrinsically limited by optical resolution. Recently, the growing importance of fluorescence microscopy as a tool of investigation, analysis, control and diagnosis in the field of biology has gained great attention of biologists due to (1) the extraordinary development of new fluorescent molecular probes and (2) the development of improved low light level imaging systems and confocal microscopy techniques, for example, the development and design of detectors (e.g. avalanche photodiodes), light sources (e.g. laser diodes) and compact ultra-fast electronic devices. Advanced fluorescence microscopes, including confocal fluorescence microscopy, two-photon excitation fluorescence microscopy and near-field scanning optical microscopy (NSOM), have been widely applied in biological studies.

In between, the single-molecule techniques nowadays represent practical methods for the elucidation of the structural rearrangements of biological relevant macromolecules. Single-molecule-sensitive techniques, such as fluorescence correlation spectroscopy (FCS) grants access to processes on single molecule scale by extracting information from molecular dynamics, such as diffusion, binding, enzymatic reactions and co-diffusion. As a result of various recent advances, this technique shows promise even for intracellular applications. Another important process that occur in the excited state is fluorescence resonance energy transfer (FRET), which supports a wide range of different applications, including real-time monitoring of conformational rearrangements (e.g. protein folding). In detail, the method of FCS could be used to determine the translational diffusion coefficient for a single fluorescent species undergoing Brownian motion. The application of FCS to monitor the fluorescence of fluorescently labeled proteins and nucleic acids and to the fluorescent lipid probes in phospholipids bilayers has been widely reported (Maiti *et al.*, 1997; Kinjo *et al.*, 1998; Fradin *et al.*, 2003). However, if excited molecules can rotate during the excited-state, the emitted fluorescence is partially depolarized and the rotational motion of a fluorophores causes fluctuations in fluorescence intensity. In this case, we can obtain information on the molecular motions, which depend on the size and the shape of molecules and also on the fluidity of their microenvironment from the extent of fluorescence depolarization (Deprez *et al.*, 2004; Guiot *et al.*, 2006).

This chapter is focused on the principle and the diverse properties of advanced techniques in fluorescence spectroscopy used in the following sections. Present chapter helps better understanding of the essential role of fluorescence studies and its applications in biological processes. Physical bases and the general characteristics of fluorescence emission process are overviewed in the first part. The principles and instrumentations of steady-state fluorescence anisotropy, time-resolved fluorescence anisotropy and the effect of rotational Brownian motion are described in the second part. The theories of Fluorescence correlation spectroscopy for the determination of translational diffusion and its instrumentation are overviewed in the third part. Its dual-color variant, Fluorescence cross correlation spectroscopy (FCCS) would also be discussed in this part.

## ***1.1 General Definitions: Characteristics of fluorescence and the fluorescence microscope***

### ***1.1.1 Photoluminescence process***

Photoluminescence (PL) is a process in which a substance absorbs photons (electromagnetic radiation) and then re-radiates photons. The efficiency of this process is characterized by the quantum yield value which derives from the value between number of luminescence photons versus absorbed photons. The possible processes are: photon absorption, internal conversion, fluorescence, intersystem crossing, phosphorescence, delayed fluorescence and triplet-triplet transitions which are convenient to be visualized through the Perrin-Jablonski diagram (Lakowicz, 1983). Once a molecule is excited by absorbing one photon, it reaches a metastable state and therefore it may returns to the ground state with emission of light, but many other pathways for de-excitation are also possible (Figure 3): internal conversion (direct return to the ground state without emission of fluorescence), intersystem crossing (possibly followed by emission of phosphorescence), intramolecular charge transfer and conformational change. As shown in Figure 3, The singlet electronic states are denoted as  $S_0$  (fundamental electronic state),  $S_1$ ,  $S_2$ , ... and the triplet states,  $T_1$ ,  $T_2$ , ... Vibrational levels are associated with each electronic state. The vertical arrows corresponding to absorption start from the 0 (lowest) vibrational energy level of  $S_0$  because the majority of molecules are in this level at room temperature. Absorption of a photon can bring a molecule to one of the vibrational levels of  $S_1$ ,  $S_2$ , ...

Emission of photons accompanying the  $S_1 \rightarrow S_0$  relaxation is called fluorescence. Apart from a few exceptions (e.g. emission from  $S_2$  in the case of azulene; simultaneous emission from  $S_1$  and  $S_2$  in the case of indole in some solvents), fluorescence emission occurs from  $S_1$  and therefore its characteristics (spectrum, quantum yield, lifetime) do not depend on the excitation wavelength. It should be noted that emission of a photon is as fast as absorption of a photon ( $\approx 10^{-15}$ s). However, excited molecule stays in the  $S_1$  state for a certain time (a few tens of picoseconds to a few hundreds of nanoseconds, depending on the type of molecule and the medium) before emitting a photon or undergoing other de-excitation processes. Thus, after excitation of a population of molecules by a very short pulse of light, the fluorescence intensity decreases exponentially with a characteristic time, reflecting the average lifetime of the molecules in the  $S_1$  excited state.

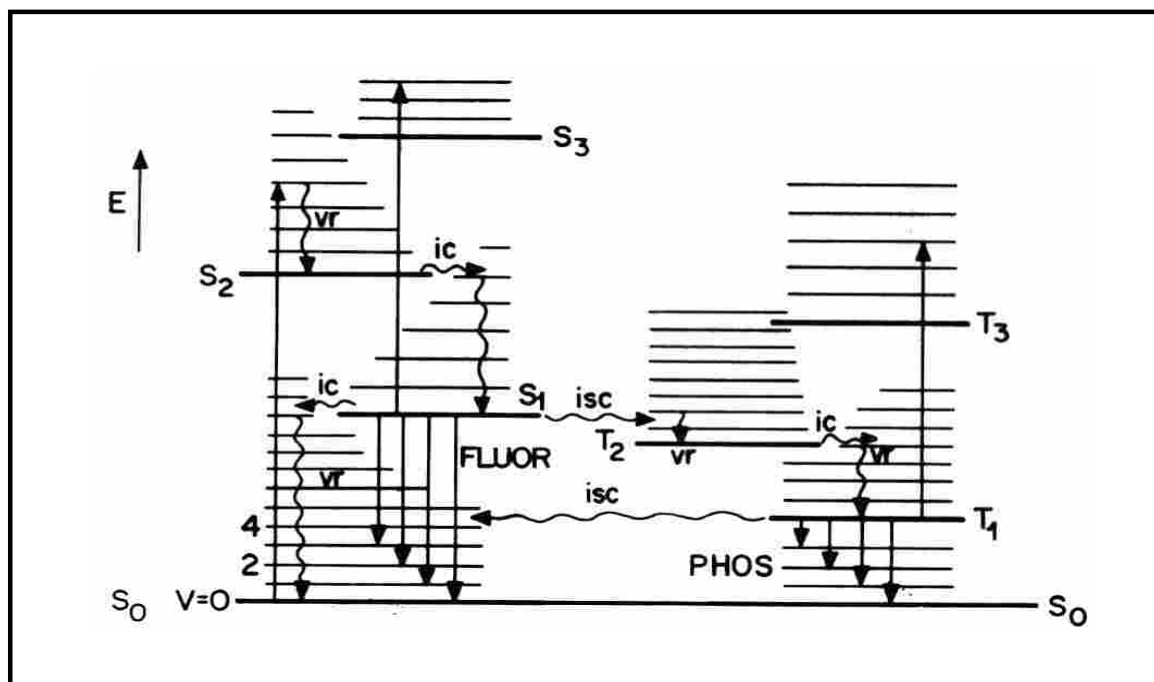


*Figure 3 : Illustration of Perrin-Jablonski diagram.*

Perrin-Jablonski diagram and illustration of the relative positions of absorption, fluorescence and phosphorescence spectra. *From (Lakowicz, 1983).*

Internal conversion is a non-radiative transition between two electronic states of the same spin multiplicity. In solution, the absorption process is followed by a vibrational relaxation towards the lowest vibrational level of the final electronic state. The excess vibrational energy can be indeed transferred to the solvent during collisions of the excited molecule with the surrounding solvent molecules.

Intersystem crossing is also a possible de-excitation process from  $S_1$  toward the  $T_1$  triplet state. It is a non-radiative transition between two isoenergetic vibrational levels belonging to electronic states of different multiplicities. Crossing between states of different multiplicity is in principle forbidden, but spin-orbit coupling (e.g. coupling between the orbital magnetic moment and the spin magnetic moment) can be large enough to make it possible. Generally speaking, it is consisted of four phenomena: 1) Phosphorescence. In solution at room temperature, non-radiative de-excitation from the triplet state  $T_1$  is predominant over radiative de-excitation, the latter phenomenon is called phosphorescence (Transition from  $T_1$  to  $S_0$ ). The phosphorescence spectrum is located at wavelength higher than the fluorescence spectrum because the energy of the lowest vibrational level of the triplet state  $T_1$  is lower than that of the singlet state  $S_1$ . The phosphorescence lifetime is much longer than fluorescence lifetime, typically from micro to milliseconds. 2) Thermally activated delayed fluorescence (Delayed fluorescence of E-type). Reverse intersystem crossing  $T_1 \rightarrow S_1$  can occur when the energy difference between  $T_1$  and  $S_1$  is small and when the lifetime of  $T_1$  is long enough. This results in emission with the same spectral distribution as normal fluorescence but with a much longer decay time constant because the molecules stay in the triplet state before emitting from  $S_1$ . This fluorescence emission is thermally activated; consequently, its efficiency increases with increasing temperature. 3) Triplet-triplet annihilation (Delayed fluorescence of P-type). A collision between two molecules in the  $T_1$  state can provide enough energy to allow one of them to return to the  $S_1$  state in concentrated solutions. Such a triplet-triplet annihilation thus leads to a delayed fluorescence emission. The decay time constant of the delayed fluorescence process is half the lifetime of the triplet state in dilute solution, and the intensity has a characteristic quadratic dependence with excitation light intensity. 4) Triplet-triplet transition. Once a molecule is excited and reaches triplet state  $T_1$ , it

can absorb another photon at a different wavelength because triplet-triplet transitions are spin allowed. These transitions can be observed provided that the population of molecules in the triplet state is large enough, which can be achieved by illumination with an intense pulse of light.

## ***1.1.2 Steady-state characteristics of fluorescence emission***

### ***1.1.2.1 Emission and excitation spectra***

The fluorescence emission spectrum reflects the distribution of the probability of the various transitions from the lowest vibration level of  $S_1$  to the various vibration levels of  $S_0$ . When a system (be it a molecule or atom) absorbs a photon, it gains energy and enters an excited state. One way for the system to relax is to emit a photon, thus losing its energy. When the emitted photon has less energy than the absorbed photon, this energy difference is the Stokes shift (Stokes, 1852; Lakowicz, 1983). Both absorption and radiation (emission) of energy are unique characteristics of a particular molecular structure (Figure 4) in a given environment. Generally speaking, there is a “mirror effect” between the fluorescent emission spectra and excitation spectra, which is called mirror-image rule. Although often true, many exceptions to the mirror-image rule occur because of the dissimilarity between the two spectra which could deviate the existence of several molecular forms, and hence introduce the excitation and emission wavelength differences.

Stokes shift has significant characteristics in practical research. If the Stokes shift is not far enough, it would be difficult to separate the excitation wavelength and emission wavelength by use of filters, and hence the fluorescent signal detection efficiency would be diminished. In addition, emission spectrum could be distorted by re-absorption. This important parameter can also provide information on the excited states. For instance, when the dipole moment of a fluorescent molecule is higher in the excited state than in the ground state, the Stokes shift increases with solvent polarity. In addition, fluorescence has another general property: that is known as the same fluorescence emission spectrum is generally observed irrespective of the excitation wavelength, which is denoted as Kasha’s rule (Kasha, 1950).

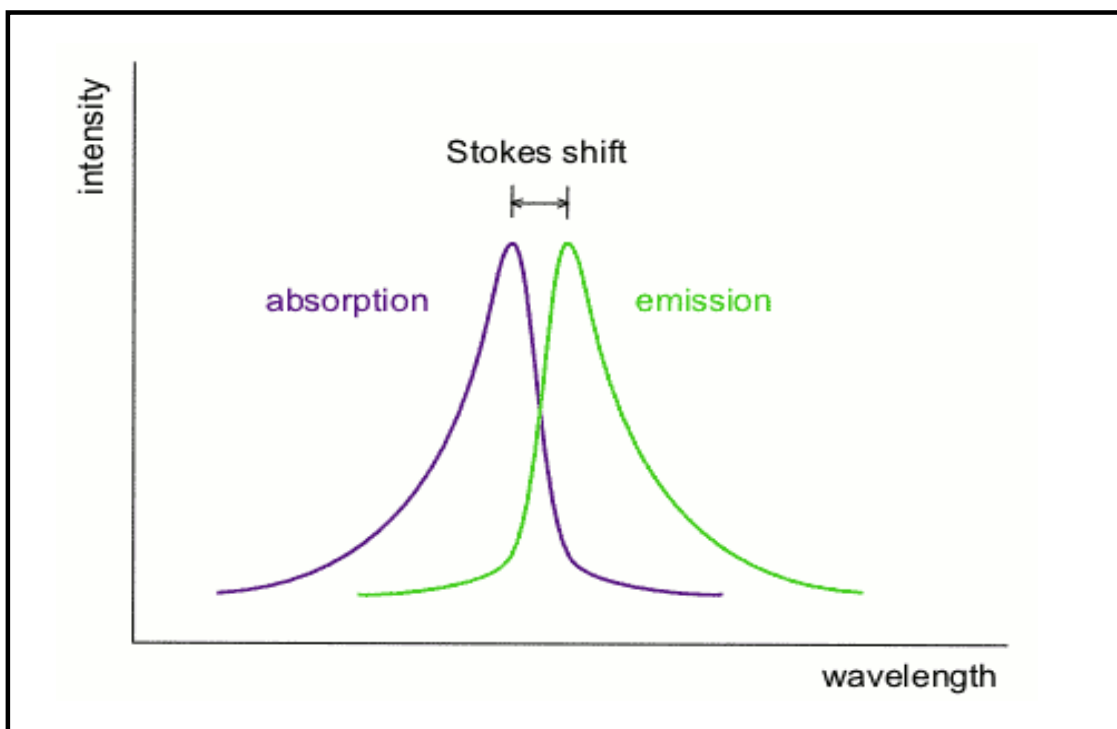


**Figure 4 : Illustration the Stokes shift.**

Characteristics of the fluorescence excitation and emission spectra, which is termed as the stokes shift. *From (Lakowicz, 2006).*

### ***1.1.2.2 Lifetimes and quantum yields***

Lifetimes and quantum yields are two important characteristics of fluorescence. The fluorescence quantum yield  $Q$  is defined as the number of emitted photons relative to the number of absorbed photons. The rate constants for the various excitation processes will be denoted as follows:  $K_0$ : rate constant for radiative deactivation  $S_1 \rightarrow S_0$  with emission of fluorescence. Here the fluorescence emission processes is characterized by the probability of  $K_0 = \tau_0^{-1}$ ;  $K_{nr}$ : overall non-radiative rate constant, which is in sum of rate constant for internal conversion and rate constant for intersystem crossing, collisional processes and other non-radiative processes . Consider a dilute solution system in which the de-excitation processes resulting from intermolecular interactions are not taken into account, the fluorescence species A whose concentration is  $[f]$  (in mol L<sup>-1</sup>), a very short pulse of light at time 0 brings a certain number of molecules A to the  $S_1$  excited state by absorption of photons. These excited molecules then return to  $S_0$ , either radiatively or non-radiatively, or undergo intersystem crossing. As in classical chemical kinetics, the rate of disappearance of excited molecules is expressed by the following differential equation:

$$\frac{df^*}{dt} = -(K_0 + K_{nr})f^* \quad (1.1.1)$$

Integration of this equation yields the time evolution of the concentration of excited molecules  $[f^*]$ . Let  $I_F$  (which equals to  $[f^*]$ ) be the emitted fluorescence intensity at time  $t$  and  $I_0$  (which equals to  $[f^*]_0$ ) be the fluorescence intensity at time 0. Integration leads to

$$I_F(t) = I_0 \exp\left(-\frac{t}{\tau_F}\right) \quad (1.1.2)$$

Where  $\tau_F$ , the lifetime of excited state  $S_1$ , is given by

$$\tau_F = \frac{1}{k_0 + k_{nr}} \quad (1.1.3)$$

The fluorescence decay time  $\tau_F$  is one of the most important characteristics of a fluorescent molecule because it defines the time window of observation of dynamic phenomena. As illustrated by Valeur (Valeur, 2002), no accurate information on the rate of phenomena occurring at time-scales shorter than about  $\tau/100$  ('private life' of the molecule) or longer than about  $10\tau$  ('death' of the molecule) can be obtained, whereas at intermediate times ('public life' of the molecule) the time evolution of phenomena can be followed.

Over the whole duration of the decay, the relation between the number of emitted fluorophores ( $N_{em}$ ) and fluorescence intensity  $I_0$  is given by

$$N_{em} = \int_0^{\infty} I_F(t) dt = \tau_F I_0 \quad (\text{I.1.4})$$

At time  $t = 0$ , the number of excited molecules equals to the number of absorbed photons ( $N_{ab}$ ). In this case, the fluorescence intensity is defined as

$$I_0 = K_0 N_{ab} \quad (\text{I.1.5})$$

The fluorescence quantum yield  $Q$  is the fraction of excited molecules that return to the ground state  $S_0$  with emission of fluorescence photons. Using the radiative lifetime, as previously defined in equation I.3.3, the fluorescence quantum yield can also be written as:

$$Q = \frac{N_{em}}{N_{ab}} = \frac{\tau_F}{\tau_0} \quad (\text{I.1.6})$$

In case of  $k_{nr} \ll k_0$ , the fluorescence decay time is close to the radiative lifetime  $\tau_0$ , therefore the fluorescence quantum yield which is close to 1.0. However, such proportionality may not be valid if de-excitation pathways (ways that out of dynamic quenching and variation in temperature) introduce interactions with other molecules. A typical case where the fluorescence quantum yield is affected without any change in excited-state lifetime is the formation of a ground-state complex that is non-fluorescent.

### ***I.1.2.3 Fluorescence polarization and emission anisotropy***

The theory for fluorescence anisotropy can be derived by consideration of a single molecule. For most experiments the sample is excited with vertically polarized light and the electric vector of the excitation light is oriented vertically. The intensity of the emission is measured through a

polarizer. When the emission polarizer is oriented perpendicular to the direction of the polarized excitation the observed intensity is called  $I_H$ . Likewise, when the polarizer is parallel to the excitation the intensity is called  $I_V$ . The anisotropy, where  $I_V - I_H$  normalized by the total fluorescence intensity ( $I_V + 2I_H$ ), is defined as:

$$r = \frac{I_V - I_H}{I_V + 2I_H} \quad (\text{I.1.7})$$

The polarization ratio in this process could be defined as:

$$P = \frac{I_V - I_H}{I_V + I_H} \quad (\text{I.1.8})$$

The primary causes of fluorescence depolarization of an ensemble of molecules are:

1) photoselection process over randomly orientated molecules where the absorption and emission transition moments are parallel. 2) non-parallel absorption and emission transition moments. 3) Brownian rotation motion. In addition we have to mention the transfer of the excitation energy to another molecule with different orientation. The detailed influences of the three primary depolarization processes will be discussed in the following.

Most chromophores absorb light along a preferred direction (absorption transition moment) depending on the electronic state. In contrast, the emission transition moment is the same whatever the excited state reached by the molecule upon excitation, because of internal conversion towards the first singlet state.

1) Photoselection process.

Light is an electromagnetic wave consisting of an electric field  $E$  and a magnetic field  $B$  perpendicular both to each other and to the direction of propagation, and oscillating in phase. For natural light, these fields have no preferential orientation, but for linearly polarized light, the electric field oscillates along a given direction; the intermediate case corresponds to partially polarized light. Thus, when a population of fluorophores (isotropic distribution) is illuminated by a linearly polarized incident light, those whose transition moments are oriented in a direction close to that of the electric vector of the incident beam are preferentially excited. This process takes place in few femtoseconds and we may consider molecule in solution as immobile during absorption. If the incident light is vertically polarized, the probability of excitation of a

chromophore is proportional to the square of the scalar product, i.e.  $\cos^2\alpha$ ,  $\alpha$  is defined as angle between the absorption transition moment ( $M_A$ ) and the electric vector ( $E$ ) of the incident light. This probability is maximum when  $E$  is parallel to  $M_A$  of the molecule; it is zero when the  $E$  is perpendicular. Therefore the distribution of the orientation of excited fluorophores is anisotropic, and the emitted fluorescence is also anisotropic (Figure 5A,B).

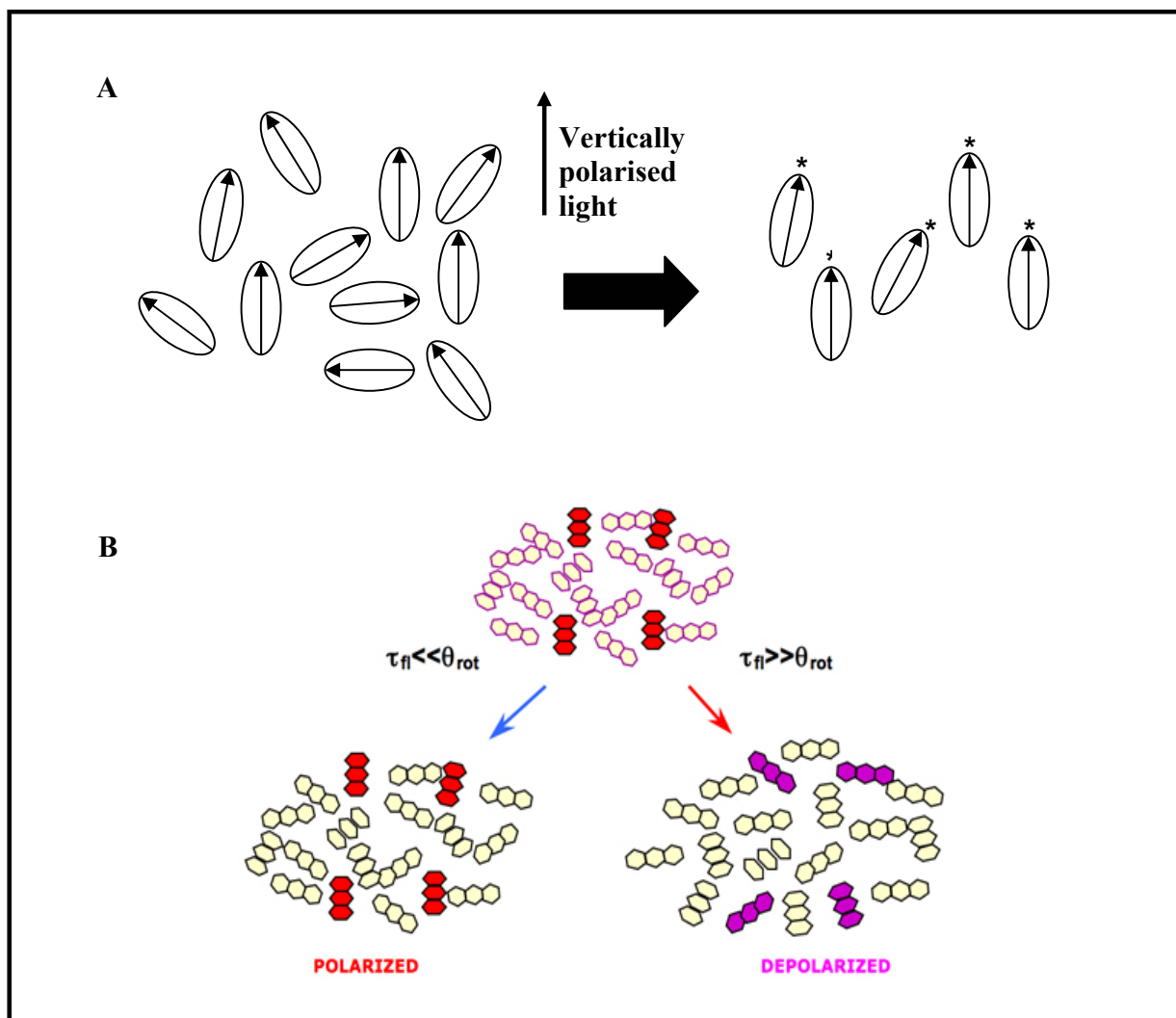


**Figure 5 : Illustration of principle of photoselection process.**

**A:** Demonstration of molecules and its excitation dipole are randomly oriented in solution. After being excited by vertically polarized light, the excited molecules are not randomly oriented.

**B:** In case of  $\theta_{rot} \ll \tau_{fl}$ , the emitted light of the fluorescent probe will be depolarized. However, if  $\theta_{rot} \gg \tau_{fl}$ , the emission will remain strongly polarized even though the presence of rotational

motions.  $\tau_{fl}$  is the fluorescence lifetime of the excited fluorescent probe;  $\theta_{rot}$  is the rotational correlation time  $\theta$  of the molecule that it is bound to.

*From (Lakowicz, 2006).*

Let assume a population of randomly orientated fluorophores before excitation without Brownian motion. The absorption and emission transition moments are supposed parallel. Each single molecule is oriented with angles  $\alpha$  relative to the vertical axis and  $\omega$  relative to the horizontal axis.

$$\begin{aligned} I_V &= I^2 \cos^2 \alpha \\ I_H &= I^2 \sin^2 \alpha \sin^2 \omega \end{aligned} \quad \text{(I.1.9)}$$

The population of excited molecules is oriented with values of  $\omega$  from 0 to  $2\pi$  with equal probability. Hence we can eliminate the  $\omega$  dependence in Equation I.1.9 because the average value over the random population of  $\sin^2\omega$  is 1/2, therefore,

$$\begin{aligned} I_H &= I^2 \overline{\sin^2 \alpha} \times \frac{1}{2} \\ I_V &= I^2 \overline{\cos^2 \alpha} \end{aligned} \quad \text{(I.1.10)}$$

Using Equation I.1.7, one finds that

$$r = \left( \overline{3 \cos^2 \alpha} - 1 \right) / 2 \quad \text{(I.1.11)}$$

Taken into account the excitation probability  $\cos^2\alpha$ , the fraction of molecules to the oriented direction can be evaluated, therefore the average of  $\cos^2\alpha$  over all excited molecules could be calculated as 3/5. Using equation I.1.11, we obtain the maximum value of  $r_0 = 0.4$  for a randomly oriented population of molecules. Here the value  $r_0$  is the theoretical anisotropy in the absence of any motion, which is defined as fundamental anisotropy. But in practice, the experimental value usually ranges from 0.32 to 0.39 because of the fundamental and limiting anisotropy (Valeur, 1993).

2) In case of a population of randomly orientated fluorophores without Brownian motion but with the absorption and emission transition moments non-parallel, the evaluated  $r_0$  values should be changed. This situation can occur when excitation brings the fluorophores to an excited state other than the first singlet state from which fluorescence is emitted. Let  $\beta$  be the angle between the absorption and emission transition moments, and  $\psi$  be the angle between the planes

$$r_0 = \frac{2}{5} \times \left( 3 \cos^2 \beta - 1 \right) / 2 \quad \text{(I.1.12)}$$

of the absorption and emission transition moments ( $\cos^2 \psi = 1/2$  because of the fact that all values of  $\psi$  are equiprobable), the fundamental anisotropy of a fluorophores is given by the relation I.1.12.

Therefore, the theoretical values of  $r_0$  ranges from  $r_0 = 0.4$  corresponds to an angle  $\beta = 0^\circ$  (parallel transition moments) and  $r_0 = -0.2$  for  $\beta = 90^\circ$  (perpendicular transition moments). It should be noted that the fundamental anisotropy value is zero when  $\beta = 54.7^\circ$ . When  $\beta$  exceeds  $54.7^\circ$  the anisotropy becomes negative. Consequently, for any fluorophores randomly distributed in solution, with one-photon excitation, the value of  $r_0$  must be within the range from -0.2 to 0.4. For two-photon excitation, the fluorophores interacts simultaneously with two photons, and each interaction is proportional to  $\cos^2 \alpha$  (Lakowicz, 2006), hence the photo selection function introduces  $\cos^4 \alpha$  probability to calculate the anisotropies expected for collinear transitions, and therefore for  $\beta = 0^\circ$ , the expected fundamental anisotropy for two-photon excitation is 0.57.

3) Now we assume the molecules are not immobile but undergo Brownian motions. In considering the effect of rotational Brownian motion, the anisotropy evaluation would be more complicated. If excited molecules can rotate during the excited-state lifetime, the emitted fluorescence is partially (or totally) depolarized. The preferred orientation of emitting molecules resulting from photoselection at time zero is indeed gradually affected as a function of time by the rotational Brownian motions. Let  $\omega$  be the angle of the emission moment with the vertically orientated polarizer at time  $t$  when the fluorescence photon is emitted. The projection of the emission transition moment  $\vec{E}$  on the three axes with a cylindric symmetry around the vertical axis (Figure 6) yields the average over all molecules are given by:

$$\begin{aligned} I_V &= I^2 \overline{\cos^2 \omega} \\ I_H &= I^2 \overline{\sin^2 \omega} \sin^2 \Phi \end{aligned} \tag{I.1.13}$$

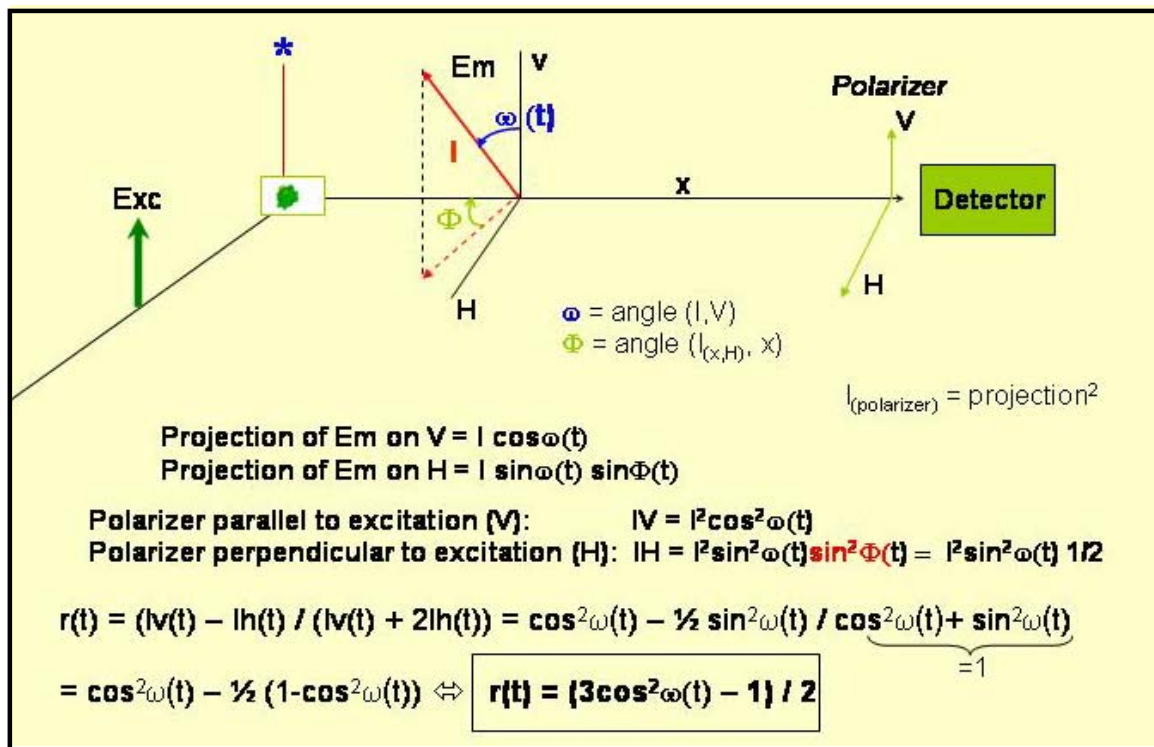


**Figure 6 : Relationship between anisotropy and the angle of emission.**

System coordinates for characterizing the orientation of the emission transition moments. The definitions of angles was demonstrated in this figure and relationship between anisotropy and the angle of emission was illustrated.

From (Jean-Claude BROCHON, 2006, courses ENS-ECNU in Shanghai).

In summary, the experimental anisotropy is a function of all depolarization process  $d_i$  defined as Soleillet law:

$$\begin{aligned} r &= r_0 \times P \times d_i = r_0 \times d_1 \times d_2 \\ &= 0.4 \times \left[ \left( 3 \langle \cos^2 \beta \rangle - 1 \right) / 2 \right] \times \left[ \left( 3 \langle \cos^2 \omega \rangle - 1 \right) / 2 \right] \end{aligned} \quad (\text{I.1.14})$$

For a spherical molecule, the Perrin Einstein relation for anisotropy due to Brownian motion is expressed as:

$$r(t) = r_0 \exp(-t/\theta) \quad (\text{I.1.15})$$

Let  $D$  defined as the rotational diffusion coefficient of a spherical molecule, in the Perrin Einstein equation, where  $\theta = 1/6D$ ,  $\theta$  is the rotational correlation time that describes how fast a molecule tumbles in solution.

For global hydrated macromolecule  $\theta$  is related to the molecular weight of the molecule by the relation:

$$\theta = \frac{\eta V}{RT} = \frac{\eta M}{RT} \times (v + h) \quad (\text{I.1.16})$$

Where  $\eta$  is the viscosity;  $T$  is the temperature in  $^\circ\text{K}$ ;  $R$  is the gas constant with the value of  $R=8.31 \times 10^7 \text{ erg/M } ^\circ\text{K}$ ;  $V$  is the volume of the rotating unit;  $v$  is the specific volume of the protein and  $h$  is the hydration.

From the extent of fluorescence depolarization, we can obtain information on the molecular motions which depend on the size and the shape of molecules, on and the fluidity of their microenvironment.

In practice, the fluorescence anisotropy (FA) measurements are based on the assessment of the rotational motions of species. FA can be considered as a “competition” between the molecular motion and the lifetime of fluorophores in solution. If linear polarized light is used to excite an ensemble of fluorophores only those fluorophores, aligned with the plane of polarization will be excited. There are two scenarios for the emission: a) provided the fluorescence lifetime of the excited fluorescent probe is long enough in comparison with the rotational correlation time  $\theta$  of the molecule ( $\tau_{fl} \gg \theta_{rot}$ ), the molecule orientation will randomize in solution during the process of emission and anisotropy can be accurately measured. b) if the fluorescence lifetime of the fluorophore is much shorter than the rotational correlation time  $\theta$  ( $\tau_{fl} \ll \theta_{rot}$ ), the rotation of the

excited molecule will be small and the relaxation to an isotropic orientation cannot be detected, therefore the anisotropy is not properly measured.

It is instructive to know the quantitative information that can be obtained only if the time-scale of rotational motions is of the order of 20-40 times the excited-state lifetime  $\tau$  (Deprez et al., 2000). No information can be obtained from emission anisotropy measurements if the motions are too slow with respect to  $\tau$ . In addition, a distinction should be made between free and hindered rotation which are two typical processes in concerning of Brownian motion, consequently special attention should be paid to anisotropic media such as lipid bilayers and liquid crystals.

### ***1.1.3 Time - resolved characteristics of fluorescence emission, fluorescence lifetime***

#### ***1.1.3.1 Steady-state and time-resolved fluorescence spectroscopy***

Steady-state and time-resolved measurements are broadly considered as two primary fluorescence measurement types. Steady-state measurement, the most common type, is that performed with constant illumination and observation. In detail, the sample is illuminated with a continuous beam of light, and the intensity or emission spectrum is recorded. A steady-state observation is simply an average over time of the intensity decay of the sample. Equations I.1.17 and I.1.18 ( see Table 1, p38) can be used to illustrate how the lifetime were determined by use of time-resolved fluorescence intensity measurement.

Table 1 displays such relationship in considering a fluorophores that displays a single decay time ( $\tau$ ) and a single rotational correlation time ( $\theta$ ). The steady-state anisotropy  $\langle r \rangle$  is given by the average of  $r(t)$  over time:

$$\langle r \rangle = \frac{\int_0^{\infty} r(t)I(t)dt}{\int_0^{\infty} I(t)d(t)} \quad \text{(I.1.19)}$$

In this equation the denominator is present to normalize the anisotropy to be independent of total intensity. In the numerator the anisotropy at any time  $t$  contributes to the steady-state anisotropy according to the intensity at time  $t$ . substitution of equations I.1.17, I.1.18, into I.1.19 yields the well known Perrin equation in case of single exponential decay and single rotational correlation time of the molecule:

$$\langle r \rangle = \frac{r_0}{1 + (\tau/\theta)} \quad (\text{I.1.20})$$

Using this equation, it is possible to calculate the rotational correlation time expected for fluorophores in solvents or for labeled macromolecules from steady-state anisotropy value.

**Table 1. Relationship between steady-state and time-resolved fluorescence measurements.**

	STATIC < steady-state >	TIME RESOLVED
<b>Fluorescence</b>	I = Intensity	$I(t) = I_0 e^{-(t/\tau)}$ $\tau$ = fluorescence lifetime here $t = \tau \Rightarrow I = I_0 / e$ <b>(I.1.17)</b>
<b>Anisotropy</b>	r = anisotropy	$r(t) = r_0 e^{-(t/\theta)}$ $\theta$ = rotational correlation time here $t = \theta \Rightarrow r = r_0 / e$ <b>(I.1.18)</b>

### ***1.1.3.2 Interest of performing time-resolved fluorescence measurements***

In considering the relationship between steady-state and time-resolved measurements, it turns out that during the time averaging process, much of the molecular informations available from fluorescence are lost. Generally, the more complex shape of anisotropy decay contains information about the macromolecule shape and its possible flexibility. For time-resolved measurements, the fluorescence of a sample is monitored as a function of time after excitation by a flash of light. The time resolution can be obtained in a number of ways, depending on the required sensitivity and time resolution: with fast detection electronics (nanoseconds and slower); with a streak camera (picoseconds and slower); with optical gating (femtoseconds-nanoseconds)

Typically, nanosecond time-resolved measurement requires complex and expensive instrumentation, while steady-state fluorescence measurements are simple. However, these more complex time-resolved measurements are of greater value given the relationship between steady-

state and time-resolved measurements. For example, 1) anisotropy decays of fluorescent macromolecules are frequently more complex than a single exponential, because the precise shape of the anisotropy decay contains information about the shape and possible flexibility of macromolecule. Unfortunately, this shape information is lost during time averaging (equation I.1.19) and irrespective of the form of  $r(t)$ , equation I.1.19 yields a single rotational correlation time value. Therefore, in practice, the information from  $r$  alone is not sufficient to reveal the shape or flexibility of the molecule. In addition, in solution with a mixture of molecules of different size but with the same lifetime, it is hard to analyse the complexity of the mixture of those molecules only by measuring the steady-state anisotropy. However, in most cases, steady-state fluorescence anisotropy is well suitable for monitoring molecular interactions providing the anisotropy change is large enough, and to bring information on the stoichiometry of the complexes. 2) The intensity decays also contain information that is lost during the averaging process. Frequently, macromolecules can exist in more than a single conformation, and the decay time for a bound probe may depend on conformation, because the given fluorophores can be in different environment. The intensity decay could reveal two or more decay times, and thus reveal the presence of several conformational states. The steady-state intensity will only reveal an average intensity dependent on a weighted averaged of the decay times and consequently on the relative contribution of the different conformations. 3) In the presence of energy transfer, the intensity decay may reveal how acceptor is distributed in space around the donor. 4) Time-resolved measurements reveal whether quenching is due to diffusion or to complex formation with the ground-state fluorophores.

In summary, much of the molecular information content is available only by time-resolved measurements in fluorescence. Hence these measurements are of great importance in fluorophores related studies.

## ***1.2 Fluorescence anisotropy and instrumental considerations***

### ***1.2.1 Steady-state fluorescence anisotropy: definition and principle***

Steady-state anisotropy is the measured anisotropy when the incident light intensity is constant. In a configuration where the exciting light is vertically polarized and the emitted fluorescence is observed at right angles in a horizontal plane (Figure 7), the average anisotropy  $r$  is expressed by using the general definition of an averaged quantity, with the total normalized

fluorescence intensity. According to Equation I.1.7, the  $r$  value in relation with steady-state anisotropy can be determined with a spectrofluorometer equipped with a polarizer. If the fluorescence is detected through a monochromator instead of filter, it is not sufficient to keep the excitation polarizer vertical and to measure fluorescence intensities in rotating the emission polarizer because the transmission efficiency of a monochromator depends on the polarization of the light which should be calibrated. For a horizontally polarized exciting light, the vertical component ( $I_{HV}$ ) and the horizontal component ( $I_{HH}$ ) of the fluorescence detected through the emission monochromator are different, although these components are equal before entering the monochromator according to the Curie symmetry principle (Valeur, 1993). A  $G$  factor, defined as  $G = I_{HV} / I_{HH}$ , is the ratio of intensities measured through the monochromator. It deviates from 1 and can be used as a correcting factor for the determination of the ratio  $I_V/I_H$ , because it represents the ratio of the sensitivities of the detection system for vertically and horizontally polarized light:

$$\frac{I_{VV}}{I_{VH}} = G \times \frac{I_H}{I_V} \quad (\text{I.2.1})$$

Therefore, the determination of the emission anisotropy requires four intensity measurements:  $I_{VV}$ ,  $I_{VH}$ ,  $I_{HV}$  and  $I_{HH}$  (V: vertical; H: horizontal; the first subscript corresponds to the orientation of the excitation polarizer and the second subscript to the emission polarizer) (Figure 8).

Equation I.1.7 then becomes

$$r = \frac{I_{VV} - G \times I_{VH}}{I_{VV} + 2G \times I_{VH}} \quad (\text{I.2.2})$$

The excitation polarization spectrum is obtained by recording the variations of  $I_{VV}$ ,  $I_{VH}$ ,  $I_{HV}$  and  $I_{HH}$  and by calculating  $r(\lambda)$  by means of Eq. I.2.2 with  $G = I_{HV} / I_{HH}$ . This factor should always be determined since rotation of the prism emission polarizer can cause the focused image of the fluorescence to change position, and therefore altering the effective sensitivity.

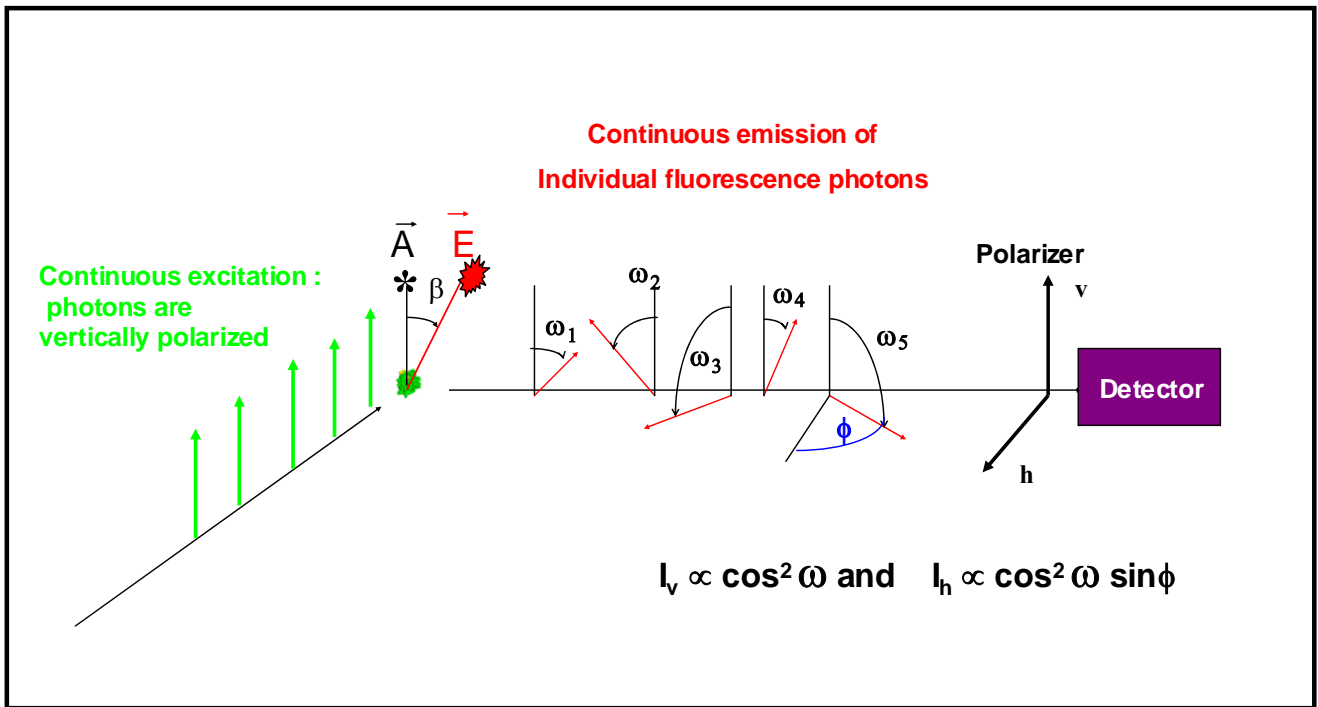


**Figure 7: Configuration of the excitation and emission polarizers for observing a signal proportional to the total fluorescence intensity.**

In this figure, V represents vertical; H represents horizontal. The angles between each orientation directions are indicated in figures. *From (Valeur, 1993).*

### ***I.2.2 Time-resolved fluorescence anisotropy: definition and principle***

It should be noted that detailed information are available from time-dependent anisotropy data. The form of the anisotropy decay depends on the size, shape, and flexibility of the labelled molecule. The measured decay can be compared with the decays calculated from various molecular models.

Consider a diluted solution of a fluorophores. When a pulse of linearly polarized light of appropriate wavelength passes through this sample, fluorophores with their absorption transition vectors aligned parallel to the polarization plane of the light are preferentially excited (see above). Those with vectors perpendicular are not excited at all. This leads to a biased population of excited molecules, which tend to relax to a randomly oriented ensemble because of Brownian rotational diffusion. Simultaneously, the initial excited population decays to the electronic ground state by fluorescence and other processes. The polarization plane of the fluorescence photon is determined by the actual orientation of the emission transition dipole of the molecule at the time of emission: it is therefore well defined shortly after the onset of excitation, but becomes increasingly random as time proceeds. The anisotropy,  $r$ , is related to the extent of this randomization and  $r(t)$  is the kinetics of the process (Figure 8). Fluorescence anisotropy kinetics cannot be recorded directly, but can be extracted from the decays of polarized emission components. Thus the polarized intensity decays can be used to calculate the time-dependent anisotropy

$$r(t) = \frac{I_V(t) - G \times I_H(t)}{I_V(t) + 2G \times I_H(t)} \quad \text{(I.2.3)}$$

where  $I_V(t)$  and  $I_H(t)$  are the polarized components parallel and perpendicular to the direction of polarization of the incident light. The time-dependant anisotropy decays are then analyzed to determine which model is most consistent with the data. The emission anisotropy can be calculated from the experimental decays of the polarized components by means of equation I.2.3, but only if the decay times are much larger then the width of the excitation pulse.

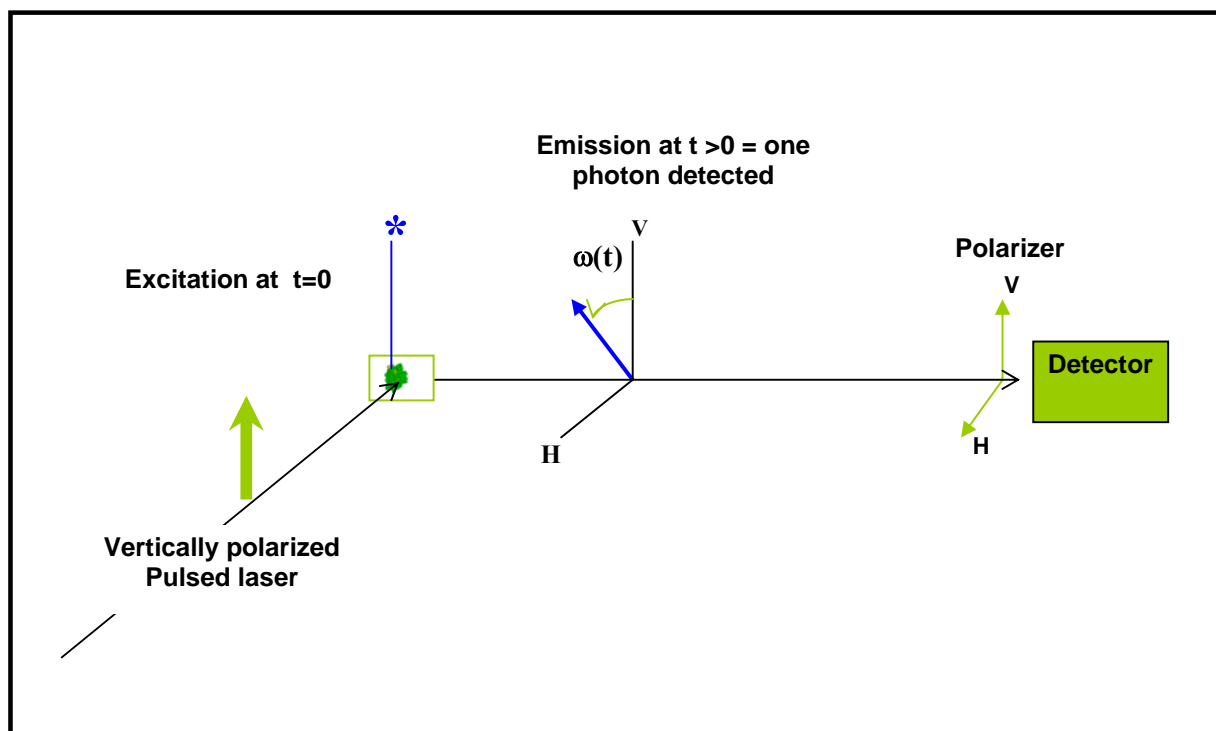


**Figure 8 :** Configuration of the time-resolved anisotropy when excited the sample with pulsed laser.

From (Valeur, 1993).

In summary, anisotropy decays can be measured using the time-domain (TD) or the frequency-domain (FD) method, the latter is nowadays not so often used.

### ***1.2.3 Instrumentation and design of pulse fluorometers***

#### ***1.2.3.1 Single-photon timing technique***

Nowadays, pulse fluorometry is the most popular technique for the determination of decay parameters. Most instruments are based on the time-correlated single-photon counting (TCSPC) method, better called as single-photon timing (SPT) method. The basic principle relies on the fact that the probability of detecting a single photon at time  $t$  after an exciting pulse is proportional to the fluorescence intensity at that time. After timing and recording the single photons following a large number of exciting pulses, the fluorescence intensity decay curve is reconstructed. Figure 9 shows the schematic of a conventional single-photon counting. The excitation source can be either a flash lamp, diode laser or a mode-locked laser. An electrical pulse associated with the

optical excitation pulse is generated and routed to the start input of the electronic stopwatch (in fact a time-to-amplitude converter, TAC). Meanwhile, the sample is excited by the laser pulse and emits fluorescence. The optics is turned so that the photomultiplier detects the first single fluorescence photon after each exciting pulse, if any. The very fast photomultiplier generated a corresponding electrical pulse which is routed to the “stop” input of the TAC. The latter generates an output pulse whose amplitude is directly proportional to the time interval between the arrival of start and the stop pulses. The height analysis of this pulse is achieved by an analogue-to-digital converter and a multi-channel analyzer (MCA), which increases by one and the content of the memory channel corresponding to the digital value of the pulse height. Therefore the times between excitation and emission are stored as a histogram. Providing only one photon is detected per excitation pulse after a large number of excitation and detection events, this histogram represents the waveform of the decay. Obviously, the larger the number of events, the better is the accuracy of the decay curve. The SPT technique offers several advantages: 1) high sensitivity explains; 2) outstanding dynamic range and linearity; 3) well-defined statistics allowing proper weighting of each point in data analysis.

### ***1.2.3.2 Instrumentation of anisotropy fluorometers***

Classic time-resolved spectrofluorometer is illustrated in Figure 10. The excitation source is of major importance. Lasers as excitation sources are of course much more efficient and versatile, at the penalty of high cost. Mode-locked lasers can generate pulses over a broad wavelength range. The pulse widths are in the picosecond or femtosecond range with a high repetition rate. This rate must be limited to a few MHz in order to let the fluorescence of long lifetime sample vanish before a new exciting pulse is generated.

Meanwhile, the time resolution of the instrument is governed not only by the excitation pulse width but also by the electronics and the detector. During one cycle of measurement, the TAC is not able to take into account any additional signal start and therefore a dead time is linked to the start frequency. For this reason, it is better to collect the data in the reverse configuration: the fluorescence pulse acts as the start pulse and the corresponding excitation pulse as the stop pulse. In this way, only a small fraction of start pulses result in stop pulses and the collection speed is better.

Microchannel plate photomultipliers are preferred to standard photomultipliers. They exhibit fast time responses (around 25ps) and do not show a significant color wavelength effect.



## ***1.2.4 Examples of application of fluorescence anisotropy in field of biology***

### ***1.2.4.1 Biochemical application of steady-state fluorescence anisotropy***

Steady-state anisotropy measurements are ideally suited for measuring the association and disassociation of macromolecules. The suitability is due to the additively law of anisotropy and is also based on the fact that the anisotropy almost always changes in response to a change in size, therefore in correlation time (see equation I.1.18). In this case, the average anisotropy ( $r$ ) is given by

$$r = \sum_i f_i r_i \quad \text{(I.2.4)}$$

Where  $r_i$  is the anisotropy of the individual species and  $f_i$  is the relative fluorescence molecules respectively. Based on this equation, it is easy to determine the  $K_{EQ}$  ( $K_d$  or  $K_{app}$ ). Also, the experiments are simplified by the independence of the anisotropy from the overall protein concentrations.

Lukas et al. (1986) has illustrated the use of anisotropy to study protein binding by calmodulin. One example is myosin light-chain kinase (MLCK). The amino acid (RS20) sequence that binds to calmodulin contains a single tryptophan residue. Since calmodulin contains only tyrosine, the peptide RS<sub>20</sub> can be selectively observed by excitation at 295nm. Upon addition of calmodulin the emission intensity at RS<sub>20</sub> increases and the emission shifts to shorter wavelengths. These changes indicate a shielded environment for the tryptophan residue in the complex. The anisotropy of RS<sub>20</sub> increases dramatically on addition of calmodulin which could be used to determine the 1:1 binding stoichiometry.

In addition, Deprez et al. (2004) have studied the inhibition mechanism of HIV-integrase (IN) by styrylquinoline derivatives, which was another example of anisotropy measurements. In the presence of styrylquinoline derivatives, the steady-state fluorescence anisotropy was used to assay their effects on the formation of IN-viral DNA complexes as well as on the 3'-processing activities of IN-DNA complex. To determine the apparent  $K_d$  value, fluorescein-labeled DNA was incubated with increasing concentrations of IN in reaction buffer. Steady-state anisotropy was then recorded in a thermostated cell. The fraction saturation and the cooperative binding of IN were calculated through anisotropy saturation. Results suggest that two inhibitor-binding modes exist for styrylquinoline derivatives: the first one prevents the binding of the viral DNA

and then the two subsequent reactions (i.e., 3'-processing and strand transfer), because the IC<sub>50</sub> values obtained in activity and DNA-binding tests were similar. Whereas the second one prevents the binding of target DNA, thus inhibiting strand transfer, because when using the preassembled IN-preprocessed DNA complexes to assay the potency of stytylquinoline against the strand transfer reaction, the inhibition occurred independently of 3'-processing even if the efficiency was decreased by about 5- to 10-fold.

Because of the efficiency and simplicity of anisotropy measurement, the anisotropy could be used to study reaction kinetics occurring within a second time scale. Xu et al. has reported the use of anisotropy to observe the unwinding of double-helical DNA by helicase (Xu et al., 2003). When measuring a fluorescein-labeled DNA in the presence of helicase, the anisotropy increases immediately upon addition of helicase to the DNA, showing that the binding reaction occurs rapidly. The anisotropy then remains constant because there is no source of energy to disrupt the hydrogen bonded base pairs. Upon addition of ATP the anisotropy drops rapidly to a value lower than the starting value. The final anisotropy is lower because the labeled single stranded DNA is no longer bound to its complementary strand. The single-strand oligomer has a lower molecular weight and is more flexible than the double-strand oligomer. These results show that anisotropy measurements can be used to follow the kinetics of biochemical reactions on a relative rapid timescale.

#### ***1.2.4.2 Biochemical application of time-resolved fluorescence anisotropy***

We saw that time-resolved anisotropy decay measurements are practical to reveal the size, shape and flexibility of the labeled molecule. It is a powerful method for investigating the molecular motions via the determination of correlation times. Meanwhile, it is important to understand the factors which affect the anisotropy decays. Nowadays, time-resolved fluorescence anisotropy has been extensively employed in many studies of proteins in solution, including folding reactions (Jones et al., 1995), interactions with ligands (Hauer et al., 1999), and self-assembly properties (Brochon et al., 1993). Information about the oligomeric state of proteins can also be obtained by determination the rotational correlation time ( $\theta$ ). Deprez et al. have investigated the self-assembly properties of HIV-1 integrase by time-resolved fluorescence anisotropy using tryptophanyl residues as a probe (Deprez et al., 2000). They found that the HIV-1 integrase monomer is the predominant form of integrase at a concentration of 0.2  $\mu\text{m}$  in the presence of  $\text{Mn}^{2+}$ , under conditions where integrase is highly active.  $\text{Zn}^{2+}$  plays a role in the

multimerization process, while  $Mn^{2+}$  and  $Mg^{2+}$  have a tendency to dissociate high-order multimeric forms. Furthermore,  $Mn^{2+}$  and  $Mg^{2+}$  display differential effects on the dissociation and also on the proper conformation of the monomer. On the other hand, detergents such as CHAPS or NP-40 were found here to perturb the quaternary structure of integrase.

In general, for a spherical molecule the anisotropy is expected to decay with a single rotational correlation time ( $\theta$ ). However, anisotropy decays are usually multi-exponential, which can be the result of numerous factors. Multi-exponential anisotropy decays are expected for non-spherical fluorophores or proteins. The correlation times in the anisotropy decay are determined by the rates of rotation about the various molecular axes. Malicka et al. has performed lifetime distribution analysis to study the influence of leucine configuration in position 5 on changes of the peptide chain of cyclic analogues of enkephalines containing a fluorescence donor and acceptor in different solvents (Malicka et al., 2001). The configuration change of Leu5 in all the analogues of enkephalins studied containing donor-acceptor pairs has no apparent influence on Trp lifetime distributions. In contrast, there is a significant solvent effect on the shape of lifetime distribution.

Moreover, anisotropy decays are also affected by the segmental flexibility of the macromolecule. For instance, tryptophan anisotropy decays of proteins frequently display correlation times that are too short to be due to rotational diffusion of the whole protein. These components are usually due to independent motions of the tryptophan residue within the protein or on the surface of the protein. The rates and amplitudes of tryptophan side-chain motions have been used to study the nanosecond dynamics of proteins (Valeur, 1993).

Anisotropy decays of membrane-bound probes have been particularly informative, which were illustrated in recent studies *in vivo* (Varma & Mayor, 1998). Membrane-bound probes often display unusual behavior in which the anisotropies do not decay to zero. This occurs because some probes do not rotate freely in membranes, at least not within the ns decay times of most fluorophores. The extent of rotation is often limited by the anisotropic environment of a membrane.

### ***1.3 Fluorescence correlation spectroscopy***

Current biological research is focused not only on the identification, but also on the precise physico-chemical characterization of elementary processes on the level of individual proteins and nucleic acids. Most technologies are difficult to track freely diffusing single molecules. Single-

molecule detection (SMD) is a powerful technique because it avoids ensemble averaging and allows single events to be observed. Therefore there is no need to synchronize a population of molecule, which is technically difficult to be carried out in solution. However, SMD has its limitations. In principle, the most stable fluorophores typically emit  $10^5$  to  $10^6$  photons prior to irreversible photodestruction. Single molecules can only be observed for a brief period of time (1 second or less) which may be too short to observe many biochemical processes because of the modest detection efficiency of optical systems and the need for high emissive rates for detection of the emission over background. When the fluorophore is bleached the experiment must be started again with a different molecule. In addition, SMD requires immobilization on a surface, which can affect the functioning of the molecule and show its access to substrates or/and ligands because of unstirred boundary layers near the surface. Accounted for those limitations of SMD, fluorescence correlation spectroscopy (FCS) is first introduced and developed in the early 1970s by Magde, Elson and Webb (Magde *et al.*, 1972; Elson and Magde, 1974).

In this section, a general definition of the FCS technique is introduced, which would provide information about the determination of molecular diffusion coefficients. Principles and biological applications of this advanced technique would also be presented here.

### ***1.3.1 Fluorescence correlation spectroscopy: definition***

Fluorescence correlation spectroscopy (FCS) exploits fluorescence fluctuations induced by low numbers of diffusing labelled particles in a very small volume in a confocal setup to analyze their concentrations and mobilities. In contrast to other fluorescence techniques, the FCS does not require surface immobilization and can be performed on molecules in solution. The observed molecules are continuously replenished by diffusion into a small observed volume. FCS thus allows continuous observation for long periods of time and does not require selection of specific molecules for observation. The parameter of primary interest in FCS is not the emission intensity itself, but rather time-dependent intensity fluctuations that are the result of some dynamic process, typically translation diffusion into and out of a small volume defined by a focused laser beam and a confocal aperture. In general, all physical parameters that give rise to fluctuations in the fluorescence signal are accessible by FCS. It is, for example, rather straightforward to determine local concentrations, diffusion coefficients or characteristic rate constants of inter- or intra-

molecular reactions of fluorescently labelled biomolecules in the range of nanomolar concentration.

A small volume of observation can be obtained by different techniques including confocal microscopy, among them, the versatile technique FCS is a method based on observation of a single molecule or few molecules (Figure 11). There is a burst of emitted photons due to multiple excitation-emission cycles from the same fluorophores. Typically, the delay time ranges from  $10^{-2}$  to  $10^2$  ms. If the fluorophores diffuses rapidly out of the volume the photon burst is short lived. If the fluorophores diffuses more slowly the photon burst displays a longer duration. Under typical conditions the fluorophores does not undergo photo-bleaching during the time it remains in the illuminated volume, but transitions to the triplet state frequently occur. By correlation analysis of the time-dependant emission, one can determine the diffusion coefficient of the fluorophores. In this case “time-dependent” refers to the actual time and not to a time delay or time-dependent decay following pulsed excitation. FCS measurements are best performed when observing a small number of fluorophores ( $< 10$ ). In order to detect a small number of fluorophores with a focused laser beam the sample needed to be dilute, typically near 1 nM. Since the samples are diluted, the unwanted background due to fluorescent impurities and scatter needed to be suppressed by effective filtering. Because of all these requirements, FCS was not widely used before 1990. By the early 1990s, a number of technical breakthroughs made FCS a practical technology, including confocal optics, high-efficiency avalanche photodiode (APD) detectors that offer a quantum efficiency  $> 50\%$  in the red range of the visible spectrum (a factor that of five over of that of traditional photomultiplier), stable lasers, multiphoton excitation and commercially available instruments (Qian and Elson, 1991; Koppel *et al.*, 1994; Berland *et al.*, 1995). As a result there was a rapid increase in the application of FCS. In addition to translation diffusion, intensity fluctuation can occur due to ligand-macromolecule dynamics, intersystem crossing, internal macromolecule dynamics, rotational diffusion, and excited-state reactions. The data are interpreted in terms of correlation functions. Different equations are needed to describe each process, and usually two or more processes affect the data at the same time. It is also necessary to account for the size and shape of the observed volume as well as the laser beam profile.

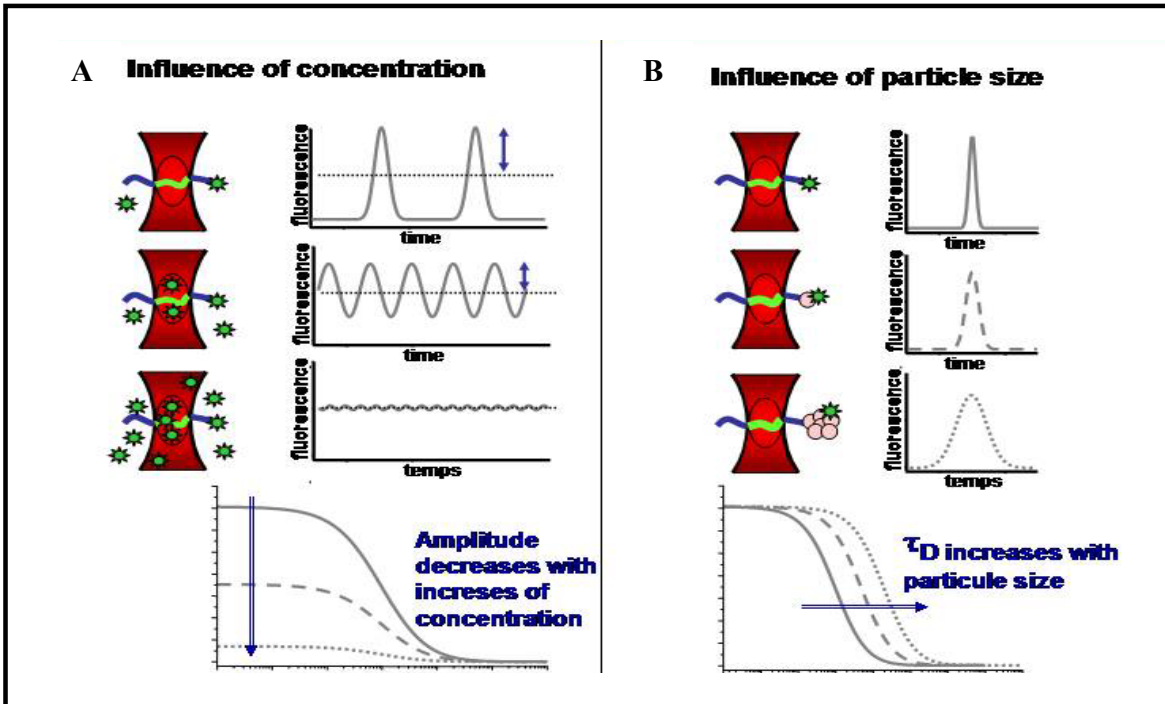


**Figure 11 : The principle of FCS measurements.**

Labelled particles diffuse through the detection volume, producing a fluctuating fluorescence signal.

**A:** The inverse of the amplitude is proportional to the particle concentration.

**B:** The increase of the diffusion time is proportional to the particle size.

*From (Jean-Claude BROCHON, 2006, courses ENS-ECNU in Shanghai).*

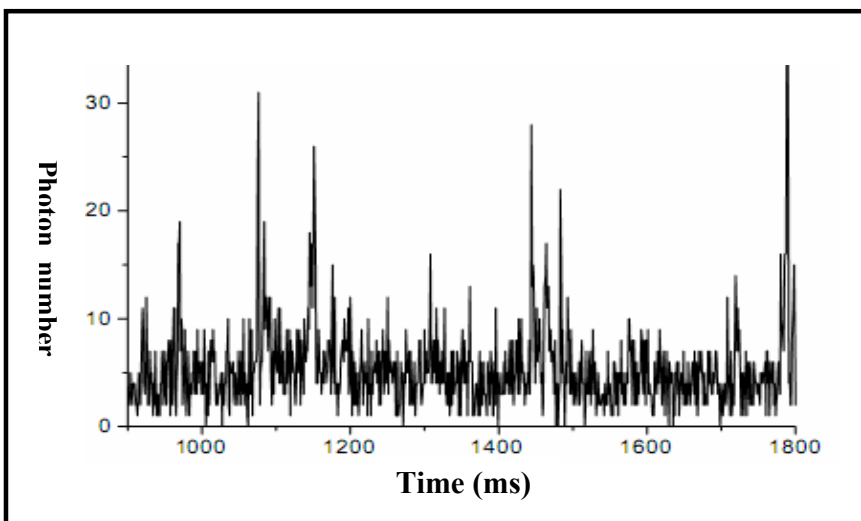


**Figure 12 :Illustrations of the fluctuation about an average fluorescence count at given time.**

*From (Eigen and Rigler, 1994).*

### ***1.3.2 Conceptual basis of Fluorescence correlation spectroscopy and determination of diffusion constant***

Principle in FCS function is quite simple: fluctuations in the fluorescence signal are quantified by temporally autocorrelating the recorded intensity signal. Such fluctuation in a small open region created by a focused laser beam arises from the motion of fluorescent species in and out this region via translational diffusion or flow. Fluctuations can also arise from chemical reactions accompanied by a change in fluorescence intensity: association and disassociation of a complex; conformational transitions; photochemical reactions etc. Figure 12 (Thompson, 1991; Eigen and Rigler, 1994; Webb, 2001)

The fluctuations  $\delta I_F(t)$  of the fluorescence around the mean value  $\langle I_F \rangle$ , defined as:

$$\delta I_F(t) = I_F(t) - \langle I_F \rangle \quad (\text{I.3.1})$$

Which are analyzed in the form of an autocorrelation function  $g(\tau)$  which relates the fluorescence intensity  $I_F(t)$  at time  $t$  to the fluorescence intensity  $I_F(t+\tau)$  at time  $t+\tau$ :

$$g(\tau) = \frac{\langle I_F(t)I_F(t + \tau) \rangle}{\langle I_F^2(t) \rangle} = \frac{\int I_F(t)I_F(t + \tau)dt}{\int I_F^2(t)dt} \quad (\text{I.3.2})$$

When combining equation I.3.1 and equation I.3.2 together, the autocorrelation of the fluorescence fluctuations is given by

$$g(\tau) = 1 + \frac{\langle \delta I_F(t)\delta I_F(t + \tau) \rangle}{\langle I_F^2(t) \rangle} \quad (\text{I.3.3})$$

In order to interpret the FCS data we need a theoretical model to describe the fluctuations. Considering all the fluctuations arise only from changes in the local concentration changes  $\delta C$  within the effective volume of the focal spot, in case of excitation by two-photon FCS, the variation may be written as:

$$\delta I_F(t) = \int \delta I_F(r, t)dr \propto \int \delta C(r, t)I_E^2(r)dr \quad (\text{I.3.4})$$

Here the  $I_E(r)$  represents the spatial distribution of the excitation energy with the maximum amplitude  $I_0$  at time  $t$ ,  $I_F(r)$  is the excitation intensity at each position  $r$ , and  $C(r,t)$  is the distribution of fluorophores.

Considering a Brownian diffusion system within only particles that are freely diffusing in three dimensions with the diffusion coefficient  $D$ , the so-called number density autocorrelation term can be calculated: (Elson 1974, So 1998)

$$\langle \partial C(\mathbf{r}, t) \partial C(\mathbf{r}', t + \tau) \rangle = \langle C \rangle (4\pi D \tau)^{-3/2} \exp\left(\frac{-|\mathbf{r} - \mathbf{r}'|^2}{4 D \tau}\right) \quad (\text{I.3.5})$$

Thereby,  $\langle \delta I_F(t) \delta I_F(t+\tau) \rangle$  and  $\langle \partial C(\mathbf{r}, t) \partial C(\mathbf{r}', t+\tau) \rangle$  can be connected by equation:

$$\langle \delta I_F(t) \delta I_F(t + \tau) \rangle = \alpha^2 \int d\mathbf{r} \int d\mathbf{r}' I_E^2(\mathbf{r}, t) I_E^2(\mathbf{r}', t) \langle \partial C(\mathbf{r}, t) \partial C(\mathbf{r}', t + \tau) \rangle \quad (\text{I.3.6})$$

If a three-dimensional Gaussian profile in the focal volume was assumed, the equation I.3.2 could be defined as:

$$g(\tau) = 1 + \frac{1}{\sqrt{8N}} \left(1 + \frac{\tau}{\tau_D}\right)^{-1} \left(1 + \left(\frac{\omega_0}{z_0}\right)^2 \frac{\tau}{\tau_D}\right)^{-1/2} \quad (\text{I.3.7})$$

Where  $\tau_D = \omega_0^2/8Dt$  is the characteristic time for diffusion in case of two-photon excitation, and  $\omega_0$  and  $z_0$  are the distance from the centre of the illuminated area in the  $x, y$  plane and  $x, z$  plane respectively at which the detected fluorescence has dropped by a factor  $e^2$ .  $N$  is the average number of fluorescent particles in the excitation volume. It should be noted that in case of one photon excitation,  $\tau_D = \omega_0^2/4Dt$ .

For spherical particle,  $D$  is inversely proportional to its hydrodynamic radius  $R$  according to the Stokes-Einstein equation:

$$D = KT / 6 \pi \eta R \quad (\text{I.3.8})$$

Where  $K$  is the Boltzmann constant ( $1.38 * 10^{-23} \text{ J K}^{-1} \text{ mol}^{-1}$ ),  $T$  is the temperature (K), and  $\eta$  is the viscosity of the solution (Pas), the diameter of the particles can be calculated from  $\tau_D$ .

### ***1.3.3 Fluorescence cross-correlation spectroscopy: definition and conceptual basis***

Fluorescence cross-correlation spectroscopy (FCCS) is a dual-color variant of FCS. It can monitor molecular interactions and enzymatic reactions as well as dynamic colocalization (Kettling et al., 1998).

When performing an autocorrelation analysis, one effectively compares a measured signal with itself at some later time and looks for recurring patterns. In electronics it has been common practice for decades to correlate two different signals and thus get a measure for the crosstalk. In fact, cross-correlation analysis is just the straightforward way to generalize the method described above. Looking out for common features of two independently measured signals, one not only removes unwanted artifacts introduced by the detector, but also provides much higher detection specificity. For FCCS, two spectrally distinct fluorophores are used to label two species in order to study their interactions (Figure 13). If the differently labelled particles are bound to each other, they diffuse together through the focal volume, i.e. in a synchronized way, inducing simultaneous fluctuations of the fluorescence signals in the two colour channels and thus a positive cross-correlation readout. Division of the cross-correlation amplitude by one of the autocorrelation amplitudes is a direct measure of the degree of molecular binding or dynamic colocalization in trafficking.

In contrast to the autocorrelation applications described above that focus mostly on analysis of the functional form of the correlation curves, the most important parameter is now simply the cross-correlation amplitude, and this amplitude is a direct measure for the concentration of double-labelled particles diffusing through the focal volume. In principle, one simply focuses on the occurrence of coincident fluctuations in the two emission channels, induced by concerted motion of spectrally distinguishable labels. All kinds of reactions leading either to a separation or an association of the two labelled species can thus be monitored. Under ideal conditions (i.e. no crosstalk between the detectors), the amplitude of FCCS measurements is zero unless double-labelled particles are present in the sample. This makes fast yes-or-no decisions based on this parameter feasible.

The mathematical calculation of FCCS is extended by using both the blue  $F_i(t)$  and the red  $F_j(t)$  signal either for the original  $F(t)$  or for the shifted copy  $F(t+\tau)$ . For stationary samples, both forward  $G_{ij}$  and backward  $G_{ji}$  cross-correlation give the same result. As the cross-correlation amplitude is directly proportional to the number of double-labelled molecules.

$$G_{ij}(\tau) = \frac{\langle \delta F_i(t) \delta F_j(t + \tau) \rangle}{\langle F_i(t) \rangle \langle F_j(t) \rangle} \quad (\text{I.3.9})$$

A correct evaluation of concentrations measured by cross-correlation requires good prior knowledge of the system or a careful calibration procedure of the two basic parameters resulting from FCS analysis, the effective volume element and the lateral characteristic residence time.

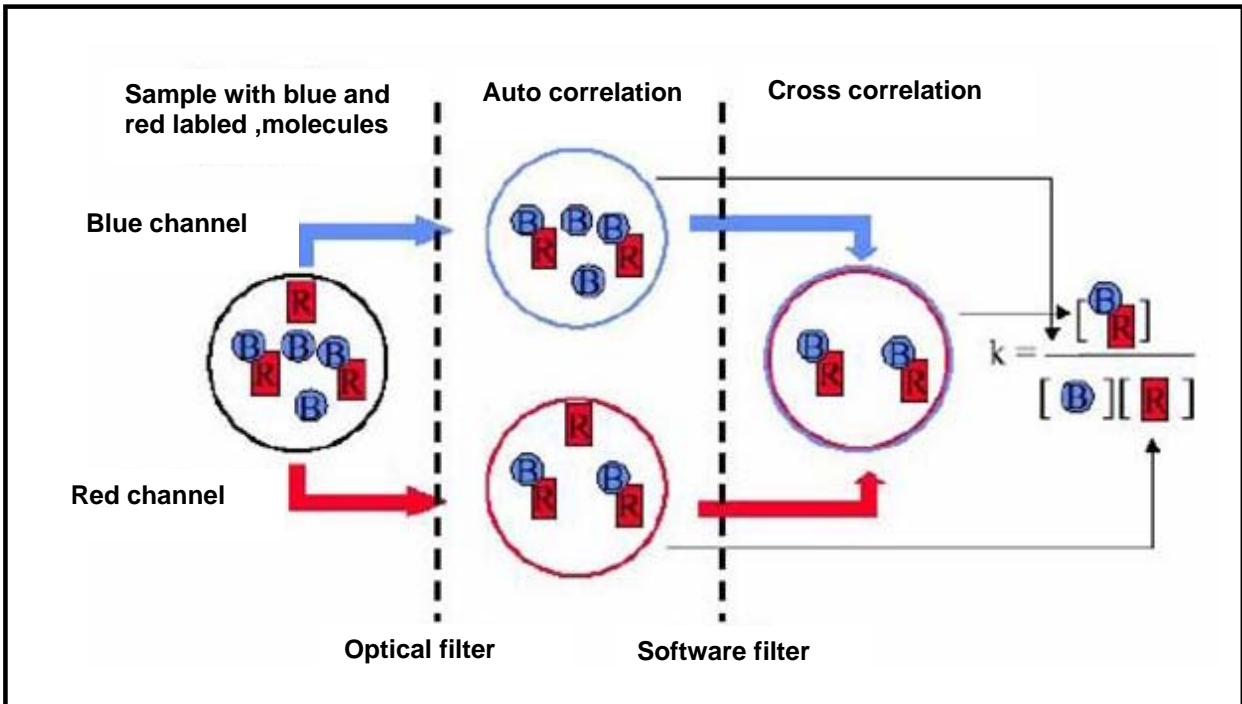


**Figure 13 : Principles of dual-color cross-correlation fluorescence spectroscopy.**

The fluctuations in two spectral regions red (R) and blue (B) are recorded in separate channels. Combining both single-channel setups in a two-channel apparatus, the two partially independent signals can be compared, looking for common features (RB). *From (Schwille, 2001).*

### ***1.3.4 Instrumentations and methods of FCS and FCCS***

#### ***1.3.4.1 Two-photon excitation fluorescence microscopy***

In conventional fluorescence spectroscopy, a fluorophore is excited by absorption of one photon whose energy corresponds to the energy difference between a ground state and an excited

state. Excitation is also possible by the simultaneous absorption of two photons of lower energy (e.g. in longer wavelength) via a short-lived virtual state (Figure 14).

Two-photon excitation is a nonlinear process; there is a quadratic dependence of absorption on excitation light intensity. The probability of two-photon absorption depends on both spatial and temporal overlap of the incident photons. The cross-sections for two-photon absorption are small. Consequently, only fluorophores located in a region of very large photon flux can be excited. Mode-locked, high-peak power lasers like titanium-sapphire lasers can provide enough intensity for two-photon excitation in microscopy.

Based on the quasi-simultaneous absorption of several long-wavelength photons, multiphoton excitation (MPE) provides intrinsic spatial sectioning due to the higher order dependence of the fluorescence on the excitation intensity. Figure 15 indicates that fluorescence is no longer observed along the double cone of the focused incident light, but is emitted solely from a small ellipsoidal region in the centres, where the intensity is sufficient for efficient excitation. As scattering is reduced for longer wavelengths, it also offers larger penetration depths in biological tissue. When combined two-photon excitation technique with FCS, MPE offers advantages especially beneficial to intracellular measurements (Berland et al., 1995), such as reduced autofluorescence and less photobleaching in off-focus areas. It also allows excitation of intrinsic tryptophan fluorescence in the visible spectral range. Moreover, for cross-correlation studies, two or more spectrally distinct dyes may be excited by a single laser line in automatically overlapping excitation volumes, thereby significantly simplifying optical alignment (Heinze et al, 2000). This versatile technique can be extended also to autofluorescent proteins, and it has more practical applications *in vivo*.

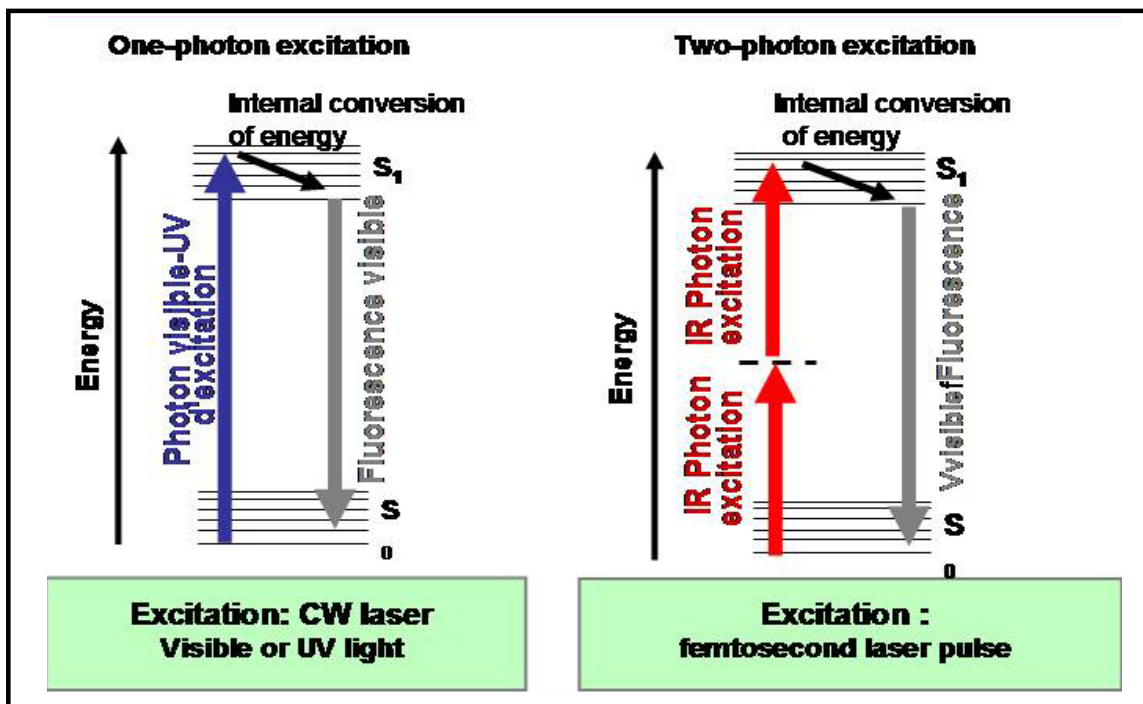


Figure 14 : Schematic of two-photon excitation compared to one-photon excitation.

The dashed line represents the virtual state that mediates the absorption. From (Schwille &Haustein, 2003).

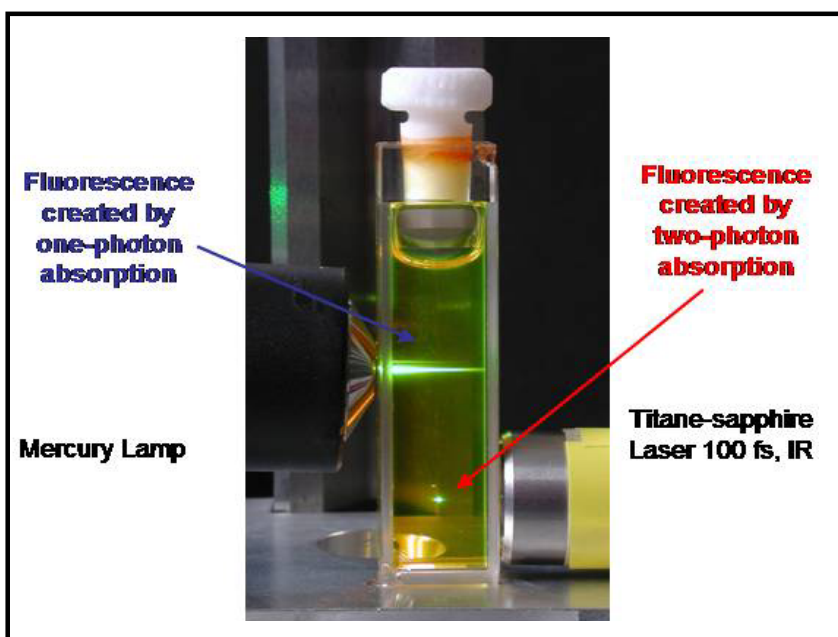


Figure 15 :Illustrations Of two-photon excitation Compared to one-photon excitation.

The Fluorescence created by two-photon excitation is more focus. From (Eigen and Rigler, 1994)

### ***1.3.4.2 Instrumentation of FCS and FCCS***

Most FCS instruments have been designed around optical microscopes. In recent years, two-photon FCS has been successfully developed and it offers the advantage of three dimensional resolutions (Chen et al., 2001). A typical optical configuration is shown in Figure 16. The excitation volume is confined through two-photon excited laser. The size of excitation volume depends on the magnification, numerical aperture and laser properties. The detector is a photomultiplier or an avalanche photodiode operating in the analogy mode, or more often in single-photon counting mode, and is connected to an amplifier. The autocorrelation function can be instantaneously obtained from the analysis of the fluorescence intensity fluctuations by hardware of a fast correlator. For the determination of rotational mobility, polarizer is introduced in the excitation and/or emission path.

In general, the basic characteristics of FCCS setups (Figure 17) are the choice of laser lines, dichroic mirror and filters. 1) An inverted microscope with attached confocal optics represents a very convenient means to measure fluorescence fluctuations in a very small volume. 2) The microscope lenses used in FCS should be of very high numerical aperture (at least 0.9) to minimize the size of the focal volume and therefore maximize the fluctuation amplitude for a given fluorophores concentration. The sample is generally present in aqueous solution and is observed in an inverted microscope through a standard cover slide. 3) Previous FCCS instrumentation uses two lasers typically: an argon laser for 488nm and a HeNe laser for 633nm. The two lasers are aligned to the same confocal spot for simultaneous excitation of the two fluorophores of different colors. However, bringing two laser beams to perfect and stable overlap is often difficult. Thus, simple single laser line is preferable in FCCS which offers the advantage to avoid the alignment of two excitation lasers for two-wavelength excitation into the same focal spot. Presently, such single laser line FCCS has been achieved and been extensively used. 4) For separating the excitation and emission wavelengths in FCS, usually dichroic beam splitters and interference filters are used. For multi-wavelength lasers, the excitation wavelength is selected with a suitable bandpass filter in the excitation pathway. 5) Detector is one of the most essential components of the FCS device that registers the emitted photons with very high efficiency. Recent avalanche photodiode detectors have a quantum yield of up to 70% at 600nm, with typically dark count rate of 50cps or lower. The advances of these devices have greatly enhanced the practicability of FCS, because very often count rates can be as low as a few hundred cps even

with avalanche detectors. 6) The computation of the autocorrelation function (ACF) of the fluorescent light intensity is central to the FCS experiment. Generally, the ACF is constructed from the detected photon pulses by an electronic autocorrelator. Modern autocorrelator will allow to measure the ACF simultaneously over a range of delay times of  $10^{-8}$ s to  $>1000$ s, with a choice of either auto- or cross-correlation mode.



**Figure 16 : Instrumentation of two-photon FCS.**

FCS uses a confocal type of microscope setup. The resulting optically delimited detection volume features a size of typically less than one femtoliter.

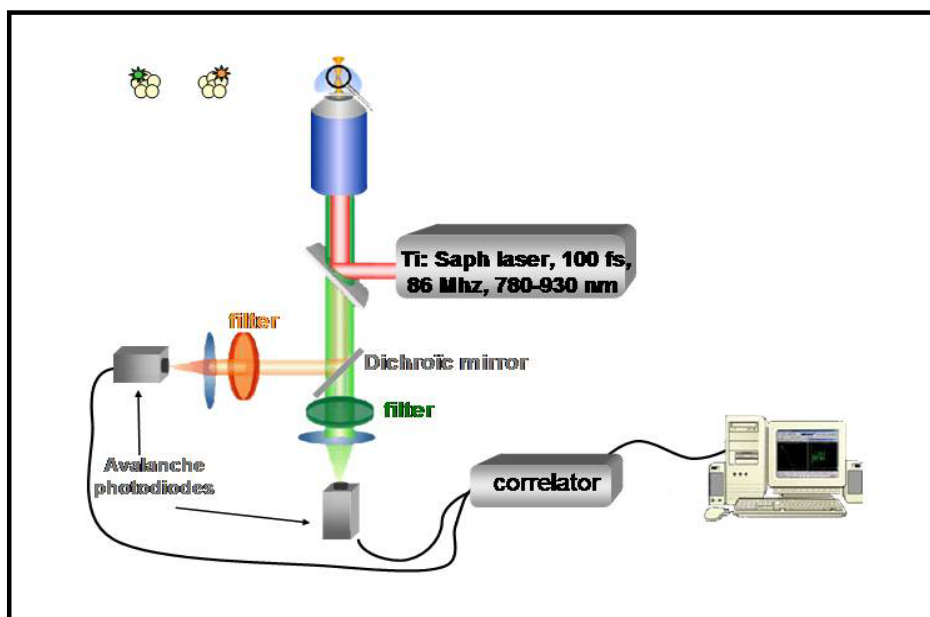


**Figure 17 : Schematic setup of two-photon FCCS.**

FCCS uses a confocal type of microscope setup. The laser light enters the objective from the back and is focused in the sample and is separated from the excitation by the primary dichroic mirror. The two spectrally distinct fluorophores are further separated by filters in front of the detector APD. Signals are collected by correlator and analysed through computer.

### ***1.3.5 Example of application of FCS and FCCS in the field of biology***

#### ***1.3.5.1 Biochemical application of two-photon FCS***

The biological function of molecules depends not only on their structure, but also on their mobility and dynamic properties, which are strongly influenced by the environment. The technique FCS allows inherent averaging over a large number of single-molecule passages through the measurement volume and thus is ideally suited to assess molecular movements, transport and diffusion both in simple artificial systems and directly in living cells.

An ideal target for FCS is therefore molecular binding and aggregation. For example, the individual diffusion characteristics allowed Diez et al. to determine the dissociation constant for the  $F_1b_2$  complex of *Escherichia coli* ATP synthase and hence the Gibbs free energy of binding (Diez et al., 2004). Borsch et al. monitored the conformational changes, provided the diffusion coefficient is sufficiently altered by structural rearrangements, such as the 15% increase seen for the  $F_1$  part of the  $H^+$ -ATPase upon nucleotide binding (Borsch et al., 1998). Shusterman et al. reported the polymer-like dynamics and structural flexibility of large double-strand and single-strand DNA can also be assessed and characterized in this manner (Shusterman et al., 2004).

Like other diffusion techniques, FCS exploits the specificity of fluorescent labeling with its advantages in use much lower probe concentration and laser power. Depending on the properties of the system of interest, FCS may be more convenient to apply or may provide information that is inaccessible by other techniques. For example, FCS may be used for the precise determination of diffusion coefficients of DNA molecules of different sizes in living cells, crowded solutions, cytosol extracts and artificial actin networks (Dauty and Verkman, 2005). The results have indicated that the actin cytoskeleton is the cause of obstructed diffusion. FCS can also provide fast way to assess the binding of small molecules to membranes, as the free molecules can be clearly distinguished from the membrane-bound molecules because they diffuse at least one order of magnitude faster. Rusu et al, reported the ligand molecules are allowed to bind to liposomes or to a large membrane sheet that is almost completely planar on the scale of the focus (Rusu et al., 2004), that is, a supported lipid bilayer, a free-standing lipid bilayer of a giant unilamellar vesicle or the plasma membrane of a live eukaryotic cell (Rigler and Elson, 2001).

Though technique of FCS has several advantages, the use of fluorescence autocorrelation for binding analysis is limited to applications in which the binding events significantly and specifically modify the diffusion of the labeled species. That is to say, the sensitivity of

autocorrelation analysis is restricted. Otherwise, both binding partners need to be labeled and cross-correlation (FCCS) is preferable.

### ***1.3.5.2 Biochemical application of two-photon FCCS***

To overcome these limitations for reactions of comparable weight, technique of FCCS was established. This technique was first introduced by Eigen and Rigler and this concept was experimentally demonstrated by monitoring the annealing kinetics of two differently labelled ssDNA strands (Eigen and Rigler, 1994). Among the multitude of successful applications *in vitro* are enzymatic cleavage (Kettling et al., 1998) and protein aggregation (Bieschke and Schwille, 1998).

The first experimentally realized dual-color FCCS was conducted by Schwille et al. with the use of a confocal microscope setup with filters for spectral separation and avalanche photodiodes for detection (Schwille et al., 1997). Synthetic DNA oligonucleotides labelled with a different dye at each end were introduced as a test system, and the kinetics of oligonucleotide cleavage by restriction endonucleases were monitored by FCCS (Kettling et al., 1998). An analogous, protein-based FCCS assay was developed by Kohl et al., who engineered fusion proteins consisting of a green and a red fluorescent protein and a peptide linker with a protease cleavage site. Proteolytic assays were done on purified fusion proteins in solution first and then in the live cell (Kohl et al., 2002).

Dual-color FCCS has also been applied to living cells to monitor the  $\text{Ca}^{2+}$  dependent binding of (CaM) (Kim et al., 2004). Calmodulin is a versatile intracellular  $\text{Ca}^{2+}$  sensor that binds to a variety of effector molecules. Autocorrelation measurements of Alexa Fluor 633-labelled CaM show that intracellular diffusion of the small CaM molecule (17KDa) is substantially more hindered in conditions that promote binding (the addition of  $\text{Ca}^{2+}$  and ATP) than in conditions of low  $\text{Ca}^{2+}$  concentration. By doing FCCS measurements of Alexa Fluor 633-labelled CaM in combination with enhanced green fluorescent protein (eGFP)-labelled  $\text{Ca}^{2+}$ /CaM-dependent kinase II (CaMK II), the binding of CaM to CaMK II as a target could be specifically monitored. For quantitative analysis of the cross-correlation data in terms of binding degrees and dissociation constants, a theoretical framework was developed that takes into account potential changes in chromophore brightness upon binding and the binding stoichiometry of the binding of 1 CaM molecules to a single CaMK II oligomer (Kim et al., 2005).

A different field of research in which FCCS provides a new perspective on cellular processes is intracellular trafficking and endocytosis. In the first experiment for the applicability of FCCS to living cells, the technique was used to follow the endocytic uptake of cholera toxin (Bacia et al., 2002). Cholera holotoxin consists of an A subunit and a B subunit, which were specifically labelled with a green dye and a red dye, respectively. A strong positive intracellular cross-correlation signal was obtained from endocytic vesicles, but this was diminished in the perinuclear region, where the pathways of the A and B subunits diverge. Moreover, by using mixtures of differently labelled cargo, it was shown that positive cross-correlation serves as an indicator of cotransport in small, rapidly moving endocytic entities on the order of 100nm in size.

In summary, fluorescence correlation spectroscopy has been proven to be a very versatile technique for both *in vivo* and *in vitro* applications. Based on light irradiation only, it is minimally invasive and thus extremely useful for investigating biological systems. As this method is concerned with fluctuations around the thermodynamic equilibrium, no external stress has to be applied to determine the relaxation parameters. The confocal setup guarantees high spatial resolution, which is combined with its inherently high temporal resolution to render it complementary to most other fluorescence techniques. A large number of parameters can be determined by FCS and FCCS, among them not only the mobility constants and concentrations, but also fast internal dynamics and photophysical processes. The accessible time-scale ranges from several sub-microseconds to several hundred milliseconds. The observation of very slow processes is limited by the finite photochemical lifetime of fluorophores, if they are exposed to strong illumination intensities.

---

# **MOTIVATION AND OBJECTIVE**

---

Photobiology, which deals with the interaction of light with biological matter, forms the core of biophotonics (Prasad, 2003). Macromolecules, although large as molecules, are still much smaller than the wavelength of light. They could not be seen through direct observation by using optical microscopes. Though there was a breakthrough of biophysical detection methods in the beginning of the twenty-first century (eg. X-ray crystallography; Nuclear magnetic resonance; etc...), a number of questions related with the structure and dynamics of macromolecule in living cell and their interactions could not be answered. To address these questions, femtosecond time resolution has been achieved for the probing of fast kinetics by optical spectroscopy. Light microscopy combined with fluorescence probes can also locate single molecules inside cells. Up to the late 1970s, exciting new methods have been developed that allow the study of single molecules. Present thesis will discuss the applications of some advanced methods related with fluorescence spectroscopy in understanding the biological processes, aiming at proving the feasibility of these methods in biological samples.

Firstly, dual-color fluorescence cross-correlation spectroscopy (FCCS) has been applied to monitor the enzymatic kinetics of *E.Coli* RecQ helicase and that of the human Rec5 $\beta$  helicase. When monitoring the unwinding activity of *E.Coli* RecQ helicase by use of two differently labelled single-stranded DNA molecules, the unwinding kinetics can be interpreted directly as the decrease of measured cross-correlation signal amplitude at time zero to that at a longer time scale (over 120 min). Similarly, the strand annealing activity of human Rec5 $\beta$  helicase could also be monitored by use of the same FCCS detection system. The only difference is in this case, the strand annealing kinetics is interpreted as the increase of cross-correlation signal amplitude because of the hybridisation process. After plotting the cross-correlation amplitude values versus time, the kinetic rate parameter may be evaluated directly from these data.

Secondly, steady-state fluorescence anisotropy has been utilized to analyse the impact of the two main Raltegravir resistance pathways (N155H and G140S/Q148H) on HIV viral replication and the catalytic properties of recombinant INs. Both DNA-binding and catalytic parameters of IN are determined by this steady-state anisotropy-based assay using the same sample. Briefly, IN binding to Fluorescein-labeled DNA (double-stranded 21-mer ODN mimicking the U5 viral DNA end) increases the steady-state anisotropy value ( $r$ ), allowing the calculation of the fraction of DNA sites bound to IN. This step can be recorded at 25°C. By shifting the temperature to 37°C, the activity dependent decrease in the  $r$  value allows quantification of the 3'-processing

activity of IN. The ability of forming DNA/IN complex and the 3'-processing activity for both wild-type IN and mutants IN are performed in this study using steady-state fluorescence anisotropy.

Thirdly, time-resolved photoluminescence decay (PL) and spectrometer measurements are conducted to characterize the fluorescent properties of MPA-capped CdTe quantum dots (QDs). The PL properties of the self-assembled CdTe QDs covered by MPA layers are studied in concerning with the size of nanoparticles and the environmental temperature. Maximum entropy data analyse method is used in data processing.

---

# **MATERIAL AND METHODES**

---

## ***II.1 Reagents and buffers***

All chemicals were reagent grade, and all buffers were prepared in high quality deionized water from a Milli-Q ultrapure water purification system (Millipore) having resistivity greater than 18.2 megaohms.cm. The compositions for all the buffers are listed in the following:

### ***II.1.1 HIV integrase related buffers***

#### ***II.1.1.1 HIV-IN purification buffers***

##### **1L Buffer A:**

Tris-HCl pH8 (final concentration 50mM)

380 $\mu$ L 99% beta-mercaptoethanol (final concentration 4mM)

Distilled water was used to reach final volume of 1L, and the buffer prepared should be filtered by use of D=0.4 $\mu$ m filter (Millipore) before the stockades.

##### **50mL 2M Imidazole:**

10g Hydrochloride Imidazole

50mL Buffer A

Gently vortexer and then filtered by use of D=0.4 $\mu$ m filter (Millipore) before usage.

##### **50mL Suspension Buffer:**

0.5 mL 2M Imidazole solution

25mL Buffer A

Dissolved a pill of EDTA-free antiprotease (Roche) in the solution and then filtered by use of D=0.4 $\mu$ m filter (Millipore).

##### **20mL Elution Buffer:**

10mM 2M Imidazole solution

10mL Buffer A

1  $\mu$ L 1M ZnSO<sub>4</sub> (final concentration 50mM)

Filtered by use of D=0.4 $\mu$ m filter (Millipore)

##### **2L Dialysis Buffer:**

116.8g NaCl (final concentration 1M)

800mL H<sub>2</sub>O  
40mL HEPES pH7 (final concentration 20mM)  
200mL glycerol (final concentration 10%)  
766 µL beta-mercaptoethanol (final concentration 4mM)  
100 µL ZnSO<sub>4</sub> (final concentration 1M)  
Distilled water was used to make a final volume of 2L.

### ***II.1.1.2 HIV-IN enzymatic reaction buffers***

#### **HIV-IN DNA-binding and 3'-processing buffer:**

20mM Tris-HCl pH 7.2  
1mM dithiothreitol  
20mM NaCl  
5mM MgCl<sub>2</sub>

The final volume of sample reaction was 200 µL.

### ***II.1.2 RecQ helicase related buffers***

#### ***II.1.2.1 RecQ helicase purification buffers***

##### **50mL 2M Imidazole:**

10g Hydrochloride Imidazole  
50mL Buffer A

Gently vortexer and then filtered by use of D=0.4µm filter (Millipore) before stock.

##### **50mL Suspension Buffer:**

0.5 mL 2M Imidazole  
20mM Tris-HCl pH7.9  
500mM NaCl

Dissolved a pill of EDTA-free antiprotease (Roche) in the solution and then filtered by use of D=0.4µm filter (Millipore).

##### **2L Dialysis Buffer:**

25mM Tris-HCl pH 7.5

3mM MgCl<sub>2</sub>

500mM NaCl

2mM dithiothreitol

Distilled water was used to make a final volume of 2L.

### ***II.1.2.2 RecQ helicase enzymatic reaction buffers***

#### ***E.Coli RecQ DNA-binding buffer:***

20mM HEPES pH 7.2

0.3mM dithiothreitol

40mM NaCl

1mM MgCl<sub>2</sub>

The final volume of sample reaction was 200 μL.

#### ***E.Coli RecQ DNA-unwinding buffer:***

20mM HEPES pH 7.2

0.3mM dithiothreitol

40mM NaCl

1mM MgCl<sub>2</sub>

For unwinding, ATP (1 mM) is added to the final volume of 200 μL.

#### ***RecQ5β DNA strand annealing buffer:***

20mM HEPES pH 7.2

1mM dithiothreitol

40mM NaCl

10mM MgCl<sub>2</sub>

The final volume of sample reaction was 200 μL.

## ***II.2 Protein and oligonucleotides purification***

### ***II.2.1 HIV integrase purification***

HIV-IN (32 kDa) was purified under native conditions. The pET-15b-IN plasmid which contains the cDNA encoding the HBX2 HIV integrase was used in present study. His-tagged integrase protein was overexpressed in *Escherichia coli* BL21 (*DE3*) and get further purification

under native conditions. Briefly, at an OD of 0.8, fusion protein expression was induced in bacterial cultures by the addition of IPTG (1 mM). Cultures were further incubated for 3 h at 37 °C, after which cells were centrifuged. The cell pellet was resuspended in ice-cold buffer A [20 mM Tris-HCl (pH 8), 1 M NaCl, 4 mM  $\beta$ -mercaptoethanol, and 5 mM imidazole], treated with lysozyme for 1 h on ice, and sonicated. After centrifugation (30 min at 10 000 rpm), the supernatant was filtered (0.45  $\mu$ m) and incubated for at least 2 h with Ni-NTA agarose beads (Pharmacia). The beads were washed twice with 10 volumes of buffer A, 10 volumes of buffer A plus 50 mM imidazole, and 10 volumes of buffer A plus 100 mM imidazole. His-tagged integrase was then eluted with buffer A supplemented with 50  $\mu$ M ZnSO<sub>4</sub> and 1 M imidazole. The integrase concentration was adjusted to 0.1 mg/mL in buffer A. The fusion protein was cleaved using thrombin and dialyzed overnight against 20 mM Tris-HCl (pH 8), 1 M NaCl, and 4 mM  $\beta$ -mercaptoethanol. After removal of biotinylated thrombin by incubation with streptavidin-agarose magnetic beads (Novagen, Madison, WI), a second dialysis was performed for 2 h against 20 mM Tris-HCl (pH 8), 1 M NaCl, 4 mM  $\beta$ -mercaptoethanol, and 20% (v/v) ethylene glycol. Fractions were aliquoted and rapidly frozen in liquid nitrogen and stored at -80 °C.

## ***II.2.2 RecQ helicase purification***

### ***II.2.2.1 E.coli RecQ helicase purification***

His-tagged RecQ helicase was overexpressed in *E. coli* BL21 (*DE3*) and purified under native conditions. Briefly, harvested cells were suspended in 30 ml of suspension buffer (20 mM Tris-HCl, pH 7.9, 0.5 mM imidazole, 500 mM NaCl) and were lysed using a French pressure cell. The lysate was then sonicated in order to shear DNA into small fragments. The lysate was cleared by centrifugation at 7,000g for 30 min at 4 °C. The supernatant was applied to the column charged with histidine binding resin (Novagen). The column was washed with 20 mM Tris-HCl (pH 7.9) buffer containing 100 mM NaCl, 60 mM imidazole. The proteins bound to the column were eluted stepwise using 20 mM Tris-HCl (pH 7.9) buffer containing 500 mM imidazole. RecQ helicase-containing fractions, identified by both DNA-dependent ATP hydrolysis and helicase activity assays, were pooled. The histidine tag was cleaved using biotinylated thrombin during a dialysis step. The removal of biotinylated thrombin was accomplished using streptavidin-agarose magnetic beads (Novagen, Madison, WI). RecQ helicase was further purified by FPLC size exclusion chromatography (Superdex 200; Amersham Biosciences).

Finally, ion exchange chromatography (DEAE Sephadex A-50) was used to remove the contaminating DNA. The active fractions were pooled, dialyzed against storage buffer (25 mM Tris-HCl, pH 7.5, 3 mM MgCl<sub>2</sub>, 500mM NaCl, 2 mM dithiothreitol), and stored at -80 °C. The protein was pure as judged by Coomassie staining and electrospray mass spectrometry. Protein concentration was determined spectrophotometrically using an extinction coefficient at 280 nm of  $1.54 \times 10^4 \text{ M}^{-1} \text{ cm}^{-1}$ .

### ***II.2.2.2 RecQ5 $\beta$ helicase purification***

The human RECQ5 $\beta$  proteins were produced as C-terminal fusions with a self-cleaving chitin-binding domain and purified as described under native conditions. The plasmids pET15b containing RECQ5 $\beta$  genome was transformed into the *Escherichia coli* strain BL21- codonPlus (Stratagene). The cells were grown to the midexponential phase ( $A_{600}$  of 0.5–0.6) at 37°C and the protein expression was induced by 0.25 mM IPTG (isopropyl  $\beta$ -Dthiogalactoside) at 15°C for 18 h. The cells were lysed in buffer containing 50 mM Tris/HCl (pH 7.5), 500 mM NaCl, 0.1% Triton X-100, 0.1  $\mu\text{M}$  PMSF and 10% ethylene glycol. The cell lysate was clarified by centrifugation (23000g for 45 min at 4°C) and the supernatant was applied to a 20 mL Ni<sup>2+</sup>-column connected to an ÄKTA FPLC system. The bound proteins were eluted with a 400 mM imidazole (volume = 300 mL). Fractions containing the proteins of interest were identified by SDS/PAGE. Proteins were further purified using size-exclusion chromatography (Superdex 200, Amersham). The active fractions were pooled, dialyzed against storage buffer (25 mM Tris-HCl, pH 7.5, 3 mM MgCl<sub>2</sub>, 500mM NaCl, 2 mM dithiothreitol), and stored at -80 °C. The protein was pure as judged by Coomassie staining and electrospray mass spectrometry.

### ***II.2.3 Oligonucleotides purification and preparation***

Unlabeled and fluorescently labeled oligonucleotides were purchased from Eurogentec (Liege, Belgium) and further purified by electrophoresis on an 12 or 15% denaturing acrylamide/urea gel for long (> 10-mer) or short (7- and 10-mer) oligonucleotides, respectively. The DNA duplex substrates were prepared by mixing equimolar amounts of complementary single-stranded (ss) strands in 20mM Hepes (pH 7.2), 40mM NaCl. The mixture was heated to 85°C for 5 min and annealing was allowed by slow cooling to 25°C.

## ***II.3 Enzymatic activity measurements***

### ***II.3.1 Steady-state fluorescence based activity measurements***

#### ***II.3.1.1 DNA-binding assay of HIV-IN***

Steady-state anisotropy values were recorded on a Beacon 2000 instrument (PanVera, Madison, WI), in a cell thermostatically held at 25°C for the DNA-binding step. Unless otherwise stated, we studied the formation of IN-DNA complexes by incubating fluorescein- labeled dsODNs with IN in 20 mM Tris (pH 7.2), 1 mM dithiothreitol, 20 mM NaCl, 5 mM MgCl<sub>2</sub> (the sample volume was 200 µl). The fractional saturation function ( $Y$ ) was calculated as follows, shown in equation II.3.1.

$$Y = \frac{r - r_{\text{ODN}}}{r_{\text{max}} - r_{\text{ODN}}} \times 100 \quad \text{(II.3.1)}$$

where  $r_{\text{max}}$  and  $r_{\text{ODN}}$  are the anisotropies of IN-bound and free ODN, respectively (no significant concomitant change in fluorescence intensity was observed).

#### ***II.3.1.2 HIV-IN 3'-processing assay***

The HIV-IN was first incubated with fluorescein-labeled DNA substrates at 25°C. After the DNA-binding step, the temperature was raised from 25 to 37 °C for monitoring the catalytic process. The 3'-processing activity was assessed by quantifying the decrease in the anisotropy value  $r$ . Two independent methods were used for quantification as follows. (i) In fixed-time experiments, the reaction was stopped by adding SDS (0.25% final), disrupting all the IN-DNA complexes in the sample. In such experiments, the solution contained two fluorescent species: the nonprocessed ODN and the fluorescein-labeled dinucleotide released by the cleavage reaction. The fraction of dinucleotides released ( $F_{\text{dinu}} = [\text{GT}]/[\text{DNA}]_{\text{total}}$ ) is given by Equation II.3.2,

$$F_{\text{dinu}} = \frac{r_{\text{NP}} - r}{r_{\text{NP}} - r_{\text{dinu}}} \quad \text{(II.3.2)}$$

where  $r_{\text{NP}}$  and  $r_{\text{dinu}}$  are the anisotropy values for pure solutions of non-processed dsODN and dinucleotide, respectively (fluorescence did not change significantly during the reaction). We used the 5'-GT-3'F dinucleotide (Eurogentec) to determine  $r_{\text{dinu}}$ . (ii) In real-time conditions, an additional fluorescent population corresponding to IN complexed with the unprocessed dsODN, is present in the sample. In this case,  $F_{\text{dinu}}$  was calculated as follows,

$$F_{\text{dinu}} = \frac{r_{t=0} - r}{r_{\text{max}} - r_{\text{dinu}}} \quad (\text{II.3.3})$$

where  $r_{\text{max}}$  is the characteristic  $r$  value obtained for optimal activity, and  $r_{t=0}$  is the  $r$  value obtained at the end of the DNA binding step (before the start of the reaction). The 3'-processing activity obtained with Equations II.3.2 and II.3.3 is referred to as  $\text{Activity}_{\text{SDS}}$  and  $\text{Activity}_{\text{real-time}}$ , respectively.  $\text{Activity}_{\text{real-time}}$  was not used if  $r_{t=0}$  was higher than 0.22 (aggregation of IN on DNA not negligible).

In the DNA/IN complex formation step, fluorescein-labeled dsODN was incubated with HIV-IN (varying concentrations) at 25°C in 20mM Tris buffer (pH 7.2) supplemented with 1 mM dithiothreitol, 20 mM NaCl, and 5 mM MgCl<sub>2</sub>. The  $r$  values were recorded.  $\Delta r$  ( $= r - r_{\text{ODN}}$ ) was plotted against competitor concentration to determine  $K_{d,\text{app}}$  (concentration of competitor decreasing the initial  $\Delta r$  value by 50%). The subsequent 3'-processing catalytic reactions were performed by increasing the temperature to 37°C. The fluorescein-labeled double-stranded 21-mer ODN mimicking the U5 viral DNA end was adopted as the DNA substrates.

### ***II.3.1.3 DNA-binding assay of RecQ helicase***

Binding of RecQ helicase to DNA was analyzed by fluorescence polarization using a Beacon fluorescence polarization spectrophotometer (PanVera). RecQ helicase in varied concentration was added to a 150µl aliquot of 20mM HEPES, pH 7.4, 1mM MgCl<sub>2</sub>, 40mM NaCl, 0.3mM dithiothreitol containing 5 nM of Alexa488-labeled DNA (substrate with varied size indicated in related manuscripts). Each sample was incubated for 5 min at 25 °C, after which fluorescence polarization was measured. In order to ensure that the mixture had reached equilibrium, the sample was further incubated for 30 min, and a second reading then was taken. No significant change was observed between the two measurements, indicating that equilibrium was reached.

### ***II.3.2 Fluorescence cross-correlation measurements***

Dual-color FCCS measurements were performed with two-photon excitation using a single laser line on a home-built system (previously described in (Delelis et al., 2008) for the FCS mode) using a 100-fs pulse 80-MHz mode-locked Mai Tai Ti:Sapphire tunable laser (Spectra Physics, Mountain View, California, USA) and a Nikon TE2000 inverted microscope. Briefly, before entering through the epifluorescence port of the microscope, the laser beam was expanded

with a two-lens afocal system to over-fill the back aperture of the objective (Nikon, Plan Apo, 100x, N.A. 1.4, oil immersion). The setup was optimized to obtain a diffraction-limited focal spot. Measurements were typically carried out in a 50- $\mu$ L solution dropped on a coverslip treated with dimethyldichlorosilane. The fluorescence signal from Alexa488 (Al) and Texas Red (Te) was collected by the same objective and separated from the excitation by a dichroic mirror (Chroma 700DCSPXR). The output signal from the microscope was further filtered by a Chroma E700SP-2p filter – to reject the residual excitation light – and splitted by a dichroic mirror (Chroma 580dcxr). Additional filters (Chroma HQ510/50 and HQ630/60m-2p for Alexa488 and Texas Red, respectively) were used to minimize cross-talk (Fig. 1B) and the splitted fluorescence signal was focused on two avalanche photodiodes (Perkin Elmer LifeScience, SPCM-AQR-14 single-photon counting module with less than 90 dark-counts/sec), mounted at right angle. The detectors were connected to a digital correlator (ALV 6000, ALV-GmbH, Langen, Germany) that computes the normalized cross-correlation function  $g_{Al/Te}(\tau)$  (or  $g(\tau)$ ) of the two fluorescence intensity fluctuations, according to equation II.3.4:

$$g_{Al/Te}(\tau) = \frac{\langle I_G(t) \cdot I_R(t + \tau) \rangle}{\langle I_G(t) \rangle \cdot \langle I_R(t) \rangle} \quad (\text{II.3.4})$$

where  $I_G(t)$  and  $I_R(t)$  are the number of detected fluorescence photons per time unit for green (Alexa488) and red (Texas Red) channels, respectively. Assuming a 3D Gaussian distribution of the excitation intensity, the cross-correlation function for a free Brownian diffusion process is given by equation II.3.5:

$$g_{Al/Te}(\tau) = \frac{1}{N} \cdot \frac{1}{\left(1 + \frac{\tau}{\tau_D}\right) \cdot \sqrt{1 + \frac{\omega_0^2}{z_0^2} \cdot \frac{\tau}{\tau_D}}} \quad (\text{II.3.5})$$

where  $N$  is the mean number of doubly fluorescently labelled species in the excitation volume, and  $\tau_D$  is the corresponding translational diffusion time.  $\omega_0$  and  $z_0$  are the lateral and axial dimensions of the excitation volume, respectively. The calibration of the excitation volume was done using a 5 nM water solution of Alexa Fluor 488 (succinimidyl ester; Molecular Probes, Eugene, OR; diffusion coefficient,  $D = 426.3 \mu\text{m}^2/\text{s}$  at  $21^\circ\text{C}$ ). The excitation wavelength was 780

nm and the excitation power was 25 mW. Assuming a Gaussian beam shape and according to equation II.3.5 and  $\tau_D = \omega_0^2/8D$ , the lateral  $\omega_0$  and axial  $z_0$  dimensions were estimated to be 0.380 and 1.40  $\mu\text{m}$ , respectively.

The cross-correlation curves were fitted using a Levenberg-Marquardt nonlinear least-squares fitting algorithm according to the analytical model (Equation II.3.5) using Igor Software (WaveMetrics). The excitation power was adjusted using a variable attenuator, consisting of an achromatic half-wave plate and a polarizing beam splitter (Micro Controle Spectra Physics, France). In the present study, we determined that an excitation power of 25 mW was suitable for two-photon excitation of both Alexa488 and Texas Red (fluorescence intensities exhibited quadratic dependences and  $\tau_D$  values were constant as a function of the incident power below 30 mW. Photobleaching occurred principally above 30 mW). The optimal two-photon excitation wavelength for the FCCS experiments using Alexa488 and Texas Red was found to be 780 nm. Recording times were typically between 2.5 and 5 min (average of 5-10 cycles of 30 s). For all experiments with doubly labelled (double-stranded) DNA substrates in the absence of ATP, the amplitude of the cross-correlation function,  $g(0)$ , was found to be consistent with the autocorrelation amplitudes obtained for the two independent channels, confirming the absence of singly labelled (single-stranded) DNA before the beginning of the reaction (data not shown). The cross-correlation initial amplitude  $g(0)$  was measured at different concentration of short dsDNA (doubly labelled) and found linearly decreasing with the substrate concentration till 5 nM. Therefore we may reasonably assume that the dissociation of the doubly strand DNA in reaction system is negligible with a concentration of 5 nM. In addition,  $T_m$  measurements to quantify small amount of single stranded DNA of 13 nt length is rather difficult because of the very low OD at 5 nM concentration. The decrease in the  $g(0)$  value was used to calculate the unwinding activity as a function of time according to Equation II.3.6:

$$\frac{[\text{DNA}]_{\text{unwound}}}{[\text{DNA}]_{\text{total}}} = \frac{g(0)_{t=0} - g(0)_t}{g(0)_{t=0} - g(0)_{t \rightarrow \infty}} \quad (\text{II.3.6})$$

with  $g(0)_{t=0}$  and  $g(0)_{t \rightarrow \infty}$  corresponding to the cross-correlation amplitudes at the beginning (zero time) and at the end (infinite time) of the reaction, respectively. When measuring the strand annealing activity of human RecQ5 $\beta$  helicase, the increase in the  $g(0)$  value was used to calculate the strand annealing activity as a function of time according to Equation II.3.7:

$$\frac{[\text{DNA}]_{\text{annealed}}}{[\text{DNA}]_{\text{total}}} = \frac{g^{(0)}_t - g^{(0)}_{t=0}}{g^{(0)}_{t \rightarrow \infty} - g^{(0)}_{t=0}} \quad (\text{II.3.7})$$

with  $g^{(0)}_{t=0}$  and  $g^{(0)}_{t \rightarrow \infty}$  corresponding to the cross-correlation amplitudes at the beginning (zero time) and at the end (infinite time) of the reaction, respectively. The single-turnover rate constant,  $k_{\text{obs}}$ , was then calculated from:  $[\text{DNA}]_{\text{unwound/annealed}} / [\text{DNA}]_{\text{total}} = 1 - \exp(-k_{\text{obs}}t)$ .

### ***II.3.3 Quantified maximum entropy method of time-resolved fluorescence data (MEM)***

The time-resolved emission was obtained using the time-correlated single photon counting technique. The excitation light pulse source was a Ti-sapphire subpicosecond laser (Mai Tai Spectra Physics, Mountain View, CA) associated with a second harmonic generator tuned at 420 nm. The repetition of the laser was set down to 4 Mhz. Fluorescence emission was detected through a monochromator (SpectraPro 150, ARC,  $\Delta\lambda=15$  nm) by a microchannel plate photomultiplier (Hamamatsu R1564U-06) connected to an amplifier Phillips Scientific 6954 (gain 50). The excitation light pulse was triggered by a Hamamatsu photodiode (S4753). A time-correlated single-photon counting card SPC-430 (Becker-Hickl GmbH, Berlin, Germany) was used for the acquisition of both excitation light pulse and fluorescence emission. The profile of the instrumental response of the laser pulse (30 ps) was recorded by detecting the light scattered by a water solution. In case of two photon excitation, the photomultiplier sensitivity does not allow the detection of excitation profile at 840nm. A TAMRA solution was used as a reference assuming a lifetime of 1.75ns. The time scaling was either 59.5ps per channel and 4096 channels were used. The fluorescence decay and the instrumental response profile were alternatively collected during 10 and 120 s, respectively. Routinely the total count of the decay reached 10-25 millions. In order to insure a single-photon counting condition, the counting rate never exceeded 1% of the laser excitation frequency to avoid pile-up effect, if necessary, a neutral density filter was used to attenuate the excitation intensity. The microcuvette (3x3-mm suprasil cuvettes) was thermostated with a Haake type-F3 circulating bath. The photoluminescence decay parameters were analyzed by the quantified maximum entropy method (MEM).

---

**APPLICATION OF FCCS TO STUDY  
THE ENZYMATIC KINETICS OF  
RECQ HELICASE**

---

## ***III.1 General introduction to the relationship between DNA and helicases***

### ***III.1.1 Structure and function of DNA***

Genetic information is frequently carried in the linear sequence of nucleotides in DNA. Generally speaking, a DNA molecule consists of two long polynucleotide chains composed of four types of nucleotide subunits. Each of these chains is known as a DNA chain, or a DNA strand. Hydrogen bonds between the base portions of the nucleotides hold the two chains together (Figure 18). Nucleotides are composed of a five-carbon sugar to which is attached one or more phosphate groups and a nitrogen-containing base. In the case of the nucleotides in DNA, the sugar is deoxyribose attached to a single phosphate group, and the base may be either adenine (A), cytosine (C), guanine (G), or thymine (T). The nucleotides are covalently linked together in a chain through the sugars and phosphates, which thus form a “backbone” of alternating sugar-phosphate-sugar-phosphate. The way in which the nucleotide subunits are lined together gives a DNA strand a chemical polarity. If we think of each sugar as a block with a protruding knob (the 5' phosphate) on one side and a hole (the 3' hydroxyl) on the other (Figure 19), each completed chain, formed by interlocking knobs with holes, will have all of its subunits lined up in the same orientation. Moreover, the two ends of the chain will be easily distinguishable, as one has a hole (the 3' hydroxyl) and the other a knob (the 5' phosphate) at its terminus. This polarity in a DNA chain is indicated by referring to one end as the *3' end* and the other as the *5' end*.

The three-dimensional structure of DNA—the double helix—arises from the chemical and structural features of its two polynucleotide chains. Because these two chains are held together by hydrogen bonding between the bases on the different strands, all the bases are on the inside of the double helix, and the sugar-phosphate backbones are on the outside (Figure 18). In each case, a bulkier two-ring base (a purine) is paired with a single-ring base (a pyrimidine); A always pairs with T, and G with C (Figure 18). This complementary base-pairing enables the base pairs to be packed in the energetically most favorable arrangement in the interior of the double helix. In this arrangement, each base pair is of similar width, thus holding the sugar-phosphate backbones an equal distance apart along the DNA molecule. To maximize the efficiency of base-pair packing, the two sugar-phosphate backbones wind around each other to form a double helix, with one complete turn every ten base pairs. The members of each base pair can fit together within the double helix only if the two strands of the helix are antiparallel—that is, only if the polarity of

one strand is oriented opposite to that of the other strand (see Figure 18). A consequence of these base-pairing requirements is that each strand of a DNA molecule contains a sequence of nucleotides that is exactly complementary to the nucleotide sequence of its partner strand (Alberts et al., 2000).

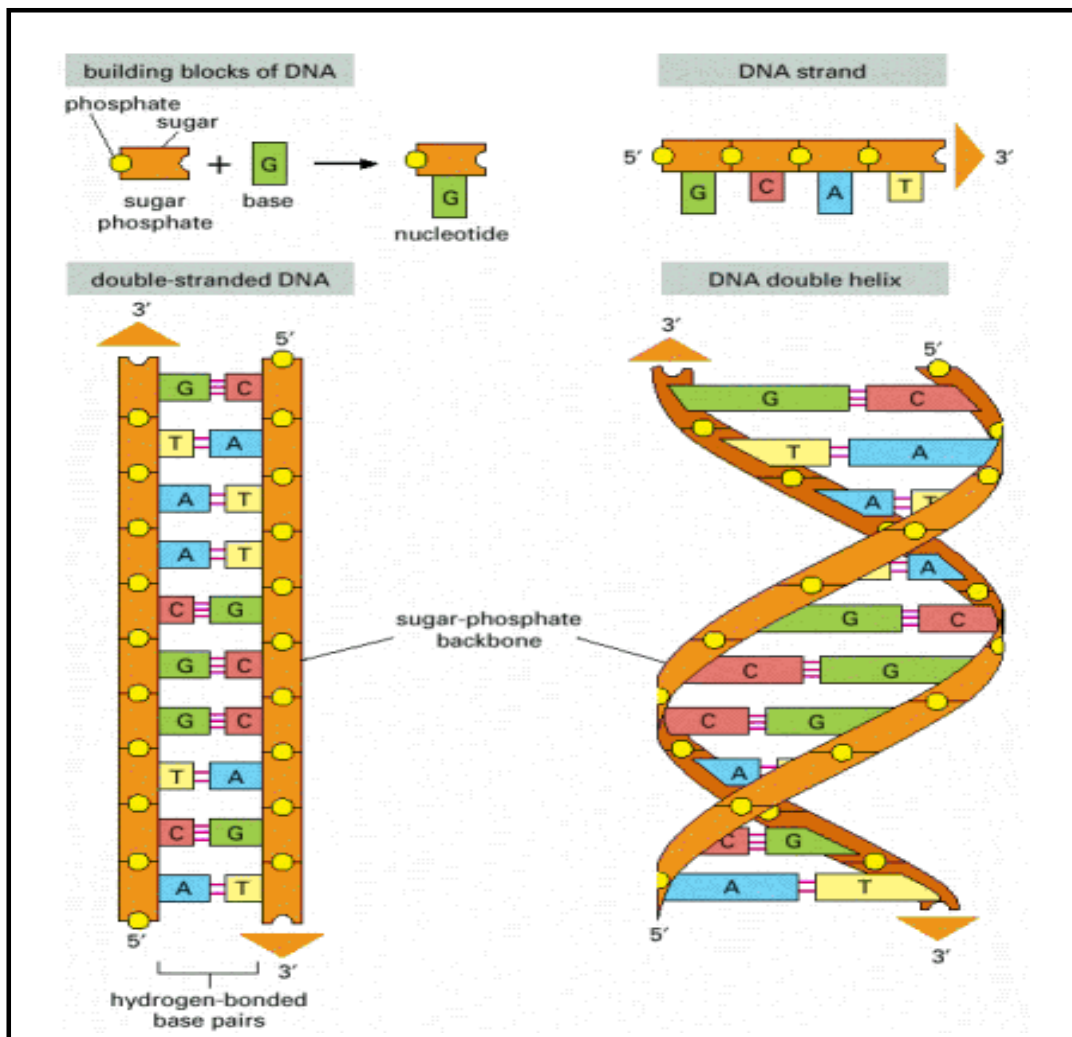


**Figure 18 : DNA and its building blocks.**

DNA is made of four types of nucleotides A, C, G, and T. A DNA molecule is composed of two DNA strands held together by hydrogen bonds between the paired bases. The *arrowheads* at the ends of the DNA strands indicate the polarities of the two strands, which run antiparallel to each other in the DNA molecule. *From (Alberts et al., 2000)*

### ***III.1.2 The function of helicase in cellular processes involved with DNA***

Many cellular processes, like DNA replication, transcription, translation, recombination, DNA repair and ribosome biogenesis, involve the separation of nucleic acid strands. Helicases are often utilized to separate strands of DNA double helix or a self-annealed RNA molecule using the energy from ATP or GTP hydrolysis, a process characterized by the breaking of hydrogen bonds between annealed nucleotide bases. The ATP or GTP indispensability has been proven in many studies by use of the non-hydrolysable ATP analogues or ADP analysis (Gorbalenya & Koonin, 1993; Gwack et al., 1999; Li et al., 2009). It is well known that, genes carry biological information that must be copied accurately for transmission to the next generation each time a cell divides to form two daughter cells. The DNA in genomes does not direct protein synthesis itself, but instead uses RNA as an intermediary molecule. When the cell needs a particular protein, the nucleotide sequence of the appropriate portion of the immensely long DNA molecule in a chromosome is first copied into RNA (a process called transcription). It is these RNA copies of segments of the DNA that are used directly as templates to direct the synthesis of the protein (a process called translation). The flow of genetic information in cells is therefore from DNA to RNA to protein.

All cells, from bacteria to humans, express their genetic information in this way—a principle so fundamental that it is termed the central dogma of molecular biology. Take DNA replication as an example. Prior to cell division, the DNA material in the original cell must be duplicated so that after cell division, each new cell contains the full amount of DNA material. The process of DNA duplication is usually called replication. Several enzymes and proteins are involved with the replication of DNA (Lehninger et al., 1993). At a specific point, the double helix of DNA is caused to unwind possibly in response to an initial synthesis of a short RNA strand using the enzyme helicase. Proteins are available to hold the unwound DNA strands in position. Each strand of DNA then serves as a template to guide the synthesis of its complementary strand of DNA. DNA polymerase III is used to join the appropriate nucleotide units together. The replication process is shown in Figure 19. It is so important that the cells duplicate the DNA genetic material exactly, that the sequence of newly synthesized nucleotides is checked by two different polymerase enzymes. The second enzyme can check for and actually correct any

mistake of mismatched base pairs in the sequence. The mismatched nucleotides are hydrolyzed and cut out and new correct ones are inserted.

In above DNA replication processes, the first and the foremost step are to unwind the double-strand DNA at the replication fork so that DNA polymerase can replicate the DNA strands. Specific enzymes, termed helicases, utilise the energy of ATP hydrolysis to power strand separation. In this case, the  $Mg^{2+}$  is an indispensable cofactor to control the ATP and RecQ helicase interactions. Generally, helicase requires a covalently attached flanking 5' or 3' single-stranded region of nucleic acid. There is a conformational change of helicase in the conversion of the energy ATP/GTP to ADP/GDP in order to facilitate the movement of helicase along DNA strand, and therefore to unwind the double-stranded DNA. The cooperative interactions are predominantly induced through the specific interactions of the  $\gamma$  phosphate and the ribose with the protein. The binding of  $Mg^{2+}$  cations seem to play a role in affecting the ADP and protein interactions. Taking bacterial helicase PcrA as an example, it functions as a monomer and comprises four domains (A1, A2, B1 and B2). Domain A1 contains a P-loop NTPase fold, and participates in ATP binding and hydrolysis. Domain B1 is homologous to domain A1 but lacks a P-loop. Domain A2 and B2 have unique structures. From analysis of the PcrA helicase crystal structures bound to nucleotide analog and appropriate double- and single-stranded DNA, the inchworm moves PcrA helicase action mechanism was proposed. The PcrA enzyme translocates in the 3' to 5' direction. When the helicase encounters a region of double-stranded DNA, it continues to move along one strand and displaces the opposite DNA strand as it progresses. Interactions with specific pockets on the helicase help destabilize the DNA duplex, aided by ATP-induced conformational changes (Berg et al., 2006).  $Mg^{2+}$  has a dual function in nucleotide-helicase interactions. At low  $Mg^{2+}$  concentration NTP binds stronger than ADP and the enzyme is predominantly in the high ssDNA-affinity state. At higher ( $Mg^{2+}$ ), NTP binds weaker than NDP and the helicase subunits can exist in alternating low- and high- affinity for RepA helicase.

Though most processes associated with DNA replication function to copy the genetic message as faithfully as possible, several biochemical processes require the recombination of genetic material between two DNA molecules. In genetic recombination, two daughter molecules are formed by the exchange of genetic material between two parent molecules. DNA recombination plays important roles in DNA replication, DNA repair, generating genetic diversity, viral integration and also in genes manipulations. For example, in the bacteriophage T4

life cycle, where the DNA replication, recombination and repair are tightly coupled, a recombination-dependent replication mechanism occurs by conversion of recombination intermediates into replication forks. Meanwhile, the T4 recombination-dependent replication is closely related to recombinational repair. In this case, the bacteriophage T4 UvsW helicase involves the branch migration and the removal of RNA from R-loops. It has been evidenced that the T4 UvsW protein is a functional analog of the *E.Coli* RecG helicase, which displays ssDNA-dependent ATPase activity. The T4 UvsW protein also acts as an RNA-DNA helicase because of its ability to dissociate both DNA and RNA from R-loops during branch migration (Kelly et al., 1997).

In addition of genetic information expression from DNA to RNA, the RNA synthesis and processing also play an indispensable role in gene expression. In this case, RNA helicases are necessary to participate in all biochemical steps involving RNA including transcription, splicing, transport, translation and ribosome biogenesis. Biochemically, RNA helicases are capable of binding and hydrolyzing NTP, mainly the ATP. The ATPase activity is an essential function of RNA helicase, which is demonstrated to be the primary source of energy during pre-mRNA splicing. The unwinding activity and the RNA-protein interaction disruption activities of RNA helicases are also observed in recent studies. For example, the human hepatitis G virus NS3 protein has been proven to have DEXH motifs which are typical of the DEXH protein subfamily of the DEAD box family. It possesses NTPase and RNA helicase activities which could displace RNA or DNA duplexes in a 3' to 5' direction. Furthermore, the oligonucleotide-stimulated ATPase and helicase activities are sensitive to monovalent ions, which convinced the existence of helicase motif VI of the Hepatitis G virus and the Hepatitis G virus NS3 proteins are necessary for the RNA binding activity of these proteins (Gwack et al., 1999).

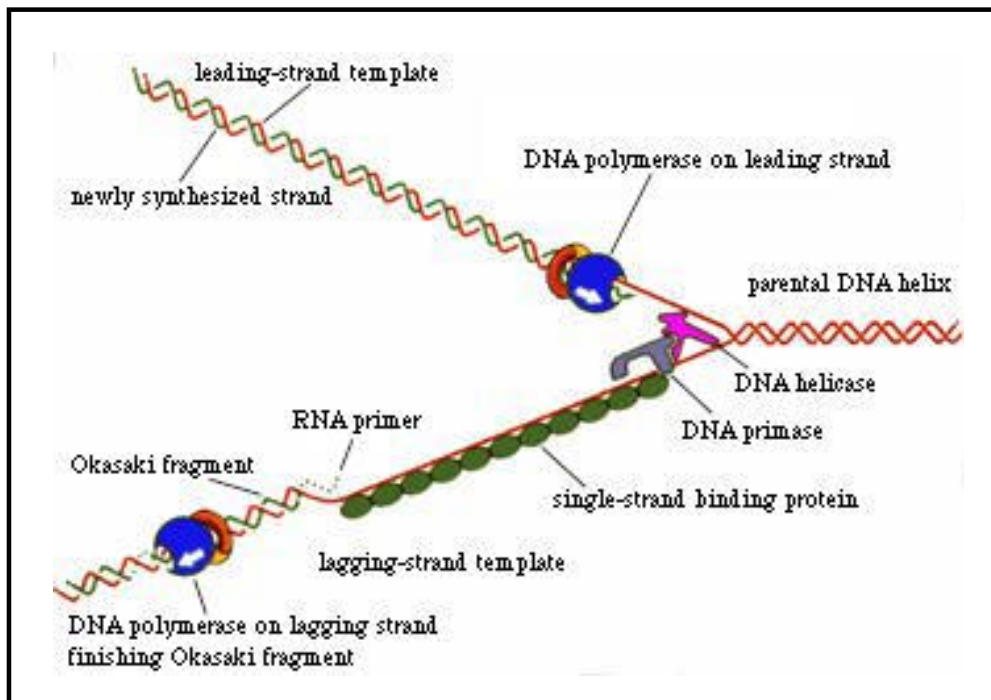


**Figure 19 : Schematic of DNA replication process.**

One function of DNA helicase is to unwind the double-stranded DNA at the replication fork so that DNA polymerase can replicate the DNA strands. *From (Lehninger et al., 1993)*

### ***III.1.3 Helicase characteristics and helicase deficiency diseases***

#### ***III.1.3.1 Classification of helicases***

Helicases are ubiquitous enzymes that unwind or transport double-strand nucleic acids during replication, recombination, transcription and DNA repair. Functioned as molecular motors, the helicases are essential to DNA and RNA metabolism. For the separation of the duplex, they are usually considered as a motor translocates along strand of nucleic acid. Based on the sequence homology, helicases were divided into five superfamilies (SFs) by Gorbalenya and Koonin in 1993 (Gorbalenya & Koonin, 1993). Motif I and motif II exist amongst all five superfamilies in which motif I is characterized by the sequence of GxxxxGK(T/S) and the formation of a loop at N-terminal of protein, which mainly in charge of nucleotide binding (Subramanya et al., 1996). Motif II also known as “walker B motif”, includes the sequence of

DExx, which contributes to nucleotides hydrolysis. Subtle differences in motif II also resulted in further grouping of the helicases into DExH box helicase and DEAD box helicase in SF1 and SF2, respectively. Most of helicases discovered at present are members in SF1 or SF2 categories, which contain all the seven characterized helicase motifs. The structure for the prototype in SF2 helicase family, *E.Coli* RecQ helicase, has been illustrated in Figure 20. The catalytic core of *E.Coli* RecQ helicase contains one ATP binding site and another ssDNA binding site, which preserve the unwinding activity for *E.Coli* RecQ helicase. SF3 and SF4 contain 3 helicase motifs and 5 motifs, respectively. The helicases in SF5 group are characterized by the sequence similarities to  $\beta$ -subunit of ATP synthase. (Table 2).

**Table 2. Primary superfamilies of helicase.** Based on the number of conserved motifs and motifs sequence similarities, helicases are classified in five superfamilies.

Superfamily (SF)	Family	Features
SF1	Hel4, Tral, PcrA, UvrD, Dda, Pif UL5, Sen1, Rep, (+)RNA helicase virales, setx	Contain all seven helicase motifs
SF2	RecQ, CI, UvrB, PriA, UL9, 18R, Ercc3, SNF2, Rad3, eIF-4A family DEAD, PRP family DEAH, BRCA1, ATRx	Contain all seven helicase motifs
SF3	Rep, 2C, AI 1, T ant,	Contain 3 helicase motifs
SF4	DnaB	Contain 5 helicase motifs; unwind with DNA 5'to3' polarity; usually forming hexameric ring
SF5	Rho	Sequence similar to $\beta$ -subunit of ATP sythase

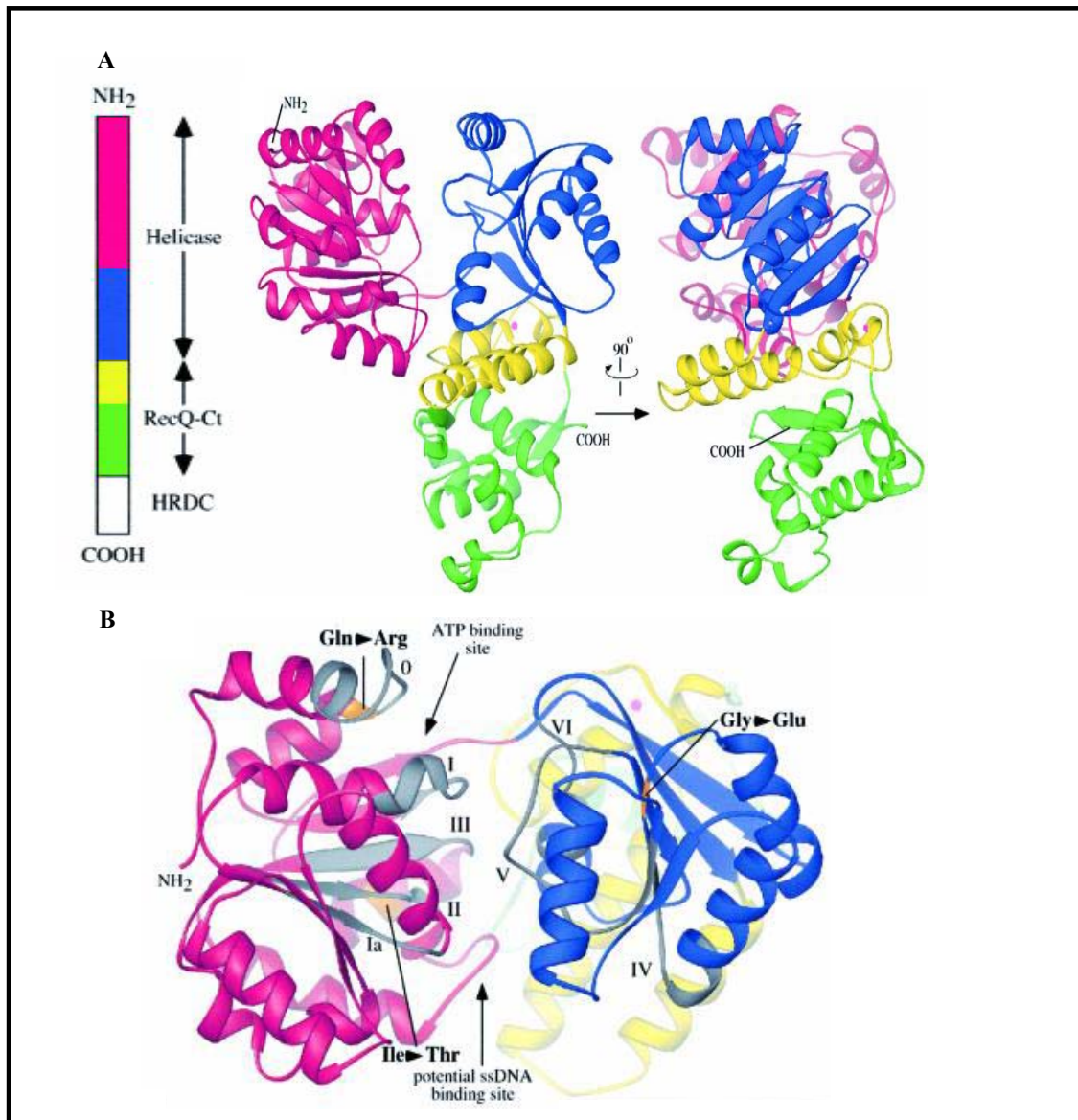


**Figure 20 : Schematic illustration of *E.Coli* RecQ helicase structure.**

**A :** Three conserved regions exist in the structure of *E.Coli* RecQ helicase, they are helicase domain (~40 KDa), RecQ C-terminal domain (~19 KDa) and helicase-RNaseD-C-terminal domains (~9 KDa). The catalytic core of *E.Coli* RecQ only contains the helicase domain and the RecQ C-terminal domain, which possesses four sub-domains labeled in this figure by different colors (red; blue; yellow and green).

**B :** In the helicase domains, the helicase motifs are colored in grey. Two indispensable binding sites are indicated in this figure.

From (Bernstein et al., 2003).

### ***III.1.3.2 Helicase function schemes for DNA unbinding and translocation***

During unwinding of dsDNA, and to translocate processively without dissociation from DNA, the helicase must use at least two DNA-binding sites to keep contact with the DNA lattice; one binds to ssDNA for translocation, whereas the other binds to dsDNA for DNA unwinding. These two DNA binding sites may be located at different domains within a single polypeptide of a monomer or be held by two different polypeptides within a dimer or an oligomer for providing multiple DNA-binding sites.

Corresponding to the first possibility, the active “rolling” model (Figure 21A) requires that the enzyme be oligomeric and at least dimeric. Each promoter possesses an identical DNA binding site. Both sites could bind either ssDNA or dsDNA, and binding of ssDNA and dsDNA cannot occur simultaneously in the same subunit. Binding of ATP leads to the enzyme interacting alternatively with the ssDNA and dsDNA at the junction region. Furthermore, hydrolysis of ATP destabilizes hydrogen bonds between the base pairs of the duplex. This model was originally based on the observed allosteric effects of ATP and ADP on the ssDNA and dsDNA binding properties of the *Escherichia coli Rep* dimer (Wong&Lohman, 1992). However, the crystal structures of Rep helicase bound to ssDNA alone or bound to both ssDNA and ADP have revealed that the protein remained monomeric; no protein-protein interactions were observed (korolev et.al., 1997).

Corresponding to the second possibility, the “inchworm” model (Figure 21B) was proposed, in which the helicase is assumed to possess two nonidentical DNA binding sites (Yarranton&Geftter, 1979); the “leading” site binds both ssDNA and dsDNA and interacts with the duplex to be unwound during successive unwinding cycles, whereas the “lagging” site interacts only with ssDNA. The disruption of the dsDNA at the leading site and the translocation of the enzyme are the result of conformational change of the enzyme modulated by binding and hydrolysis of ATP. Recent crystal structures of complexes of PcrA helicase with a partial dsDNA duplex substrate show that the ssDNA and dsDNA bind, respectively, on two domains of this monomeric helicase (Velankar et.al., 1999). These data provided direct proof to support an inchworm mechanism (Soulтанas&Wigley, 2000).

An essential difference between the “inchworm” and “rolling” model is that an oligomer is absolutely required for translocation and unwinding in the case of the rolling model, whereas a monomeric form or any oligomeric form could function in the inchworm model. Thus, the

knowledge of the oligomeric structure of a helicase is of fundamental concern in understanding the mechanism by which the protein unwinds DNA. In detail, for *E.Coli* RecQ helicase, the “inchworm” model is preferred; as to the human RecQ5 $\beta$  helicase, a model has been proposed by Ren et al. (Ren et al., 2008) recently which involved with the role of the zinc-binding motif in the functional combination of the “unwinding activity” and “strand annealing” activity.

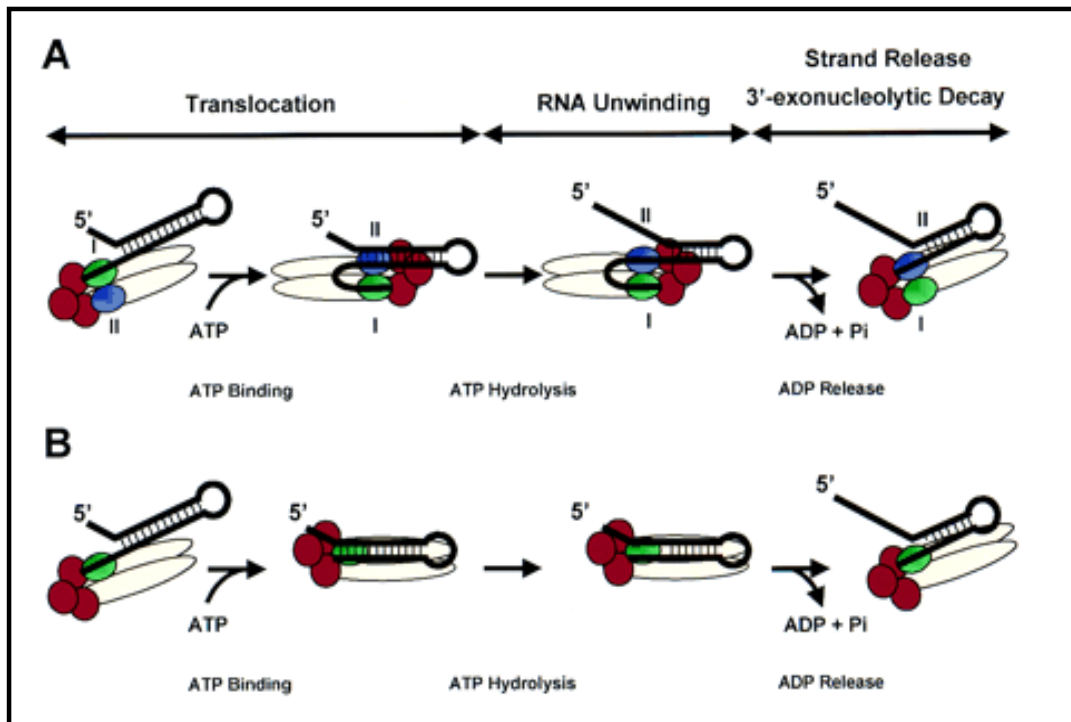


**Figure 21 : Two potential mechanisms for RhlB-activated degradation of structure RNA by the degradosome.**

**A:** A model prompted by the active, rolling model for DNA unwinding and translocation by the Rep DNA helicase. The Rne protein (beige oval) serves as a scaffold to coordinate the action of the RhlB helicase (subunit I, green oval; subunit II, purple oval) with PNPase (red circles). This allows single-stranded RNA generated by the RNA helicase to be passed directly to the 3' exonuclease PNPase (see text). The nucleotide-bound state of RhlB would result in a cycle of conformational and RNA affinity changes that result in translocation, RNA unwinding, and strand release/exonucleolytic degradation.

**B:** A second model based on the inchworm mechanism proposed for the PcrA DNA helicase. In this case, RhlB acts as a monomeric protein (shown in green) that can bind both single- and double-stranded RNA. Degradation of single-stranded RNA by PNPase (red circles) takes place during the translocation step. *From (Wong and Lohman 1992; Korolev et al. 1997; Velanker et al. 1999).*

### ***III.1.3.3 Helicases deficiency diseases***

Several genetic human diseases are related to helicase dysfunctions. Such as helicase ATRx (SF2) is related to alpha thalassemia X-linked Mental Retardation syndrome which characterized by mental retardation and unique craniofacial features, alpha thalassemia. Similarly, BACH1 (SF2) is related to breast cancer and ERCC3 (SF2) and ERCC2 (SF2) to Xeroderma pigmentosum B and D, which shows cutaneous hyperpigmentation in sun-exposed regions of the body during the first months of life. ERCC6 (SF2) is associated with Cockayne syndrome, which develops in infants between age 1 and 2 with clinic features such as poikiloderma, mental retardation, pigmentary, retinopathy and hearing loss; FANCF (SF2) and FANCG (SF2) are known to related to Fanconi anemia, which patients are commonly associated with high frequency of bone marrow failure, developmental abnormalities, and high risk of cancer, particularly acute myelogenous leukaemia. Furthermore, SETX (SF1) is associated with Amyotrophic lateral sclerosis, a neurodegenerative disease causing a progressive loss of motor neurons (Uhring&Poterszman, 2006).

The most prominent helicase-related illnesses are Bloom's syndrome (BS), Werner syndrome (WS) and Rothmund-Thomson syndrome (RTS) and they all associated with the dysfunction of RecQ family helicase- SF2. The common features of these three autosomal recessive disorders are chromosomal abnormalities and predisposition of cancers. BS related gene codes a protein named bloom protein (BLM). It's the main subject of this thesis, which will be discussed in detail hereafter. BS patients appear to be dwarfism with sun-sensitive erythema, immunodeficiency, and sterility. Symptoms of WS are associated with premature ageing after adolescence for example: graying and loss of hair, wrinkling and ulceration of skin, diabetes, cataracts, osteoporosis, hypertension, and atherosclerosis (Martin, 1978; Salk et.al., 1985). WS cells show higher frequency of chromosomal deletion, insertion, and translocation (Salk et.al., 1981; Fukuchi et.al., 1989). Main phenotypes of RTS are abnormalities on skin and skeleton, such as, skin hyperpigmentation, poikiloderma, congenital skeletal defects, and tendency of osteosarcomas (Dick et.al., 1982; Varughese et.al., 1992; Drouin et.al., 1993).

WS and RTS are related to the dysfunction of two RecQ helicases WRN (Werner protein) and RecQ4, repectively. Comparing to WS and BS, which displayed high correlations between WRN and BLM gene mutations and the related syndromes, some RTS cases (about 34%) have no obvious mutagenesis connection with RecQ4(Kital et al., 1999; Lindor et al., 2000; Wang et al.,

2003). RecQ4 had no detectable helicase activity *in vitro*, but it was proved to have a DNA dependent ATPase activity and RPA-inhibitable annealing activity (Macris et.al., 2006). Its deficiency in cells results in mosaic trisomies and isochromosomes. In contrast, WRN and BLM are all effective helicases on variable DNA substrates, including fork DNA, D-loop, holiday junction and G-quadruplex DNA, *in vitro* (Brosh et al., 2002). WRN has a unique nuclease motif at its N-terminal region as compared to other RecQ helicases in human which gives WRN a new role as an exonuclease (Choudhary et al., 2004). Cooperation of the helicase activity and exonuclease activity may facilitate the replication fork regression hence indicates its function in resolving stalled replication forks (Machwe et al., 2005; Machwe et al., 2006; Machwe et al., 2007). WRN's association with telomere repeat binding factor 2 may also suggest its involvement in alternative lengthening of telomeres (ALT) to maintain telomere length (Opresko et al., 2002). The telomeric DNA contains hundreds of tandem repeats of a six-nucleotide sequence. One of the strands is G rich at the 3' end, and it is slightly longer than the other strand. In human beings, the repeating G-rich sequence is AGGGTT. The structure adopted by telomeres has been proposed to form a loop-like structure in order to protect the end of the chromosome and stabilized by specific telomere-binding proteins. This process is consistent with the phenotype of WS, because the length of telomere is considered as an indicator of senescent process of animal. Shortly speaking, several premature aging syndromes are associated with short telomeres, eg. Werner syndrome, Friedreich's ataxia and the chromosome X fragile syndrome. The genes that have been mutated in these diseases all have roles in the repair of DNA damage. The dissociation and association of the long terminal reversed sequence for telomerase can also induce severe heart disease as well as cancer. Presently, the research on the clinical treatment of cancer has drawn more attention on the repetition sequence on the telomerase enzyme.

At a cellular level these genetic disorders all reveal high levels of genomic instability. Such molecular defects are readily studied in model organisms, and particularly in a genetic model like yeast.

## ***III.2 E.Coli RecQ Helicase Unwinding Activity as Monitored by Dual Color Fluorescence Correlation Spectroscopy***

### ***III.2.1 Introduction***

RecQ helicase belongs to the Superfamily 2 helicase, named for similarity to *Escherichia coli* RecQ helicases. It plays an important role in maintenance of genome stability. They function through unwinding paired DNA and translocating in the 3' to 5' direction (Bernstein & Keck., 2003).

RecQ helicases are conserved between prokaryotes and eukaryotes, and a multi-gene family exists in metazoan (Uhring & Poterszman, 2006). In prokaryotes RecQ is necessary for plasmid recombination and DNA repair from UV-light induced DNA damage. In eukaryotes, replication does not proceed normally in the absence of RecQ proteins, which also function in aging, silencing, recombination and DNA repair (Machwe et al., 2005). Three of human RecQ helicases, WRN (Yu et al., 1996), BLM (Ellis et al., 1995), and RECQ4 (Kitao et al., 1999), are associated with human genetic diseases, Werner, Bloom, and Rothmund-Thomson syndromes, respectively. These syndromes are characterized by premature ageing, graying and loss of hair, cancer, type II diabetes, osteoporosis and atherosclerosis, all of which are diseases that are common at old age. These diseases are associated with high incidence of chromosomal abnormalities, including chromosome breaks, complex rearrangements, deletions and translocations, site specific mutations and in particular sister chromatid exchanges that are believed to be caused by a high level of somatic recombination.

To better understand how helicases unwind the duplex nucleic acids, the *E.Coli* RecQ, which is highly conserved across a wide variety of organisms and is composed of 610 amino acids, are chosen as the prototype helicase of this family. The proteins displays a 3'-5' polarity in DNA unwinding and can unwind diverse DNA substrates including DNA with 5'-3' overhangs, nicked or forked DNA, and three- or four- way junctions as well as G4 DNA (a guanine-rich parallel four-stranded DNA structure (Umezu et al., 1990; Wu & Maizels, 2001)). The *E.Coli* RecQ helicase bound to DNA with an apparent binding stoichiometry of 1 protein monomer/10 nucleotides and while destabilizing the hydrogen bonds between the complementary base pairs by using the energy from the hydrolysis of nucleoside 5'-triphosphate, usually an ATP (Matson et al., 1994; Lohman & Bjornson 1996). It has a single strong DNA binding site with a low association constant at 25°C and both the single-stranded DNA and double-stranded DNA bind

competitively to the same site. The intrinsic affinities are salt-dependent and the formation of DNA-helicase complex is accompanied by a net release of 3-4 Na<sup>+</sup> ions (Dou et. al., 2004).

Nowadays, several continuous fluorometric helicase assays in real time have been developed to measure the unwinding of duplex nucleic acids by helicase (Roman & Kowalczykowski, 1989; Bjornson et al., 1994; Houston & Kodadek, 1994; Raney et al., 1994; Egglestone et al., 1996). However, the detection sensibility and the ability to monitor the dynamic helicase unwinding processes in real time are limited.

Dual-color FCCS has been considered as a promising fluorescent technique in monitoring enzyme kinetics in dynamic process (Eigen & Rigler, 1994; Ulrich et al., 1998). It allows very sensitive detection of molecular dissociations, which is based on the computation of the cross-correlation of the fluctuations in the fluorescence emission of two spectrally distinct dyes that label the two molecular dyes. Fluorescent fluctuations can be detected in a tiny volume at nanomolar concentration. A maximum cross-correlation is measured for non-dissociated samples for which the diffusion of both dyes through the excitation volume occurs simultaneously. Upon dissociation the degree of cross-correlation decreases owing to the independent random passage of the two dyes through the excitation volume. Some recent applications concern the use of the method FCCS as rapid assay for kinetic reactions in homogeneous sample solutions (Kolterman et al., 1998; Winkler et al., 1999).

Here, we report for the first time the successful use of the FCCS method to measure *E.Coli* RecQ helicase DNA unwinding activities in real time under two enzymatic significant conditions: single turnover condition (protein concentration > substrate concentration) and Michaelis-Menten condition (substrate concentration > protein concentration). The cooperative DNA-binding mode and the strong *E.Coli* RecQ helicase concentration-dependence of the single-turnover kinetic constant were also studied. Influences of temperature (25°C; 37°C), the number of ss 3'-tails present on the DNA substrate and the total length of the substrate on helicase unwinding activities were monitored. The RecQ helicase binding ability to DNA substrates were also discussed with that of ATP. In particular, comparison between the effects of Single strand binding (SSB) proteins and the complementary ssDNA in varied size on *E.Coli* RecQ helicase enzymatic kinetics was carried on in present study.

### ***III.2.2 Manuscript***

This manuscript has been handed in to Journal of Biological Chemistry and it is under review.

## Multiple *Escherichia coli* RecQ Helicase Monomers Cooperate to Unwind Long DNA Substrates: A Fluorescence Cross-Correlation Spectroscopy Study

Na Li<sup>1</sup>, Etienne Henry<sup>1</sup>, Elvire Guiot<sup>1,2</sup>, Pascal Rigolet<sup>3</sup>, Jean-Claude Brochon<sup>1</sup>, Xu-Guang Xi<sup>3</sup> and Eric Deprez<sup>1</sup>

<sup>1</sup> Laboratoire de Biologie et Pharmacologie Appliquées (LBPA), CNRS UMR8113, Ecole Normale Supérieure Cachan, Institut d'Alembert, 61 av. du Président Wilson, 94235 Cachan, France.

<sup>2</sup> Present address: Laboratoire de Neurobiologie des Processus Adaptatifs, CNRS UMR7102, 9 quai St-Bernard, 75005 Paris, France.

<sup>3</sup> Laboratoire de Génotoxicologie et Cycle Cellulaire, CNRS UMR2027, Institut Curie-Section de Recherche, Centre Universitaire, Bat 110, 91405 Orsay, France.

Running head : Functional cooperativity of RecQ Helicase for DNA unwinding

Address correspondence to: E. Deprez, LBPA, CNRS UMR8113, ENS-Cachan. Tel. 33-147-40-23-94; Fax. 33-147-40-76-84; Email [deprez@lbpa.ens-cachan.fr](mailto:deprez@lbpa.ens-cachan.fr)

The RecQ family helicases catalyse the DNA unwinding reaction in an ATP hydrolysis-dependent manner. In this study, we investigated the mechanism of DNA unwinding by the *Escherichia coli* RecQ helicase, using a new sensitive helicase assay based on fluorescence cross-correlation spectroscopy (FCCS) with two-photon excitation. The FCCS-based assay allows the measurement of unwinding activity under both single- and multiple-turnover conditions, without any limitation related to the size of the DNA strands that constitute the DNA substrate. We found that the monomeric helicase is sufficient for performing unwinding on short DNA substrates. Nevertheless, using longer DNA substrates under single-turnover conditions, we observed an increase in the activity, originating from multiple helicase monomers simultaneously bound to the same DNA. This functional cooperativity strongly depends on several factors, including the DNA substrate length, the number of single-stranded 3'-tails and the temperature. Concerning the latter parameter, a strong cooperativity was observed at 37°C while only a modest or no cooperativity was evidenced at 25°C, regardless of the nature of the DNA substrate. Consistently, the functional cooperativity was found to be tightly coupled to a cooperative

DNA-binding mode. Additionally, we show that the cooperative binding of helicase to the DNA substrate indirectly accounts for the sigmoidal dependence of unwinding activity on ATP concentration, which also occurs only at 37°C but not at 25°C. Finally, we further examined the influences of the spontaneous DNA re-hybridization (following helicase translocation) and the single-stranded DNA binding property of helicase on the unwinding activity as measured in the FCCS assay.

Helicases are molecular motor enzymes that unwind and translocate along nucleic acids in an ATP hydrolysis-dependent manner (1;2). RecQ DNA helicase is a ubiquitous family of helicases playing a key role in the maintenance of genome stability in a wide range of organisms, from bacteria to higher eukaryotes (for a review, see (3)). These enzymes are involved in many DNA metabolism processes such as recombination, DNA replication and DNA repair. In humans, defects in RecQ family helicases, encoded by the *blm*, *wrn* and *RecQ4* genes, give rise to Bloom, Werner and Rothmund-Thomson syndromes, respectively, characterized by genomic instability and cancer susceptibility. The *Escherichia coli* RecQ helicase, the prototype enzyme of this family, is involved in different processes including homologous recombination and double strand break repair mediated by the

RecF machinery (4), as well as suppression of illegitimate recombination (5).

The structure-function relationship of helicases is difficult to understand at the molecular level, since distinct protein organizations can lead to similar activities. One example is related to the oligomeric status of the active helicase that strongly varies from one helicase family to the other, *i.e.* hexameric rings for *Escherichia coli* DnaB and Rho, bacteriophage T4 gp41 and T7 gp4 (6-12), dimeric forms for Rep and UvrD helicases (13;14), and monomeric for PcrA and RecQ helicases (15-18). Despite extensive biochemical and structural studies of helicases, the mechanism of DNA unwinding remains obscure and several enzymatic features of the RecQ family helicases are not clearly understood. In particular, the oligomeric status of the active *E. coli* RecQ helicase is unclear since enzymologic studies of the unwinding reaction – under pre-steady-state conditions – strongly suggest a monomeric active form (18), while a previous study reports a sigmoidal dependence of the unwinding activity on ATP concentration, suggesting a multimeric active form (19). Other difficulties in the interpretation of enzymatic parameters are related to side phenomena that strongly influence the measurement of helicase activity such as: (i) the DNA re-hybridization occurring after the unwinding process, (ii) the ability of helicase to bind to the single-stranded DNA product, reducing subsequent turnover. The relative impact of these intrinsic properties of either the DNA or the helicase molecule, respectively, can be difficult to estimate, depending on the method used for monitoring the unwinding activity (20).

Fluorescence correlation spectroscopy (FCS)<sup>1</sup> measures the translational diffusion of molecules as the temporal behaviour of fluorescence intensity fluctuations within a small excitation volume, described by the autocorrelation function (21-23). Nevertheless, this approach, via the determination of the diffusion coefficient, is not very sensitive in measuring molecule interactions or dissociation events when the two interacting entities have similar molecular sizes. This main limitation can be overcome by using dual-colour fluorescence

cross-correlation spectroscopy (FCCS) which monitors the cross-correlation of the fluorescence fluctuations of the two interacting species – labelled by spectrally distinct fluorophores – and, then, quantifies the amount of fluorescently double-labelled species. A maximum cross-correlation amplitude is obtained when the two molecular species diffuse simultaneously and in a systematic manner through the excitation volume, indicating a physical interaction, while a decrease in this amplitude accounts for an independent diffusion due a dissociation event. This approach was shown to be suitable for monitoring varying enzymatic activities or processes such as proteolysis (24), endonucleolytic cleavage by restriction enzymes (25;26), DNA repair (27) and DNA recombination (28).

Here, we describe the use of two-photon excitation FCCS for monitoring the unwinding activity of helicase. This assay is sensitive and suitable for studying unwinding activity as it allows real-time kinetic studies in the low nanomolar range, is compatible with both single- and multiple-turnover enzymatic conditions and does not require separation of the single-stranded (ss) DNA product from the double-stranded (ds) DNA substrate by gel-electrophoresis. As mentioned above, the cross-correlation of the two fluorescence signals in FCCS is related to the concomitant diffusion of the two fluorescently labelled molecules. Thus, using doubly labelled ds DNA substrates, a significant decrease in the amplitude of the cross-correlation function is expected upon unwinding activity, originating from the physical separation of the two DNA strands (the principle of the FCCS-based helicase assay is indicated in Fig. 1A). In contrast to the resonance energy transfer (FRET) approach, FCCS is not sensitive to fluorophore orientation and/or interfluorophore distance; the loss of the cross-correlation signal is only sensitive to the helicase-mediated strand separation and not to other phenomena such as, for instance, unrelated local motions of fluorophores at the DNA ends that may also influence the donor-acceptor distance. Recently, an helicase assay based on fluorescence anisotropy was described but real-time kinetic studies suffered from difficulties inherent to

helicase binding to the ss DNA product (20). Moreover, this assay was only compatible with single-turnover conditions, *i.e.* when enzyme concentration is over DNA substrate concentration. The FCCS assay has no such limitation since the basic principle is not simply based on a difference in size between the substrate and the reaction product but on the extent of the concomitant diffusion of the two DNA strands.

In this work, the unwinding activity of *E. Coli* RecQ helicase was studied under both single- and multiple-turnover conditions using FCCS. We found that RecQ helicase monomers can function cooperatively or non-cooperatively, depending on several parameters, including the length of the DNA substrate and the temperature of the DNA-binding step. Remarkably, the cooperative properties of helicase at the DNA-binding level were found to be predictive of the subsequent cooperative effects observed at the catalytic level. We also demonstrate that the cooperative dependence of the unwinding activity on ATP concentration indirectly originates from the cooperative DNA-binding mode of RecQ helicase, reconciling apparent contradictory results in the literature concerning the possibility to have a monomeric active form while the activity displays a strong cooperativity on ATP concentration (Hill coefficient  $\approx 3$ ), previously interpreted as compelling evidence in support of a multimeric active form (minimally trimeric) (19). Altogether, our data indicate that oligomerization is not a prerequisite for the RecQ helicase activity, but, under specific conditions, the cooperative assembly of the helicase/DNA complex leads to the possibility that multiple monomers may align along the same DNA substrate and function in a cooperative manner. Finally, we further examined the influences of both the spontaneous DNA re-hybridization – following helicase translocation – and the ss DNA binding property of helicase on the unwinding activity as measured in our assay. To address these questions, the effects of short ss oligonucleotides and the single-stranded DNA-binding protein (SSB) on the catalytic rate constant of RecQ helicase were evaluated.

## EXPERIMENTAL PROCEDURES

***RecQ helicase purification, SSB and oligonucleotides***- The *E. coli* RecQ helicase was purified as previously described (20;29). The SSB protein was purchased from Sigma. Unlabelled and fluorescently labelled oligonucleotides (Table I) were purchased from Eurogentec (Liege, Belgium) and further purified by electrophoresis on an 12 or 15% denaturing acrylamide/urea gel for long (>10-mer) or short (7- and 10-mer) oligonucleotides, respectively. Double-stranded DNAs were obtained by mixing equimolar amounts of complementary DNA strands in 20 mM Hepes (pH 7.2), 100 mM NaCl. The mixture was heated to 85°C for 5 min and annealing was allowed by slow cooling to 25°C.

***Fluorescence cross-correlation spectroscopy***- Dual-color FCCS measurements were performed with two-photon excitation using a single laser line on a home-built system (previously described in (30) for the FCS mode) using a 100-fs pulse 80-MHz mode-locked Mai Tai Ti:Sapphire tunable laser (Spectra Physics, Mountain View, California, USA) and a Nikon TE2000 inverted microscope. Briefly, before entering through the epifluorescence port of the microscope, the laser beam was expanded with a two-lens afocal system to over-fill the back aperture of the objective (Nikon, Plan Apo, 100x, N.A. 1.4, oil immersion). The setup was optimized to obtain a diffraction-limited focal spot. Measurements were typically carried out in a 50- $\mu$ l solution dropped on a coverslip treated with dimethyldichlorosilane. The fluorescence signal from Alexa488 (Al) and Texas Red (Te) was collected by the same objective and separated from the excitation by a dichroic mirror (Chroma 700DCSPXR). The output signal from the microscope was further filtered by a Chroma E700SP-2p filter – to reject the residual excitation light – and split by a dichroic mirror (Chroma 580dcxr). Additional filters (Chroma HQ510/50 and HQ630/60m-2p for Alexa488 and Texas Red, respectively) were used to minimize cross-talk (Fig. 1B) and the split fluorescence signal was focused on two avalanche photodiodes (Perkin Elmer LifeScience, SPCM-AQR-14 single-photon

counting module with less than 90 dark-counts/sec), mounted at right angle. The detectors were connected to a digital correlator (ALV 6000, ALV-GmbH, Langen, Germany) that computes the normalized cross-correlation function  $g_{Al/Te}(\tau)$  (or  $g(\tau)$ ) of the two fluorescence intensity fluctuations, according to Equation 1:

$$g_{Al/Te}(\tau) = \frac{\langle I_G(t) \bullet I_R(t + \tau) \rangle}{\langle I_G(t) \rangle \bullet \langle I_R(t) \rangle} \quad (1)$$

where  $I_G(t)$  and  $I_R(t)$  are the number of detected fluorescence photons per time unit for green (Alexa488) and red (Texas Red) channels, respectively. Assuming a 3D Gaussian distribution of the excitation intensity, the cross-correlation function for a free Brownian diffusion process is given by Equation 2:

$$g_{Al/Te}(\tau) = \frac{1}{N} \bullet \frac{1}{\left(1 + \frac{\tau}{\tau_D}\right) \bullet \sqrt{1 + \frac{\omega_0^2}{z_0^2} \bullet \frac{\tau}{\tau_D}}} \quad (2)$$

where  $N$  is the mean number of doubly fluorescently labelled species in the excitation volume, and  $\tau_D$  is the corresponding translational diffusion time.  $\omega_0$  and  $z_0$  are the lateral and axial dimensions of the excitation volume, respectively. The calibration of the excitation volume was done using a 5 nM water solution of Alexa Fluor 488 (succinimidyl ester; Molecular Probes, Eugene, OR; diffusion coefficient,  $D = 426.3 \mu\text{m}^2/\text{s}$  at  $21^\circ\text{C}$ ). The excitation wavelength was 780 nm and the excitation power was 25 mW. Assuming a Gaussian beam shape and according to Equation 2 and  $\tau_D = \omega_0^2/8D$ , the lateral  $\omega_0$  and axial  $z_0$  dimensions were estimated to be 0.380 and 1.40  $\mu\text{m}$ , respectively.

The optimal two-photon excitation wavelength for the FCCS experiments using Alexa488 and Texas Red was found to be 780 nm. In the present study, we determined that an excitation power of 25 mW was suitable for two-photon excitation of both Alexa488 and Texas Red (fluorescence intensities exhibited quadratic dependences and  $\tau_D$  values were constant as a function of the incident power below 30 mW. Photobleaching occurred principally above 30

mW). The excitation power was adjusted using a variable attenuator, consisting of an achromatic half-wave plate and a polarizing beam splitter (Micro Controle Spectra Physics, France). Recording times were typically between 2.5 and 5 min (average of 5-10 cycles of 30 s). The cross-correlation curves were fitted using a Levenberg-Marquardt nonlinear least-squares fitting algorithm according to the analytical model (Equation 2) using Igor Software (WaveMetrics). For all experiments with doubly labelled ds DNA substrates in the absence of ATP, the amplitude of the cross-correlation function,  $g(0)$ , was found to be consistent with the autocorrelation amplitudes obtained for the two independent channels, confirming the absence of singly labelled ss DNA before the beginning of the reaction (data not shown). The decrease in the  $g(0)$  value was used to calculate the unwinding activity as a function of time according to Equation 3:

$$\frac{[\text{DNA}]_{\text{unwound}}}{[\text{DNA}]_{\text{total}}} = \frac{g(0)_{t=0} - g(0)_t}{g(0)_{t=0} - g(0)_{t \rightarrow \infty}} \quad (3)$$

with  $g(0)_{t=0}$  and  $g(0)_{t \rightarrow \infty}$  corresponding to the cross-correlation amplitudes at the beginning (zero time) and at the end (infinite time) of the reaction, respectively.

**DNA unwinding assay-** The RecQ helicase unwinding activity was measured by dual-color FCCS measurements (see above for the description of the FCCS set-up) in 20 mM Hepes (pH 7.2), 40 mM NaCl, 1 mM  $\text{MgCl}_2$ , 0.3 mM DTT (named reaction buffer). The concentration of doubly labelled DNA substrate was typically 5 nM. The DNA-binding step (performed at either  $T_{\text{binding}}^\circ = 25^\circ\text{C}$  or  $37^\circ\text{C}$ ) corresponds to the addition of RecQ helicase to the DNA solution. The unwinding reaction was then initiated by adding 1 mM ATP and recorded at  $T_{\text{reaction}}^\circ = 25^\circ\text{C}$  (unless otherwise stated). For multiple-turnover experiments ( $[\text{DNA substrate}] > [\text{RecQ helicase}]$ ), the varying concentrations of total DNA substrate were obtained by mixing doubly labelled DNA substrate (constant concentration of 5 nM) with varying concentrations of the corresponding unlabelled DNA substrate.

**DNA-binding assay: Steady-state fluorescence anisotropy-** The interaction between RecQ helicase and Alexa488-labelled oligonucleotides (either ds or ss) was detected by steady-state fluorescence anisotropy using a Beacon 2000 instrument (PanVera, Madison, USA) (20;31-33). To determine the apparent  $K_d$  value ( $K_{d,app}$ ), Alexa488-labelled DNA (5 nM) was incubated with increasing concentrations of RecQ helicase in 20 mM Hepes (pH 7.2), 40 mM NaCl, 1 mM  $MgCl_2$ , 0.3 mM DTT, and the steady-state anisotropy ( $r$ ) was then recorded. The fractional saturation was calculated as  $(r-r_{free})/(r_{bound}-r_{free})$ , where  $r_{bound}$  and  $r_{free}$  represent the bound and free DNA anisotropy, respectively. The Hill coefficient,  $\tilde{n}$ , was calculated by directly fitting the titration curve using the Hill function of the origin 6.0 software.  $K_{d,app}$  represents the concentration of RecQ helicase required to titrate the DNA to half saturation.

## RESULTS

First, we assessed whether the unwinding activity of *E. coli* RecQ helicase lead to a significant and measurable decrease in the cross-correlation amplitude,  $g_{AI/Te}(0)$  (or  $g(0)$ ), as measured by FCCS, using ds DNA substrates harbouring a ss DNA tail at each 3'-extremity (Fig. 1C, left. Sequences and nomenclature are reported in Table I). As seen in Fig. 2, when RecQ helicase and doubly labelled DNA substrate were mixed together, only addition of ATP lead to a time-dependent decrease in the  $g(0)$  value, demonstrating that the drop in the cross-correlation amplitude is actually due to the RecQ helicase-mediated unwinding of the DNA substrate (compare Fig. 2A and 2B). However, although the  $g(0)_{t \rightarrow \infty}$  value was weak, it was reproducibly different from 0 (about 0.02), suggesting that this value accounts for the crosstalk between the detection channels. Indeed, the same amplitude value was obtained using mixtures of non-complementary Alexa488- and Texas Red-labelled oligonucleotides (data not shown). The  $g(0)_{t \rightarrow \infty}$  value was then further considered in the calculation of the fraction of unwound DNA (see Equation 3). The unwinding kinetics was next studied as a function of the DNA substrate size under both single- and

multiple-turnover conditions. In the following sections, the temperature of the DNA-binding step ( $T^{\circ}_{binding}$ ) was either 25 or 37°C, and the reaction temperature ( $T^{\circ}_{reaction}$ ) was 25°C, unless otherwise specified.

### **Kinetic study under single-turnover conditions-**

Typically, the time-dependent process described in Fig. 2A was plotted and fitted by a single exponential model (Fig. 3A) corresponding to a single-turnover process, *i.e.* when enzyme is in excess over DNA. A similar experimental design was applied for studying the influences of both parameters, (i) enzyme concentration and (ii) the size of the DNA substrate, on the first-order kinetic rate constant  $k_{obs}$  ( $T^{\circ}_{binding} = 37^{\circ}C$ ;  $T^{\circ}_{reaction} = 25^{\circ}C$ ). Interestingly, the  $k_{obs}$  value increased by increasing the DNA length (from 13- to 66-bp) and was found to be also dependent on the enzyme concentration (Fig. 3B). This dependence was DNA size-dependent and saturable, with for instance, a modest and strong transition effects observed for 13- and 66-bp substrates, respectively (Fig. 3B). The stronger dependence of the first-order kinetic rate constant on helicase concentration, observed for longer DNA substrates, highly suggests functional cooperativity between different helicase molecules. Therefore, the stimulation of the unwinding reaction by increasing the DNA size, probably originates in the possibility that multiple RecQ helicase monomers function simultaneously on the same DNA substrate.

During the time-course of our study, we observed that this cooperative behaviour was also strongly affected by varying the temperature of the DNA-binding step (before addition of ATP). As shown in Fig. 3C for the 66-bp substrate, the  $k_{obs}$  value ( $T^{\circ}_{reaction} = 25^{\circ}C$ ) was much less dependent on helicase concentration when the pre-incubation step was done at  $T^{\circ}_{binding} = 25^{\circ}C$ , compared to  $T^{\circ}_{binding} = 37^{\circ}C$ . We then measured the helicase binding to DNA at two temperatures, 25 and 37°C, using steady-state fluorescence anisotropy (20;31;33). DNA-binding isotherms for RecQ helicase clearly show different DNA-binding mechanisms depending on the temperature (Fig. 4A-D): A cooperative DNA-binding mode was evidenced at 37°C (only for DNA substrates > 13-mer), while the cooperativity was much less at 25°C.

Moreover, the Hill coefficient increased as a function of the DNA substrate size at 37°C, while the DNA-binding remained almost non-cooperative at 25°C, regardless of the DNA substrate size (Fig. 4E). Altogether, our data suggest a direct relationship between the presence of the cooperative DNA-binding mode during the pre-incubation step and the subsequent dependence of the unwinding activity on helicase concentration and DNA length.

We wondered whether the cooperative behaviour could be influenced by the number of ss/ds junctions (*i.e.* number of ss 3'-tails) in the DNA substrate. We then tested the unwinding activity using 45- or 66-bp DNA substrates, containing either 0 (blunt), one or two ss/ds junctions (see Fig. 1C, right). Using blunt DNA substrates, no activity was detected (Fig. 5A & B). This result confirms that unwinding activity of RecQ helicase occurs onto DNA substrates containing at least one 3' ss DNA flanking region, while blunt-ended DNA substrates display no or marginal unwinding activity, according to previous studies (18;34;35). Moreover, using both 45- and 66-bp DNA substrates, the unwinding activity was systematically less dependent on the enzyme concentration when using one ss/ds junction-containing compared to two ss/ds junction-containing DNA substrates (Fig. 5A & B). The cooperative DNA-binding properties were then studied on these DNA substrates. Fig. 5C shows that the Hill coefficient significantly changed with the number of ss 3'-tails, with a dramatic change when comparing one ss/ds junction-containing and two ss/ds junction-containing DNA substrates. Clearly, the cooperativity was favoured by the presence of ss 3'-tails. This occurred mainly at 37°C, while cooperative effects were weaker at 25°C regardless of the DNA substrate (consistent with results shown in Fig. 4E). Altogether, our results suggest that the cooperative DNA-binding mode and the strong helicase concentration-dependence of the single-turnover kinetic rate constant are two closely related phenomena that account for the number of active monomers simultaneously present on the DNA substrate. In other words, the cooperative DNA-binding mode is predictive of the subsequent cooperative reaction mode, *i.e.*

when at least two helicase monomers may catalyse the unwinding reaction on the same DNA molecule, in a synergistic /cooperative manner. The corresponding assembly mechanism directly depends on the number of ss 3'-tails present on the DNA substrate as well as the total length of the substrate.

***Kinetic study under multiple-turnover conditions-*** FCCS experiments were also conducted for measuring the unwinding activity under Michaelis-Menten conditions, *i.e.* with excess of DNA substrate over enzyme concentration. The concentration of total DNA substrate was varied using mixtures of labelled/unlabelled ds DNAs (constant concentration of labelled ds DNA, 5 nM, and varying concentrations of unlabelled ds DNA) as fluorescence fluctuation spectroscopy and FCS/FCCS analysis are not compatible with high concentrations of fluorescent entities in the excitation volume. Results and corresponding Eadie-Hofstee plots are shown in Fig. 6 for two DNA substrates, 66-bp (Fig. 6A) and 22-bp (Fig. 6B). In contrast to the single-turnover rate constant  $k_{obs}$  (measured under conditions of excess enzyme over DNA substrate) which was found to be strongly dependent on the DNA size, no strong influence of the DNA size on the multiple-turnover  $k_{cat}$  parameter was observed ( $k_{cat,22-mer} = 0.126 \text{ min}^{-1}$  and  $k_{cat,66-mer} = 0.110 \text{ min}^{-1}$ ), confirming that only a high enzyme:DNA ratio is compatible with a synergistic activity of multiple helicase monomers on the same DNA substrate.

***Spontaneous re-hybridization after unwinding decreases the apparent unwinding rate-*** We next addressed quantitatively the influence of the re-hybridization process occurring immediately after DNA unwinding and helicase translocation on the unwinding rate constant. This process could underestimate the helicase activity as monitored by FCCS, in particular for long DNA substrates. The unwinding activity was then measured by FCCS using the 66-bp DNA substrate under single-turnover conditions, as described above, except that increasing concentrations of ss oligonucleotides (from 7 to 45 nucleotides) were added to the preformed helicase/DNA substrate complexes before addition of ATP.

In Fig. 7A, all ss oligonucleotides correspond to DNA sequences complementary to one strand of the duplex region of the substrate (see Table I). Two distinct effects were observed depending on the size of the ss DNA. For short ss DNAs (7- and 10-mer), the unwinding activity was first stimulated for low concentrations of ss DNA, with concentrations of about 100 nM to reach the optimal activity. Beyond this critical concentration, the unwinding activity was inhibited. In contrast, only an inhibition effect was observed using longer ss DNAs such as 32- and 45-mer. Moreover, non-complementary 7- and 10-mer sequences did not display any stimulation phase (Fig. 7B). These results indicate that the stimulation phase is due to hybridization of short ss DNA to the unwound complementary strand while the inhibition is probably due to trapping effects, *i.e.* binding of helicase to ss DNA. Indeed, the longer complementary ss DNAs, 32- and 45-mer, with higher affinities for helicase ( $K_{d,app} = 26$  and 12 nM, respectively, Fig. 7C), mainly displayed inhibition effects. In contrast, the affinities of helicase for shorter ss DNAs, 7- and 10-mer, were much lower ( $K_{d,app} = 95$  and 88 nM, respectively, Fig. 7C) and thus, concentrations up to 100 nM were not sufficient for trapping helicase to an extent that substantially counteracts the stimulating hybridization effect. Therefore, no inhibition, but stimulation of the unwinding rate occurs with such oligonucleotide concentrations that favour the hybridization process between the short oligonucleotide and the newly unwound complementary strand over the re-hybridization process between the two unwound strands.

These effects of short ss oligonucleotides on the unwinding activity were compared to the effects of the SSB protein under similar experimental conditions (Fig. 8A). A similar stimulating effect on the single-turnover rate constant (maximum 4-fold) was observed up to 150 nM SSB. The SSB-dependent stimulation of activity can be interpreted by two distinct mechanisms: (i) SSB prevents the re-hybridization process in a similar manner to short ss oligonucleotides since SSB strongly inhibits annealing (36-39); (ii) SSB binds to the ss DNA products and then increases the

concentration of available helicase for catalysis. Under single-turnover conditions, only the first mechanism probably accounts for the stimulating effect. As shown in Fig. 8B, the stimulating effect was significantly higher under multiple-turnover conditions (approximately 18-fold). Thus, we hypothesize that, in this latter case, both mechanisms contribute to the stimulation of helicase activity. However, under both single- and multiple-turnover conditions, we found that high SSB concentrations (>150 nM) reduced helicase activity, with a more pronounced effect under single-turnover conditions. It was previously shown that *E. coli* RecQ helicase physically interacts with SSB (40;41). A related stimulating effect of SSB on the unwinding activity was also reported by the authors. Nevertheless, the relative high  $K_d$  value characterizing this interaction (6  $\mu$ M), cannot fully explain the stimulating effects we observed under our experimental conditions (below 150 nM SSB). In contrast, this  $K_d$  value is more compatible with a relationship between the formation of helicase/SSB complexes and the observed inhibitory effect for SSB concentrations above 150 nM. This is consistent with the observation that the SSB-mediated inhibition is more potent under single-turnover conditions because, under multiple-turnover conditions (*i.e.* excess of DNA over helicase), ss DNA products may compete with RecQ helicase for the binding to SSB.

## DISCUSSION

In this study, we report that the FCCS approach is particularly well-suited for monitoring the helicase activity. This approach allowed us to study the unwinding activity of *E. coli* RecQ helicase under both single- and multiple-turnover conditions. Interestingly, under the single-turnover condition, strong functional cooperative effects were observed depending on several factors, namely the total length of DNA, the number of ss 3'-tails and the temperature. The dependences of the single-turnover kinetic rate constant on both the helicase concentration and the size of the DNA substrate suggest cooperative/synergistic effects, compatible with simultaneous unwinding of the same DNA substrate by multiple helicase

monomers. Consequently, the apparent unwinding activity is highly stimulated by increasing the DNA substrate length and by using high helicase:DNA ratio. In accordance with this statement, such a dependence on the DNA size was not observed under multiple-turnover conditions, *i.e.* using conditions of DNA excess over helicase. Furthermore, we observed a direct relationship between the cooperative properties of helicase binding to DNA and the subsequent cooperative effects at the catalytic level. All above-mentioned factors (DNA size, number of ss 3'-tails and temperature) influence both the cooperative DNA-binding mode and the functional cooperativity. No cooperative DNA-binding was evidenced in a recent study performed by Zhang *et al.* at 25°C (18). To date, only a cooperative response of *E. coli* RecQ helicase activity on ATP was previously described – at 37°C – (19). Here, we show that the *E. coli* RecQ helicase behaves cooperatively only at 37°C and that the cooperative DNA-binding mode of helicase at this temperature fully accounts for the sigmoidal response of the helicase activity on ATP concentration (see below).

FCCS, as other fluorescence-based methodologies (*e.g.* fluorescence anisotropy and FRET), is a sensitive method that directly measures the helicase activity without any requirement of separation of the ss DNA product from the ds DNA substrate by gel-electrophoresis. Using steady-state fluorescence anisotropy, the difference in size between the helicase/ds DNA substrate complex and the released fluorescently labelled strand is measured (20). This means that the fluorescence anisotropy approach is only compatible with single-turnover conditions (to ensure initial saturation of the DNA substrate). Additionally, the decrease in the anisotropy, concomitant to the unwinding activity, can be very low when helicase remains bound to the labelled strand, complicating analysis. However, this specific problem was circumvented by authors by using a short labelled strand (<13-mer) with lower affinity for helicase (confirmed in Fig. 7C). In contrast to fluorescence anisotropy, FCCS does not measure a size change; it is only sensitive to the concomitant diffusion of the two

fluorescently labelled DNA strands, with a high cross-correlation amplitude characterizing the duplex molecule and a significant decrease in this amplitude upon physical separation of the two strands. Thus, there is no limitation related to the size of the DNA strands that initially constitute the DNA substrate.

It is important to note that the inherent problem of the ss DNA-binding properties of helicase, if no technically limiting when using FCCS, strongly underestimates the unwinding activity, especially under multiple-turnover conditions. In fact, the binding of helicase to ss DNA products competes with the binding to ds DNA substrates, limiting activity. SSB partially counteracts this effect and, consequently, increases apparent catalytic activity (42). Moreover, the other stimulating effect of SSB on helicase activity, via inhibition of the spontaneous re-annealing of unwound strands, is probably common to both single- and multiple-turnover catalytic modes. The participation of the two mechanisms for stimulating helicase activity under multiple-turnover conditions, while only one is expected to be involved under single-turnover conditions (re-annealing inhibition), probably explains why SSB stimulates DNA unwinding more efficiently under multiple-turnover compared to single-turnover conditions (Fig. 8). However, the nature of the exact mechanism of SSB-mediated stimulation is not clear so far since it was recently described that SSB could also stimulate *E. coli* RecQ helicase through a direct physical SSB-RecQ helicase interaction (40;41). However, taking into account the  $K_d$  value characterizing this interaction (6  $\mu$ M), it seems unlikely that this interaction could be responsible for the SSB-mediated stimulating effect observed under our experimental conditions. The apparent  $K_d$  value characterizing the SSB-single-stranded DNA interaction as measured by fluorescence anisotropy ( $K_{d,app} = 94$  nM; Fig. 8C) is more compatible with the observed stimulating effect below 150 nM SSB. In contrast, one could reasonably imagine that the inhibition phase, observed for SSB concentrations above 150 nM, could be due, at least partially, to the helicase/SSB interaction. Another explanation could be that high SSB

concentrations may displace helicase from the DNA substrate ss 3'-tails.

Short complementary ss oligonucleotides (typically 7- or 10-mer) display similar stimulating effects on helicase activity, *i.e.* by minimizing spontaneous re-hybridization. However, as found with SSB, this stimulation is limited and rather modest as it is followed by a marked inhibition phase, due to competitive interactions detrimental for activity. In the case of short ss oligonucleotides, this inhibition can be easily explained by their significant affinities for helicase ( $K_{d,app} = 95$  and  $88$  nM, respectively). Indeed, longer ss oligonucleotides, 32- or 45-mer, with still higher affinities ( $K_{d,app} < 25$  nM), display only inhibition profiles. In contrast to FRET, the cross-correlation signal in FCCS is independent on the interfluorophore distance and on the structural dynamics of the attached fluorophores. FCCS is only sensitive to the physical and complete separation of the two DNA strands and, consequently, less sensitive to early catalytic events. This suggests that spontaneous re-hybridization could be more problematic in FCCS compared to the FRET/stopped-flow approach. Indeed, the calculated processivity of  $0.5\text{-}2.2$  bp.s<sup>-1</sup>, as determined in this study by FCCS, is globally consistent with other studies,  $1\text{-}3$  bp.s<sup>-1</sup> (19;20;29), but much less than the rate of  $84$  bp.s<sup>-1</sup>, as determined recently by FRET/stopped-flow (18). Thus, the stimulating effects of SSB and ss short oligonucleotides can be qualified as modest and only partially increase the apparent unwinding rate.

We found that the DNA-binding of *E. coli* RecQ helicase is characterized by a cooperative DNA-binding mode at 37°C, but is essentially non-cooperative at 25°C. Moreover, the cooperativity coefficient continuously increases as a function of the size of the DNA substrate and strongly depends on the number of ss 3'-tails; a high cooperativity index was obtained for long DNA substrates harbouring two ss 3'-tails. It was previously shown that the binding of RecQ helicase to DNA is non-cooperative at 25°C using DNA substrates containing one ss 3'-tail (18). The present results obtained under similar conditions confirm this statement. Altogether, our results highlight a different

DNA-binding mode of *E. coli* RecQ helicase depending on the temperature, suggesting a specific protein conformation compatible with cooperative assembly that occurs at 37°C but not at 25°C. The cooperativity is strongly related to the DNA size and the very low cooperativity measured for the short DNA substrate (13-bp), even at 37°C, is compatible with the binding size of 9-10 nt – for a monomeric unit – previously determined (18;43). As RecQ helicase is active on short DNA substrates, although no cooperativity is associated to such activity, we conclude that the monomer is sufficient to ensure DNA unwinding. However, increasing the length of the DNA substrate favours the binding of multiple catalytic entities and stimulates the apparent unwinding activity. Such a functional cooperativity, associated to a cooperative DNA-binding mode, suggests that RecQ helicase monomers can function in a concerted manner on the same DNA molecule, resulting in a substantial increase in the unwinding activity when multiple monomers are simultaneously bound to the DNA substrate. This property appears to be common to several monomeric helicases such as Hepatitis C virus helicase (44;45), bacteriophage T4 Dda (46) and yeast Pif1p (47). Several models have been proposed to explain the stimulating effect of activity including the possibility that one monomer helicase can prevent spontaneous re-hybridization behind another monomer following its translocation. It is important to note that no cooperativity was evidenced at the DNA-binding level at least for two of these monomeric helicases, *i.e.* Hepatitis C virus helicase (45) and Dda (46). For *E. coli* RecQ helicase, we show that the functional cooperativity correlates with the presence of a cooperative DNA-binding mode. In fact, all factors that modulate the Hill coefficient characterizing the helicase/DNA interaction, also influence the functional cooperativity. The physical meaning of this correlation remains to be elucidated. In particular, the influence of the number of ss 3'-tails on the cooperativity index is unclear. It was previously suggested that RecQ helicase preferentially binds to ss/ds DNA junctions (18). In first approximation, such a preference could explain the influence of the number of ss/ds junctions on the cooperativity. Nevertheless, our

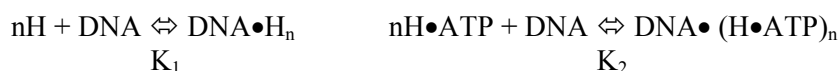
results indicate a synergistic effect of the presence of the two 3'-OH ss tails, regardless the length of the duplex DNA region (above 13-mer). Moreover, the cooperativity increases when the size of the duplex DNA region increases, while all DNA substrates used were characterized by identical ss tail lengths (already shown to be an important parameter in controlling the number of loaded helicases on the DNA substrate (45)). Our results indicate that the duplex region, not only the ss/ds DNA junction, plays a key role in the cooperative DNA-binding mode, although the elucidation of the mechanism behind the cooperative effects between the two 3'-tails requires further investigations.

Interestingly, a previous study has described a cooperative dependence (sigmoidal response) of *E. coli* RecQ helicase on ATP concentration (at 37°C), characterized by a Hill coefficient of 3.3, suggesting that helicase functions as an allosteric multimeric enzyme (minimally trimeric and possibly hexameric) (19). This finding is in apparent contradiction with others studies showing that RecQ helicase functions as a monomer (18;29). Moreover, one study underlines that RecQ helicase binds DNA with no cooperativity (18). It is worthy to note that in the latter case, the study was performed at 25°C, *i.e.* under condition where no cooperativity was observed in our assays. In contrast, we found that a significant cooperative DNA-binding mode exists for RecQ helicase at 37°C. We now address the possibility that the cooperative behaviour of helicase activity on ATP concentration is only apparent and originates in the cooperative DNA-binding of helicase rather than an allosteric transition. Equation 11 (see appendix) shows that the helicase activity may exhibit a cooperative response in ATP concentration simply due to indirect cooperative effects at the DNA-binding level, in absence of any allosteric transition and higher-order oligomeric organization, reconciling most of the apparent contradictions in the literature. To further investigate the relationship between the cooperative DNA binding mode of helicase and its cooperative behaviour for ATP dependence, we measured the unwinding rate using varying concentrations of ATP, at two temperatures: 25

and 37°C. In accordance with our model, Fig. 9 shows a stronger cooperative behaviour at 37°C compared to 25°C. The Hill coefficient at 37°C, 2.6 (Fig. 9A), is compatible with the Hill coefficient characterizing the helicase/DNA complex formation for a similar DNA length, 2.9 (Fig. 4A). The corresponding coefficients at 25°C were also consistent, 1.3 (Fig. 9A) and 1.4 (Fig. 4B), respectively. The slightly lower Hill coefficient characterizing the response in ATP concentration compared to the previously published value (3.3 in (19)) could be due to the nature of the DNA substrate used which is shorter in our study. X-ray structure of the catalytic core of *E. coli* RecQ helicase (named RecQ $\Delta$ C; 516 amino acids) shows a monomeric protein (48), in total agreement with biochemical and biophysical characterizations of the full-length protein (610 amino acids) by time-resolved fluorescence anisotropy and analytical ultracentrifugation (29). Altogether, our results indicate that RecQ helicase monomers bind cooperatively to long DNA substrates and cooperate for DNA unwinding, although the catalytic unit is actually the monomeric form which is functionally sufficient on short substrates. Finally, this cooperative DNA-binding mode accounts for the sigmoidal response of helicase unwinding activity to ATP.

## APPENDIX

Considering the DNA-binding step, helicase (H) can bind to DNA in either the free or the ATP-bound form:



$$\text{with } K_1 = \frac{[DNA][H]^n}{[DNA \bullet H_n]} \quad (4) \quad \text{and } K_2 = \frac{[DNA][H \bullet ATP]^n}{[DNA \bullet (H \bullet ATP)_n]} \quad (5)$$

The conservation relationship for DNA substrate can be written as:

$$[DNA]_{\text{total}} = [DNA] + [DNA \bullet H_n] + [DNA \bullet (H \bullet ATP)_n] \quad (6)$$

ATP can bind to the DNA-free or the DNA-bound helicase:



$$\text{with } K_3 = \frac{[H][ATP]}{[H \bullet ATP]} \quad (7) \quad \text{and } K_4 = \frac{[DNA \bullet H_n][ATP]^n}{[DNA \bullet (H \bullet ATP)_n]} \quad (8)$$

Eq. 6 can be simplified because  $[DNA] \rightarrow \varepsilon$  under conditions compatible with cooperative DNA-binding (excess of helicase over DNA):

$$[DNA]_{\text{total}} = [DNA \bullet H_n] + [DNA \bullet (H \bullet ATP)_n] \quad (9)$$

Eq. 8 and 9 can be rearranged as:

$$[DNA]_{\text{total}} = [DNA \bullet (H \bullet ATP)_n] \left(1 + \frac{K_4}{[ATP]^n}\right) \quad (10)$$

The initial rate of DNA unwinding ( $v$ ) is then given by:

$$v = \frac{k[DNA]_{\text{total}}[ATP]^n}{K_4 + [ATP]^n} \quad (11)$$

where  $k$  represents the catalytic rate constant.

## REFERENCES

1. Patel, S. S. and Donmez, I. (2006) *J.Biol.Chem.* **281**, 18265-18268
2. Singleton, M. R., Dillingham, M. S., and Wigley, D. B. (2007) *Annu.Rev.Biochem.* **76**, 23-50
3. Killoran, M. P. and Keck, J. L. (2006) *Nucleic Acids Res.* **34**, 4098-4105
4. Nakayama, H., Nakayama, K., Nakayama, R., Irino, N., Nakayama, Y., and Hanawalt, P. C. (1984) *Mol.Gen.Genet.* **195**, 474-480
5. Hanada, K., Ukita, T., Kohno, Y., Saito, K., Kato, J., and Ikeda, H. (1997) *Proc.Natl.Acad.Sci.U.S.A* **94**, 3860-3865
6. Galletto, R., Jezewska, M. J., and Bujalowski, W. (2004) *J.Mol.Biol.* **343**, 101-114
7. Galletto, R., Jezewska, M. J., and Bujalowski, W. (2004) *J.Mol.Biol.* **343**, 83-99
8. Yu, X., Jezewska, M. J., Bujalowski, W., and Egelman, E. H. (1996) *J.Mol.Biol.* **259**, 7-14
9. Yu, X., Horiguchi, T., Shigesada, K., and Egelman, E. H. (2000) *J.Mol.Biol.* **299**, 1279-1287
10. Norcum, M. T., Warrington, J. A., Spiering, M. M., Ishmael, F. T., Trakselis, M. A., and Benkovic, S. J. (2005) *Proc.Natl.Acad.Sci.U.S.A* **102**, 3623-3626
11. Singleton, M. R., Sawaya, M. R., Ellenberger, T., and Wigley, D. B. (2000) *Cell* **101**, 589-600

12. Jeong, Y. J., Levin, M. K., and Patel, S. S. (2004) *Proc.Natl.Acad.Sci.U.S.A* **101**, 7264-7269
13. Cheng, W., Hsieh, J., Brendza, K. M., and Lohman, T. M. (2001) *J.Mol.Biol.* **310**, 327-350
14. Maluf, N. K., Fischer, C. J., and Lohman, T. M. (2003) *J.Mol.Biol.* **325**, 913-935
15. Soultanas, P., Dillingham, M. S., Wiley, P., Webb, M. R., and Wigley, D. B. (2000) *EMBO J.* **19**, 3799-3810
16. Soultanas, P. and Wigley, D. B. (2000) *Curr.Opin.Struct.Biol.* **10**, 124-128
17. Velankar, S. S., Soultanas, P., Dillingham, M. S., Subramanya, H. S., and Wigley, D. B. (1999) *Cell* **97**, 75-84
18. Zhang, X. D., Dou, S. X., Xie, P., Hu, J. S., Wang, P. Y., and Xi, X. G. (2006) *J.Biol.Chem.* **281**, 12655-12663
19. Harmon, F. G. and Kowalczykowski, S. C. (2001) *J.Biol.Chem.* **276**, 232-243
20. Xu, H. Q., Zhang, A. H., Auclair, C., and Xi, X. G. (2003) *Nucleic Acids Res.* **31**, e70
21. Hausteine, E. and Schwille, P. (2007) *Annu.Rev.Biophys.Biomol.Struct.* **36**, 151-169
22. Clamme, J. P., Azoulay, J., and Mely, Y. (2003) *Biophys.J.* **84**, 1960-1968
23. Zhang, X., Ercelen, S., Duportail, G., Schaub, E., Tikhonov, V., Slita, A., Zarubaev, V., Babak, V., and Mely, Y. (2008) *J.Gene Med.* **10**, 527-539
24. Kohl, T., Hausteine, E., and Schwille, P. (2005) *Biophys.J.* **89**, 2770-2782
25. Rarbach, M., Kettling, U., Koltermann, A., and Eigen, M. (2001) *Methods* **24**, 104-116
26. Kettling, U., Koltermann, A., Schwille, P., and Eigen, M. (1998) *Proc.Natl.Acad.Sci.U.S.A* **95**, 1416-1420
27. Collini, M., Caccia, M., Chirico, G., Barone, F., Dogliotti, E., and Mazzei, F. (2005) *Nucleic Acids Res.* **33**, e165
28. Jahnz, M. and Schwille, P. (2005) *Nucleic Acids Res.* **33**, e60
29. Xu, H. Q., Deprez, E., Zhang, A. H., Tauc, P., Ladjimi, M. M., Brochon, J. C., Auclair, C., and Xi, X. G. (2003) *J.Biol.Chem.* **278**, 34925-34933
30. Delelis, O., Carayon, K., Guiot, E., Leh, H., Tauc, P., Brochon, J. C., Mouscadet, J. F., and Deprez, E. (2008) *J.Biol.Chem.* **283**, 27838-27849
31. Guiot, E., Carayon, K., Delelis, O., Simon, F., Tauc, P., Zubin, E., Gottikh, M., Mouscadet, J. F., Brochon, J. C., and Deprez, E. (2006) *J.Biol.Chem.* **281**, 22707-22719
32. Pinskaya, M., Romanova, E., Volkov, E., Deprez, E., Leh, H., Brochon, J. C., Mouscadet, J. F., and Gottikh, M. (2004) *Biochemistry* **43**, 8735-8743
33. Deprez, E., Barbe, S., Kolaski, M., Leh, H., Zouhiri, F., Auclair, C., Brochon, J. C., Le Bret, M., and Mouscadet, J. F. (2004) *Mol.Pharmacol.* **65**, 85-98
34. Zhang, X. D., Dou, S. X., Xie, P., Wang, P. Y., and Xi, X. G. (2005) *Acta Biochim.Biophys.Sin.(Shanghai)* **37**, 593-600
35. Hishida, T., Han, Y. W., Shibata, T., Kubota, Y., Ishino, Y., Iwasaki, H., and Shinagawa, H. (2004) *Genes Dev.* **18**, 1886-1897
36. Cheok, C. F., Wu, L., Garcia, P. L., Janscak, P., and Hickson, I. D. (2005) *Nucleic Acids Res.* **33**, 3932-3941
37. Mortier-Barriere, I., Velten, M., Dupaigne, P., Mirouze, N., Pietrement, O., McGovern, S., Fichant, G., Martin, B., Noirot, P., Le Cam, E., Polard, P., and Claverys, J. P. (2007) *Cell* **130**, 824-836
38. Martin, S. L. and Bushman, F. D. (2001) *Mol.Cell Biol.* **21**, 467-475
39. Kantake, N., Madiraju, M. V., Sugiyama, T., and Kowalczykowski, S. C. (2002) *Proc.Natl.Acad.Sci.U.S.A* **99**, 15327-15332
40. Shereda, R. D., Bernstein, D. A., and Keck, J. L. (2007) *J.Biol.Chem.* **282**, 19247-19258
41. Shereda, R. D., Reiter, N. J., Butcher, S. E., and Keck, J. L. (2009) *J.Mol.Biol.* **386**, 612-625
42. Roman, L. J., Dixon, D. A., and Kowalczykowski, S. C. (1991) *Proc.Natl.Acad.Sci.U.S.A* **88**, 3367-3371
43. Dou, S. X., Wang, P. Y., Xu, H. Q., and Xi, X. G. (2004) *J.Biol.Chem.* **279**, 6354-6363
44. Levin, M. K., Gurjar, M., and Patel, S. S. (2005) *Nat.Struct.Mol.Biol.* **12**, 429-435
45. Levin, M. K., Wang, Y. H., and Patel, S. S. (2004) *J.Biol.Chem.* **279**, 26005-26012
46. Byrd, A. K. and Raney, K. D. (2004) *Nat.Struct.Mol.Biol.* **11**, 531-538
47. Boule, J. B. and Zakian, V. A. (2007) *Nucleic Acids Res.* **35**, 5809-5818
48. Bernstein, D. A., Zittel, M. C., and Keck, J. L. (2003) *EMBO J.* **22**, 4910-4921

## FOOTNOTES

\* We thank Pr. Zhao Yulong from East China Normal University, Shanghai, for his interest to this work. This work was supported by grants from Centre National de la Recherche Scientifique (CNRS), Ecole Normale Supérieure de Cachan, East China Normal University ECNU-Shanghai and Institut d'Alembert.

<sup>1</sup>The abbreviations used are: Al, Alexa488; ds, double-stranded; FCS, Fluorescence Correlation Spectroscopy; FCCS, Fluorescence Cross-Correlation Spectroscopy; FRET, Fluorescence Resonance Energy Transfer; ss, single-stranded; SSB, Single-Stranded DNA-Binding protein; Te, Texas Red.

## FIGURE LEGENDS

**Fig. 1. Principle of the FCCS experiment for measuring the helicase activity-** (A) The amplitude of the cross-correlation function  $g_{Al/Te}(\tau)$  is maximum in the absence of any unwinding activity when using double-stranded DNA substrates, doubly labelled with Alexa488 (Al) and Texas Red (Te). A significant decrease in the  $g_{Al/Te}(\tau)$  amplitude is expected, concomitant to the occurrence of unwinding activity. (B) Characteristic fluorescence emission spectra of Al-labelled (black line) and Te-labelled (Grey line) oligonucleotides upon two-photon excitation ( $\lambda = 780$  nm). Emission spectra were recorded separately with a home-built set-up using a SpectraPro-275 digital triple grating spectrograph coupled to a liquid nitrogen cooled CCD detector (Princeton Instruments, Acton, Massachusetts). Fig. 1B also shows transmission profiles (dashed lines) of the dichroic mirror (Chroma 580dcxr) as well as the two additional filters (Chroma HQ510/50 and HQ630/60m-2p for Al and Te, respectively). (C) DNA substrates used in this study. Left, the DNA substrates harbor a duplex region of varying size (from 13- to 66-bp) and two ss DNA 3'-tails (10-b). Right, two other versions of the 45- and 66-bp DNA substrates were tested: The first one contains only one ss 3'-tail and the other one is blunt. Details of sequences are reported in Table I. The names of DNAs are indicated in parentheses (see also Table I for nomenclature).

**Fig. 2. Relationship between the helicase unwinding activity and the decrease in the amplitude of the cross-correlation function-** Example of a reaction mixture containing 5 nM of doubly labelled 45-bp DNA substrate ( $P_{55*Al}/Q_{55*Te}$ ) and 10 nM of *E. coli* RecQ helicase in the reaction buffer (see Experimental procedures). The helicase/DNA complexes were formed at 37°C and further incubated for 10 min. The temperature was then lowered to 25°C and the unwinding reaction was monitored upon addition of 1 mM ATP (A) or equivalent volume of the reaction buffer without ATP (B).

**Fig. 3. Single-turnover study of the unwinding reaction-** (A) Example of time-course of the unwinding reaction under single-turnover conditions corresponding to the 45-bp DNA substrate ( $P_{55*Al}/Q_{55*Te}$ ). DNA and *E. coli* RecQ helicases concentrations were 5 and 10 nM, respectively ( $T_{binding}^{\circ} = 37^{\circ}C$ ;  $T_{reaction}^{\circ} = 25^{\circ}C$ ). The amount of unwound DNA was estimated according to the cross-correlation function  $g_{Al/Te}(\tau)$  and Equation 3. The single-turnover rate constant,  $k_{obs}$ , was then calculated from:  $[DNA]_{unwound} / [DNA]_{total} = 1 - \exp(-k_{obs}t)$ . (B)  $k_{obs} = f([RecQ \text{ helicase}])$  for different DNA substrate lengths. DNA concentration was 5 nM. Temperature of the DNA-binding step (before addition of ATP) was  $T_{binding}^{\circ} = 37^{\circ}C$  ( $T_{reaction}^{\circ} = 25^{\circ}C$ ). White circles, 66-bp ( $V_{76*Al}/W_{76*Te}$ ); Black circles, 45-bp ( $P_{55*Al}/Q_{55*Te}$ ); White squares, 22-bp ( $H_{32*Al}/I_{32*Te}$ ); Black squares, 13-bp ( $E_{23*Al}/F_{23*Te}$ ). (C) Influence of the pre-incubation temperature (corresponding to the DNA-binding step: White circles,  $T_{binding}^{\circ} = 37^{\circ}C$ ; Black circles,  $T_{binding}^{\circ} = 25^{\circ}C$ ) on the subsequent reaction rate (measured at  $T_{reaction}^{\circ} = 25^{\circ}C$ ). DNA concentration was 5 nM (66-bp substrate ( $V_{76*Al}/W_{76*Te}$ )).

**Fig. 4. DNA-binding properties of the *E. coli* RecQ helicase-** DNA-binding was performed in the reaction buffer and measured by steady-state fluorescence anisotropy (see details in Experimental procedures) at 25°C (black circles) or 37°C (black squares). All DNA substrates were singly labelled with Alexa488: **(A)** 66-bp (V<sub>76</sub>\*Al/Y<sub>76</sub>); **(B)** 45-bp (P<sub>55</sub>\*Al/R<sub>55</sub>); **(C)** 22-bp (H<sub>32</sub>\*Al/K<sub>32</sub>); **(D)** 13-bp (E<sub>23</sub>\*Al/G<sub>23</sub>). **(E)** Hill coefficient as a function of the DNA substrate length at two temperatures: 25°C (black circles) or 37°C (black squares).

**Fig. 5. Influence of the number of single-stranded 3'-tails on the cooperative DNA-binding and reaction modes-** The study of  $k_{obs} = f([RecQ \text{ helicase}])$  (see experimental conditions in the legend of Fig. 3B;  $T_{binding}^{\circ} = 37^{\circ}C$ ;  $T_{reaction}^{\circ} = 25^{\circ}C$ ) was repeated by varying the number of ss 3'-tails for two DNA substrate lengths: **(A)** 45-bp: black circles, two ss 3'-tails (P<sub>55</sub>\*Al/Q<sub>55</sub>\*Te); black squares, one ss 3'-tail (P<sub>55</sub>\*Al/N<sub>45</sub>\*Te); white squares, blunt (M<sub>45</sub>\*Al/N<sub>45</sub>\*Te). **(B)** 66-bp: black circles, two ss 3'-tails (V<sub>76</sub>\*Al/W<sub>76</sub>\*Te); black squares, one ss 3'-tail (V<sub>76</sub>\*Al/T<sub>66</sub>\*Te); white squares, blunt (S<sub>66</sub>\*Al/T<sub>66</sub>\*Te). **(C)** Hill coefficients for the different DNA substrates at two temperatures: 25°C (black) or 37°C (white). DNA-binding experiments were carried out as described in the legend of Fig. 4. The names of DNA substrates are indicated in parentheses (see also Table I for nomenclature).

**Fig. 6. Multiple-turnover study of the unwinding reaction-** Michaelis-Menten plots for two DNA substrate lengths (inset, corresponding Eadie-Hofstee plots). **(A)** 66-bp substrate. **(B)** 22-bp substrate. 5 nM of doubly labelled DNA substrate (V<sub>76</sub>\*Al/W<sub>76</sub>\*Te or H<sub>32</sub>\*Al/I<sub>32</sub>\*Te for the 66-bp or the 22-bp substrate, respectively) were mixed with varying concentrations of the unlabelled version of the DNA substrate (X<sub>76</sub>/Y<sub>76</sub> or J<sub>32</sub>/K<sub>32</sub> for the 66-bp or the 22-bp substrate, respectively), and pre-incubated at  $T_{binding}^{\circ} = 37^{\circ}C$  with 10 nM of *E. coli* RecQ helicase in the reaction buffer. The temperature was then lowered to 25°C and the unwinding reaction was initiated by adding 1 mM ATP ( $T_{reaction}^{\circ} = 25^{\circ}C$ ). The total concentration of DNA substrate ([S] = labelled + unlabelled) is reported on the x-axis. Equilibrium and kinetic parameters are reported in the inset.

**Fig. 7. Dual effect of complementary single-stranded oligonucleotides on the unwinding rate constant-** **(A)** The unwinding experiment was performed with the 66-bp DNA substrate (V<sub>76</sub>\*Al/W<sub>76</sub>\*Te) in the presence of increasing concentrations of complementary ss oligonucleotides. DNA substrate and *E. coli* RecQ helicase concentrations were 5 and 35 nM, respectively ( $T_{binding}^{\circ} = 37^{\circ}C$ ;  $T_{reaction}^{\circ} = 25^{\circ}C$ ). White squares, 7-mer (B<sub>7</sub>); Black squares, 10-mer (D<sub>10</sub>); Black circles, 32-mer (L<sub>32</sub>); White circles, 45-mer (O<sub>45</sub>). **(B)** Control experiments with non-complementary random sequences. White triangles, 7-mer (B'<sub>7</sub>); Black triangles, 10-mer (D'<sub>10</sub>). **(C)** Apparent K<sub>d</sub> values characterizing the interaction between RecQ helicase and ss oligonucleotides as a function of the oligonucleotide length. K<sub>d,app</sub> values were measured by steady-state fluorescence anisotropy using the following Alexa488-labelled oligonucleotides: A<sub>7</sub>\*Al, C<sub>10</sub>\*Al, H<sub>32</sub>\*Al and M<sub>45</sub>\*Al for 7-, 10-, 32- and 45-mer, respectively.

**Fig. 8. Comparative study of SSB effects on the unwinding activity of *E. coli* RecQ helicase under single- and multiple-turnover conditions-** The unwinding experiments were performed with the 66-bp DNA substrate (V<sub>76</sub>\*Al/W<sub>76</sub>\*Te) in the presence of increasing concentrations of SSB. **(A)** Single-turnover conditions (see experimental conditions in the legend of Fig. 7A). **(B)** Multiple-turnover conditions (see experimental conditions in the legend of Fig. 6). **(C)** DNA-binding isotherms (measured by fluorescence anisotropy) of SSB (at 25°C) using either ss DNA (V<sub>76</sub>\*Al; circles) or ds DNA (V<sub>76</sub>\*Al/Y<sub>76</sub>; triangles).

**Fig. 9. Differential cooperative effects of ATP on the helicase unwinding activity as a function of the temperature-** The unwinding experiments were performed with the 66-bp DNA substrate (5 nM) in the presence of 35 nM of *E. coli* RecQ helicase and increasing concentrations of ATP. **(A)**  $T_{binding}^{\circ} = T_{reaction}^{\circ} = 37^{\circ}C$ . **(B)**  $T_{binding}^{\circ} = T_{reaction}^{\circ} = 25^{\circ}C$ .

**TABLE I. Nomenclature and sequences of oligonucleotides used in this study.**

Name	Length	Sequence <sup>a</sup>
A <sub>7*Al</sub>	7	5'- GTC AGT G -3'-Al <sup>b</sup>
B <sub>7</sub>	7	5'- GTC AGT G -3'
B' <sub>7</sub>	7	5'- CGT GAT G -3'
C <sub>10*Al</sub>	10	5'- TTA GTC AGT G -3'-Al
D <sub>10</sub>	10	5'- TTA GTC AGT G -3'
D' <sub>10</sub>	10	5'- TTG CGT GAT A -3'
E <sub>23*Al</sub>	23	5'- CAG ACT CCC TAG A <u>AGTTAGGTT</u> -3'-Al
F <sub>23*Te</sub>	23	5'- TCT AGG GAG TCT G <u>GATTGTTATT</u> -3'-Te <sup>c</sup>
G <sub>23</sub>	23	5'- TCT AGG GAG TCT G <u>GATTGTTATT</u> -3'
H <sub>32*Al</sub>	32	5'- AAT CCG TCG AGC AGA GTT AGG G <u>AGTTAGGTT</u> -3'-Al
I <sub>32*Te</sub>	32	5'- CCC TAA CTC TGC TCG ACG GAT T <u>GATTGTTATT</u> -3'-Te
J <sub>32</sub>	32	5'- AAT CCG TCG AGC AGA GTT AGG G <u>AGTTAGGTT</u> -3'
K <sub>32</sub>	32	5'- CCC TAA CTC TGC TCG ACG GAT T <u>GATTGTTATT</u> -3'
L <sub>32</sub>	32	5'- AAT CCG TCG AGC AGA GTT AGG AGA TCC CTC AG -3'
M <sub>45*Al</sub>	45	5'- AGA TCC CTC AGA CCC TTT TAG TCA GTG TGG AAA ATC TCT AGC AGT -3' -Al
N <sub>45*Te</sub>	45	5'- ACT GCT AGA GAT TTT CCA CAC TGA CTA AAA GGG TCT GAG GGA TCT -3'-Te
O <sub>45</sub>	45	5'- ACT GCT AGA GAT TTT CCA CAC TGA CTA AAA GGG TCT GAG GGA TCT -3'
P <sub>55*Al</sub>	55	5'- AGA TCC CTC AGA CCC TTT TAG TCA GTG TGG AAA ATC TCT AGC AGT <u>AGTTAGGTT</u> -3'-Al
Q <sub>55*Te</sub>	55	5'- ACT GCT AGA GAT TTT CCA CAC TGA CTA AAA GGG TCT GAG GGA TCT <u>GATTGTTATT</u> -3'-Te
R <sub>55</sub>	55	5'- ACT GCT AGA GAT TTT CCA CAC TGA CTA AAA GGG TCT GAG GGA TCT <u>GATTGTTATT</u> -3'
S <sub>66*Al</sub>	66	5'- AAT CCG TCG AGC AGA GTT AGG AGA TCC CTC AGA CCC TTT TAG TCA GTG TGG AAA ATC TCT AGC AGT -3'-Al
T <sub>66*Te</sub>	66	5'- ACT GCT AGA GAT TTT CCA CAC TGA CTA AAA GGG TCT GAG GGA TCT CCT AAC TCT GCT CGA CGG ATT -3'-Te
U <sub>66</sub>	66	5'- ACT GCT AGA GAT TTT CCA CAC TGA CTA AAA GGG TCT GAG GGA TCT CCT AAC TCT GCT CGA CGG ATT -3'
V <sub>76*Al</sub>	76	5'- AAT CCG TCG AGC AGA GTT AGG AGA TCC CTC AGA CCC TTT TAG TCA GTG TGG AAA ATC TCT AGC AGT <u>AGTTAGGTT</u> -3'-Al
W <sub>76*Te</sub>	76	5'- ACT GCT AGA GAT TTT CCA CAC TGA CTA AAA GGG TCT GAG GGA TCT CCT AAC TCT GCT CGA CGG ATT <u>GATTGTTATT</u> -3'-Te
X <sub>76</sub>	76	5'- AAT CCG TCG AGC AGA GTT AGG AGA TCC CTC AGA CCC TTT TAG TCA GTG TGG AAA ATC TCT AGC AGT <u>AGTTAGGTT</u> -3'
Y <sub>76</sub>	76	5'- ACT GCT AGA GAT TTT CCA CAC TGA CTA AAA GGG TCT GAG GGA TCT CCT AAC TCT GCT CGA CGG ATT <u>GATTGTTATT</u> -3'

<sup>a</sup>Bases corresponding to non complementary ss 3'-tails are underlined; <sup>b</sup>Al: Alexas488; <sup>c</sup>Te: Texas Red.

Figure 1

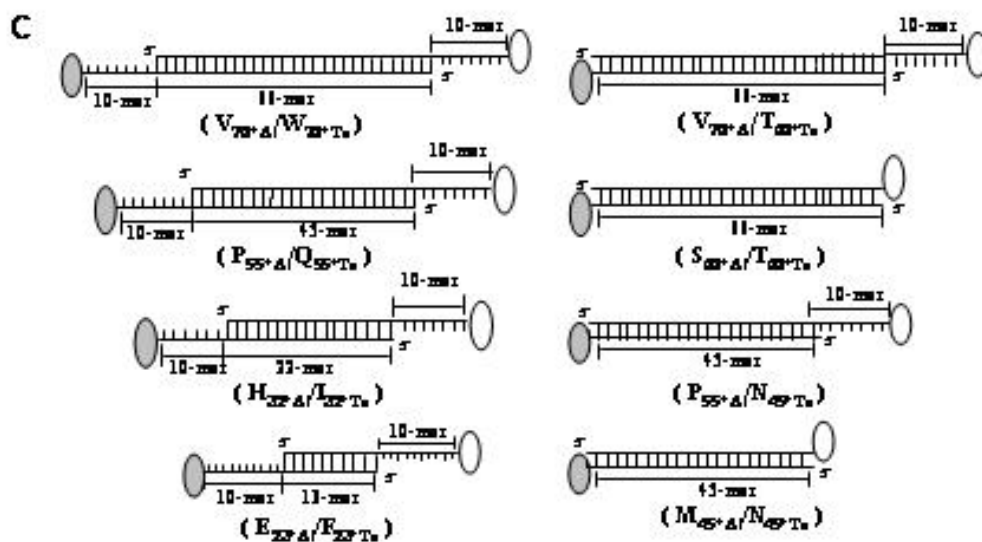
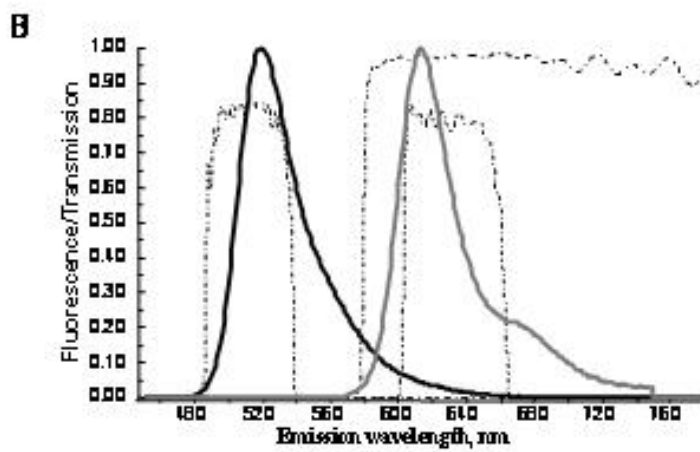
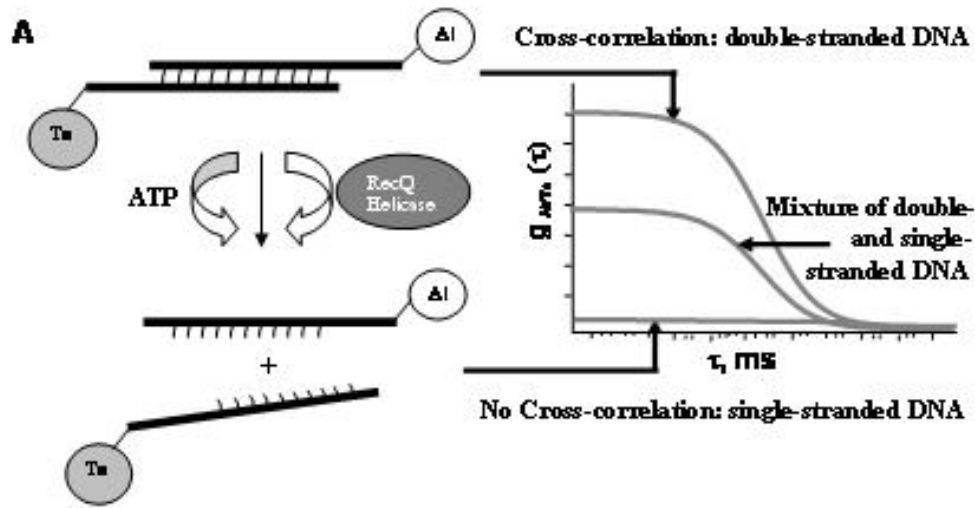


**Figure 2**

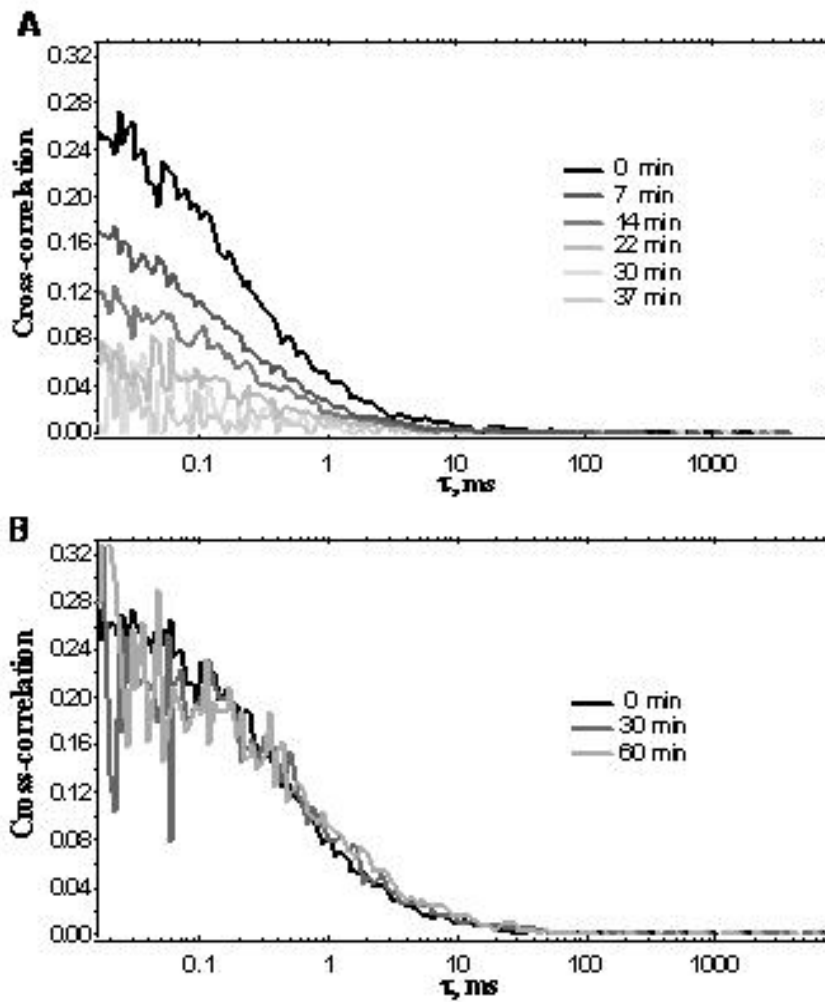


**Figure 3**

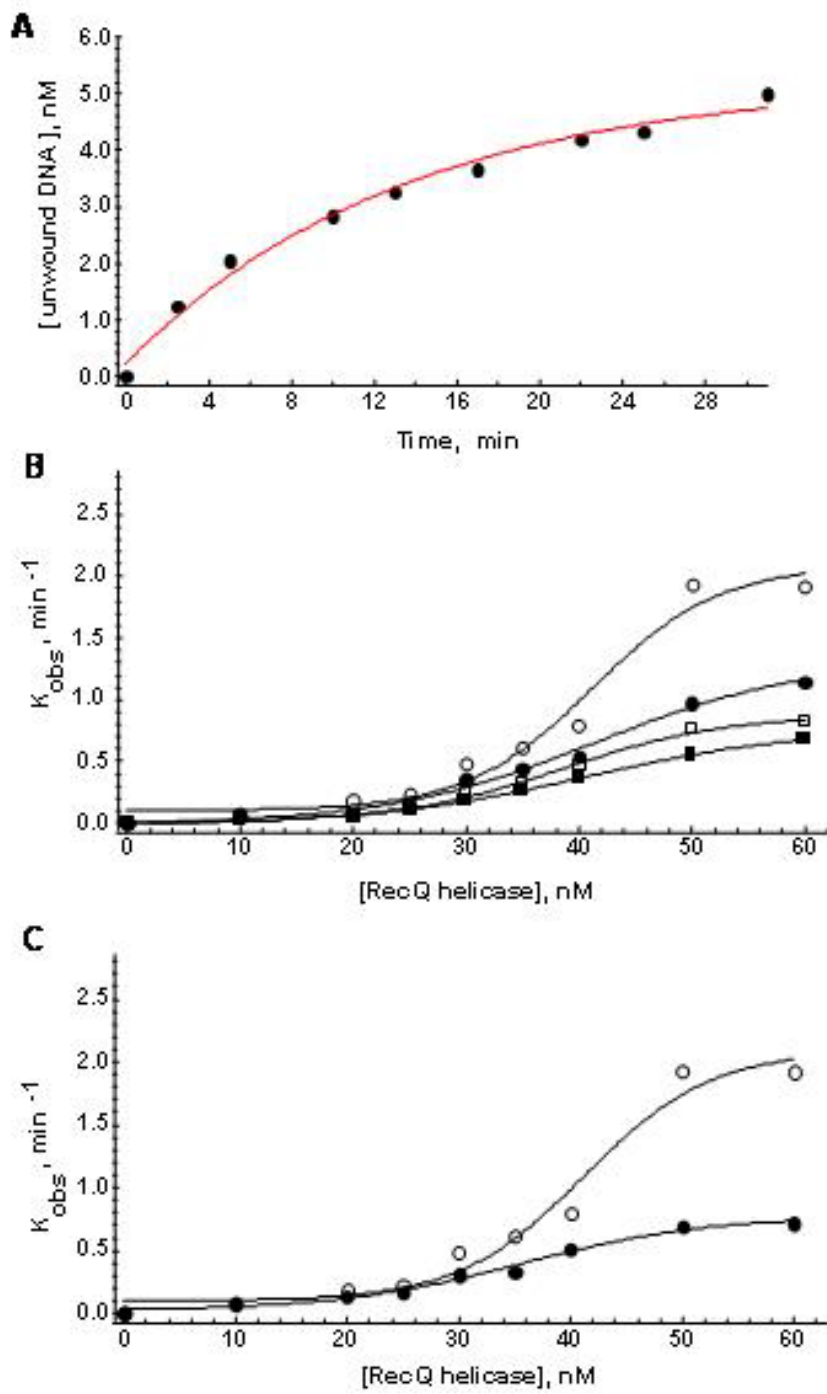
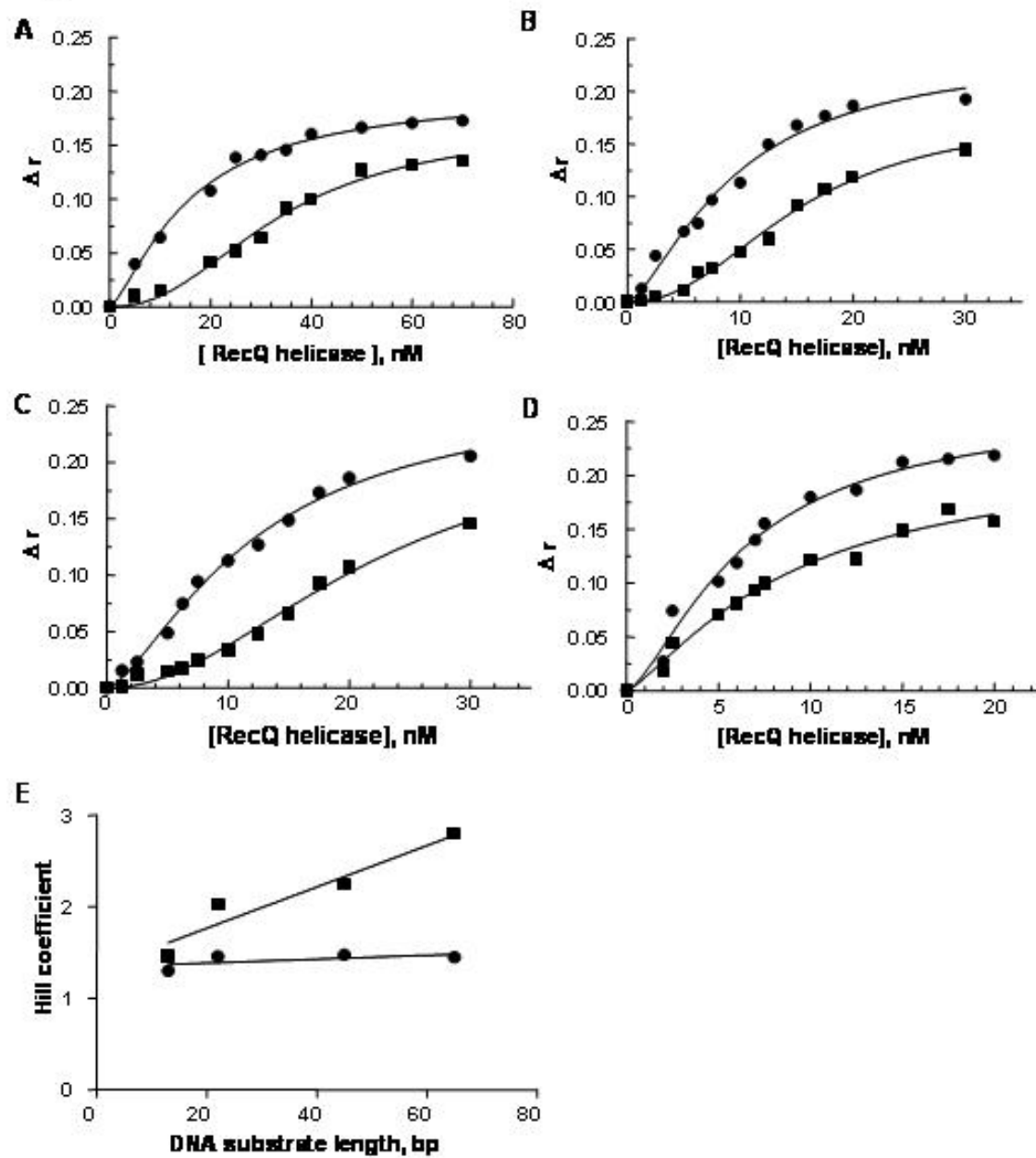


Figure 4



**Figure 5**

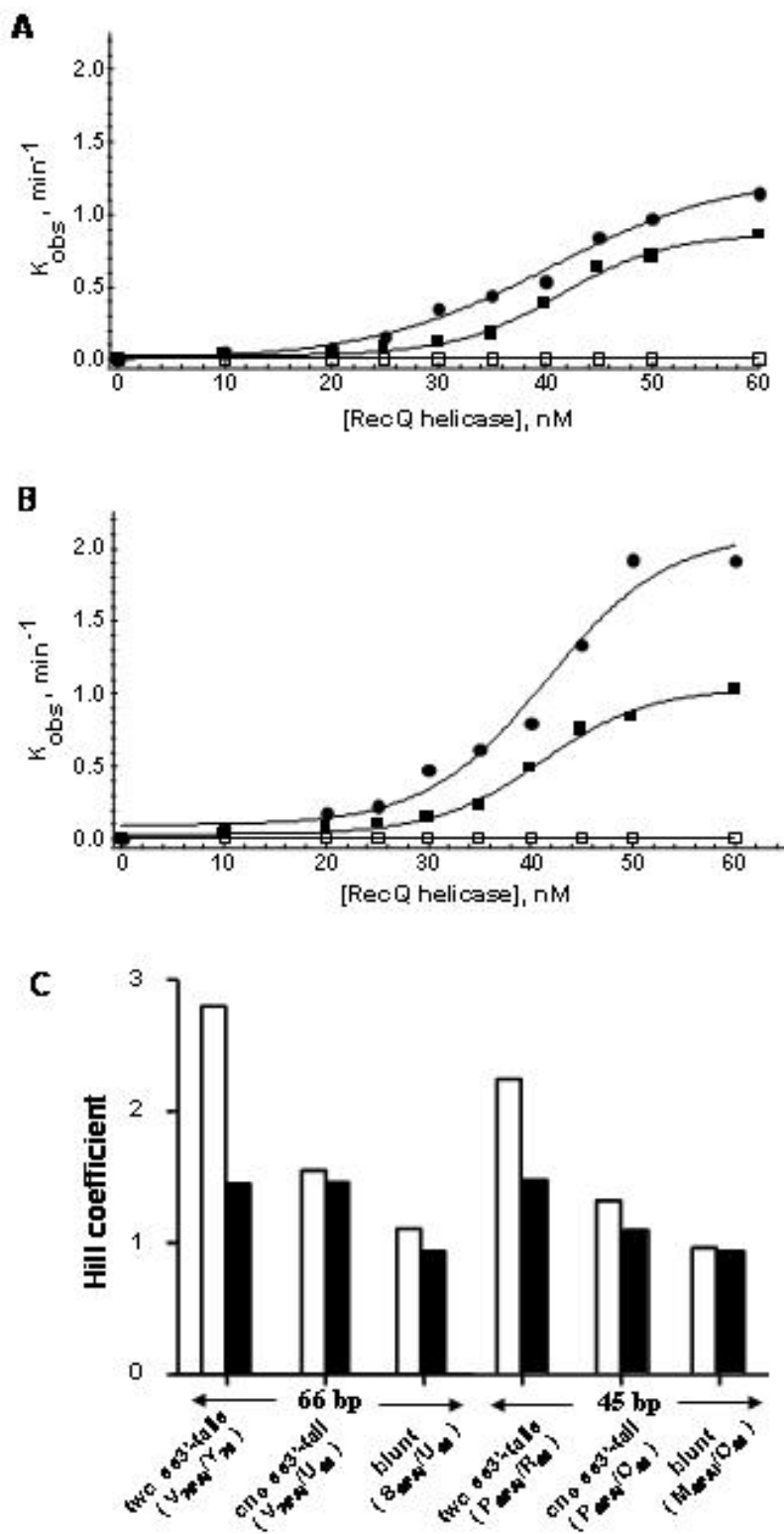


Figure 6

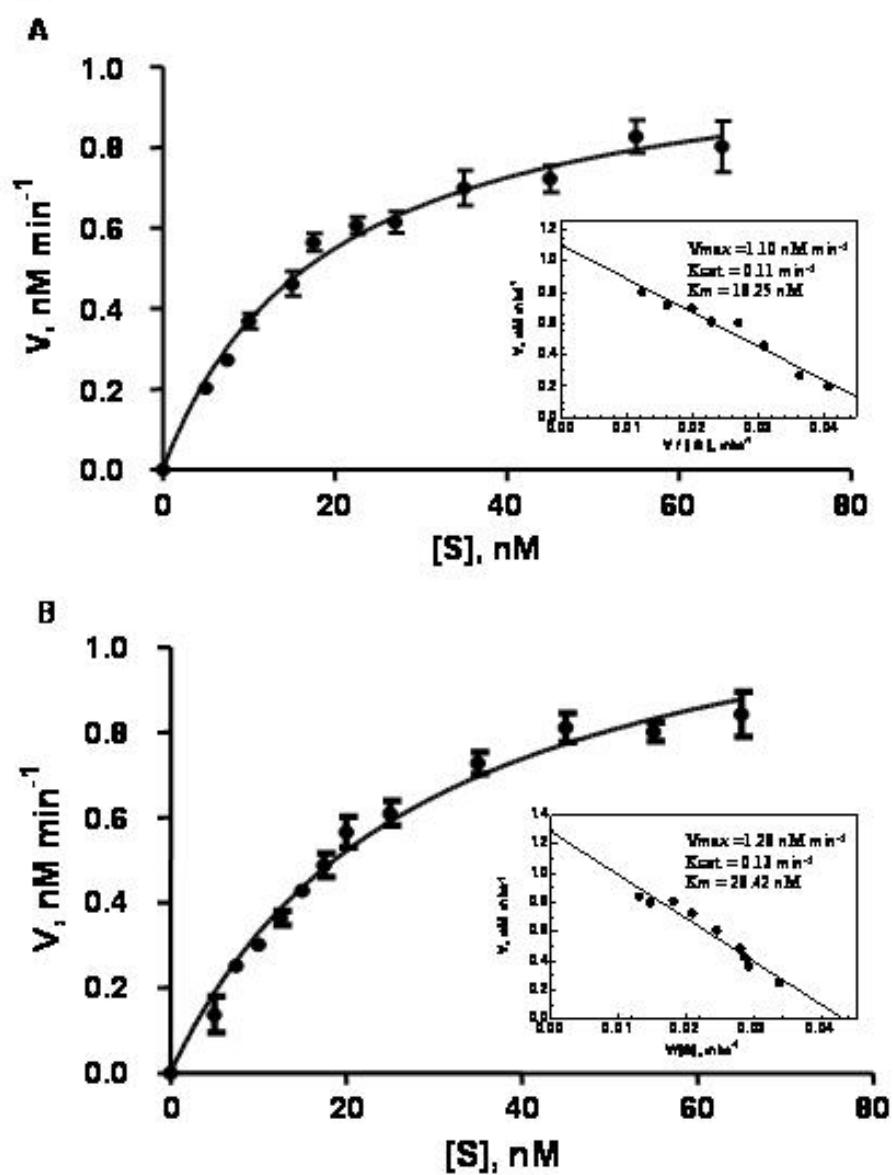


Figure 7

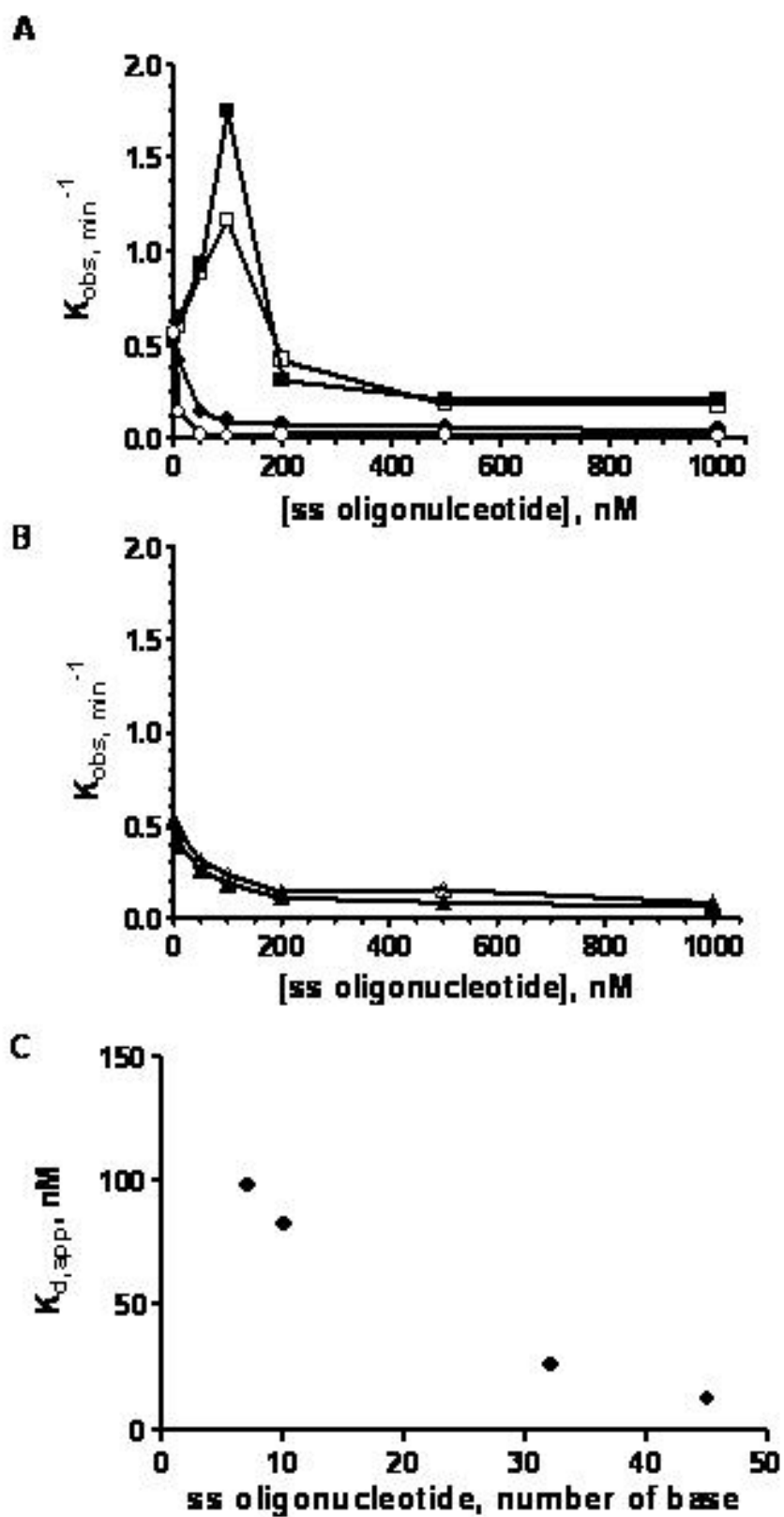
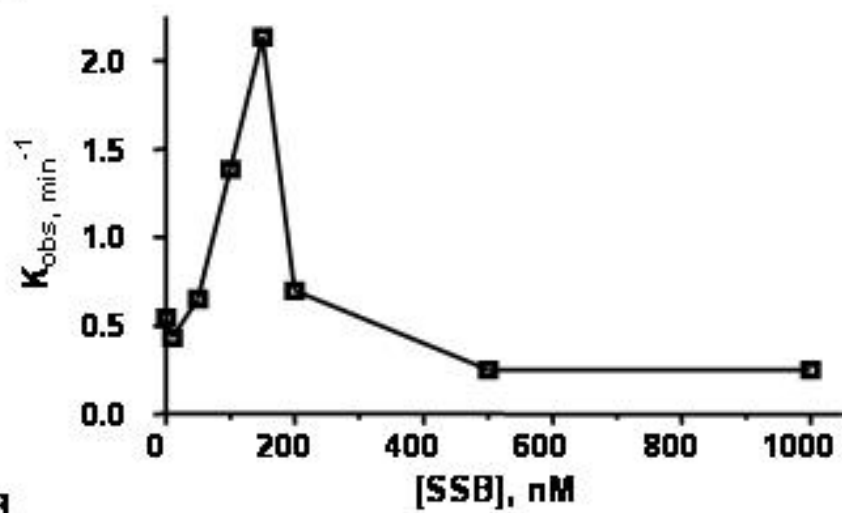
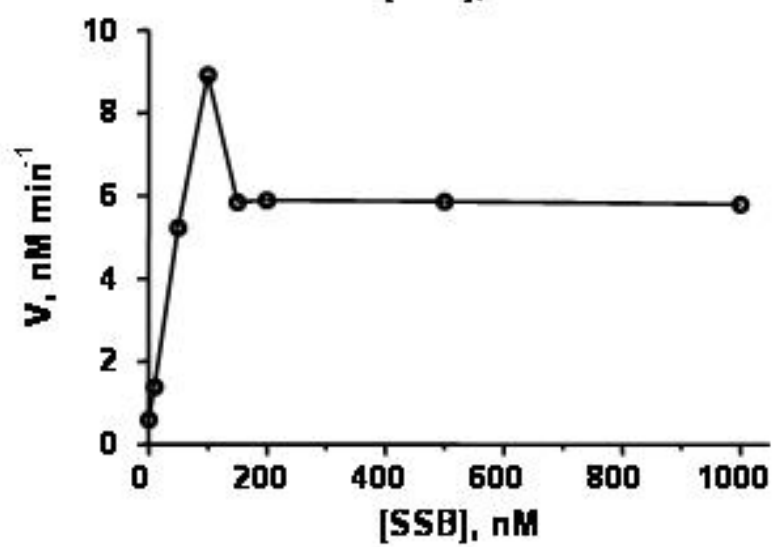


Figure 8

A



B



C

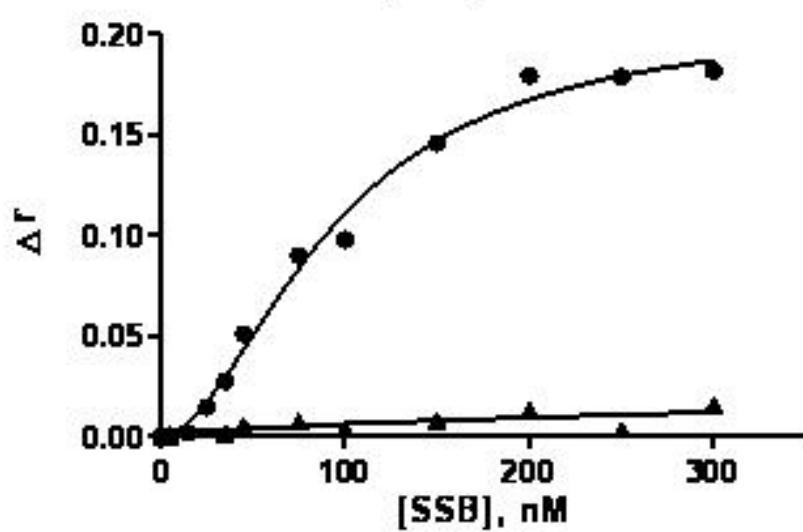
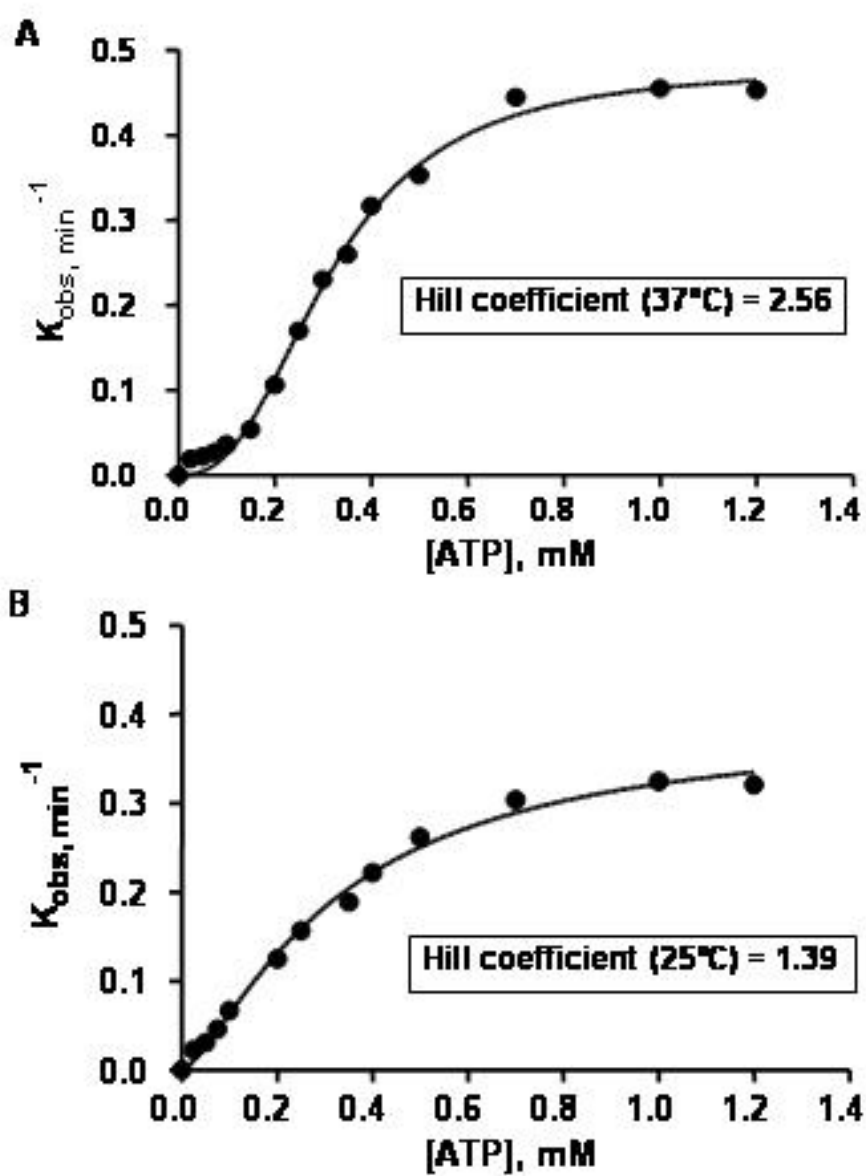


Figure 9



### ***III.2.3 Conclusion***

It is convinced for the first time in our present study that the FCCS approach is particularly well-suited for monitoring the unwinding activity of *E. coli* RecQ helicase. Based on the principle of this advanced fluorescence technique, the helicase activity of *E. coli* RecQ enzyme was studied under both single- and multiple-turnover conditions.

Firstly, we have elucidated the interactions between helicase and its DNA substrates by use of steady-state fluorescence anisotropy measurements. The thermodynamic characteristics of the DNA binding ability for *E. coli* RecQ helicase have been discussed. We showed that the *E. coli* RecQ helicase behaves cooperatively only at 37°C, and no cooperative DNA-binding for this enzyme was observed at 25°C. Such thermodynamic binding behaviour of *E. coli* RecQ helicase was compared with that of ATP (Harmon & Kowalczykowski, 2001), results revealed that the cooperative DNA-binding mode of helicase at 37°C fully accounts for the sigmoidal response of the helicase activity on ATP concentration. Meanwhile, under the single-turnover condition, strong cooperative effects were also observed depending on the total length of DNA and the number of single-stranded 3'-tails, which helped us to understand the relationship between the cooperative properties of helicase binding to DNA and the subsequent cooperative effects at the catalytic level.

Subsequently, the enzymatic kinetics of *E. coli* RecQ helicase to unwind dsDNA substrates was monitored by FCCS techniques. The strong dependencies of the single-turnover kinetic rate constant on both the helicase concentration and the size of the DNA substrate suggest cooperative/synergistic effects compatible with simultaneous unwinding catalysis by several helicase monomers on the same DNA substrate under single-turnover conditions. Consequently, the apparent unwinding activity was strongly stimulated by increasing the length of the DNA substrate and by using high helicase:DNA ratio. This observation was coincident with the RecQ helicase DNA binding behaviours, which had a temperature and DNA size dependency. Indeed, such a dependency on the DNA size was not observed under multiple-turnover conditions, i.e. when the DNA concentration was over the helicase concentration.

Moreover, we addressed quantitatively the influence of the re-hybridization process occurring immediately after DNA unwinding and helicase translocation on the unwinding rate constant. This process could underestimate the helicase activity as monitored by FCCS, in particular for long DNA substrates. It is important to note that the inherent problem of the ssDNA-binding properties of helicase, if not technically limiting with FCCS, strongly underestimates the unwinding activity, especially under multiple-turnover conditions. In fact,

the binding of helicase to ssDNA products competes with the binding to dsDNA substrates, limiting activity. SSB partially counteracts this effect and increase apparent catalytic activity (Roman et al., 1991). Furthermore, the stimulating effect of SSB on helicase activity via inhibition of the spontaneous re-annealing of unwound strands is probably common to both single- and multiple-turnover catalytic modes. The participation of the two mechanisms for stimulating helicase activity under multiple-turnover conditions, while only one is expected to be involved under single-turnover conditions (re-annealing inhibition), probably explains why SSB increases helicase activity more efficiently under multiple-turnover compared to single-turnover conditions. However, the exact mechanism of SSB-mediated stimulation is not clear so far since it was recently described that SSB could also stimulate *E. coli* RecQ helicase through a direct physical SSB-RecQ helicase interaction (Shereda et al., 2007; Shereda et al., 2009). However, taking into account the  $K_d$  value (6  $\mu\text{M}$ ) characterizing this interaction, it seems unlikely that this interaction could be responsible for the SSB-mediated stimulating effect under our experimental conditions. The apparent  $K_d$  value characterizing the SSB-single-stranded DNA interaction as measured by fluorescence anisotropy ( $K_{d,app} = 94$  nM) is more compatible with the observed stimulating effect below 150 nM SSB. In contrast, one could imagine that the inhibition phase, observed for SSB concentrations above 150 nM, could be due, partially, to this helicase/SSB interaction. Another reason to explain the inhibition phase is that higher SSB concentrations may displace helicase from the DNA substrate ss 3'-tails. Short complementary ss oligonucleotides (typically 7- or 10-mer) display similar stimulating effects on helicase activity, i.e. by minimizing spontaneous re-hybridization. However, as found with SSB, this stimulation is rather modest and followed by a marked inhibition phase, due to competitive interactions. In the case of short ss oligonucleotides, this inhibition can be easily explained by their significant affinities for helicase ( $K_{d,app} = 95$  and 88 nM, respectively). Indeed, longer ss oligonucleotides, 32- or 45-mer, with still higher affinities ( $K_{d,app} < 25$  nM), display only inhibition profiles. Thus, the stimulating effects of SSB and ss short oligonucleotides can be qualified as modest and only partially increase the apparent unwinding rate.

In conclusion, the FCCS technique is a sensitive method to directly measure the helicase activity that does not require any separation of the single-stranded DNA product from the double-stranded DNA substrate. It has several advantages when comparing with other fluorescence-based methodologies (eg. fluorescence anisotropy and FRET), which makes the technique promising in the real-time kinetic detections. FCCS is also characterized by its sensitivity to the concomitant diffusion of the two fluorescently labelled DNA strands, with

high cross-correlation amplitude characterizing the duplex molecule and a significant decrease in this amplitude upon physical separation of the two strands, without any limitation due to the size of the DNA strands that initially constitute the DNA substrate. Therefore, the FCCS approach is particularly well-suited for monitoring the RecQ helicase enzymatic activity.

### ***III.3 Human RecQ5 $\beta$ Unwinding and Strand-Annealing Activity as Monitored by Dual Color Fluorescence Correlation Spectroscopy***

#### ***III.3.1 INTRODUCTION***

Helicases are ubiquitous enzymes that play essential roles in nearly all DNA metabolic processes, including DNA replication, recombination and repair (Gorbalenya & Koonin, 1993). In human, five RecQ homologs have been identified to date; they are RecQ1, BLM, WRN, RecQ4 and RecQ5. Most of them are associated with severe autosomal recessive diseases, notably, Bloom, Werner, and Rothmund-Thomson syndromes (Uhring&Poterszman, 2006). However, such an association has not been demonstrated for RecQ5.

The human RecQ5 exists in RecQ5 $\alpha$ , RecQ5 $\beta$  and RecQ5 $\gamma$  three isoforms (Sekelsky et al., 1999; Shimamoto et al., 2000). They are generated by differential splicing of RecQ5 gene. RecQ5 $\beta$  is the only isoform proved to have helicase activity. In chicken DT40 cell line, single depletion of RecQ5 has no effect on cell proliferation, cell death, chromosome stability, sister chromatid exchanges (SCEs) frequency, sensitivity to methyl methane sulfonate (MMS), mitomycin C (MMC) and ultraviolet (UV). In combination with BLM depletion, the RecQ5 depletion shows more severe effects than RecQ1 depletion on these factors. The SCEs frequency of BLM/RecQ5 double depletion cells was higher than that of BLM single depletion cells up to 22 folds after treatment of MMC (Wang et al., 2003; Otsuki et al., 2008). Human RecQ5 can, in association with RPA, inhibit D-loop formation catalyzed by Rad51 (K133R) and accessory factor Hop2-Mnd1. This process is also ATP hydrolysis dependent. This proved the involvement of RecQ5 in homologous recombination (HR) process for DNA double strand breaks repair. Similar to BLM, RecQ5 can be in physical contact with Rad51 and interrupt the presynaptic filament assembly process to interfere the HR pathway at the beginning step. However, RecQ5 cannot replace BLM to promote dHJ (double Holliday junction) dissolution associated with TOPOIII $\alpha$  given that RecQ5 are physically associated with TOPOIII $\alpha$  (Shimamoto et al., 2000).

At present, only RecQ5 $\beta$  has been biochemically characterized (Otsuki et al., 2008). It possesses both DNA-unwinding and DNA-strand annealing activities. Moreover, ability to promote strand exchange on forked DNA structures was also reported in RecQ5 $\beta$  (Kanagaraj et al., 2006). However, the molecular mechanism that underlines the co-ordination of DNA-unwinding and strand annealing activities of RecQ5 $\beta$  remains largely elusive. In addition, the RecQ5 $\alpha$  and RecQ5 $\beta$  proteins offer an attractive model system to characterize the enzymatic

activities of a RecQ helicase domain in isolation and in association with other sub-domains on the same poly peptide (Ren et al., 2008). This unique property allows us to take RecQ5 $\beta$  as a model to address some unresolved questions with any DNA helicase. Though lots of biochemical studies have been conducted to elucidate the biochemical function of RecQ5 $\beta$  helicase, the mechanism underlying its strand annealing activities remains unclear. Most of the debates were focused on whether the RecQ5 $\beta$  helicase itself possesses the ability to perform the strand annealing behaviour or just because of the binding of RecQ5 $\beta$  to the DNA substrate which increases the proximity of two unwound single strand DNA and therefore facilitate the strand annealing. In the latter case, no enzymatic activity was performed for RecQ5 $\beta$ .

In present study, advanced fluorescence detection method FCCS was employed to measure RecQ5 $\beta$  helicase ssDNA-binding, dsDNA unwinding and ssDNA strand annealing activities in real time. Temperature effects on ssDNA substrate strand annealing with and without RecQ5 $\beta$  have been demonstrated, the *E.Coli* RecQ helicase was also used to as a control, which would confirm whether RecQ5 $\beta$  helicase itself possesses the strand annealing activity. The influences of indispensable co-factor, Mg<sup>2+</sup>, on strand annealing activity were also discussed here. Results in our present study could provide more knowledge to better understand a DNA helicase with a definite intrinsic DNA-strand annealing function.

### ***III.3.2 MATERIALS AND METHODS***

***RecQ5 $\beta$  helicase purification and oligonucleotides-*** The human RecQ5 $\beta$  helicase was produced as C-terminal fusions with a self-cleaving chitin-binding domain and purified as described previously (Garcia et al., 2004). Unlabeled and fluorescently labeled oligonucleotides (Figure 1C) were purchased from Eurogentec (Liege, Belgium) and further purified by electrophoresis on a 12% denaturing acrylamide/urea gel for long (> 10-mer) oligonucleotides. Double-stranded (ds) oligonucleotides were obtained by mixing equimolar amounts of complementary single-stranded (ss) strands in 20mM Hepes (pH 7.2), 40mM NaCl. The mixture was heated to 85°C for 5 min and annealing was allowed by slow cooling to 25°C.

***Fluorescence Cross-Correlation Spectroscopy-*** FCCS measurements were performed as described in article III.2.

***DNA Binding assay: Steady-state Fluorescence Anisotropy-*** The interaction between RecQ5 $\beta$  helicase and Alexa488-labeled oligonucleotides (either ds or ss) was detected by steady-state fluorescence anisotropy using a Beacon 2000 instrument (PanVera, Madison,

USA) (Guiot et al., 2006). To determine the apparent  $K_d$  value ( $K_{d, app}$ ), Alexa488-labeled DNA (5nM) was incubated with increasing concentrations of RecQ5 $\beta$  helicase in 20mM Hepes (pH7.2), 50mM NaCl, 10mM MgCl<sub>2</sub>, 1mM DTT, and the steady-state anisotropy ( $r$ ) was then recorded. The fraction saturation  $Y$  was calculated as  $(r-r_{free})/(r_{bound}-r_{free})$ , where  $r_{bound}$  and  $r_{free}$  represent the bound and free DNA anisotropy, respectively. The temperature of incubation was varied in a wide range (at 5°C; 10°C; 15°C; 25°C; 37°C). The Hill number,  $\tilde{n}$ , was calculated by directly fitting the titration curve using the Hill function of the origin6.0 software.  $K_{d, app}$  represents the concentration of RecQ5 $\beta$  helicase required to titrate the DNA to half saturation.

**DNA unwinding assay-** The RecQ5 $\beta$  helicase unwinding activity was measured by dual-color FCCS measurements (see above for the description of the FCCS set-up) in 20 mM Hepes (pH 7.2), 40 mM NaCl, 10 mM MgCl<sub>2</sub>, 0.3 mM DTT (named reaction buffer). The concentration of doubly labelled DNA substrate was typically 5 nM. The DNA-binding step corresponding to the addition of RecQ helicase to the DNA solution was performed at room temperature. The unwinding reaction was then initiated by adding 2 mM ATP and recorded at  $T^{\circ}_{reaction} = 25^{\circ}C$  (unless otherwise stated). The observed unwinding kinetic constant,  $K_{obs}$ , was calculated as illustrated in FCCS set-up in article III.2.

**DNA strand-annealing assay-** The RecQ5 $\beta$  helicase DNA-annealing activity was measured by dual-color FCCS measurements in the reaction buffer (20mM HEPES (pH 7.2), 50mM NaCl, 10mM MgCl<sub>2</sub>, 1mM DTT). The Alexas488-labeled single strand DNA at the final concentration of 5 nM was added to reaction buffer. The DNA-annealing step (at 5°C; 10°C; 15°C; 25°C; 37°C) corresponds to the addition of RecQ5 $\beta$  helicase to the DNA solution. Where required, ATP was also added to a final concentration of 2mM. After incubation of proteins RecQ5 $\beta$  with Alexas488-labeled ssDNA at the indicated concentration, the reaction was initiated by adding 5 nM TexasRed-labeled oligonucleotide which is partially complementary to the Alexas488-labeled ssDNA. The auto strand annealing activity occurred between the same DNA substrate without RecQ5 $\beta$  was monitored at the same temperatures. The resulting DNA products were analyzed as described for the helicase reactions.

### **III.3.3 RESULTS**

#### ***3'-5' DNA helicase activities of RecQ5 $\beta$***

To understand the strand annealing activity of RecQ5 $\beta$  DNA helicase, we investigated the strand separation ability of this protein under single-turnover process, where enzyme is in excess over DNA. First we compared the unwinding activities of RecQ5 $\beta$  helicase by use of

dsDNA substrates harbouring a ssDNA tail at each 3'-extremity (Fig.1B, left) and the blunt dsDNA (Fig 1B, right). The influence of oligonucleotide length on RecQ5 $\beta$  helicase activity was also studied (45-bp and 66-bp dsDNA). The results showed that RecQ5 $\beta$  efficiently unwound a partial DNA duplex substrate regardless of the oligonucleotide length. Little strand separation effects had been observed in this enzyme for blunt dsDNA (Figure 2), which confirmed the preference for RecQ5 $\beta$  to single-stranded tailed dsDNA substrate. Next, the effects of RecQ5 $\beta$  helicase concentration on DNA strand separation were studied by incubating DNA substrates with 10 nM RecQ5 $\beta$  and 100nM RecQ5 $\beta$  enzyme respectively. Two distinct phenomena were observed in this case, 1) at lower RecQ5 $\beta$  concentration (10nM), the RecQ5 $\beta$  helicase activity was significantly inhibited for longer DNA substrate (Figure 2A, 2C). With a first-order kinetic rate constant,  $K_{obs}$ , of a value 0.040 min<sup>-1</sup> for 66-bp partial double-stranded DNA in comparison with that of 0.109 min<sup>-1</sup> for 45-bp DNA substrate. 2) However, at higher RecQ5 $\beta$  concentration (100nM), an increased helicase activity for RecQ5 $\beta$  was monitored for longer DNA substrate, with a value of 0.135 min<sup>-1</sup> for 66-bp dsDNA but 0.100 min<sup>-1</sup> for 45-bp dsDNA (Figure 2B, 2D). Altogether, our data suggested the DNA substrate preference of RecQ5 $\beta$  helicase and showed a dose-dependent manner in unwinding a partial DNA duplex.

#### ***RecQ5 $\beta$ possesses DNA strand-annealing activity***

To better understand the dose-dependent manner of RecQ5 $\beta$  helicase activity and to directly analyze the putative ssDNA annealing activity of RecQ5 $\beta$ , we incubated different concentrations of RecQ5 $\beta$  with the two single-stranded 32mer or 76mer oligonucleotides (each at 5 nM) that were used to prepare the 10 nucleotides 3'-ssDNA tailed DNA substrate as shown by Li et al. (Li et al., 2009). Each 3'-end was labelled by the Alexas488 or TexasRed respectively to allow strand annealing being monitored by the technique FCCS described in Materials and Methods. The incubations and fluorescence cross-correlation detections were carried on at 25°C. Principle of FCCS detection was illustrated in Figure 1A. According to the FCCS results, when incubating DNA substrates with 200nM RecQ5 $\beta$  helicase, ~90% of the labelled ssDNA was annealed to its complement for both 22-bp and 66-bp dsDNA (Figure 3A.B). When analysing the reaction kinetics using a fixed RecQ5 $\beta$  concentration (200 nM), we observed that about 50% of the labelled oligonucleotide was annealed in less than 5 min (Figure 3C). In contrast, such significant strand annealing phenomena did not occur when replacing RecQ5 $\beta$  with 200nM *E.Coli* RecQ helicase (even though there existed a slight annealing in the absence of RecQ5 $\beta$  helicase and in the presence of *E.Coli* RecQ helicase). Moreover, no oligonucleotide length dependence had been

observed when concerning the efficiency of RecQ5 $\beta$ -mediated strand annealing (Figure 3A.B). The enzymatic kinetics of RecQ5 $\beta$  annealing activity on 22-bp and 66-bp dsDNA substrate was quite comparable.

Previous study reported that the RecQ5 $\beta$  helicase requires Mg<sup>2+</sup> to catalyze DNA unwinding (Garcia et al., 2004). Here, we try to test whether there was a similar co-factor requirement for the strand annealing function. Firstly, we testified the Mg<sup>2+</sup> concentration-dependent RecQ5 $\beta$  binding affinity to 32-nt ssDNA. Significant inhibition effects of Mg<sup>2+</sup> concentration on the cooperativity of RecQ5 $\beta$  to ssDNA substrate were observed (Figure 4B). This was explained by a continuously decreased steady-state anisotropy value at higher Mg<sup>2+</sup> concentration. Next, we choose the most frequently used Mg<sup>2+</sup> concentration in recent strand annealing studies, 10mM, as Mg<sup>2+</sup> treatment concentration in experimental group. The RecQ5 $\beta$  annealing activity was monitored in presence and in absence of Mg<sup>2+</sup> to better understand Mg<sup>2+</sup> influence for strand annealing function. As shown in Figure 4A, when incubating 5nM complementary 32-nt ssDNA with 200nM RecQ5 $\beta$  helicase with and without Mg<sup>2+</sup>, no great differences on RecQ5 $\beta$  strand annealing activity were observed between Mg<sup>2+</sup> treatment and no Mg<sup>2+</sup> treatment group. This was best demonstrated the strand annealing activity promoted by RecQ5 $\beta$  had no Mg<sup>2+</sup>-dependence (even though a slight stimulation of strand annealing activity at the 10mM Mg<sup>2+</sup> incubation). Results obtained here confirmed the possibility that ssDNA annealing reaction promoted by RecQ5 $\beta$  has different Mg<sup>2+</sup> co-factor requirements from those needed to support RecQ5 $\beta$  unwinding activity.

To gain further insight into the mechanism of RecQ5 $\beta$ -mediated DNA strand annealing, we investigated the effects of temperature (varied at 5°C, 10°C, 15°C, 25°C, 37°C) on the DNA annealing kinetics. 200nM RecQ5 $\beta$  was incubated with two 3'-single-stranded 32mer nucleotides (5 nM) at varied temperatures as indicated above. Quantitative analysis of the FCCS measurements has shown that the DNA strand annealing kinetics of RecQ5 $\beta$  increased as the increase of temperature (Figure 5A). At the lowest incubation temperature (5°C), ~30% of the labelled ssDNA was annealed to its complement for 22-bp dsDNA; this value increased significantly for the incubation at 15°C with about 53% dsDNA formed, and at the highest temperature (37°C), more than 95% labelled ssDNA was fully complemented to dsDNA. When considering the same ssDNA substrate strand annealing kinetics without addition of any RecQ5 $\beta$  helicase (Figure 5B), similar temperature dependence has also been observed. However, the auto-annealing efficiency was much less significant than that observed by incubating with RecQ5 $\beta$ . It was clearly indicated in Figure 5B that at the highest temperature (37°C), only 40% dsDNA was formed and such kinetics was decreased as the decrease of

temperature; and at the lowest temperature (5°C), just 7% dsDNA was formed. To see more clearly the temperature influence on RecQ5 $\beta$  strand annealing activity, the percentage of newly formed dsDNA was corrected by eliminating the effects of spontaneous annealing in FCCS measurements. After being corrected by spontaneous annealing of ssDNA substrates, a significant temperature-dependent effect could also be observed concerning dsDNA products formed under experimental condition. These data further confirmed the possibility that RecQ5 $\beta$  itself possesses a strand annealing activity.

#### ***ssDNA substrate binding affinity of RecQ5 $\beta$***

The observations that strand annealing activity of RecQ5 $\beta$  had temperature dependence promote us to understand the single-stranded DNA binding behaviors of RecQ5 $\beta$  helicase under different incubation temperatures. Existed studies had revealed the substrate preference for different helicases at room temperature. Generally, DNA RecQ helicases have relative abilities to stably bind DNA molecules, and moreover, they have the preference to the different of DNA substrate forms (eg. Replication forks, bubble, D-loop, 3 branches junction, holiday junction, double strand with flap and even G-quadruplex (G4) (Wang et al., 2003). For example, *E.Coli* RecQ binds to and unwinds a large variety of duplex DNA substrates, including ssDNA tailed and forked duplex molecules (Harmon & Kowalczykowski, 2001). Sgs1 also binds a number of oligonucleotide-based duplex DNA molecules in varied extents (Bennett et al., 1999). However, the human WRN helicase has preference to the four-stranded holiday junction (HJ) and it does not stably bind to other type of duplex DNA substrates even though this enzyme could efficiently unwind all kinds of oligonucleotides (Broch et al., 2002). It has been reported that RecQ5 $\beta$  possesses both DNA-unwinding and DNA-strand annealing activities. It has the ability to promote strand exchange on forked DNA structures and could unwind a wide variety of DNA substrates (Kanagaraj et al., 2006). In present study, we try to characterize the physical interaction of RecQ5 $\beta$  with DNA molecules at different temperatures to better understand the temperature dependence of RecQ5 $\beta$  strand annealing activity. In practice, the cooperative DNA-binding properties were measured by Beacon2000 Instrument using 32-nt ssDNA substrate singly labelled with Alexa488. Changes of steady-state anisotropy values were recorded by incubating with different RecQ5 $\beta$  concentrations in the absence of ATP with incubation temperatures varied among 5°C, 10°C, 15°C, 25°C, and 37°C. Detailed schematic illustration of this DNA substrate has been reported by Li et al. (Li et al., 2009). Figure 6A-E show that RecQ5 $\beta$  had similar binding affinity to the same ssDNA substrate at varied temperatures. The apparent affinity constants  $K_{d, app}$  were 96.97 nM, 105 nM, 112.7 nM, 130.4 nM and 144.6 nM at 5°C, 10°C, 15°C, 25°C, 37°C respectively. Clearly,

the temperature has a weak effect on the cooperativity between RecQ5 $\beta$  helicase and ssDNA substrate. In other words, the number of RecQ5 $\beta$  helicase present on the same ssDNA substrate at varied incubation temperature would be comparable under present experimental condition, therefore the observed temperature-dependent strand annealing activity of RecQ5 $\beta$  helicase should be attributed to their inherent strand annealing ability. Such strand annealing ability might increase at higher incubation temperatures.

### ***III.3.4 DISCUSSION***

Within the last decade, a plethora of research has implicated RecQ helicases as important mediators of genomic stability maintenance by their cellular roles in pathways that deal with replication stress and/or DNA damage (Sharma et al., 2005). Therefore, understanding the cellular mechanisms by which RecQ helicase perform their vital functions has gained prominence since the discovery that several premature aging diseases and cancers are genetically linked to deficiencies in human RecQ helicases. Presently, most of the understandings on the RecQ family molecular, cellular and genetic functions are related with human WRN and BLM helicase, less is known about other members in human RecQ family, including human RecQ5 $\beta$  helicase (Bennette et al., 1999; Opresko et al., 2002; Macris et al., 2006). Previous studies about RecQ5 helicase have shown its ability to catalyze DNA unwinding and strand annealing (Kanagaraj et al., 2006; Ren et al., 2008), however, no experiment could confirm the annealing phenomena is attributed to strand annealing activity of RecQ5 helicase itself or just because of the binding of RecQ5 helicase to both ssDNA substrates which increases the proximity between the two complementary ssDNA and hence intrigues the annealing phenomena.

As previously illustrated in our group, the technique FCCS is particularly well-suited to characterize the helicase activity (Li et al., 2009). Here we applied the same FCCS approach to monitor the strand annealing activity of human RecQ5 $\beta$  helicase. In particular, the influence of temperature on the annealing efficiency on the same ssDNA substrate with and without enzyme was compared. In principle, two separated complementary strands of nucleic acids could spontaneously associate to form a double helix when the temperature is lowered below the melting temperature ( $T_m$ ), and the association ability should be higher at lower temperature (Berg et al., 2006). Based on such DNA hybridization theory, we assumed that under different incubation temperatures (5°C, 10°C, 15°C, 25°C, and 37°C), the spontaneous annealing between complementary 32-nt ssDNA substrates, labeled respectively by Alexas488 and TexasRed, should be less efficient at higher temperature. If this phenomenon

could be observable in our study, the increased strand annealing on the same ssDNA substrate at higher temperature by incubating with RecQ5 $\beta$  helicase should be due to its inherent ability to promote complementary strand pairing. However, opposite phenomenon has been observed concerning spontaneous pairing in our study: the annealing behavior was more significant at higher temperatures (see Fig. 5B). This could be explained by conditions used in present FCCS measurement. It is well-known that one of the most significant advantages of FCCS approach is their small laser-focused detection volume with only a few molecules could be detected (Lakowicz, 2006). It means the concentration of the fluorophores needs to be in a range when just a few molecules are present in the observed volume. In this case, there would have more fluctuations in the small observation volume at higher temperatures, and hence the possibility of complementary ssDNA to meet each other would increase as the increase of incubation temperature, and consequently the spontaneous annealing efficiency increased. Although the unexpected result was observed, we still measured the annealing behavior between the same ssDNA substrates by incubation with 200nM RecQ5 $\beta$ . Results indicated a temperature-dependent behaviour on strand annealing activities, and more importantly, the strand pairing efficiency was significantly increased after the addition of RecQ5 $\beta$  helicase (Fig. 5A). To eliminate the influence of spontaneous pairing on evaluation of RecQ5 $\beta$  enzymatic functions, the percentage of rehybridization between complementary ssDNA substrates after adding RecQ5 $\beta$  was corrected by  $\Delta\text{annealing, \%} = \text{annealing, \%}_{+\text{RecQ5}\beta} - \text{annealing, \%}_{-\text{RecQ5}\beta}$ . Figure 5C clearly indicated the temperature dependence of strand annealing activity that was induced by RecQ5 $\beta$  helicase after correction. The value can provide a preliminary evidence for RecQ5 $\beta$  inherent annealing activity.

To better understand the temperature-dependent phenomenon of RecQ5 $\beta$  strand pairing, the DNA substrate binding affinity for RecQ5 $\beta$  was also conducted. Similar binding cooperativity for RecQ5 $\beta$  helicase on the same ssDNA substrate was observed at different incubation temperatures (the value of  $K_{d,\text{app}}$  was quite comparable). It means that under experimental conditions, there was similar number of RecQ5 $\beta$  helicase that could preferably bind to the same ssDNA substrate regardless of the temperature. In combination with results obtained in Figure 5, we can propose the possibility that the inherent strand-annealing activity of RecQ5 $\beta$  helicase would be more efficient at higher temperatures. Existed studies about helicase strand-pairing activity were all carried out with incubations at 25°C (Garcia et al., 2004; Shara et al., 2005; Ren et al., 2008). Here is the first time that we correlated the strand annealing activity with the temperature. Further studies would be carried out to better understand the temperature influences on helicase strand annealing efficiency.

Meanwhile, we also characterized RecQ5 $\beta$  strand annealing efficiency had no dependence on oligonucleotide length, which is different with that in other human RecQ family members. For example, Cheek et al. had reported in human BLM helicase, the complementary 15mer oligonucleotides were not annealed to any detectable extent, while a 31mer pair could be annealed requiring a BLM concentration of more than 40 nM. Increasing the oligonucleotide length to 50nt substantially increased the extent of annealing, particularly in reactions containing a low BLM concentration (less than 20nM) (Cheek et al., 2005). The T4 phage UvsW protein possesses different annealing ability which depends on the polarity and complexity of the DNA substrates (Scott & Stephen, 2007). Nevertheless, a dsDNA length-dependent behaviour for RecQ5 $\beta$  unwinding activity was demonstrated in our present study, and this unwinding activity also shows a dose-dependent behaviour. In detail, for 3'-ssDNA tailed dsDNA substrates, when incubated with 100nM RecQ5 $\beta$  helicases; the unwinding kinetics was higher for 66-bp partial dsDNA than that of 45-bp partial dsDNA. But when incubated with 10nM RecQ5 $\beta$  helicase, the unwinding activity for 66-bp partial dsDNA was significantly inhibited. This could be explained by the spontaneous re-hybridization after the unwinding process. Longer DNA substrate possesses higher possibility to have spontaneous annealing, at low enzyme concentrations, few enzymes could bind to the unwounded dsDNA to prevent the re-hybridization, and hence, the unwinding efficiency for longer DNA substrate was inhibited. However, at higher protein concentration, there are more redundant enzymes in reaction system which could specifically bind to wounded DNA substrates to prevent spontaneous annealing and hence promote the helicase activity. Similar results have been reported by Li et al. in monitoring the unwinding activity of *E.Coli* RecQ helicase (Li et al., 2009). Unwinding results about RecQ5 $\beta$  could also provide us some knowledge to better understand their strand annealing activity. Figure 3 showed a dose-dependence of RecQ5 $\beta$  helicase when performing strand pairing activity. In combination these data with that of unwinding measurement, the inhibition effects for longer dsDNA substrate at lower enzyme concentration could also be explained by the inherent annealing kinetic which promote the re-hybridization between unwounded dsDNA and further inhibit the unwinding rate. It should be noted that when comparing with the annealing effects of RecQ5 $\beta$  and *E.Coli* RecQ helicase, only the incubation with RecQ5 $\beta$  could intrigued the strand pairing; annealing efficiency in groups incubated with *E.Coli* RecQ helicase was quite comparable with that had no enzyme. This may further confirm the inherent strand annealing activity possessed only in RecQ5 $\beta$ . The exact mechanisms for RecQ5 $\beta$  helicase to perform unwinding and strand pairing activity together need further studies.

In addition, no  $Mg^{2+}$  requirement was observed to perform RecQ5 $\beta$ -mediated strand annealing activity, which is consistent with that of BLM helicase when performing annealing activities (Cheok et al., 2005) and that of T4 phage UvsW helicase (Scott & Stephen, 2007). To determine the DNA helicase activity of RecQ5 $\beta$  protein, we testified its ability to disrupt a 3'-ssDNA tailed partial duplex and comparing that with blunt dsDNA unwinding. Little detectable unwinding activity was observed for blunt DNA regardless of the dsDNA length. For 3'-ssDNA tailed partial duplex, unwinding activity could be monitored and showed a dsDNA-length dependence. This is consistent with results reported by others in observing RecQ5 $\beta$  helicase activity (Garcia et al., 2004; Ren et al., 2008).

In conclusion, we monitored and proposed the human RecQ5 $\beta$  helicase has a novel strand pairing capability in showing that RecQ5 $\beta$  promotes efficient annealing of complementary ssDNA molecules in varied temperatures. This activity does not require  $Mg^{2+}$ , which is considered as the indispensable co-factors for RecQ5 $\beta$  helicase function. No substrate length-dependence has been observed in concerning with the annealing activity of RecQ5 $\beta$ , but such length-dependence was observed in RecQ5 $\beta$  unwinding activity monitoring. We proposed in this study that the strand pairing ability of RecQ5 $\beta$  is not a simply non-specifically binding of enzyme to the two ssDNA molecules and then to bring them into close proximity to facilitate spontaneous re-hybridization. It is the complicated protein-protein interactions between RecQ5 $\beta$  which form large molecular weight complexes and may promote ssDNA annealing by a model proposed by Ren et al., 2008 based on the zinc-binding motif of RecQ DNA helicases (Ren et al., 2008). In contrast to the BLM strand annealing manner which requires the multiple rings formed by binding to ssDNA of oligomeric protein on their outer surface, the RecQ5 $\beta$  helicase could bind tightly to the double-stranded part of the DNA substrate by zinc-binding motif and make RecQ5 $\beta$  undergo large conformational fluctuation. Present study is only a preliminary work on elucidating the inherent strand annealing activity of RecQ5 $\beta$  helicase. To better understand this annealing behaviour of RecQ5 $\beta$  protein, further studies should be carried out focused on exact mechanisms and co-factors using different RecQ5 $\beta$  mutants as experimental models.

### ***III.3.5 PROSPECTIVE***

The enzymatic mechanisms under RecQ5 $\beta$ -mediated strand annealing are not fully clarified yet and to answer the question of evidence that suggests RecQ5 should have redundant functions with another RecQ helicase to maintain genomic stability still needs more efforts. Another important issue to address is why RecQ helicases could catalyze two

antagonistic reactions: DNA unwinding and ssDNA annealing. To better understand this, further studies have to be conducted in the following aspects:

- To further compare the unwinding activity and the DNA strand annealing activity of RecQ5 $\beta$  helicase in considering the co-factors effects (eg. ion concentration, pH...etc).
- To study the effects of ATP and ATP analogues (eg.ATP $\gamma$ S, ADP) on the RecQ5 $\beta$  helicase activity and strand annealing activity.
- Mutants of RecQ5 $\beta$  helicase would be adopted to study their helicase activity and strand annealing activity.
- To propose the most possible models for the RecQ family helicase by combination the helicase activity and strand annealing activity together.

### ***III.3.6 FIGURES AND LEGENDS***

The nomenclature and sequences of oligonucleotides used in this study is the same as that listed in Table I. at page 108.

**Figure 1: Principle of the FCCS experiment for measuring the DNA strand annealing activity-** (A) The amplitude of the cross-correlation function  $g_{Al/Te}(\tau)$  is minimal in the absence of any strand annealing activity when using two complementary single strand (ss)DNA substrates, labelled respectively with Alexa488 (Al) and Texas Red (Te). A significant increase in the  $g_{Al/Te}(\tau)$  amplitude is expected, concomitant to the occurrence of annealing activity. (B) DNA substrates used in this study. The DNA substrates harbour a duplex region of varying size (22- or 66-bp) and two single-stranded DNA 3'-tails (10-b). Blunt dsDNA substrates used in measuring RecQ5 $\beta$  helicase unwinding activity are with the size of 45-bp or 66-bp respectively.

**Figure 2: DNA-unwinding properties of the human RecQ5 $\beta$  helicase-** DNA-unwinding was performed in the reaction buffer in the presence of 2mM ATP using 5nM dsDNA substrates possessing two ssDNA tails (Black circle) or using blunt DNA (Black triangle). Human RecQ5 $\beta$  helicases concentrations were 10 and 100nM respectively. Time-course of the unwinding reaction under single-turnover conditions were monitored by FCCS. The amount of unwound DNA was estimated by the same way as illustrated in MATERIALS AND METHODS (A) Time-course of the unwinding reaction for doubly labelled 3'-ssDNA tailed (10-nt) 45-bp DNA substrate (P<sub>55\*Al</sub>/Q<sub>55\*Te</sub>). RecQ5 $\beta$  concentration was 10nM; (B)

Time-course of the unwinding reaction for doubly labelled 3'-ssDNA tailed (10-nt) 45-bp DNA substrate ( $P_{55^*Al}/Q_{55^*Te}$ ). RecQ5 $\beta$  concentration was 100nM; **(C)** Time-course of the unwinding reaction for doubly labelled 3'-ssDNA tailed (10-nt) 66-bp DNA substrate ( $V_{76^*Al}/W_{76^*Te}$ ). RecQ5 $\beta$  concentration was 10nM; **(D)** Time-course of the unwinding reaction for doubly labelled 3'-ssDNA tailed (10-nt) 66-bp DNA substrate ( $V_{76^*Al}/W_{76^*Te}$ ). RecQ5 $\beta$  concentration was 100nM.

**Figure 3: Single-turnover study of the DNA strand annealing reaction-** **(A)** 5nM two complementary 32-nt ssDNA ( $H_{32Al}$  and  $I_{32Te}$ ) was incubated with RecQ5 $\beta$  helicases at different concentrations. The amount of annealed DNA was estimated from the cross-correlation function  $g_{Al/Te}(\tau)$  by:  $[DNA]_{annealed} / [DNA]_{total} = g(0)_t - g(0)_0 / g(0)_{+\infty} - g(0)_0$ . The single-turnover rate constant,  $k_{obs}$ , was then calculated from:  $[DNA]_{annealed} / [DNA]_{total} = 1 - \exp(-k_{obs}t)$ . **(B)** 5nM two complementary 76-nt ssDNA ( $V_{76Al}$  and  $W_{76Te}$ ) were incubated with RecQ5 $\beta$  helicases at different concentrations. **(C)** 5nM two complementary 32-nt ssDNA ( $H_{32Al}$  and  $I_{32Te}$ ) was incubated with 200nM RecQ5 $\beta$  helicases (black square) and that incubated without any RecQ5 $\beta$  helicases (white square). Annealing activity by incubation the same ssDNA substrates with 200nM *E.Coli* RecQ helicase was also monitored (Black triangle). For all the experiments, the incubation temperature was maintained at 25°C. Black circle, 20nM RecQ5 $\beta$ ; White circle, 80nM RecQ5 $\beta$ ; Black square, 140nM RecQ5 $\beta$ ; White square, 200nM RecQ5 $\beta$ ; Black triangle, 300nM RecQ5 $\beta$ .

**Figure 4: Influence of  $Mg^{2+}$  concentration on RecQ5 $\beta$  helicases DNA binding and DNA strand annealing activities-** **(A)** 5nM two complementary 32-nt ssDNA was incubated with 10 mM  $Mg^{2+}$  (black circle) or without  $Mg^{2+}$  (white circle) at 25°C. The reaction was initiated by adding 200nM RecQ5 $\beta$  helicases, and the annealing activity was monitored by FCCS. **(B)** 5nM 32-nt ssDNA substrates singly labelled with Alexa488 was incubated with 200nM RecQ5 $\beta$  at varied  $Mg^{2+}$  concentration. DNA-binding reaction was performed in the reaction buffer in the absence of ATP and measured by steady-state fluorescence anisotropy (see details in Experimental procedures) at 25°C.

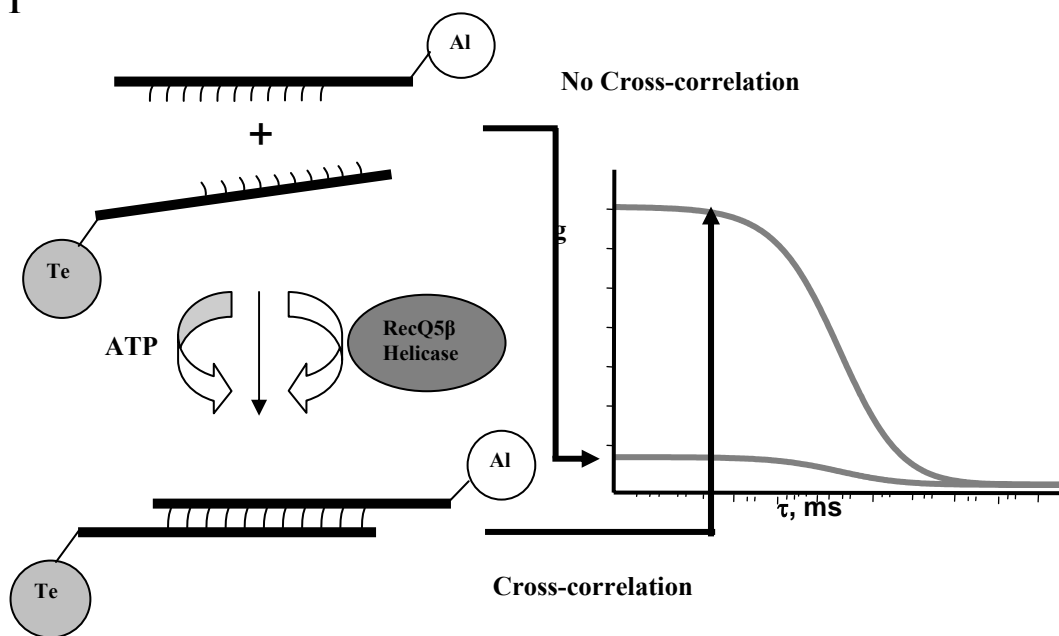
**Figure 5: Influence of temperature on the DNA RecQ5 $\beta$  helicases strand annealing reaction-** **(A)** 5nM two complementary 32-nt ssDNA was incubated with 200nM RecQ5 $\beta$  helicases at different incubation temperatures. The amount of annealed DNA was calculated as previously mentioned. **(B)** 5nM two complementary 32-nt ssDNA was incubated without RecQ5 $\beta$  helicases. The DNA auto-strand-annealing activity was monitored by FCCS. **(C)** The

influence of auto-strand annealing illustrated in Fig. 5B has been eliminated from the value obtained in Fig. 5A by use of ( $\% \text{ annealing}_{+ \text{ RecQ5}\beta} - \% \text{ annealing}_{- \text{ RecQ5}\beta}$ ). For all the experiments, the incubation temperature was maintained at 25°C. Black circle, 5°C; White circle, 10°C; Black square, 15°C; White square, 25°C; Black triangle, 37°C.

**Figure 6: DNA-binding properties of the human RecQ5 $\beta$  helicase-** DNA-binding was performed in the reaction buffer in the absence of ATP and measured by steady-state fluorescence anisotropy (see details in Experimental procedures) at varied incubation temperatures, from 5°C to 37°C. 32-nt ssDNA substrates singly labelled with Alexa488 was utilized in this assay: **(A)** incubation at 5°C; **(B)** incubation at 10°C; **(C)** incubation at 15°C; **(D)** incubation at 25°C; **(E)** incubation at 37°C.

**Figure 1**

**A**



**B**

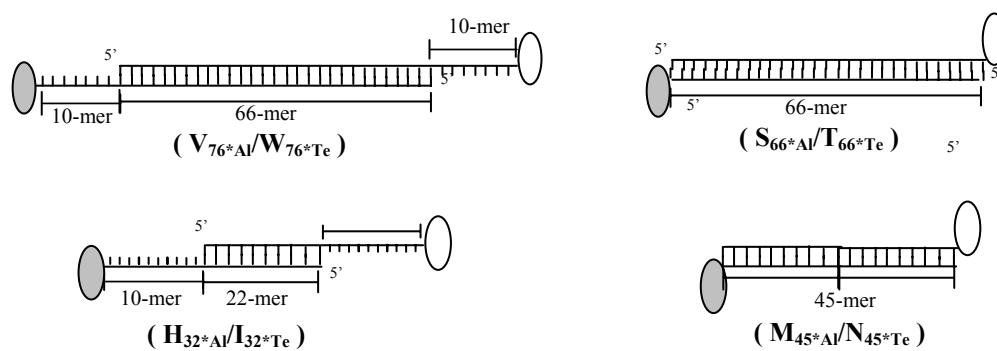


Figure 2

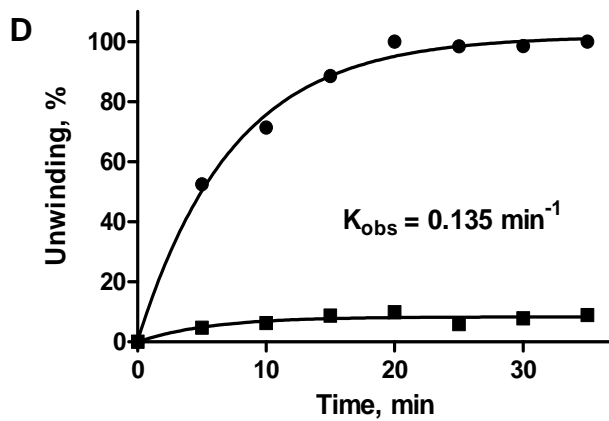
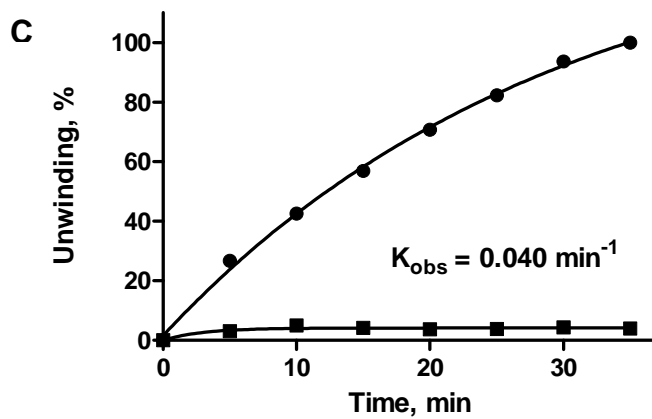
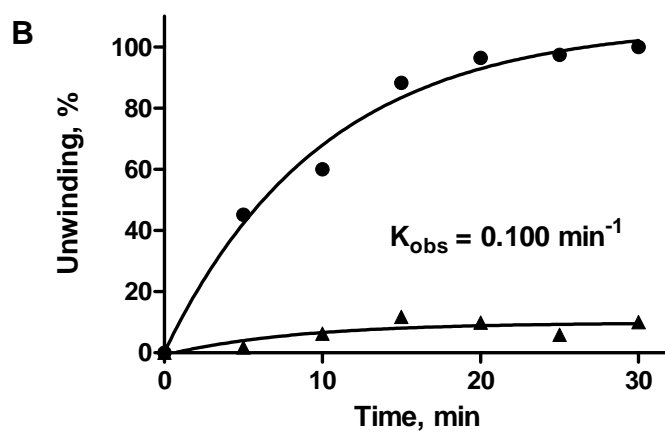
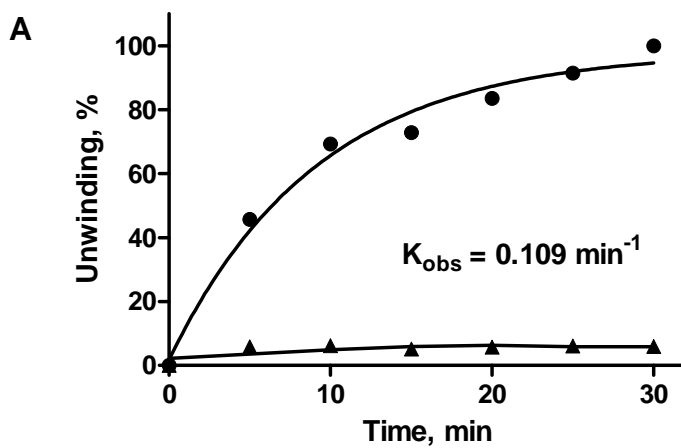


Figure 3

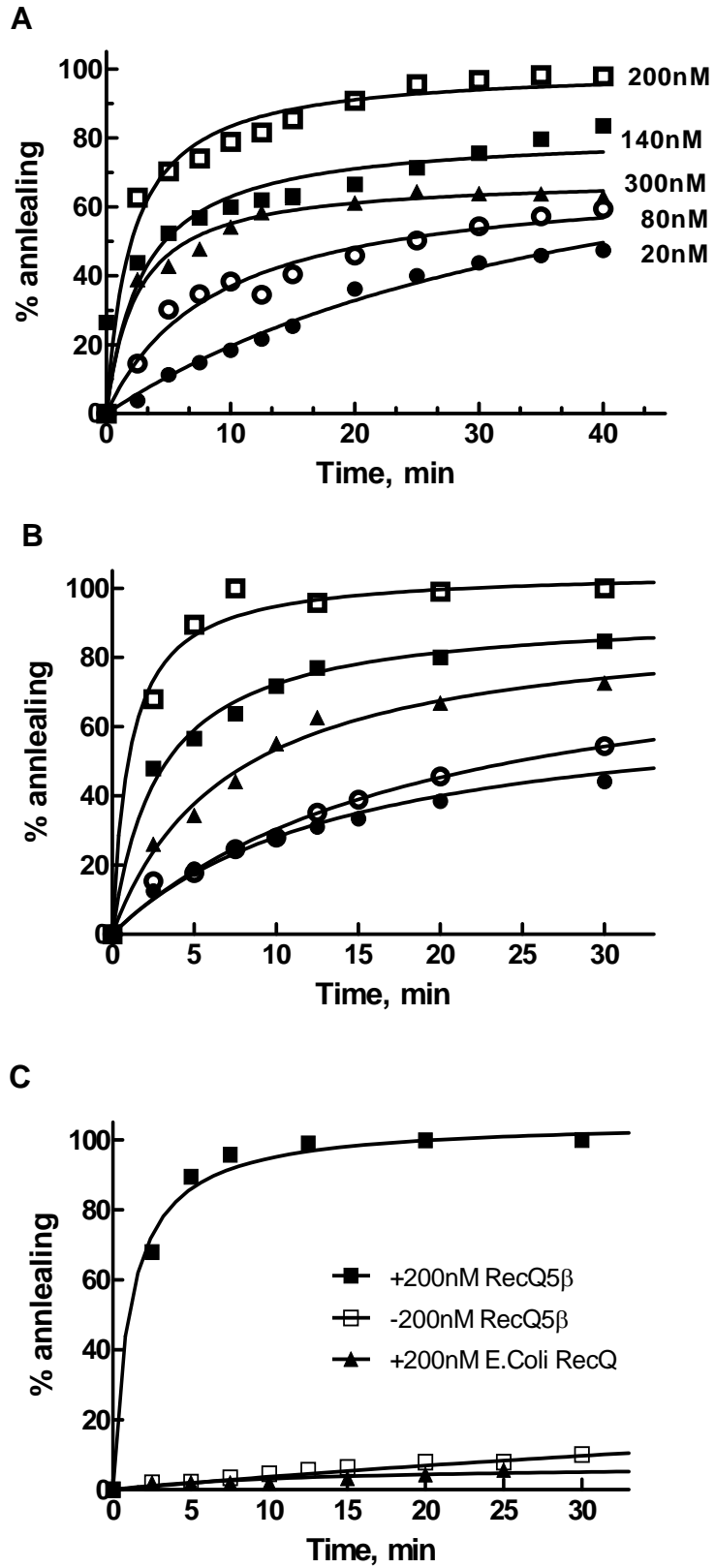


Figure 4

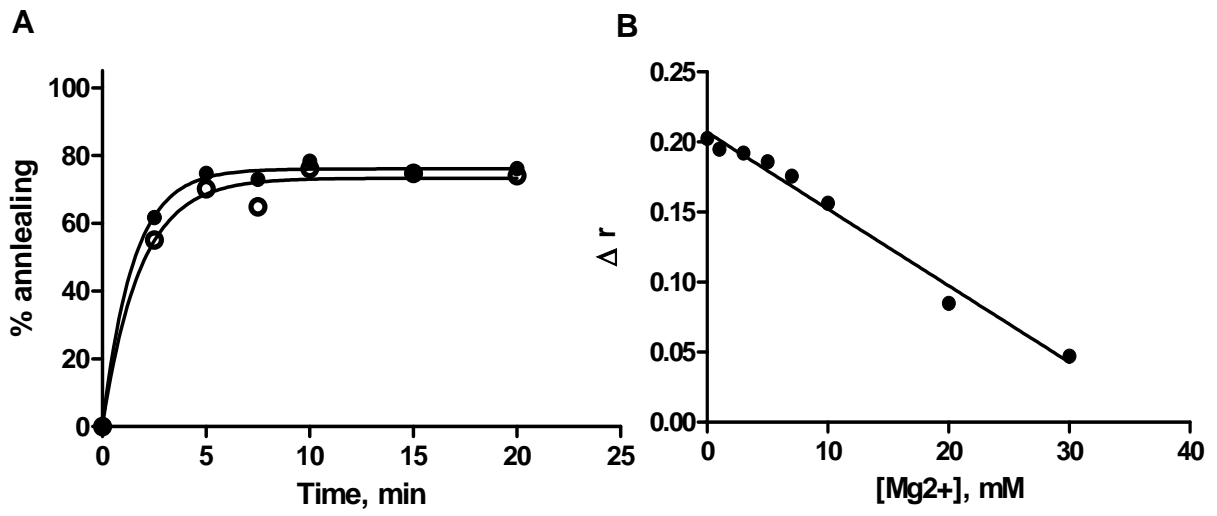


Figure 5

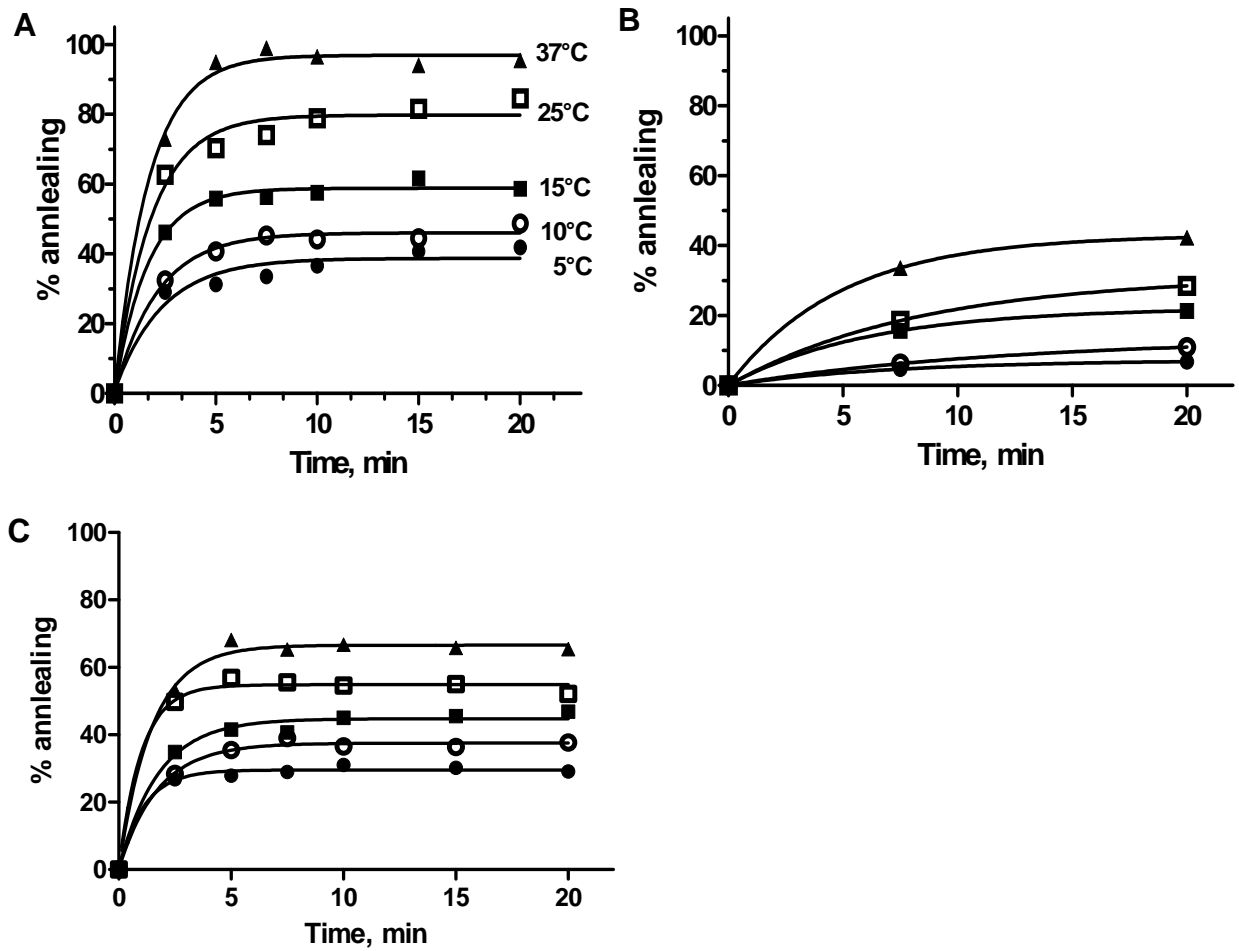
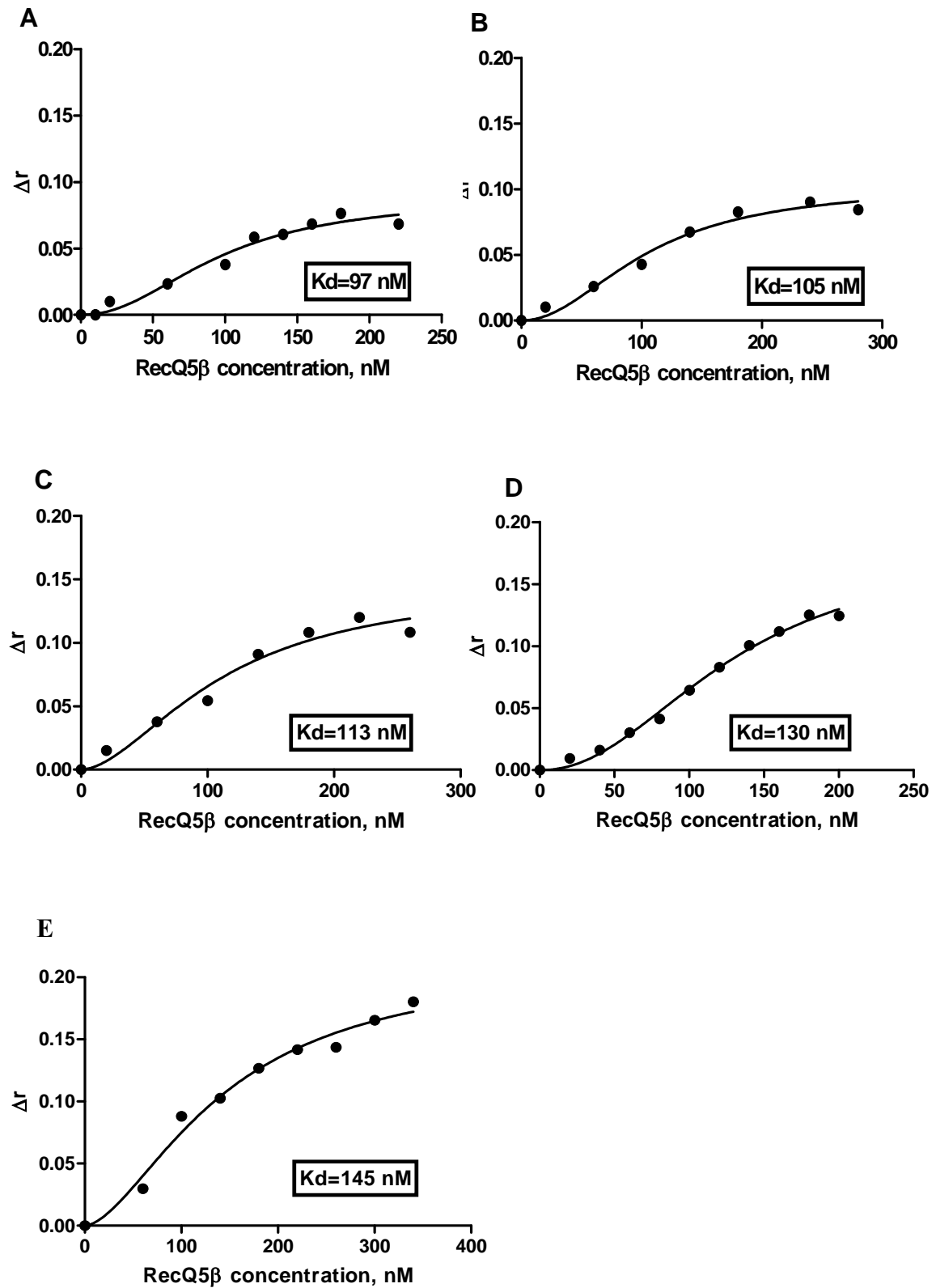


Figure 6



---

**APPLICATION OF  
FLUORESCENCE ANISOTROPY  
TO STUDY ENZYMATIC  
KINETICS OF HIV-IN**

---

## ***IV.1 The basic biology of retroviruses***

### ***IV.1.1 Structural taxonomic for the family of retroviruses***

Retroviruses have only become a common part of popular consciousness in the past decade or two with the relatively recent emergence of HIV. They comprise a large and diverse family of enveloped RNA viruses defined by common taxonomic denominators that include structure, composition; and replicative properties (Coffin, 1996). It is broadly divided into two categories- simple and complex- distinguishable by the organization of their genomes (Murphy et al., 1994).

The viral genome is typically a dimer of linear, positive-sense, single-stranded RNA with each strand being 7 to 15 kilobases (kb) in length. All retroviruses contain three major coding domains with information for virion proteins: *gag*, which directs the synthesis of internal virion proteins that form the matrix, the capsid, and the nucleoprotein structures; *pol*, which contains the information for the reverse transcriptase and integrase enzymes and protease; and *env*, from which are derived the surface and transmembrane components of the viral envelope protein. An additional, smaller, coding domain present in all retroviruses is *pro*, which encodes the virion protease (Figure 22). Retroviruses are further divided into seven groups defined by evolutionary relatedness, each with the taxonomic rank of *genus* (Figure 23). Five of these groups represent retroviruses with oncogenic potential (formerly referred to as oncoviruses), and the other two groups are the lentiviruses and the spumaviruses. All oncogenic members except the human T-cell leukemia virus-bovine leukemia virus (HTLV-BLV) genus are simple retroviruses. HTLV-BLV and the lentiviruses and spumaviruses are complex. True retroviruses, whether exogenous or endogenous, tend to cluster into four major groups. Their evolutionary limb lengths on the phylogenetic trees are quite comparable (Table3).

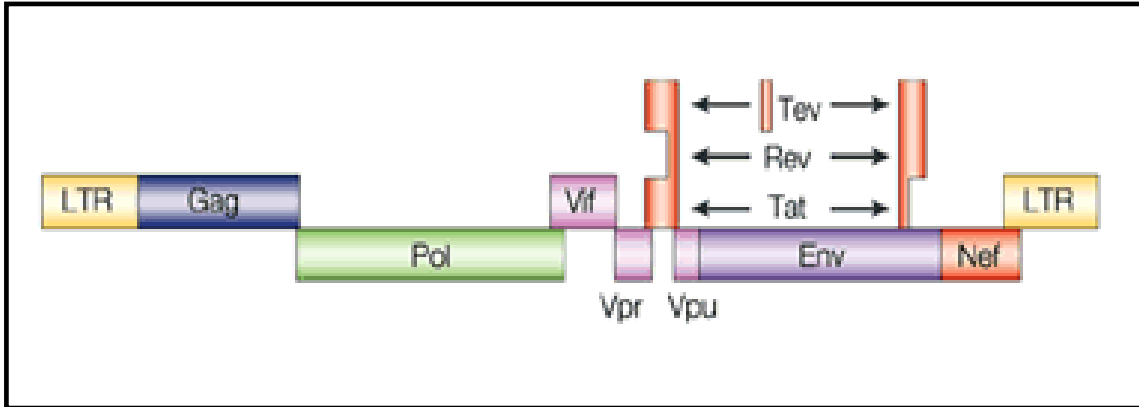


**Figure 22 : Illustration of genomorganization of HIV.**

Typical genomic organization of retrovirus is illustrated by genomorganisation of HIV. Three major coding domains *gag*, *pol*, *pro* are schematized here. LTR: Long terminal repeat; *tat*, *rev*, *vpr* are transactivators; *vif*, *nef*, *vpu* are other regulators.

From (Jill et al., 2008)

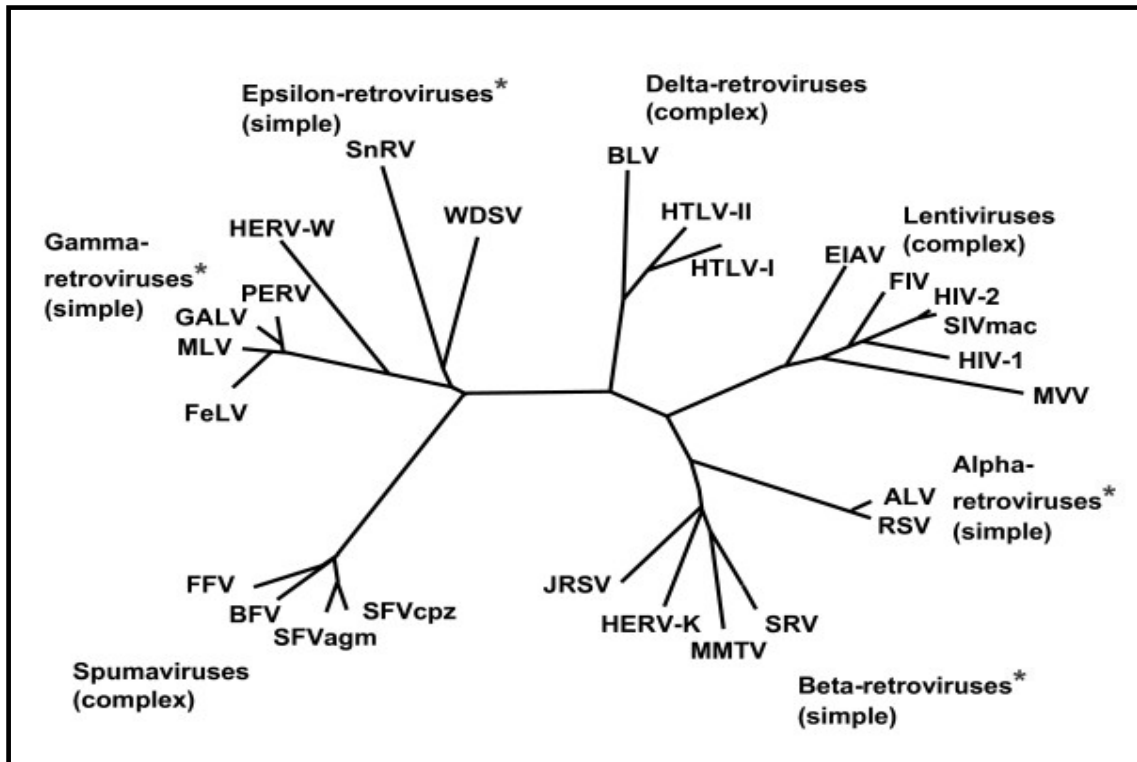


**Figure 23 : Schematic of phylogenetic tree of retrovirus.**

The tree is based on the alignment of approximately 180 amino acids corresponding to the extracellular and transmembrane domains of TM subunit of envelop proteins.

From (Weiss, 2007)

**Table 3: Classification of Retroviruses**

<i>Genes</i>	<i>Example</i>	<i>Virion morphology<sup>a</sup></i>	<i>Genome</i>
1. Avian sarcoma and leucosis viral group <sup>b</sup>	Rous sarcoma virus	Central, spherical core “C particles”	<i>simple</i>
2. Mammalian B-type Viral group	Mouse mammary tumor virus	Eccentric, spherical core “B particles”	<i>Simple</i>
3. Murine leukemia-related viral group	Moloney murine leukemia virus	Central, spherical core “C particles”	<i>Simple</i>
4. Human T-cell leukemia-Bovine leukemia viral group	Human T-cell Leukemia virus	Central, spherical core	<i>complex</i>
5. D-type viral group	Mason-Pfizer Monkey virus	Cylindrical core “D particles”	<i>Simple</i>
6. Lentiviruses	Human immunodeficiency virus	Cone-shaped core	<i>complex</i>
7. <i>Spumaviruses</i>	<i>Human foamy virus</i>	<i>Central, spherical core</i>	<i>complex</i>

**a:** Distinctive features seen in transmission electron micrographs.

**b:** Groups 1 through 5 are presently (and, hopefully, temporarily) designated by the awkward descriptive terms listed in the table, awaiting the proposal of more succinct appellations by the International Committee on taxonomy of viruses

### ***IV.1.2 Replication cycle and pathology of HIV-virus***

Human immunodeficiency viruses (HIV) are part of the lentivirus genus. It includes the disease subtypes HIV-1 and HIV-2, the third and fourth human retroviruses are also discovered in these years. Although the timescale is variable, HIV may lead to acquired immune deficiency syndrome (AIDS) and depends upon numerous factors, including treatment regimes; infections to which the person is exposed. Essentially, HIV attacks and disables a group of cells in the immune system, the CD4 cells. These are necessary for defending the person against cell mediated infections (Hooks and Gibbs, 1975). In present, approximately 33.3 millions people in the world are living with HIV. Therefore, the biology of HIV has been highly researched due to the pressing concerns of an HIV global pandemic and push for vaccine and treatment development.

The human immune system is essentially composed of three branches, each of which has a specific role in defending the body against bacterial and viral attack (Schwartz et al., 1995): the non-specific branch (eg. ear wax, gastric acid, saliva); the cell-mediated branch (using various types of ‘T’ cells to attack organisms that enter cells); the humoral branch (based on the action of antibodies). The HIV attacks and invades cells within the cell

mediated branch of the immune system-specifically the CD4 (or T) cells, also nanophages. Understanding the HIV life cycle and HIV replication has made it possible to develop the medications we use to treat HIV and AIDS.

The process of HIV replication is illustrated in Figure 24, which explains what HIV infection do to interrupt the normal cell life cycles (Venkatesh et al., 1991; Lochelt et al., 1993). 1) Viral attachment: once in the body, HIV needs a host to help it reproduce. In case of HIV, the host is the T-cell or CD4 cell. HIV seeks out CD4 cells and must attach to them by way of a “lock and key” type system. 2) Viral fusion and penetration: once attached to the cell, HIV injects proteins of its own into the cellular fluids (cytoplasm) of the T-cell. This causes a fusion of the cell membrane to the outer envelope of the HIV. 3) The uncoating: in order to use its genetic material (RNA) for reproduction, the protective coating surrounding the RNA must be dissolved. 4) Reverse transcription: once in the cell, the single stranded RNA of the HIV must be converted to the double stranded DNA. It accomplishes this with the help of the enzyme-reverse transcriptase, which uses building blocks from the T-cell to help change the HIV RNA to DNA. The DNA contains the genetic information needed for HIV reproduction. 5) Integration: To use the cell to reproduce, it must integrate the newly formed DNA into the cell nucleus. Enzyme named HIV integrase plays an indispensable role in HIV integration process. 6) Viral latency: once integration has occurred, HIV must wait for more protein building blocks to be formed by the cells or in other words, HIV is waiting for materials it needs to complete the reproductive process. 7) Final assembly: after all the materials are available, they must be cleaved and assembled into new HIV. This process is introduced by the enzyme-protease. 8) Budding: the final step of the viral life cycle is called budding. With its genetic materials tucked away and a new outer coat made from the host CD4 cell’s membrane, the newly formed HIV pinches off and enters into circulation, ready to start the whole infection process again.

**Figure24 : Replication cycle of HIV-1.**

Principle replication steps of HIV-1 and cell are potentially inhibited by commercial drug (a, b, c, and e) or by drugs in research (d and e).

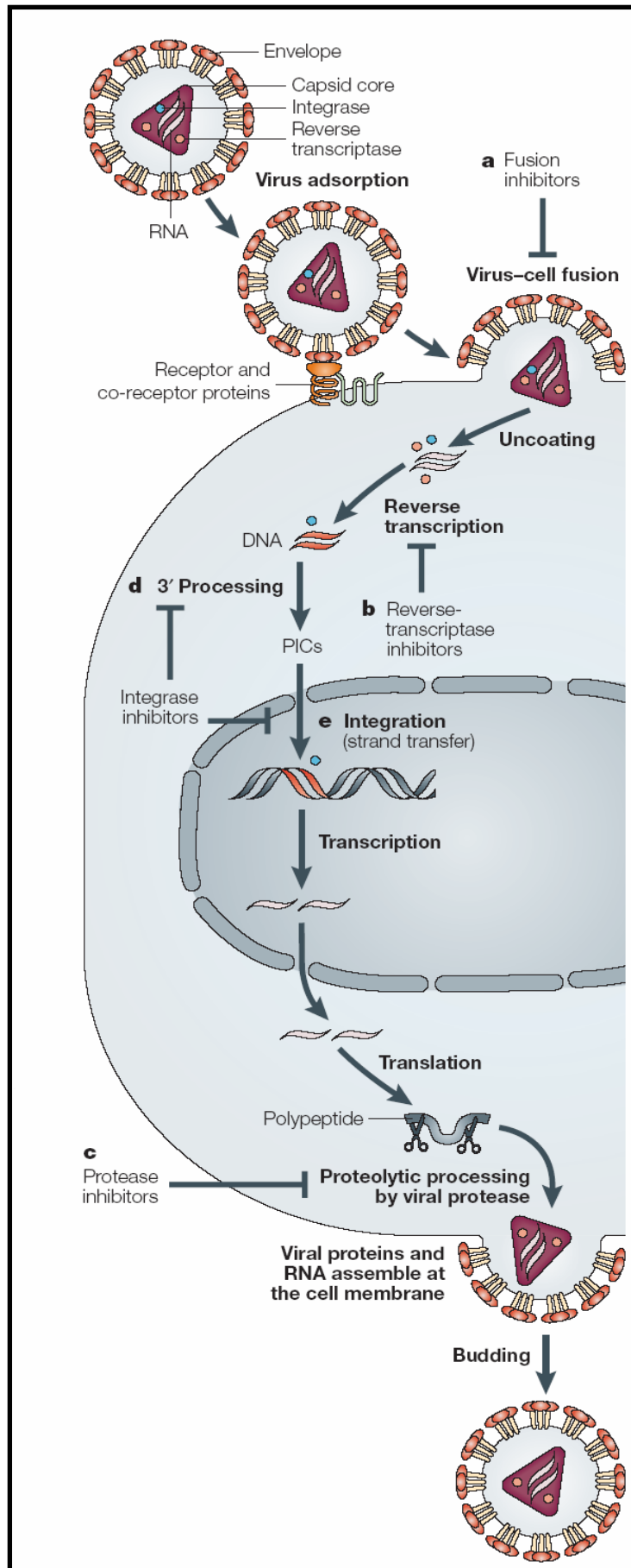
**a:** Fusion inhibitors block the enter of virus in cell.

**b:** Inhibitor of reverse transcriptase block the viral DNA synthesis.

**c:** Inhibitor of protease block the virus maturation by inhibiting viral proteolyses.

**d and e:** Inhibitor of integrase (IN). Two types of inhibitors: d) block the viral DNA 3'-processing activity of IN. e) block the viral DNA strand transfer activity of IN.

*From (Pommier et al., 2005)*



### ***IV.1.3 Introduction to anti-retroviral treatments***

In April 1997, World Health Organization (WHO) held an informal consultation on the implications of antiretroviral treatments for HIV/AIDS, with the objective of providing policy guidance on major issues relating to the use and provision of antiretroviral drugs. From that moment on, studies have been focused on developing novel antiretroviral treatments. The approach to antiretroviral therapy and the design of therapeutic regimens has been influenced by several significant findings from studies on the pathogenesis of HIV infection (Moebes et al., 1997; Erlwein et al, 1998; Wu et al., 1998). Since ongoing replication of HIV drives the disease process, causing progressive immunological damage, an ideal target of antiretroviral treatment is to obtain timely and sustained suppression of viral replication.

Medications for the treatment of infection by retroviruses, primarily HIV has been termed as antiretroviral drugs (Rethwilm, 1995; Coffin, 1996). In the current treatments, there are five groups of antiretroviral drugs, each of these groups attacks HIV in a different way (Figure.24).

In the early anti-HIV treatments, the only drugs available for treating HIV infection were nucleoside analogue reverse transcriptase inhibitors (NRTI). These drugs interfere with the action of a specific HIV enzyme-reverse transcriptase (RT)-involved in the replication cycle of HIV. The first anti-HIV drug, zidovudine (AZT), was discovered in the early 1980s to possess the ability of suppressing HIV replication in the HIV-infected individuals. Subsequently, four other NRTI- zalcitabin (ddc), didanosine (ddI), stavudine (D4T), and lamivudine (3TC) has been discovered (Schliephake&Rethwilm, 1994).

In the year of 1990s, the non-nucleoside reverse transcriptase inhibitors (NNRTI) were discovered and they are also antiretroviral medicines that prevent the HIV from multiplying (Löchelt&flüle, 1996). To prevent the RT from converting RNA to DNA, the NNRTI attaches itself to RT and in turn, HIV's genetic material cannot be incorporated into the healthy genetic material of the cell and hence prevents the cell from producing new virus. Presently, four type of NNRTI have been discovered, they are efavirenz + tenofovir + emtricitabine (EFV+TDF+FTC), delavirdine (DLV), efavirenz (EFV), and nevirapine (NVP).

HIV protease inhibitors (PIs) were first invented between 1989 and 1994, which were used in the treatment of patients with AIDS and were considered the first breakthrough in over a decade of AIDS research. Currently, there are five HIV PIs approved by FDA for the treatment of HIV infection. They are saquinavir, ritonavir, indinavir, nelfinavir, and amprenavir. These medications work at the final stage of viral replication and attempt to

prevent HIV from making new copies of them by interfering with the HIV protease enzyme. Consequently, the new copies of HIV are not able to infect new cells (Enssle et.al, 1996).

Fusion or entry inhibitors work by preventing HIV from entering healthy CD4 cells in the body. They work differently than many of the approved anti-HIV drugs, such as the PIs, the NRTI and the NNRTI, which are active against HIV after it has infected a CD4 cell. Fusion inhibitors work by attaching themselves to proteins on the surface of CD4 cells or proteins on the surface of HIV to prevent the binding of HIV's outer coat to the proteins on the surface of CD4 cells. Two fusion inhibitors have been approved by the FDA. One named enfuvirtide (T20), targeting the gp41 protein on HIV's surface; and the other one named maraviroc that targets the CCR5 protein (Chang et al., 1989; Schlicht et al., 1989; Enssle et.al, 1996).

In the year of 2007, a member of a new class of antiretroviral drugs, named Raltegravir, has been proved by FDA as a safe and effective drug for patients beginning treatments against HIV. Raltegravir is a HIV integrase inhibitor with faster onset of action and fewer adverse side effects. It inhibits the HIV integrase enzyme, which inserts the viral genome into the host cell's DNA by inhibiting essential strand-transfer activities of integrase. For example, the MK-0518 is an integrase strand transfer inhibitor (InSTI) from the hydroxypyrimidinone carboxamide class. It has demonstrated robust efficacy in treatment-experienced and treatment-naïve patients (Pommier et al, 2005).

To provide more effective treatment in preventing the replication of HIV, various agents may be used together, particularly those that inhibit the early phase and the late phase. Combined treatment would inhibit HIV replication in cells that have already been infected and prevent infection of new cells (Svarovskaia et al., 2004; Emiliani et al., 2005; Cherepanov et al., 2005; Rahman et al., 2006). When taken several antiretroviral drugs in combination, the approach is known as highly active antiretroviral therapy (HAART). There are different classes of antiretroviral drugs that act at different stages of the HIV life cycle. Based on the phase of the retrovirus life-cycle that the drug inhibits, antiretroviral drugs are broadly classified as following:

- Nucleoside and nucleotide reverse transcriptase inhibitors (NRTI), which inhibit reverse transcription by being incorporated into the newly synthesized viral DNA and preventing its further elongation.
- Non-nucleoside reverse transcriptase inhibitors (NNRTI), which inhibit reverse transcriptase directly by binding to the enzyme and interfering with its function.

- Protease inhibitors (PIs) target viral assembly by inhibiting the activity of protease, an enzyme used by HIV to cleave nascent proteins for final assembly of new virions.
- Integrase inhibitors inhibit the enzyme integrase, which is responsible for integration of viral DNA into the DNA of the infected cell. There are several integrase inhibitors currently under clinical trial, and raltegravir became the first to receive FDA approval in October 2007.
- Entry inhibitors (or fusion inhibitors) interfere with binding, fusion and entry of HIV-1 to the host cell by blocking one of several targets. Maraviroc and enfuvirtide are the two currently available agents in this class.
- Maturation inhibitors inhibit the last step in *gag* processing in which the viral capsid polyprotein is cleaved, thereby blocking the conversion of the polyprotein into the mature capsid protein (p24). Because these viral particles have a defective core, the virions released consist mainly of non-infectious particles, there are no drugs in this class currently available, though two are under investigation, bevirimat and vivecon.

However, HIV is a smart virus. It has developed mechanisms to overcome the blocks imposed by drug treatments. The life cycle of HIV can be as short as about 1.5 days from viral entry into a cell, through replication, assembly, and release of additional viruses, to infection of other cells (Coffin, 1996). They can produce several virus mutants which have a natural selection and can enable them to slip past defenses such as the human immune system and antiretroviral drugs. Through a microevolutionary process, HIV variants that are resistant to the intended inhibition are able to replicate and reproduce more virus. Over time, in the presence of drug, such as AZT, random mutations may develop and be selected for that allow these variants to be resistant to the effects of AZT. These drug resistant variants have greater fitness and can replicate in the patients even in the presence of the drug. Specifically, mutations in RT develop in the presence of AZT. These variants allow HIV to continue to replicate in human CD4 cells. HIV variants may only contain a single amino acid change in the protein sequence to render an anti-HIV drug ineffective. Briefly, the more active copies of the virus, the greater the possibilities that one resistant to antiretroviral drugs will be made, so antiretroviral combination therapy defends against resistance by suppressing HIV replication as much as possible.

In recent years, drug companies have worked together to combine these complex regimens into simpler formulas, termed fixed dose combinations. For instance, two pills

containing two or three medications each can be taken twice daily. This greatly increases the ease with which they can be taken, which in turn increases adherence, and thus their effectiveness over the long-term. Lack of adherence is a primary cause of resistance development in medication-experienced patients. Patients able to adhere at this rate and higher can maintain one regimen for up to a decade without developing resistance. This greatly increases chances of long-term survival, as it leaves more drugs available to the patient for longer periods of time.

#### ***IV.1.4 Structure and function of HIV-integrase***

In the process of retroviruses replication, integration of viral DNA into host DNA is an essential step in the replication cycle of HIV and other retroviruses (Coffin, 1996; Hindmars & Leis, 1999). An infecting retrovirus introduces a large nucleoprotein complex into the cytoplasm of the host cell. This complex, which is derived from the core of the infecting viron, contains two copies of the viral RNA together with a number of viral proteins, including reverse transcriptase and integrase (Wiskerchen & Muesing, 1995). Reverse transcription of the viral RNA occurs within the complex to make a double stranded DNA copy of the viral genome, the viral DNA substrate for integration. The viral DNA remains associated with both viral and cellular proteins in a nucleoprotein complex termed the preintegration complex (PIC). One constituent of the preintegration complex is the viral integrase (IN) protein, the key player in the integration of the viral DNA into the host genome. The other components of the preintegration complex that are transported to the nucleus along with the viral DNA and IN, and their possible functions have not been clearly clarified yet. The critical DNA cutting and joining events that integrate the viral DNA are carried out by the integrase protein itself.

IN is an enzyme that is responsible for integration of the reverse-transcribed double-stranded blunt-ended DNA into the host cell DNA. Biochemical studies have elucidated the basic chemical mechanism of integration of IN, which catalyses two reactions (Figure 25): in the first step of the integration process, two nucleotides are removed from each 3' end of the viral DNA, a reaction termed 3' end processing. Cleavage then occurs to the 3' side of a CA dinucleotide which exposes the terminal 3' hydroxyl group that is to be joined to target DNA. In the second step, DNA strand transfer, a pair of processed viral DNA ends is inserted in the target DNA (Smolov et al., 2006). In case of HIV, the sites of integration on the two target DNA strands are separated by five base pairs. Repair of this integration intermediate results in a direct duplication of five base pairs flanking the integrated viral DNA. Such repair is not

performed by IN but most likely by host proteins. There is little specificity for the sites of integration in host DNA and insertion can occur at essentially any location.

Stereochemical analysis of the reaction pathway has demonstrated that both 3'-processing and DNA strand transfer occur by a one-step transesterification mechanism (Engelman et al., 1991). *In vitro* 3'-processing and strand transfer reaction of IN has been widely carried out in recent years. A simplified *in vitro* system has proved to be invaluable for dissecting the biochemical mechanism of DNA integration.

HIV-1 integrase is comprised of three domains (Figure 26) based on the susceptibility of the linker regions to proteolysis (Engelman & Craigie, 1992), functional studies (Engelman & Craigie, 1992; Engelman et al., 1993) and the structures of the domains, which have individually determined by X-ray crystallography or NMR.

- The catalytic core domain contains the invariant triad of acidic residues, the D, D-35- E motif (Rowland & Dyke, 1990; Engelman & Craigie, 1992), comprising residues Asp 64, Asp 116 and Glu 152 in the case of HIV-1 integrase (Figure 26B). Mutagenesis of these residues and their counterparts in related retroviral integrases abolish or severely diminish all catalytic activities in parallel. This central domain is resistant to the proteolysis, and plays an essential role in fixing the divalent ion  $Mn^{2+}$  or  $Mg^{2+}$ , which is necessary to initiate the enzymatic activity of HIV-INs. Currently, different catalytic core structures have been obtained, which permits the tracing of the changes in flexible buckle conformation as well as the positioning of the lateral chain of the residue Glu 52.
- The N-terminal domain of HIV-1 integrase contains a conserved pair of His and Cys residues, a motif similar to the zinc-coordinating residues of zinc fingers. Although this domain does indeed bind zinc (Leh et al., 2000), its structure is totally different from that of zinc fingers. Since the sites of integration into target DNA are relatively non-specific, it has been suggested that this domain may interact with target DNA. Another role possibly involved in multimerization of integrase.
- The C-terminal domain interacts with a sub-terminal region just inside the very ends of the viral DNA end. The C-terminal domain of retroviral INs may therefore play a similar role to that of the site-specific DNA binding domain of transposases, which also recognize a sub-terminal sequence at the ends of the transposon DNA. It also involved in the non-specific DNA-binding, and in maintaining the stability of the IN/DNA complex.

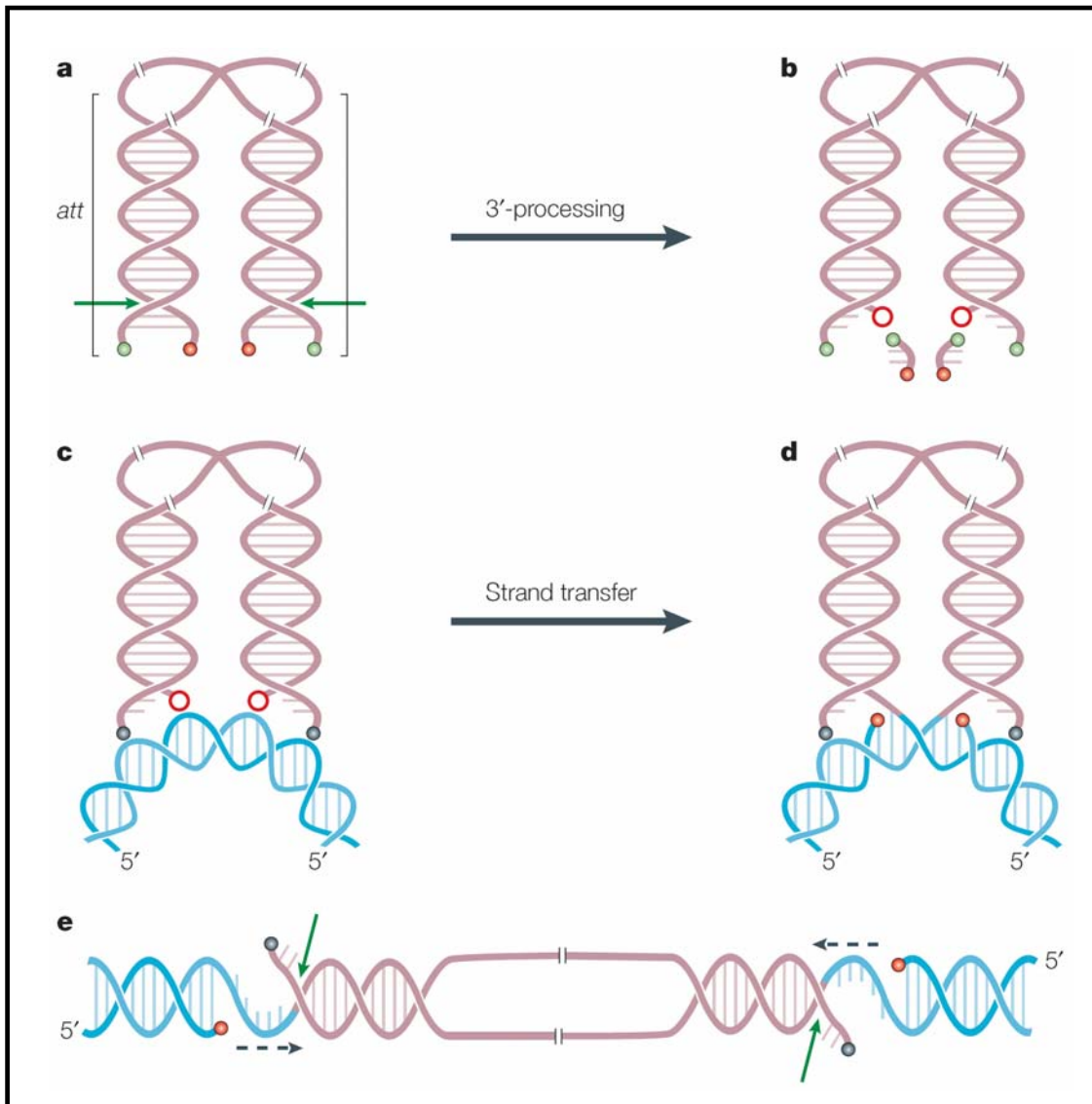


**Figure 25 : IN catalysed reactions in vivo: 3'-OH terminal is in red and the 5' terminal is in green**

**A :** Viral DNA, sequence of att is in detail. The green arrowhead indicates CA dinucleotide cleavage site in 3'-processing.

**B :** After 3'-processing, viral DNA possesses two 3'-OH terminals with free dinucleotide GT.

**C :** After the translocation into host nucleus, IN facilitates the insertion of viral DNA ends to the target DNA.

**D :** Integration on the two target DNA strands are separated by five base pairs.

**E :** Repair of this integration intermediate results in a direct duplication of five base pairs flanking the integrated viral DNA. *From (Pommier et al., 2005)*

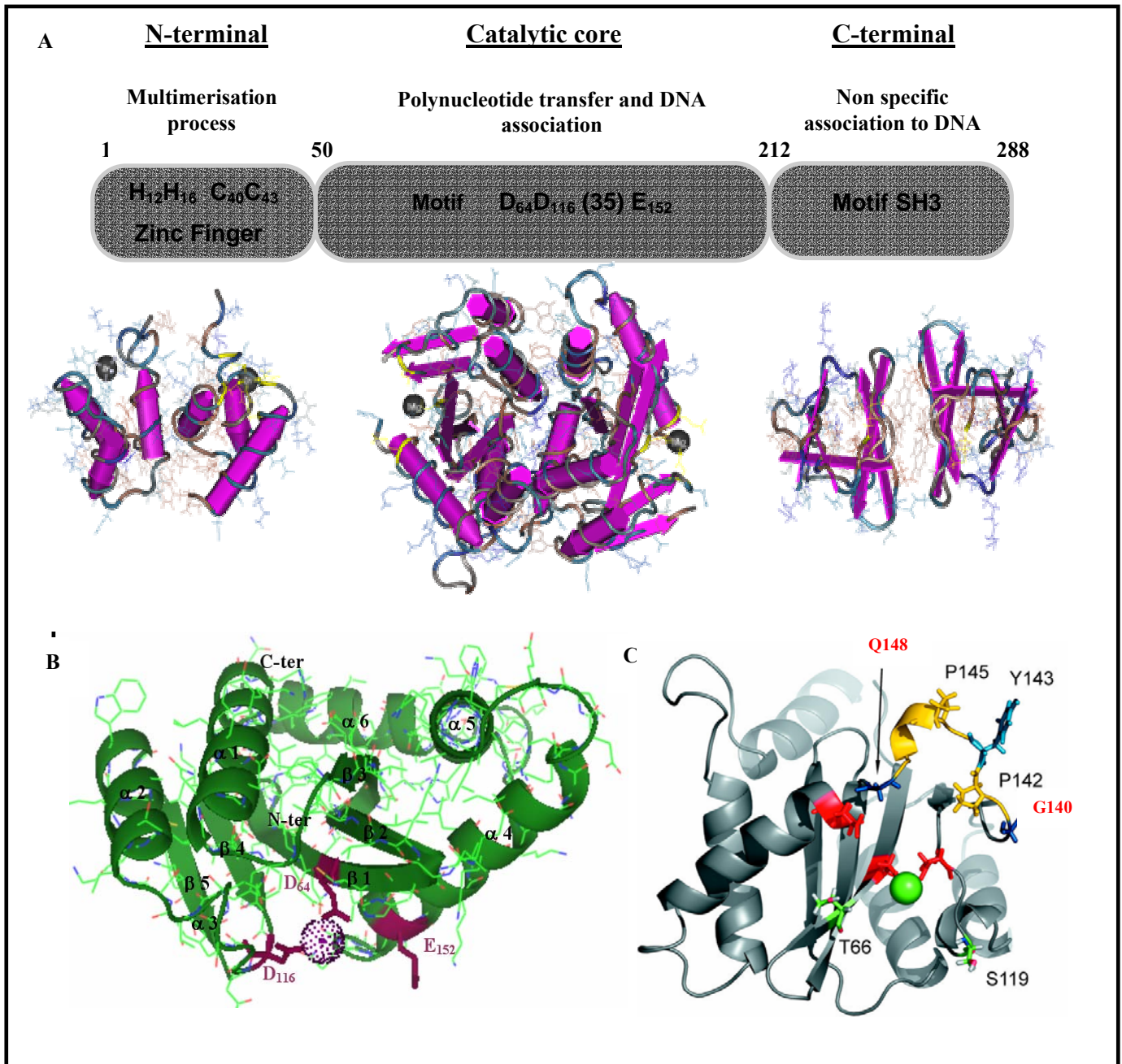


**Figure 26 : Domains structure of HIV-IN.**

**A:** HIV-INs is composed of three domains. The core domain contains the catalytic site. A triad of acidic residues, the D,D-35-E motif, play a key role in catalysis. The N-terminal domain includes the conserved HHCC motif which binds zinc. The C-terminal domain is less well conserved.

**B:** Illustration of HIV-IN catalytic core structure. The coordination of Mg<sup>2+</sup> into catalytic core is realized through the residue Asp 64 and Asp 116.

**B:** Illustration of the mutation residue site G140S and Q148H in the HIV-INs core structure.

*From (Rowland & Dyke, 1990; Engelman & Craigie, 1992)*

Several IN-inhibitors have been identified at present and the classification of these inhibitors is in accordance with their independent inhibition mechanisms. In general, IN-inhibitors could be divided into three classes (Pommier et al., 2005): 1) IN binding inhibitor (INBI); 2) IN strand transfer inhibitor (INSTI) and 3) inhibitors which could modify the oligomeric state of IN. To date, only INSTI have been shown to have a potent antiviral activity *in vivo* (Hazuda et al., 2000; DeJesus et al., 2006).

- $\beta$ -diketo acids (DKAs), acting as specific inhibitors of the strand-transfer step, provided the first proof of principle for HIV-1 IN inhibitors as antiviral agents followed by a series of metabolically stable compounds characterized by the incorporation of the diketo acid moiety into more complex heterocyclic frames (Figure 27). Among them, S-1360, L-870, 810 represent the first generation of IN inhibitors that have entered clinical studies (Hazuda et al., 2000).
- Raltegravir (RAL) is a 1-N-alkyl-5-hydroxypyrimidinone, which is a structural analogue of the DKAs class of compounds and shares their  $\beta$ -hydroxy-ketone structural motif (Figure 27). This structural motif possesses metal-chelating functions, and it is postulated that compounds bearing these functional groups interact with divalent metals within the active site of HIV-1 integrase (Grinsztejn et al., 2007). RAL and its related molecules inhibit the strand transfer process of HIV-1 viral genomic DNA insertion and as a result are referred to as INSTI. RAL has shown to have a 50% inhibitory concentration ( $IC_{50}$ ) of approximately 10 nM (Merck & Co. Inc, 2007). It has demonstrated activity against isolates resistant to NRTIs and NNRTIs, and PIs and therefore RAL drug demonstrated a rapid, potent and sustained antiretroviral effect in patients with advanced HIV-1 infection.
- Elvitegravir (EVG) is a dihydroquinoline carboxylic acid compound that, like RAL, exhibits the active IN-inhibitor-conferring  $\beta$ -hydroxy-ketone structural motif (Figure 27). EVG is a specific inhibitor of the strand-transfer step of HIV integration (DeJesus et al., 2006). This drug is active against HIV-1 and HIV-2, has a  $IC_{90}$  of 1.2 nM in peripheral blood mononuclear cells (PBMCs) and a serum-free antiviral  $IC_{50}$  of 0.2nM. EVG has also demonstrated activity against isolates resistant to NRTIs and NNRTIs, and PIs.

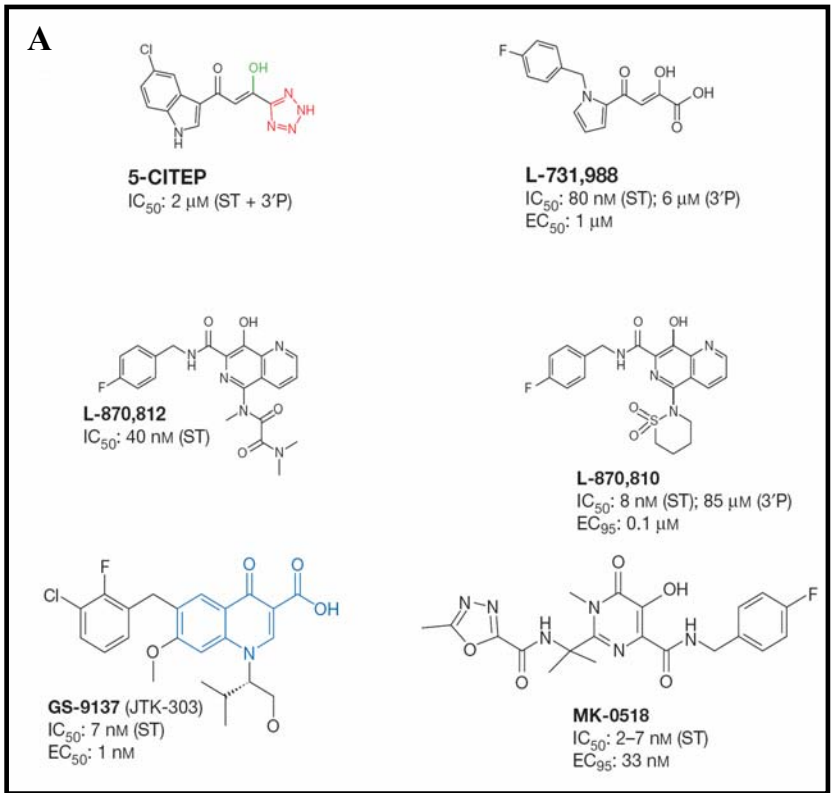
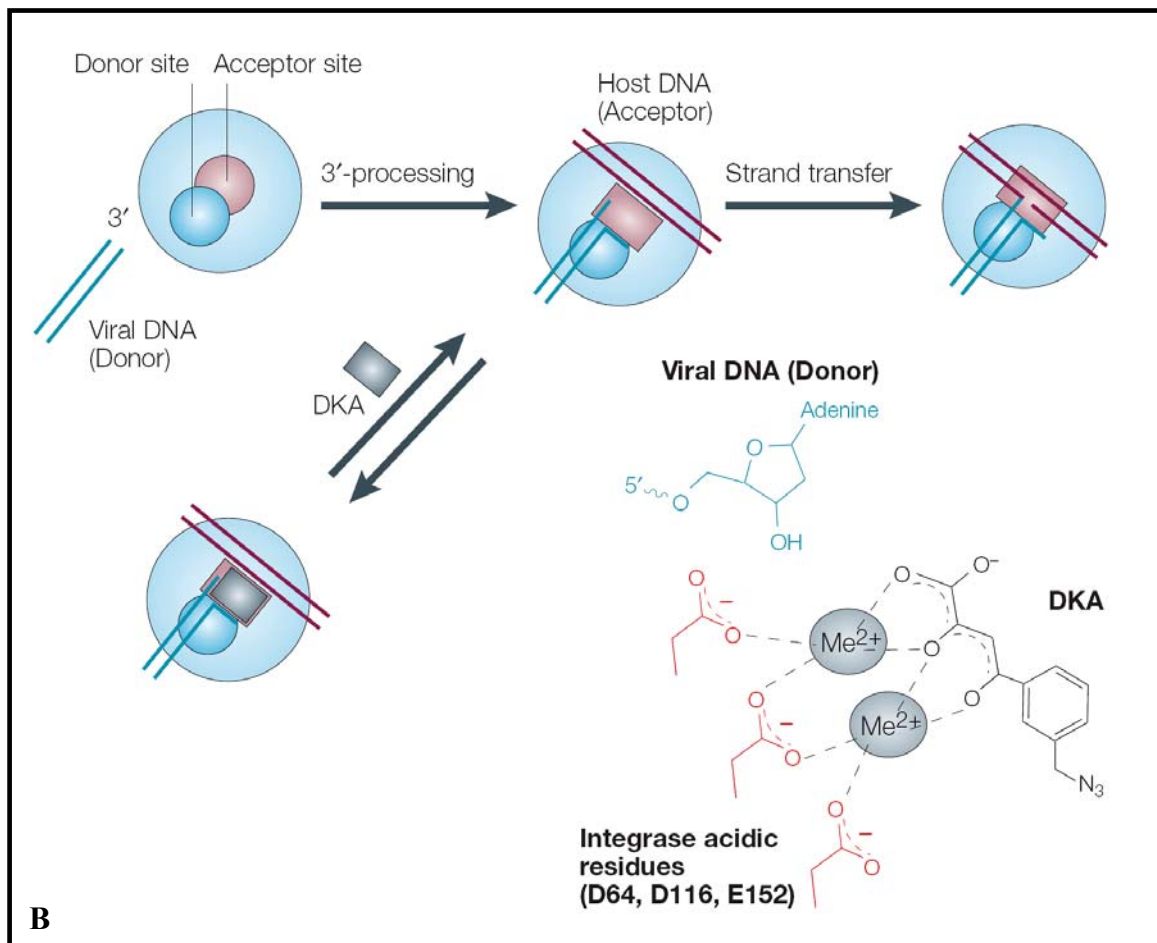


**Figure 27 : Structure of strand transfer inhibitor (INSTI).**

**A:** Characteristics of INSTIs structure: DKAs (5-CITEP, L-731,988, L-870,812, L-870,810; Quinoline derivatives: GS-9137 and carboxamide derivatives: MK-0518.

**B:** INSTIs action mechanisms. The functional groups interact with divalent metals within the active site of HIV-1 integrase  
From (Pommier et al., 2005)



## ***IV.2 The G140S mutation in HIV integrases from raltegravir-resistant patients rescues catalytic defect due to the resistance Q148H mutation***

### ***IV.2.1 Introduction***

Integrase inhibitors work by interfering with the enzyme integrase which is responsible for HIV replication. HIV-IN is one of the three enzymes essential for viral replication, which is responsible for integration of the reverse-transcribed double-stranded blunt-ended DNA into the host cell DNA. Two reactions: 3'-end processing and strand transfer are involved in IN catalyzed process. By interfering with IN, the IN inhibitors prevent HIV genetic material from integrating into the host cell, thus stopping viral replication. In October 2007, the United States Food and Drug Administration (FDA) approved the first drug in the integrase-inhibitor class for the treatment of HIV-1 as part of combination antiretroviral therapy in treatment-experienced patients, adding to the available chemotherapeutic agents for the effective treatment of HIV/AIDS.

At present, only INSTI have been shown to have a potent antiviral activity *in vivo* (Hazuda et al., 2000; DeJesus et al., 2006). The most frequently used drug RAL, a drug of the INSTI group, has already proven to be active when used with an optimized regimen in patients infected with drug-resistant viruses. However, in clinical treatments, resistance mutations are present in the IN gene of patients. According to the Merck Protocol 005 study team, by studying 35 patients with integrase mutations during virologic failure on raltegravir+OBR, two genetic pathways of mutations in the HIV-1 integrase gene were noted: N155H or Q148K/R/H (Merck & Co. Inc, 2007). Both pathways were associated with RAL resistance, with the Q148H pathway of mutations resulting in measurably larger reductions in susceptibility (25-fold versus 10-fold for N155). The acquisition of N155 or Q148 mutations were found to result in cross-resistance to structurally diverse integrase inhibitors and the acquisition of additional mutations resulted in high-level resistance both *in vitro* and *in vivo*. These mutations point directly to the catalytic site of HIV-1 integrase and the cross-resistance exhibited by HIV-1 variants with N155 or Q148 mutations is therefore consistent with the supposition that integrase inhibition takes place by affecting binding of the common pharmacophore within the active catalytic site of HIV-1 integrase. In addition, in the presence of elvitegravir during *in vitro* passage of wild-type HIV-1, two patterns of primary integrase resistance- T66I and E92Q-were found to be the most commonly selected (Malet et al., 2008). Focused on the exclusive Q148H/R/K, G140S/A or N155H mutations pathway during

virologic failure in raltegravir treatment, Mouscadet and his colleagues have carried out a detailed analysis of the molecular and structural effects of these mutations. Newly identified omega-shaped hairpin containing Q148 residue in the integrase core domain has been characterized, and they proved that these mutations greatly altered the specificity of DNA recognition by integrase (Mouscadet et al., 2009). The resistance associated mutations to integrase inhibitors and the degree of cross-resistance conferred by those mutations were also studied by Goethals et al. They reported that the Q148R mutation is selected by both raltegravir and elvitegravir and conferred resistance to a diverse panel of integrase inhibitors. Additionally, mutations selected with elvitegravir (E92Q and T66I) conferred significant resistance to many integrase inhibitors with a small reduction in susceptibility to raltegravir (Goethals et al., 2008).

In present study, we investigated the impact of the two main genetic resistance pathways (N155H and G140S/Q148H), on viral replication and the catalytic properties of recombinant INs. Because according to the studies of Malet et al. (Malet et al., 2008), the N155 pathway may shift to the Q148 pathway over time and the Q148H mutation occurs simultaneously with G140S mutation in most cases. The effect of the G140S/Q148H double mutation was particularly investigated here by constructing both the Q148H and G140S single mutants and the double mutant. We also studied the effect of IN background (laboratory or patient) on the properties of the enzymes. DNA-binding and catalytic properties of wild-type and RAL-resistant INs were studied by use of steady-state fluorescence anisotropy-based assay.

#### ***IV.2.2 Manuscript***

This manuscript has been published on « Nucleic Acids Research» vol. 37, No. 4, pp. 1193-1201.

# The G140S mutation in HIV integrases from raltegravir-resistant patients rescues catalytic defect due to the resistance Q148H mutation

Olivier Delelis<sup>1,\*</sup>, Isabelle Malet<sup>2</sup>, Li Na<sup>1</sup>, Luba Tchertanov<sup>1</sup>, Vincent Calvez<sup>2</sup>, Anne-Genevieve Marcelin<sup>2</sup>, Frederic Subra<sup>1</sup>, Eric Deprez<sup>1</sup> and Jean-François Mouscadet<sup>1</sup>

<sup>1</sup>LBPA, CNRS, Ecole Normale Supérieure de Cachan, 94235 Cachan and <sup>2</sup>Laboratoire de Virologie, Hôpital Pitié-Salpêtrière, Université Pierre et Marie Curie, 75013 Paris, France

Received November 19, 2008; Revised December 12, 2008; Accepted December 15, 2008

## ABSTRACT

Raltegravir (MK-0518) is the first integrase (IN) inhibitor to be approved by the US FDA and is currently used in clinical treatment of viruses resistant to other antiretroviral compounds. Virological failure of Raltegravir treatment is associated with mutations in the IN gene following two main distinct genetic pathways involving either the N155 or Q148 residue. Importantly, in most cases, an additional mutation at the position G140 is associated with the Q148 pathway. Here, we investigated the viral DNA kinetics for mutants identified in Raltegravir-resistant patients. We found that (i) integration is impaired for Q148H when compared with the wild-type, G140S and G140S/Q148H mutants; and (ii) the N155H and G140S mutations confer lower levels of resistance than the Q148H mutation. We also characterized the corresponding recombinant INs properties. Enzymatic performances closely parallel *ex vivo* studies. The Q148H mutation 'freezes' IN into a catalytically inactive state. By contrast, the conformational transition converting the inactive form into an active form is rescued by the G140S/Q148H double mutation. In conclusion, the Q148H mutation is responsible for resistance to Raltegravir whereas the G140S mutation increases viral fitness in the G140S/Q148H context. Altogether, these results account for the predominance of G140S/Q148H mutants in clinical trials using Raltegravir.

## INTRODUCTION

Integrase (IN) inhibitors constitute a new class of anti-retroviral agents blocking HIV-1 IN activity (1).

HIV-1 IN is one of the three enzymes essential for viral replication. IN is responsible for integration of the reverse-transcribed double-stranded blunt-ended DNA into the host cell DNA and, is therefore an attractive target for anti-HIV drugs. IN catalyses two reactions: 3'-end processing and strand transfer (2). During 3'-end processing, the terminal GpT dinucleotides are cleaved from the 3'-end of each long terminal repeat (LTR), producing CpA 3'-hydroxyl ends. This reaction takes place within a nucleoprotein complex known as the preintegration complex (PIC). The PIC is then transported through the nuclear pore into the nucleus, where strand transfer occurs. During this second step, IN transfers both newly exposed 3'-extremities of the viral DNA into the target DNA by a one-step transesterification reaction, resulting in full-site integration (3).

To date, only integrase strand transfer inhibitor (INSTI) have been shown to have a potent antiviral activity *in vivo* (4,5). Raltegravir (RAL), a drug of the INSTI group, was recently approved for therapeutic use after clinical assays demonstrated a rapid, potent and sustained antiretroviral effect in patients with advanced HIV-1 infection (6). Because of its mechanism of action, this novel antiviral agent (ARV) is likely to be active against viruses resistant to other class of antiretroviral drugs such as nucleoside reverse transcriptase inhibitors (NRTI), non-nucleoside reverse transcriptase inhibitors (NNRTI), Protease (PI) and entry inhibitors. Indeed, RAL has already proven to be active when used with an optimized regimen in patients infected with drug-resistant viruses (6). However, resistance mutations are present in the IN gene of patients who fail to respond to RAL treatment. Resistance data from a clinical study at the Hospital Pitié-Salpêtrière show that resistance to RAL develops in two main pathways, either through mutations of the N155 or the Q148 residue (7). This study also highlights two important observations: (i) the N155 pathway may

\*To whom correspondence should be addressed. Tel: +33 1 47 40 77 26; Fax: +33 1 47 40 76 84; Email: delelis@lbpa.ens-cachan.fr

© 2009 The Author(s)

This is an Open Access article distributed under the terms of the Creative Commons Attribution Non-Commercial License (<http://creativecommons.org/licenses/by-nc/2.0/uk/>) which permits unrestricted non-commercial use, distribution, and reproduction in any medium, provided the original work is properly cited.

shift to the Q148 pathway over time. (ii) In most cases, the Q148H mutation occurs simultaneously with the G140S mutation. The Q148H mutation may be present as a single mutation at the beginning of the treatment, but the G140S mutation appears after a few weeks of treatment. Thus, the Q148 and G140 residues clearly play a key role in the treatment failure on RAL. Other large-scale studies have shown that the Q148 pathway is the most frequently observed of the two pathways in RAL treatment failure (8). Other mutations, such as the E92 and E157Q, have also been described (7).

We investigated the impact of the two main genetic resistance pathways (N155H and G140S/Q148H), on viral replication and the catalytic properties of recombinant INs. In particular, we investigated the effect of the G140S/Q148H double mutation, by constructing both the Q148H and G140S single mutants as well as the double mutant. We also studied the effect of IN background (laboratory strain or patient) on the properties of the enzymes. We found that the Q148H mutation caused resistance to RAL when present alone. However, this mutation severely impaired viral replication kinetics in addition to the catalytic activity of the recombinant IN. The G140S mutation did not confer strong resistance, but restored the replication capability of the Q148H mutant. Accordingly, the *in vitro* activity of the G140S/Q148H mutant can reach a wild-type level of activity while the single mutant Q148H cannot. Our kinetic study reveals that Q148H is a catalytic mutant blocked in an inactive conformation. The G140S mutation induces a conformational transition compatible with activity. Thus, the combination of these two mutations results in a virus that is both capable of replication and highly resistant to RAL. Finally, we found that the G140S/Q148H mutant was much more resistant than the N155H mutant. These findings are consistent with the switch from the N155 to the Q148 pathway observed after a few weeks of RAL treatment.

## MATERIALS AND METHODS

### Cells and viruses

MT4 cells were cultured in RPMI 1640 containing 10% fetal calf serum. 293T and HeLa-P4 cells were cultured in Dubelcco's modified Eagle medium supplemented with 10% fetal calf serum, 100 units penicillin/ml (Invitrogen), and 100 µg streptomycin/ml (Invitrogen).

HIV-1 IN mutants were generated as previously described. Briefly, the fragment encoding IN of the replication-competent pNL43 virus was digested with AgeI and EcoRI, inserted into the Bluescript vector and IN mutants were obtained by mutagenesis (Quick change mutagenesis kit, Stratagene). We studied the E92Q, G140S, Q148H, N155H and G140S/Q148H mutations in a pNL43 background. The constructs were checked by sequencing and the fragment was then inserted into pNL43. HIV-1 virus stocks of all mutants were prepared by transfecting 293T cells. Transfection assays were carried out by the calcium phosphate method. Viral supernatants, 48 h post-transfection, were filtered through a 0.45 µm-pore-size-filter and frozen at -80°C.

HIV-1 p24<sup>gag</sup> antigen contents in viral supernatants were determined by enzyme-linked immunosorbent assay (Perkin-Elmer Life Sciences).

### HIV infectivity assay

Single-cycle titers of the virus were determined in HeLa-P4 cells. HeLa-P4 cells are HeLa CD4 LTR-LacZ cells in which *lacZ* expression is induced by the HIV transactivator protein Tat, making it possible to quantify HIV-1 infectivity precisely from a single cycle of replication. Cells were infected, in triplicate, in 96-well plates, with virus (equivalent of 3 ng of p24<sup>gag</sup> antigen). The single-cycle titers of viruses were determined 48 h after infection by quantifying β-galactosidase activity in P4 lysates in a colorimetric assay (the CPRG assay) based on the cleavage of chlorophenol red-β-D-galactopyranoside (CPRG) by β-galactosidase. For IC<sub>50</sub> determination, cells were infected with viruses and grown in the presence of increasing concentrations of RAL or the diketo-acid L731-988. The 50% inhibitory concentration (IC<sub>50</sub>) was determined as the drug concentration giving 50% inhibition of β-galactosidase levels with respect to untreated infected cells. Cell survival was also estimated with a standard MTT (3-[4,5-dimethylthiazol-2-yl]-2,5-diphenyltetrazolium bromide) assay.

### Viral infections

MT4 cells were concentrated at  $2 \times 10^6$ /ml and infected with viruses (50 ng of p24<sup>gag</sup> antigen per  $10^6$  cells). When required, cells were treated with 500 nM RAL inhibitor (Merck & Co.) or 25 µM zidovudine (AZT; Sigma) before infection. In the experiment with RAL, the medium containing the drug was replaced every three days (to maintain drug concentration). At various time points after infection, one to 3 million cells were harvested and dry cell pellets were frozen at -80°C until use.

### DNA extraction and real-time PCR

Total cell DNA was extracted with a QIAamp blood DNA minikit (QIAGEN, Courtaboeuf, France). Quantifications of total HIV-1 DNA, 2-LTR circles and integrated HIV-1 DNA were performed by real-time PCR on a LightCycler instrument (Roche Diagnostics) using the fit point method provided in the LightCycler quantification software, version 3.5 (Roche Diagnostics) as previously described (9).

Cell equivalents were calculated based on amplification of the β-globin gene (two copies per diploid cell) with commercially available materials (Control Kit DNA; Roche Diagnostics). 2-LTR circles, total and integrated HIV-1 DNA levels were determined and expressed as copy numbers per  $10^6$  cells.

### Characterization of IN protein activity *in vitro*

Two IN sequences, F4 and F12, obtained in a clinical study and corresponding to the IN sequences of a patient before and after treatment with RAL, respectively, were expressed, as previously described (7). The F4 polymorphism consists of eight mutations with respect to the

'laboratory' WT pNL43 IN: K7Q, E11D, L101I, K127R, I135V, I200L, V201I, I220L. F12 harbors these mutations together with the G140S/Q148H double mutation in the F4 background. The introduction of the entire sequence of the IN gene with the G140S/Q148H mutation from the patient into the pNL43 context did not result in a productive infection, suggesting that other viral proteins of the patient were required for efficient replication (data not shown). The comprehension of the potential influences of other viral proteins on viral replication is in progress in our laboratory.

In parallel, the E92Q, G140S, Q148H, N155H and G140S/Q148H mutations were obtained by site-directed mutagenesis from pET-15b, containing the WT sequence. The wild-type and mutant HIV-1 INs used for DNA-binding and 3'-processing assays were produced in *Escherichia coli* BL21 (DE3) and purified under non-denaturing conditions as previously described (10).

#### Steady-state fluorescence anisotropy-based assay

Steady-state fluorescence anisotropy values ( $r$ ) were recorded on a Beacon 2000 Instrument (Panvera, Madison, WI), in a cell maintained at 25°C or 37°C under thermostatic control. The principle underlying the anisotropy-based assay was published elsewhere for DNA-binding (11,12) and 3'-processing (13,14), respectively. Briefly, IN binding to fluorescein-labeled DNA (double-stranded 21-mer oligonucleotide (ODN) mimicking the U5 viral DNA end) increases the  $r$  value, making it possible to calculate the fractional saturation function:  $([DNA \cdot IN]/[DNA]_0)$ . DNA-binding step was recorded at 25°C, using ODNs fluorescein-labeled at the 3'-terminal GT nucleotide. The percentage of complexes was then calculated according to:

$$DNA \cdot IN (\%) = \frac{r - r_{free}}{r_{sat} - r_{free}} \times 100 \quad 1$$

where  $r_{free}$  and  $r_{sat}$  are the anisotropy values characterizing the free and bound oligonucleotides, respectively.

Following the DNA-binding step, the sample was then shifted to a permissive temperature for the recording of 3'-processing activity (37°C). As the fluorophore is linked to the released dinucleotide, 3'-processing activity significantly decreases the  $r$  value with respect to that for the non-processed DNA. Activity can be calculated in fixed-time experiments, by disrupting all the IN/DNA complexes with SDS (0.25% final). The fraction of dinucleotides released is given by:

$$F_{dinu} = \frac{r_{NP} - r}{r_{NP} - r_{dinu}} \quad 2$$

where  $r_{NP}$  and  $r_{dinu}$  are the anisotropy values for pure solutions of non-processed double-stranded ODN and dinucleotide, respectively. The formation of IN/DNA complexes and the subsequent 3'-processing reaction were performed by incubating fluorescein-labeled ODNs (4 nM) with IN in 20 mM Hepes pH 7.2, 1 mM dithiothreitol, 30 mM NaCl and 10 mM MgCl<sub>2</sub>. Standard 3'-processing and strand transfer activity tests

based on gel electrophoresis were performed as previously described (10).

## RESULTS

### Resistance of viral mutants to RAL

Sequence analysis of clinical isolates obtained during RAL treatment led to the identification of various mutations at specific positions. Two main profiles were identified, one based on the N155H mutation and the other based on the G140S/Q148H mutations, which seemed to be present together in most cases. After RAL administration, only mutations in the IN gene were observed (7).

We introduced IN mutations (i.e. N155H or E92Q or G140S/Q148H) into a WT pNL43 background. Two other constructs with single G140S or Q148H mutations were analyzed in parallel. Levels of p24 production were determined 48 h after transfection. They were found to be similar for all mutations (Figure 1A). We can therefore conclude that these mutations do not significantly impair virus assembly or the release step. HeLa-P4 cells were then infected for 48 h to study the early replication step. The mutations clearly had differential effects on viral infectivity (Figure 1B). The two single mutations, N155H and E92Q, neither disrupt the early steps of replication nor expression of integrated DNA, as shown by the

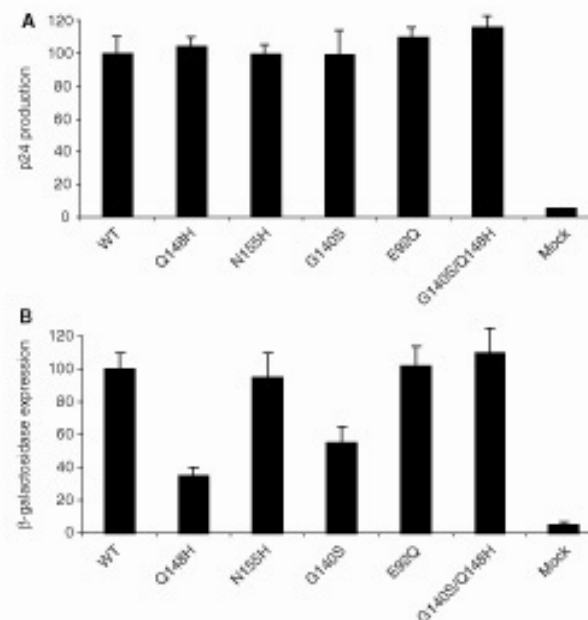


**Figure 1.** p24 and infectivity of IN mutant viruses. (A) Quantification of p24 protein, 48 h after transfection of 5  $\mu$ g of each virus DNA. (B) Viral infectivity for WT and mutants. Viral infectivity was determined in a single-cycle replication assay using HeLa p4 indicator cells and 3 ng of p24 antigen for each virus. Cells were exposed to virus during 48 h. Early steps of infections were assessed by measuring  $\beta$ -galactosidase activity in cell extracts by the CPRG method. For panels A and B, the results are expressed as percentages of the value obtained for the WT. The data shown are the means of three independent experiments.

corresponding  $\beta$ -galactosidase levels, which were similar to the WT. However, the Q148H and G140S mutations significantly decreased viral infectivity (3-fold and 2-fold less  $\beta$ -galactosidase expression for Q148H and G140S, respectively, as compared with the WT level), probably because of a defect in the integration process. Interestingly, the combination of these two mutations in the same virus resulted in levels of viral infectivity similar to those of the WT and much higher than obtained with the Q148H and G140S single mutations. These findings suggest that these two point mutations individually impair the viral infectivity but that their combination results in a wild-type level of infectivity.

We investigated the mechanism underlying the effects of these mutations on resistance to RAL, by determining the  $IC_{50}$  for each IN mutant (Figure 2A). The  $IC_{50}$  value (10 nM) obtained for the WT virus confirmed the potency of RAL as an inhibitor of HIV-1. At 24 or 72 h, no cytotoxic effects from the concentrations used in this experiment were observed in the MTT assay after infection (Figure 2B). G140S and E92Q mutants had slightly higher  $IC_{50}$  values (30 nM) than the WT. In sharp contrast, the N155H, Q148H and G140S/Q148H mutants had much higher  $IC_{50}$  values, at 130, 450 and >1000 nM, respectively. Thus, all the mutants identified in clinical

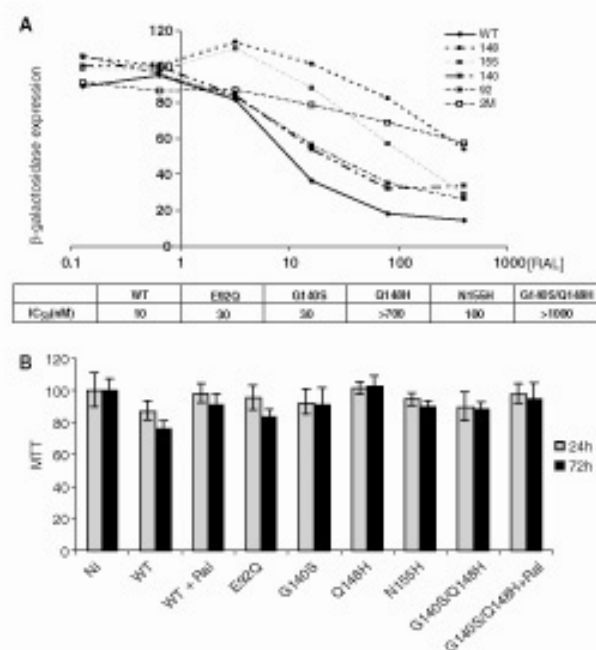


**Figure 2.** Resistance of IN mutants to RAL. (A) HeLa p4 cells were infected, in triplicate, with 3 ng of each virus, in the presence of various RAL concentrations.  $\beta$ -Galactosidase production was quantified by the CPRG assay. Data from a representative experiment (performed three times) is shown. The  $IC_{50}$  was determined as the concentration of RAL inhibiting  $\beta$ -galactosidase production by 50% with respect to untreated infected cells. (B) MTT assay. The MTT assay was performed 48 and 72 h after infection for all viruses. For the WT and G140S/Q148H mutant, the assay was performed with and without 500 nM RAL. The data shown are the means of three independent experiments.

trials using RAL were resistant to this compound, but to different extents. The same experiment was conducted with the strand transfer inhibitor L,731-988, a diketo acid which, similar to RAL, belongs to the INSTI group. The resistance profiles observed with this drug followed the same pattern as RAL (data not shown) but the values obtained were in low micromolar range for L,731-988, rather than in the nanomolar range as seen with RAL. Thus DKA, a well-characterized drug and RAL, both of which share the same mechanism of action, probably bind to the same binding site, inhibiting the strand transfer reaction by interfering with the binding of target DNA to IN.

#### Effects of mutations on viral DNA forms during replication

We investigated the effects of mutations during viral replication, by real-time PCR (qPCR) analysis, on the different viral nucleic acid species (total viral DNA, 2-LTR circles and integrated viral DNA) in cells infected with WT virus or resistant mutants.

Total viral DNA synthesis during the first 24 h after infection was similar for all mutants studied, and the kinetics of DNA synthesis were similar to those of the WT (Figure 3A). Furthermore, for all mutant and WT viruses, DNA synthesis peaked 10 h after infection, as typically reported in such studies (15), indicating that none of the mutations significantly affected the timing of the reverse transcription step. As a control, no viral DNA synthesis was detected with the WT in the presence of 25  $\mu$ M AZT. We performed the same experiment for the WT and the G140S/Q148H mutant in the presence of 500 nM RAL (a concentration 50 times higher than the  $IC_{50}$  value for the WT). Viral DNA synthesis levels were similar in the presence and absence of RAL for both the WT and the G140S/Q148H mutant (Figure 3A), confirming the absence of RAL effect on the reverse transcription step.

We quantified total viral DNA synthesis at a later time point to assess the ability of mutants to replicate in infected cells. qPCR quantification showed the kinetics of total viral DNA accumulation to be similar for the WT and all mutants, with the exception of the Q148H virus, for which smaller amount of viral DNA were detected, i.e. 5- and 10-fold less than for the WT virus, 39 and 64 h after infection, respectively. The apparent discrepancy between  $\beta$ -Gal assays and integration quantification of the G140S mutant will be further discuss in the next section. For WT infection in the presence of RAL, only a faint viral DNA signal was detected after the reverse transcription step: viral DNA, was reduced by 10- and 100-fold, 39 and 64 h after infection, respectively, when compared with WT infection in the absence of RAL, demonstrating the efficacy of this compound for blocking viral replication. In sharp contrast, RAL had only a slight effect on the DNA synthesis of the G140S/Q148H mutant (DNA synthesis was reduced by 1.2-fold at 64 h after infection), confirming the strong resistance of this double mutant. Moreover, Figure 3B clearly shows the better fitness of G140S/Q148H in comparison to the single-mutant Q148H.

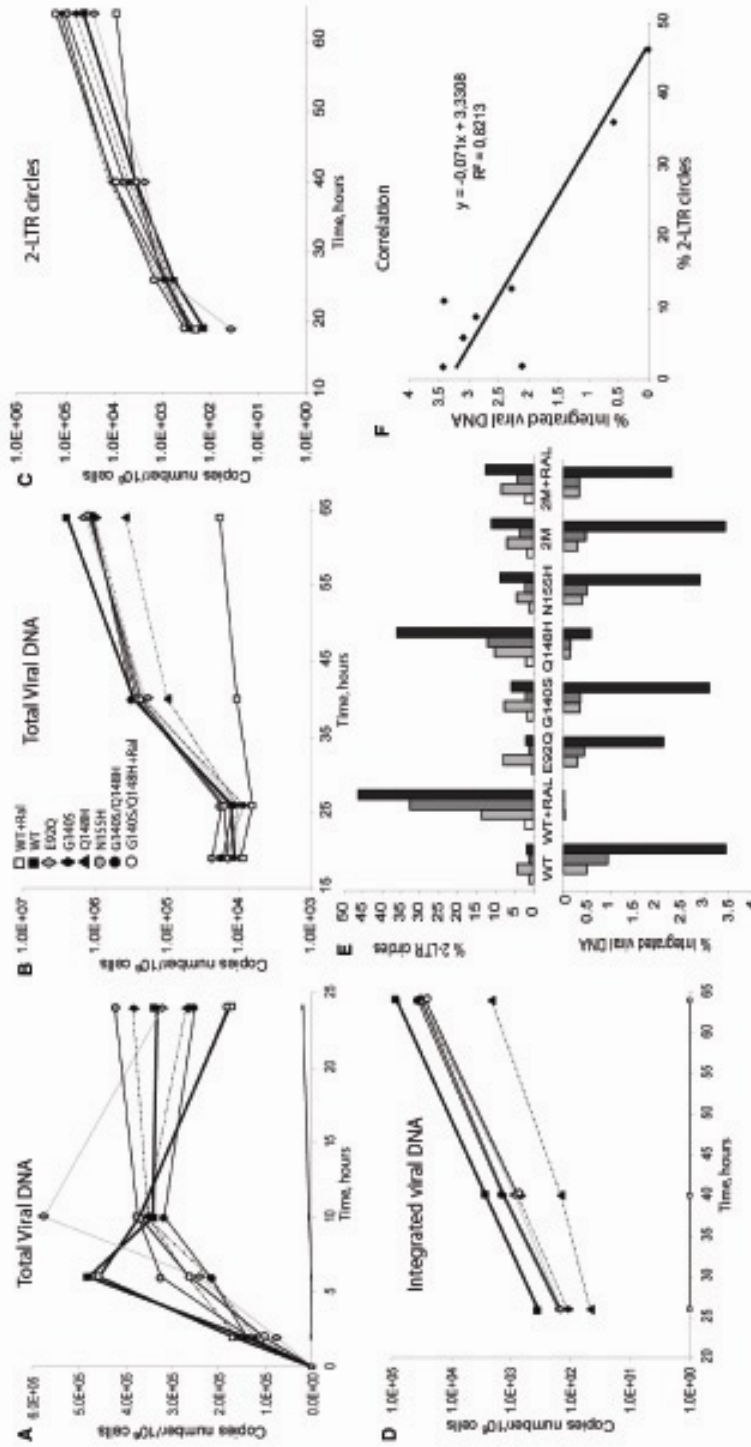


**Figure 3.** Kinetics of viral DNA synthesis. CEM cells were infected with 40 ng of p24 antigen and levels of intracellular HIV-1 DNA species were monitored by qPCR. (A) Dynamics of total viral DNA during the first 24 h of infection. WT + RAL (open square), WT (filled square), E92Q (gray diamond), G140S (filled diamond), N155H (gray circle), G140S/Q148H (filled circle), G140S/Q148H + Ral (open circle), WT + AZT (straight line). (B-D) Quantification of viral DNA over a 3-day period. (B) Total Viral DNA (C) 2-LTR circles (D) integrated HIV-1 DNA. The scales in panels A to D are logarithmic. Depicted results were obtained from a representative experiment. (E) The percentage of 2-LTR circles and integrated viral DNA were determined by calculating the ratio of 2-LTR circles copy number and integrated DNA levels, respectively, over total viral DNA. (F) Correlation between the percentages of 2-LTR circles and integrated viral DNA. The data shown are the means of three independent experiments.

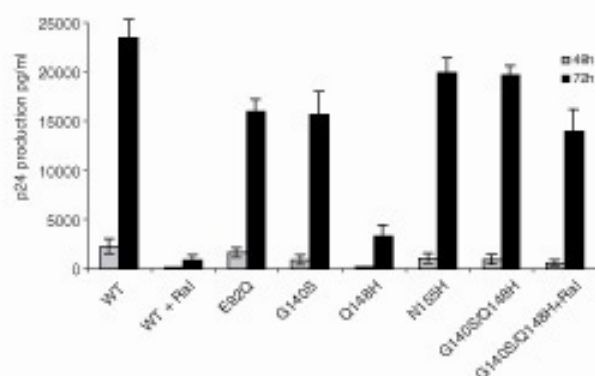


**Figure 4.** p24 production. Viral particles released in the supernatant were determined 48 and 72 h after infection by quantification of the p24 protein (see Materials and methods section). The data shown are the means of four independent experiments.

Both efficient IN inhibitors and mutations in the catalytic triad DD<sub>35</sub>E of IN have been reported to cause a decrease in the amount of integrated DNA, with a concomitant increase of 2-LTR circles (16,17), suggesting that 2-LTR circles molecules results from a defect in the integration process. We then analyzed the kinetics of 2-LTR accumulation and quantified integrated viral DNA, to obtain greater insight into the effects of the mutations and of RAL on the integration process (Figure 3C and D). The percentages of 2-LTR circles and integrated DNA viral forms are shown in Figure 3E. Again, our results clearly demonstrate that the Q148H mutant was more strongly affected than other mutants, as shown by the significant decrease in the amount of integrated DNA forms and the simultaneous accumulation of 2-LTR circles. A qualitatively similar but more pronounced effect was observed with the WT in the presence of RAL. No integrated DNA was detected, despite the sensitivity of the qPCR approach (9), demonstrating the efficiency of RAL as an inhibitor of the integration process. Remarkably, RAL had only a small effect on the levels of 2-LTR circles and integrated forms with the G140S/Q148H double mutant (Figure 3E). Figure 3F shows the correlation between accumulation of the episomic viral genome and the decrease in the amount of integrated DNA. This correlation supports the idea that the accumulation of 2-LTR circles results principally from an integration defect.

We assayed the supernatant of infected cells for the presence of viral particles, by quantifying p24 48 and 72 h after infection, to determine whether viral production was compatible with the amount of integrated DNA. Consistent with the quantification results obtained for the different DNA forms (Figure 3), only the production of p24 by the WT in the presence of RAL and by the Q148H mutant was severely impaired (p24 production decreased by 25- and 6-fold, respectively) (Figure 4). Figure 4 also confirms the resistance of G140S/Q148H as shown by the limited effect of RAL on the p24 production of the double mutant. The viral particles obtained from all IN mutants were infectious (data not shown).

Thus, IN mutations have no crucial consequences for the dynamics of viral replication, except the for the Q148H mutant, which displayed high levels of 2-LTR circle accumulation related to an integration defect. Therefore, the similar profile of this mutant as compared to mutants of the catalytic triad strongly suggests a defect of IN at the catalytic level (18). We then studied the effect of the Q148H and/or G140S mutations on 3'-processing and strand transfer activities using recombinant proteins.

#### G140S rescues the catalytic defect due to the Q148H mutation

The G140S/Q148H double mutation is one of the main profiles identified in patients resistant to RAL. These mutations seem to appear simultaneously or over a very short period of time in patients treated with this compound. We investigated the role of the G140 and Q148 residues in the resistance, by producing recombinant INs harboring either the G140S or the Q148H mutation, and the G140S/Q148H double mutant. In parallel, we also obtained recombinant proteins encoding the entire IN sequence, as found in patients with the double G140S/Q148H mutation.

A plot of 3'-processing activity (corresponding to 3 h of incubation at 37°C) as a function of IN concentration gave a characteristic bell-shaped curve, with activity peaking at a concentration of about 200 nM, for both WT IN, expressed in NL-43 context (Figure 5A, left panel) or in patients context before RAL treatment (Figure 5A, right panel) in accordance with previous results (13,14). Under the same conditions, the activities of the Q148H, G140S and G140S/Q148H were severely impaired, with the degree of impairment as follows: Q148H << G140S/Q148H ≈ G140S < WT (Figure 5). It is important to note that both proteins, WT and G140S/Q148H, in the patient background displayed stronger activity than INs in the NL-43 context. We are currently investigating the effects of the polymorphism on intrinsic IN activity.

As the increase in the IN concentration did not compensate for the defect in 3'-processing activity of the mutants (i.e. increasing the concentrations of mutant proteins did not result in wild-type levels of activity, as shown in Figure 5A), the defect was probably not because of a decrease in the overall affinity for the DNA substrate, being instead due to a catalytic defect. Accordingly, quantification of IN-DNA complexes by steady state anisotropy (Figure 5B), indicated that complex formation was not altered by any type of mutation. Our activity data after 3 h of incubation highlight some discrepancies between *in vitro* and *ex vivo* results, particularly for the G140S/Q148H double mutant virus, which replicated as well as the WT virus, despite the lower activity of the corresponding recombinant IN.

To understand this apparent discrepancy, we next studied the entire 3'-processing kinetics of WT and mutants. Interestingly, the kinetics of processing for the G140S and G140S/Q148H, although delayed in time as compared to the WT ( $t_{1,2} = 20.8$  h for mutants,  $t_{1,2} = 4.1$  h for WT), showed that these two mutants were able to reach WT levels of activity (Figure 5C). Again, this result was

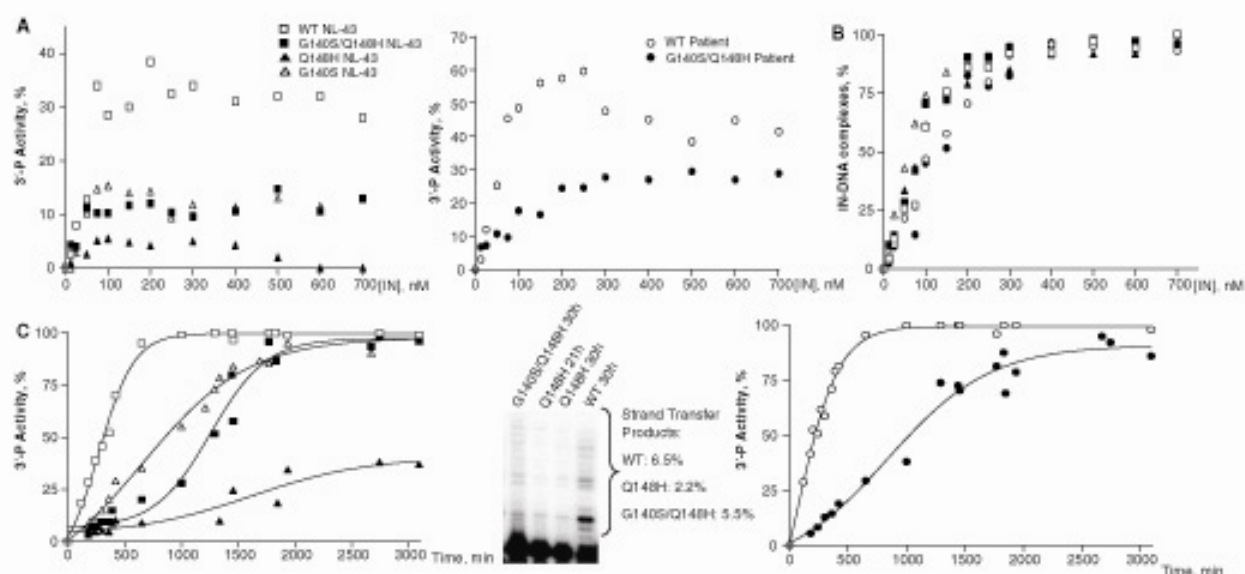


**Figure 5.** Comparative study of the DNA-binding and catalytic properties of wild-type and RAL-resistant INs. (A) 3'-Processing activity—after 3 h of incubation at 37°C—as a function of IN concentration. 3'-Processing activities were quantified as described in Materials and methods section, using a 21-mer DNA substrate (4 nM), with  $MgCl_2$  as a cofactor (10 mM) in 20 mM Hepes (pH 7.2), 1 mM DTT and 30 mM NaCl. (B) DNA binding of wild-type and mutant INs. The DNA-binding step was assessed by steady-state fluorescence anisotropy as described in Materials and methods section. Experimental conditions were similar to those described in A. IN and DNA were incubated together for 15 min before recording steady-state anisotropy. (C) Kinetics of 3'-processing for the different proteins. IN concentration was 200 nM. The same symbols were used in panels A, B and C: (open square) wild-type NL-43; (filled square) G140S/Q148H NL-43; (filled triangle) Q148H NL-43; (open triangle) G140S NL-43; (open circle) wild-type patient; (filled circle) G140S/Q148H patient. Strand transfer products are depicted (middle panel). The percentages of strand transfer (shown besides the gel) were obtained after the normalization by the 3'-processing activity.

independent of the context (NL-43 or patients) (compare left and right panels). The sigmoidal nature of the kinetics observed strongly suggests that IN must undergo a conformational transition to shift from a catalytically inactive state to an active state ( $IN^I \leftrightarrow IN^A$ ). 3'-Processing activity as analyzed by gel-electrophoresis with standard procedures (10) gave similar results (data not shown). Moreover, quantification of the product of the strand transfer reaction indicated that, under conditions in which the 3'-processing levels of the G140S/Q148H reached the WT levels, the yields of strand transfer are similar for the WT and the double mutant. In fact, after normalization by the 3'-processing activity, we found that the strand transfer efficiency was 6.5%, 2.2% and 5.5% for WT, Q148H and G140S/Q148H mutants, respectively (Figure 5C). In contrast to G140S and G140S/Q148H, the single mutant Q148H appears to be more severely impaired than the other mutants, with a 3'-processing activity increasing only slightly to 35%, after up to 50 h of incubation, with concomitant decrease in the yield of strand transfer (Figure 5C). Most likely, the  $IN^I \leftrightarrow IN^A$  transition accounts for the slow single turn-over rate constant characterizing IN (12). The effect of the Q148H mutation which strongly impairs this transition is reversed by adding the G140S mutation. These two residues belong to the catalytic loop 140–149, the flexibility of which was previously described to be essential for activity (19,20). The Q148 residue was shown to be essential to establish specific contacts with viral DNA (21,22). Our results,

showing that overall affinity of the IN-DNA complex was not influenced by the Q->H mutation at this position, do not exclude a fine repositioning of the catalytic loop relative to the viral DNA end, leading to a non-competent catalytic complex. Interestingly, two other mutations of the catalytic loop (G149A and G149A/G140A) display similar post DNA-binding defects (20). The residue G140 participates in catalytic loop hinge formation and its mutation could restore specific contacts compatible with catalysis between the loop of the double mutant and the viral DNA end. Simulation and molecular dynamics (MD) studies on the catalytic loop of IN is under progression in our laboratory. We have found that the Q148 residue belongs to a  $\Omega$ -shaped hairpin (144–148) that can move in a gate-like manner toward the active site as a rigid body. The G140 residue is not directly involved in the flexibility of the catalytic loop but plays a critical role in controlling the overall motion of the loop and finally in controlling its precise positioning relative to the phosphodiester bond to be cleaved ('*In Silico* study suggests that raltegravir-resistant mutations modify the DNA recognition properties of HIV-1 Integrase' by Tchertanov *et al.*, Third International Conference on Retroviral Integrase; September 14–18, 2008).

## DISCUSSION

To date, only INSTIs have been shown to be true inhibitors of HIV-1 DNA integration. These compounds

specifically inhibit strand transfer and target the pre-integration complex *in vivo*. RAL (or MK-0518) is a member of the INSTI family. This IN inhibitor was the first to be approved by the FDA for the treatment of AIDS. RAL is generally well tolerated although a recent study suggested an association between RAL and rhabdomyolysis (23). It is currently undergoing late-stage clinical trials with patients infected with multidrug-resistant HIV-1 viruses. However, several mutations occur very rapidly, within 11 weeks of beginning treatment. These mutations are E92Q, N155H and the G140S/Q148H double mutation, which seems to appear preferentially (8).

In this report, we analyzed the effect of mutations introduction in both the viral context and in the recombinant IN, focusing our studies on the double mutant. Our data demonstrate that each mutation described conferred resistance, but the extent of that resistance differed between mutations. The G140S/Q148H double mutation confers strong resistance to the drug and viral replication levels similar to those of the WT virus. Importantly, the G140S displays weak resistance ( $IC_{50} = 30$  nM) while the Q148H is strongly resistant to RAL ( $IC_{50} > 700$  nM). Taken together, these data suggest that resistance results principally from the Q148H mutation. In the viral context, all mutants, including G140S, displayed replication kinetics similar to those to the WT virus, with the exception of the Q148H mutant which is characterized by a slower kinetic. Consistently, all mutants are weakly impaired in the synthesis of viral DNA as well as in their propensity to integrate their genome and consequently to produce viral particles with the notable exception of the Q148H mutant. Its integration efficiency is 7-fold less in comparison to the WT. These data demonstrate that, in the case of the G140S/Q148H double mutant, the resistance to RAL is due to the Q148H and that the G140S mutation rescues the integration deficiency and thus the kinetic of replication.

It is important to note that  $\beta$ -Gal assays using the HeLa-P4 cells suggests that the G140S mutant was impaired in the viral integration process, in accordance with results of Nakahara *et al.* (24). However, we found that the integration efficiency of the G140S was similar to those found for the WT and G140S/Q148H double mutant. To date, the reason of such discrepancy is not clear but the type of cells used for integration quantification could be crucial in modulating the mutation impact, especially in the case of the G140S mutation. Indeed, Nakahara *et al.* (24) have found that the viral replication was delayed in Jurkat cells but not in PBMC cells. Such a differential response of the G140S mutation depending on the cellular context could account for the lack of correlation between  $\beta$ -Gal assays (Figure 1) and integration quantification (Figure 3).

These data were confirmed by *in vitro* activity experiments. We observed that G140S/Q148H IN, although kinetically affected as compared to the WT IN, displayed WT levels of activity if the incubation time was increased (kinetic mutant). The Q148H IN was much more severely impaired and cannot reach the WT level of activity (thermodynamic mutant). Our activity data—at long incubation time—highlight a correlation between *in vitro*

activity of IN and viral replication. Nevertheless, the slower kinetic of either G140S or G140S/Q148H, as seen *in vitro*, had no effect on the replication cycle of corresponding viruses. It is possible that the slow conformational transition involving the flexibility of the catalytic loop (see Results section) may not be kinetically limiting in the PIC context due to interactions with protein partners. Taken together, we hypothesized that the Q148H mutation primarily confers resistance to RAL. However, this mutation severely impaired viral replication. The G140S mutation counteracted this detrimental effect for the virus and increased viral fitness. These data clearly account for the high frequency of the G140S/Q148H mutant in clinical trials. It is important to note that the Q148H/R single mutation may occur 8 weeks after starting RAL treatment. However, 8–10 weeks later, the G140S mutation is also detected in patients. Our data of the compensation of the Q148H replication efficiency by the G140S explain why very rapidly after the administration of RAL, the G140S/Q148H mutant is detected. In addition, our data demonstrate that the Q148H mutant is more resistant to RAL in comparison to the N155H mutant. This observation explains why the N155 pathway often switched to the Q148 pathway. It is important to note that, during the course of our study, similar results were obtained by Nakahara *et al.* (24). The authors have studied the Q148K/R and G140S mutations as well as the G140S/Q148R and G140S/Q148K double mutants. Mutants Q148K/R displayed reduced viral fitness whatever the cell line studied (PBMC or Jurkat cells). In the case of the G140S mutant, the viral fitness is only delayed in Jurkat cells. In accordance with our results, Nakahara *et al.* have shown that the G140S mutation rescues the fitness of the Q148K/R mutant. Taken together, results from Nakahara *et al.* and our study show that the G140S mutation rescues the ability of the Q148H/K/R mutants to replicate in cells while mutation of the Q148 residue is responsible for the resistance to the drug. Note that the discrepancy concerning the nature of the mutation (K, R in the Nakahara's experiments and H in our study) is only apparent since resistance mutation were not obtained against the same anti-IN compound: S-1360 and GSK-364735 were used by Nakahara *et al.* while, in this study, we used RAL.

The development of strand transfer-specific inhibitor classes is an important achievement for the IN drug design. However, continued drug development is required as the ability of HIV to replicate under therapeutic pressure will undoubtedly lead to the emergence of IN drug-resistant viral strains characterized by comparable fitness to WT such as the double mutant G140S/Q148H.

To prevent from the appearance of cross-resistance, other sites of IN must be targeted as already done for the development of RT inhibitors. For example, sites responsible for the oligomerization of IN or/and interactions with cellular partners as LEDGF constitute good candidates. The combination of several IN inhibitors in optimal regimen will undoubtedly lead to optimal treatment for patients.

## ACKNOWLEDGEMENTS

We thank Françoise Simon for technical assistance and Hervé Leh for helpful discussions. We thank Ede Osemwota for reviewing the manuscript.

## FUNDING

This work was supported in part by the Agence Nationale de Recherche sur le SIDA (ANRS) and by the Fondation pour la Recherche Médicale (FRM). Funding for open access charge: The French Agence Nationale de Recherche contre le SIDA (ANRS).

*Conflict of interest statement.* None declared.

## REFERENCES

- Pommier, Y., Johnson, A.A. and Marchand, C. (2005) Integrase inhibitors to treat HIV/AIDS. *Nat. Rev. Drug Discov.*, **4**, 236–248.
- Sinha, S. and Grandgenett, D.P. (2005) Recombinant human immunodeficiency virus type 1 integrase exhibits a capacity for full-site integration in vitro that is comparable to that of purified preintegration complexes from virus-infected cells. *J. Virol.*, **79**, 8208–8216.
- Li, M., Mizuuchi, M., Burke, T.R. Jr. and Craigie, R. (2006) Retroviral DNA integration: reaction pathway and critical intermediates. *EMBO J.*, **25**, 1295–1304.
- DeJesus, E., Berger, D., Markowitz, M., Cohen, C., Hawkins, T., Ruane, P., Elion, R., Farthing, C., Zhong, L., Cheng, A.K. *et al.* (2006) Antiviral activity, pharmacokinetics, and dose response of the HIV-1 integrase inhibitor GS-9137 (JTK-303) in treatment-naïve and treatment-experienced patients. *J. Acquir. Immun. Defic. Syndr.*, **43**, 1–5.
- Hazuda, D.J., Young, S.D., Guare, J.P., Anthony, N.J., Gomez, R.P., Wai, J.S., Vacca, J.P., Handt, L., Motzel, S.L., Klein, H.J. *et al.* (2004) Integrase inhibitors and cellular immunity suppress retroviral replication in rhesus macaques. *Science*, **305**, 528–532.
- Grinsztejn, B., Nguyen, B.Y., Kallama, C., Gatell, J.M., Lazzarin, A., Vittecoq, D., Gonzalez, C.J., Chen, J., Harvey, C.M. and Isaacs, R.D. (2007) Safety and efficacy of the HIV-1 integrase inhibitor raltegravir (MK-0518) in treatment-experienced patients with multidrug-resistant virus: a phase II randomised controlled trial. *Lancet*, **369**, 1261–1269.
- Malet, I., Delelis, O., Valantin, M.A., Montes, B., Soulie, C., Wirden, M., Tchertanov, L., Peytavin, G., Reynes, J., Mouscadet, J.F. *et al.* (2008) Mutations associated with failure of raltegravir treatment affect integrase sensitivity to the inhibitor in vitro. *Antimicrob. Agents Chemother.*, **52**, 1351–1358.
- Miller, M.D., Danovich, R.M., Ke, Y., Witmer, M., Zhao, J., Harvey, C., Nguyen, B.Y. and Hazuda, D. (2008) Longitudinal analysis of resistance to the HIV-1 integrase inhibitor raltegravir: results from P005a Phase II study in treatment-experienced patients. *Antiviral Therapy*, **13**, A8.
- Brussel, A., Delelis, O. and Sonigo, P. (2005) Alu-LTR real-time nested PCR assay for quantifying integrated HIV-1 DNA. *Methods Mol. Biol.*, **304**, 139–154.
- Leh, H., Brodin, P., Bischerour, J., Deprez, E., Tauc, P., Brochon, J.C., LeCam, E., Coulaud, D., Auclair, C. and Mouscadet, J.F. (2000) Determinants of Mg<sup>2+</sup>-dependent activities of recombinant human immunodeficiency virus type 1 integrase. *Biochemistry*, **39**, 9285–9294.
- Agapkina, J., Smolov, M., Barbe, S., Zubin, E., Zaitsep, T., Deprez, E., Le Bret, M., Mouscadet, J.F. and Gottikh, M. (2006) Probing of HIV-1 integrase/DNA interactions using novel analogs of viral DNA. *J. Biol. Chem.*, **281**, 11530–11540.
- Smolov, M., Gottikh, M., Tashlitskii, V., Korolev, S., Demidyuk, I., Brochon, J.C., Mouscadet, J.F. and Deprez, E. (2006) Kinetic study of the HIV-1 DNA 3'-end processing. *FEBS J.*, **273**, 1137–1151.
- Delelis, O., Carayon, K., Guiot, E., Leh, H., Tauc, P., Brochon, J.C., Mouscadet, J.F. and Deprez, E. (2008) Insight into the integrase-DNA recognition mechanism: a specific DNA-binding mode revealed by an enzymatically labeled integrase. *J. Biol. Chem.*, **283**, 27838–27849.
- Guiot, E., Carayon, K., Delelis, O., Simon, F., Tauc, P., Zubin, E., Gottikh, M., Mouscadet, J.F., Brochon, J.C. and Deprez, E. (2006) Relationship between the oligomeric status of HIV-1 integrase on DNA and enzymatic activity. *J. Biol. Chem.*, **281**, 22707–22719.
- Maroun, M., Delelis, O., Coadou, G., Bader, T., Segéral, E., Mbemba, G., Petit, C., Sonigo, P., Rain, J.C., Mouscadet, J.F. *et al.* (2006) Inhibition of early steps of HIV-1 replication by SNF5/In1. *J. Biol. Chem.*, **281**, 22736–22743.
- Svarovskaia, E.S., Barr, R., Zhang, X., Pais, G.C., Marchand, C., Pommier, Y., Burke, T.R., Jr. and Pathak, V.K. (2004) Azido-containing diketo acid derivatives inhibit human immunodeficiency virus type 1 integrase in vivo and influence the frequency of deletions at two-long-terminal-repeat-circle junctions. *J. Virol.*, **78**, 3210–3222.
- Hazuda, D.J., Felock, P., Wittner, M., Wolfe, A., Stillmock, K., Grobler, J.A., Espeseth, A., Gabryelski, L., Schleif, W., Blau, C. *et al.* (2000) Inhibitors of strand transfer that prevent integration and inhibit HIV-1 replication in cells. *Science*, **287**, 646–650.
- Wiskerchen, M. and Muesing, M.A. (1995) Human immunodeficiency virus type 1 integrase: effects of mutations on viral ability to integrate, direct viral gene expression from unintegrated viral DNA templates, and sustain viral propagation in primary cells. *J. Virol.*, **69**, 376–386.
- Asante-Appiah, E. and Skalka, A.M. (1999) HIV-1 integrase: structural organization, conformational changes, and catalysis. *Adv. Virus Res.*, **52**, 351–369.
- Greenwald, J., Le, V., Butler, S.L., Bushman, F.D. and Choe, S. (1999) The mobility of an HIV-1 integrase active site loop is correlated with catalytic activity. *Biochemistry*, **38**, 8892–8898.
- Esposito, D. and Craigie, R. (1998) Sequence specificity of viral end DNA binding by HIV-1 integrase reveals critical regions for protein-DNA interaction. *EMBO J.*, **17**, 5832–5843.
- Johnson, A.A., Santos, W., Pais, G.C., Marchand, C., Amin, R., Burke, T.R. Jr., Verdine, G. and Pommier, Y. (2006) Integration requires a specific interaction of the donor DNA terminal 5'-cytosine with glutamine 148 of the HIV-1 integrase flexible loop. *J. Biol. Chem.*, **281**, 461–467.
- Zembower, T.R., Gerzonshtein, L., Coleman, K. and Palella, F.J. Jr. (2008) Severe rhabdomyolysis associated with raltegravir use. *AIDS*, **22**, 1382–1384.
- Nakahara, K., Wakasa-Morimoto, C., Kobayashi, M., Miki, S., Noshi, T., Seki, T., Kanamori-Koyama, M., Kawachi, S., Suyama, A., Fujishita, T. *et al.* (2008) Secondary mutations in viruses resistant to HIV-1 integrase inhibitors that restore viral infectivity and replication kinetics. *Antiviral Res.* [Epub ahead of print, Nov 21, 2008].

### ***IV.2.3 Conclusion***

Present study has successfully monitored the DNA-binding and 3'-processing activities of wild-type and mutants of HIV-INs in real-time by use of steady-state anisotropy measurements. RAL (or MK-0518) is a member of the INSTI family, which could specifically inhibit strand transfer and target the preintegration complex *in vivo*. It is the first integrase inhibitor to be approved by the US FDA and is currently used in clinical treatment of viruses resistant to other antiretroviral compounds. Currently it is undergoing late-stage clinical trials with patients infected with multidrug-resistant HIV-1 viruses. However, several mutations occur very rapidly, within 11 weeks of beginning treatment. They are primarily E92Q, N155H and the G140S/Q148H double mutation, which seems to appear preferentially (Miller et al., 2008).

In this study, two main genetic resistance pathways (N155H and G140S/Q148H) were investigated in both the viral context and in the recombinant IN. In particular, the effects of double mutation G140S/Q148H were studied by constructing both the Q148H and G140S single mutants and the double mutant. Results indicated that each mutation described conferred resistance, but the extent of that resistance differed between mutations. The Q148H mutation caused strong resistance to RAL when present alone, while the G140S displays weak resistance. Importantly, the G140S/Q148H double mutation confers strong resistance to the drug and viral replication levels similar to that of wild-type virus. However, this mutation of Q148H severely impaired viral replication kinetic in addition to the catalytic activity of the recombinant IN. The G140S mutation did not confer strong resistance but restored the replication capability of the Q148H mutant. Accordingly, *in vitro*, the activity of the G140S/Q148H mutant is able to reach a wild-type level of activity but not the single mutant Q148H. Our kinetic study also reveals that Q148H is a catalytic mutant blocked in an inactive conformation. It is highly possible due to the G140S mutation could induce a conformational transition compatible with activity. Thus, the combination of these two mutations results in a virus that is both able to replicate and highly resistant to RAL. Taken together, we hypothesized that the Q148H mutation primarily confers resistance to RAL, however, this mutation severely impaired viral replication. The G140S mutation counteracted this detrimental effect for the virus and increased viral fitness. Such compensation of the Q148H replication efficiency by G140S explains why rapidly after the administration of RAL, the G140S/Q148H mutant is detected. In addition, our data demonstrate that the Q148H mutant is more resistant to RAL in comparison to the N155H mutant, which explains why the N155 pathway often switched to the Q148 pathway.

The development of effective inhibitors of HIV replication targeted to indispensable replication enzymes has demonstrated the potential effectiveness of antiviral therapy for the treatment of AIDS. Drugs targeted to integrase would be a valuable complement to reverse transcriptase and protease inhibitors. Therefore, the development of strand transfer-specific inhibitor classes is an important achievement for the IN drug design. However, continued drug development is required as the ability of HIV to replicate under therapeutic pressure will undoubtedly lead to the emergence of IN drug-resistant viral strains characterized by comparable fitness to wild-type such as the double mutant G140S/Q148H. To prevent from the appearance of cross-resistance, other sites of IN must be targeted and the combination of several IN inhibitors in optimal regimen will undoubtedly lead to optimal treatment for patients.

---

**APPLICATION OF  
PHOTOLUMINESCENCE DECAY  
TO CHARACTERIZE QDS  
FLUORESCENCE PROPERTIES**

---

Fluorescence as a detection modality is used in a very diverse manner within the life science industry. At present, the nanotechnology field is undergoing phenomenal growth and the fusion of nanoscience and nanotechnology into biomedical research has brought in a true revolution that is broadly impacting biotechnology. To promote this fusion, it is clear that a wide variety of standards materials are likely to be required, to cater for different spectral regions or different sample formats. Although the existing fluorescence standards have been improved a lot, it is clear that the available coverage is patchy. For example, though the small organic fluorophores are commercially available presently, most of them are of less photostability and displaying some photobleaching especially in use of high illumination intensities fluorescence microscopy. This chapter describes the power of nanochemistry to produce the various nanoparticles and tailor their structures and functions for biomedical applications. The semiconductor nanoparticles known as Quantum dots, whose luminescence wavelength is dependent on the size and the nature of the semiconductors, would be discussed. The use of nanoparticles for optical bioimaging, optical diagnostics, and light-guided and activated therapy would also be evaluated.

## ***V.1 General introduction to the semiconductor nanoparticles***

### ***V.1.1 Definition of quantum dots***

During the past decade, advances in synthesis and biofunctionalization of colloidal semiconductor nanocrystals have generated an increasingly widespread interest among investigators in the fields of biology and medicine. These nanometer-sized crystalline particles, also called quantum dots (QDs), are composed of periodic groups of II–VI (e.g., CdSe, CdS, CdTe ...) or III–V (e.g., InP, InAs ...) or IV- VI (e.g., PbSe ...) materials. They are robust fluorescence emitters with size-dependent emission wavelengths (Figure 28). These semiconductor materials are characterized by different bulk band gap energies. The range emission wavelength is 400 to 1350 nm, with size varying from 2 to 9.5 nm (Bruchez et.al., 1998; Tsay et.al., 2004; Yu et.al., 2004).

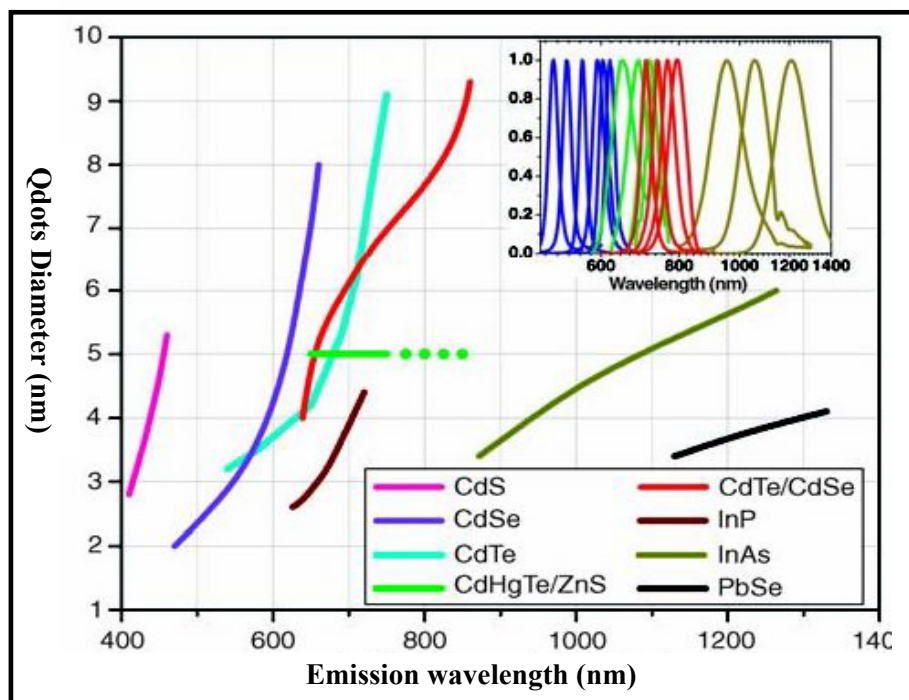


**Figure 28 : Emission maxima and size of QDs of different composition.**

All spectra width are typically around 30 to 50nm. Insert figures: Representative emission spectra for some materials.

*From (Michalet et al., 2005)*

In the early 1980s, the quantum yields of QDs were quite low because of the chemical and photochemical instability as well as the heterogeneous size distribution of nanoparticles (Kuczynski et al., 1983; Weller et.al., 1984; Ramsden and Gratzel, 1984). Such disadvantages were improved by coating the QDs core with a material that has higher bandgap. The bandgap of a semiconductor is the energy of the longest-wavelength absorption. Emission of light from bulk semiconductors is achieved by generating electron-hole pairs or excitons. When the electron and hole recombine, a photon of light is emitted. Excitons can be generated electrically or optically. The energy (wavelength) of the emitted photon is determined by the bulk properties of the material. The exciton has a characteristic dimension known as the Bohr radius; for example, in cadmium selenide the radius is 11.2 nm. If a nanocrystal is smaller than this radius, the “quantum confinement” of the exciton increases, which means that the wavelength of the emitted photon is strongly dependent on the size of the nanocrystal. The energy of the excited state also depends on the material. The use of higher bandgap shell confines the excited state to the centre of the particle. This prevents interactions with the surface (oxidization, chemical reactions ...). This shell can be designed carefully to obtain quantum yields close to 90% (Reiss et.al., 2002); this step also enhances the photostability of QDs by several orders of magnitude relative to conventional dyes (Sukhanova et.al., 2004).

The typical schematics of QDs were shown in Figure 29. Inorganic QDs are consisted of a cadmium selenide (CdSe) core by coating with several layers of zinc sulphide (ZnS) shell

which has a higher bandgap than CdSe. This shell confines the excited state to the centre of the particle to improve the chemical and photochemical stability of QDs. In order to use the nanoparticles in biological systems they need to be water soluble, which is accomplished with a polymer or silica layer. This layer is then used to attach proteins or nucleic acids.

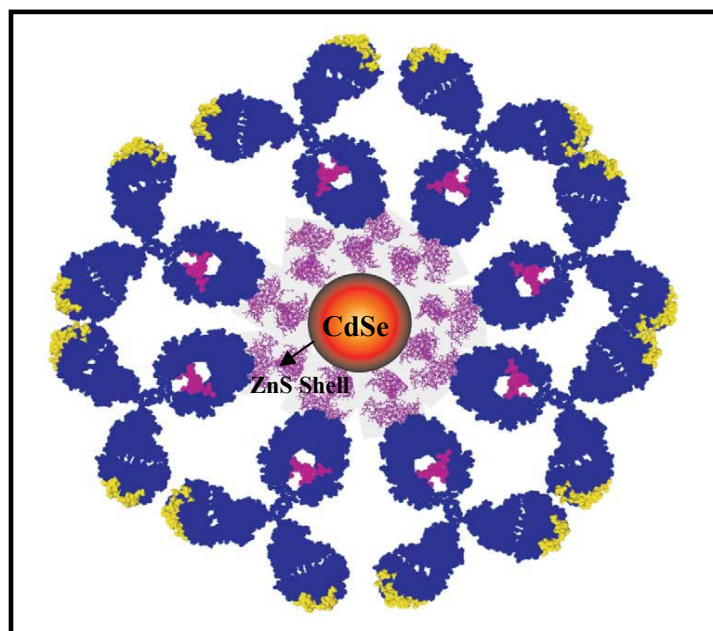


**Figure 29 : Schematic of a core-shell QDs with a biologically compatible surface.**

QDs are inorganic fluorophores and consist of a cadmium selenide (CdSe) core with several layers of a thick zinc sulfide (ZnS) shell to improve quantum yield and photostability. To provide specificity of binding, QDs are conjugated with antibody molecules (blue) by using avidin (purple) or protein A (green) as linkers.

*From (Jyoti & Sanford, 2004)*

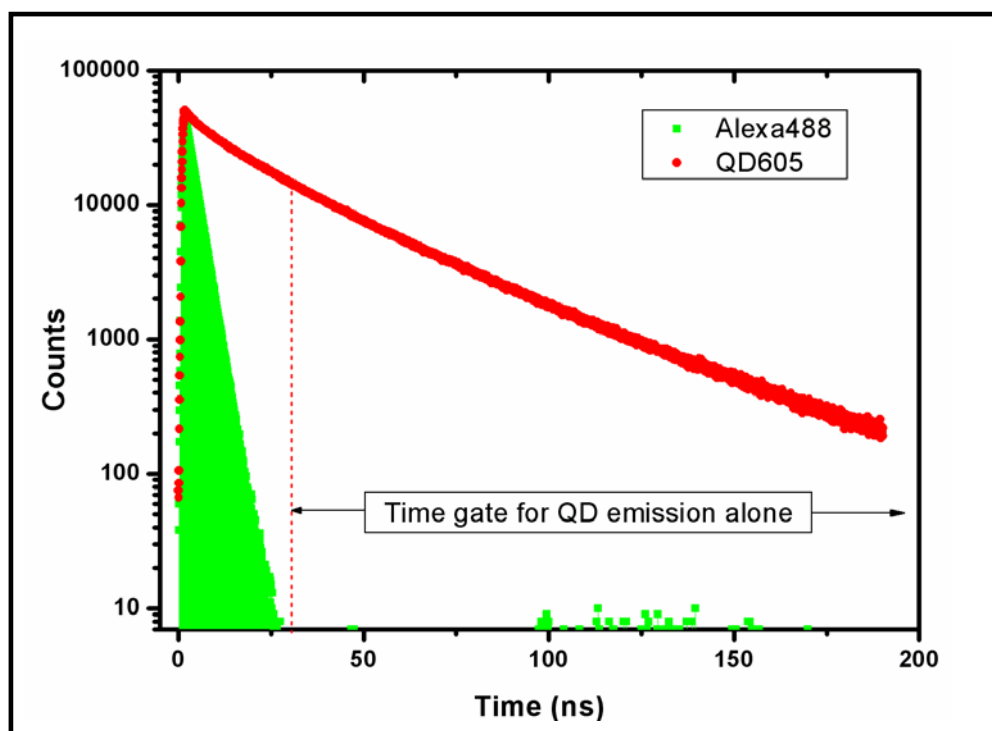


**Figure 30 : Illustration of fluorescence decay.**

The fluorescence decay demonstration of an organic dye-Alexas488 and CdTe quantum dot with mercaptopropionic acid as a stabilizer.

### ***V.1.2 Spectral properties of quantum dots***

Nanocrystals have properties very different from those of organic fluorophores due to their fundamentally different mechanism of fluorescence. Colloidal semiconductor QDs are single crystals a few nanometers in diameter whose size and shape can be precisely controlled by the duration, temperature, and ligand molecules used in synthesis (Alivisatos, 1996). The key features of nanocrystals, particularly with regard to biological applications, are summarized as following:

- **Stability.** Being composed of simple inorganic compounds, nanocrystals are typically very stable. Those with outer shells are particularly resistant to photochemical damage. Because of their minus size, a colloidal suspension of nanocrystals is generally stable and will not precipitate over time. Neither they cannot be sedimented by centrifugation (Reiss et.al., 2002).
- **Emission spectrum.** The emission spectra of homogeneously sized ODs are about twofold more narrow than typical fluorophores (Gerion et.al., 2003). The emission wavelength of a nanocrystal depends on its size and therefore it is tuneable. Additionally, the QDs do not display the long-wavelength tail common to all fluorophore which might interfere with the use of multiple fluorophores for imaging or multi-analyte measurements. Generally the emission spectra of the ODs are roughly symmetrical on the wavelength scale and lack the “red tail”. Therefore QDs are ideal to be used for optical bar codes for multiplexed fluorescence measurements.
- **Excitation spectrum.** An important spectral property of QDs is their broad excitation spectrum (Gerion et.al., 2003). This has advantage that nanocrystals can be excited at any wavelength shorter than the emission peak. It further means that a mixture of nanocrystals with different emission peaks may be excited efficiently by light of a single wavelength, which facilitates simultaneous detection, imaging or quantification for practical multiplex assays. Nanocrystals also emit very bright fluorescence, because they have a high excitation cross section and can also have high quantum yields. Furthermore, it is possible to achieve a large difference between excitation and emission wavelengths, which means that it is much easier to separate the excitation and emission light and reduce background due to scattering (Bruchez et.al., 2003).
- **Fluorescence lifetime.** Nanocrystals have a moderately long fluorescence lifetime in the range of tens of nanoseconds, which is significantly longer than for organic dyes (1-5 ns) or cellular autofluorescence (2-3 ns) as shown in Figure 30. This permits their

fluorescence to be distinguished from other sources of fluorescence in a fluorescence lifetime experiment. For example, Dahan et al., 2001, used time gated imaging to distinguish nanocrystal fluorescence from a background of cellular autofluorescence.

- Surface chemistry. Nanocrystals may be prepared with a wide variety of surface chemistries by exchanging the capping groups. Different QDs solubilization strategies have been devised over the past few years including ligand exchange with simple thiol-containing molecules or more sophisticated ones such as oligomeric phosphines, dendrons, and peptides (Chan and Nie, 1998; Pinaud et al., 2004); encapsulation by a layer of amphiphilic diblock or triblock copolymers or in silica shells, phospholipids micelles, polymer beads, polymer shells (Bruchez et al., 1998; Osaki et al., 2004); and combinations of layers of different molecules conferring the required colloidal stability to QDs (Mattoussi et al., 2000; Sukhanova et al., 2004)

### ***V.1.3 Solubilization and biological applications of quantum dots***

#### ***V.1.3.1 Biocompatibility of quantum dots***

Unique QDs properties in comparison with traditional organic dyes, including size-and composition-tunable emission, broad absorption cross sections, narrow emission spectra, wide absorption profiles, and excellent photostability, make it as a potential candidate in biological applications (Dabbousi et al., 1997; Lim et al., 2003). The core and core-shell of QDs synthesized as described are only soluble in nonpolar solvents because of their hydrophobic surface layer. For QDs to be useful probes for examination of biological specimens, the surface must be hydrophilic. During the past 20 years, most studies were focused on the quantum confinement effect and potential applications in optoelectronics of QDs. There have been no breakthroughs before 1998 when highly luminescent QDs were made water-soluble and became biocompatible by surface modification and bioconjugation (Jaiswal et al., 2003; Goldman et al., 2004).

Generally, to make QDs be solubilized in aqueous buffers, their hydrophobic surface ligands must be replaced by amphiphilic ones. Several solubilization strategies have been proposed over the past few years, including

- Ligand exchange with simple thiol-containing molecules (Chan and Nie, 1998; Pathak et al., 2001). The principle is based on the exchange of hydrophobic surfactant molecules with bifunctional molecules, which are hydrophilic on one side and hydrophobic on the other side. Most often, thiols are used as anchoring groups on the

ZnS surface and carboxyl groups are used as the hydrophilic ends. More sophisticated ones such as oligomeric phosphines (Kim and Bawendi, 2003), dendrons (Guo et al., 2003), and peptides (Pinaud et al., 2004) were also proposed. In this case, the long-term stability of the QDs depends on the bond between thiol- and ZnS which is not strong enough. Therefore, the water solubility of the core-shelled QDs capped in mercaptocarboxylic acids is limited.

- Encapsulation by a layer of amphiphilic diblock (Wu, 2003) or triblock copolymers (Gao et al., 2004) or in silica shells (Bruchez et al., 1998; Gerion et al., 2001). For surface silanization, the primary step of the process involves exchanging the surface ligand with thiol-derived silane so that the trimethoxysilane groups can be cross-linked by the formation of siloxane bonds. During further silica shell growth, other types of silanes can be added to render a different charge and provide functional groups on the surface. Because the silica shells are highly cross-linked, silanized QDs are extremely stable. However, this method is more laborious and the silica shell may eventually be hydrolyzed, its application in biological field is limited.
- Combinations of layers of different molecules conferring the required colloidal stability to QDs (Gaponik et al., 2002; Sukhanova et al., 2004). Instead of exchanging the hydrophobic surfactant, the particles in this case are coated with a cross-linked amphiphilic polymer. The hydrophobic tails of the polymer intercalate with the surfactant molecules and the hydrophilic groups stick out to ensure water solubility of the particle. Nevertheless, the final size of the particles after coating is rather large, for CdSe/ZnS QDs, the diameter is between 19 and 25 nm (Pellegrino et al., 2004), which would place restrictions on many biological applications. Other approaches, such as coating the QDs with phospholipids micelles (Dubertret et al., 2002), polymer beads (Gao et al., 2002), polymer shells (Pellegrino et al., 2004) or amphiphilic polysaccharides (Osaki et al., 2004) were also adopted.
- Recent developments include a promising water-based synthesis method that yields particles that emit from the visible to the near infra-red (NIR) spectrum and are intrinsically water-soluble, however it needs further tests of these particles in biological environments. Presently, large number of potential surface attachment groups can be used to “graft” different functionalities to individual QDs, resulting in multipotent probes. The production of biologically synthesized QDs consisting of CdSe cores coated by natural peptides led us to investigate the peptide-coating approach for the surface modification of QDs. Peptides have the advantage of being

easily customized, and with correct choice of sequence, a single-step surfactant exchange can yield all necessary functions: 1) protect the core/shell structure and maintain the original QDs photophysics, 2) solublize QDs, 3) provide a biological interface, and 4) allow the incorporation of multiple functions. The resulting particles have the excellent colloidal properties, photophysics and biocompatibility, which can easily be tailored or provide additional functionalities. Such functionalities can be improved by molecular evolution, a strategy that has proven extremely powerful for the recognition, synthesis and self-assembly of nanocrystals (Whaley et al., 2000).

### ***V.1.3.2 Potentials of QDots as fluorescent probes in biology***

Over the past few years, application of QDs in most biotechnological fields that use fluorescence has been tested, including DNA array technology, and immunofluorescence assays (Alivisatos, 2004). Meanwhile, in field of cell and animal biology, QDs have been widely utilized for biological imaging and for sensitive multicolour assays of biomolecules *in vitro*. It should be noted a key issue in biomedical applications is the potential toxicity of the quantum dots. Their constituents contain many toxic components, cadmium usually being the most significant. However, the exact toxic mechanisms for QDs in living-cell research have not been well elucidated yet. Anyway, the techniques for using QDs to labelling proteins and cells, and for carrying out long-term live cell imaging has recently drawn great attentions of biologists and will be described below.

#### ***Specific labelling of cells and tissues***

Labelling *in vivo* requires a high degree of specificity because of the abundance of background biomolecules that can generate false positives. Cellular labelling using organic dyes and fluorescent proteins has had great success (Stephen et al., 2001), nevertheless, traditional fluorophores suffer from several problems, such as photo-bleaching, spectral cross-talking and narrow excitation. QDs has the potential to overcome these problems. As demonstrated by Wu et al., (Wu et al., 2003), the QDs labelled cells are brighter and more resistant to photo-bleaching. In fact, organic dyes are often photo bleached and fade by > 90% in less than one minute, whereas the QDs are stable for more than 30 minutes under identical experimental conditions. This result suggests that multi-color QDs could be used to determine the quantitative profiles of molecular targets for single normal or diseased cells. The first attempts to use QDs to labelling proteins in cells employed QDs conjugated to transferrin (Goldman et al., 2002) or phalloidin, an actin-binding molecule (Bruchez, 1998). To label live

cells with transferrin-conjugated QDs, the cells required overnight incubation with the conjugates. By contrast, an incubation of only a few minutes is sufficient for the endocytosis of transferrin-conjugated to organic dyes (Mayor et al., 1993), which indicates either the poor affinity of the QDs conjugate for the transferrin receptor or its non-specific uptake. Thus these early studies lacked the efficacy and specificity of labelling that are requisite for using QDs bioconjugates for live cell studies. These limitations have been overcome by the development of QDs that have superior stability in an aqueous environment and improved surface coatings that minimize non-specific binding to the cell surface and the extracellular matrix, and by using bioconjugation approaches such as avidin-biotin, antibody-antigen and ligand-receptor interactions that provide a high specificity of labelling in fixed and live cells (Dahan et al., 2003; Wu et al., 2003; Lidke et al., 2004).

Generally, QDs tend to be brighter than organic dyes because of the compounded effects of extinction coefficient that are an order of magnitude larger than those of most dyes (Ballou et al., 2004), comparable quantum yield and similar emission saturation levels. The development of these live cell approaches has allowed several groups to use QDs for labelling proteins in live cells, where equally high levels of specificity have been achieved.

The most interesting property of QDs for cell and tissue labelling is immunolabeling owing to their robust optical properties. QDs conjugated to specific peptides and antibodies could provide specific labelling of tissues *in vivo* (Akerman et al., 2002), as well as specific labelling of live bacteria and protist cells (Kloepfer et al., 2003). Such fluorescence immunolabelling is widely used in cell biology to probing structure and locating signal transduction-related molecules. Recently, investigators have performed a variety of experiments in which the QDs have been used to localize molecules in cells and tissues, both in live and fixed specimens. Kaul and his colleagues reported immunofluorescence labeling of the heat shock 70 protein, mortalin, using QDs to show different staining patterns in normal and transformed cells (Kaul et al., 2003). Meanwhile, Tokumasu and Dvorak have taken advantage of the high photostability of QDs and were able to collect 40 consecutive optical sections using confocal microscopy and generated a 3-D reconstructed, high-resolution image of the membrane domain band 3 in erythrocytes (Tokumasu and Dvorak, 2003). Minet and his colleagues examined breast tumor cells, using QDs to label membrane glycoproteins to study heat stress effect (Minet et al., 2004). In addition to specific biomolecular labeling of cells, various generalized approaches are also available for tagging cells with single-color or several different-color QDs (Jaiswal et al., 2003). The specificity and ease of labeling cells with QDs have made it a widely accessible and practical application.

### ***Suitability for cell tracking***

Research of signalling pathways between and within cells also relies heavily on the brightness and sensitivity of fluorophores. Because of the stability and multicolor emission of QDs, such nanoparticles inside cells are particularly useful for cell tracking to study cell division and metastasis. QDs could act as a unique marker for tracking cancer cells *in vivo* during metastasis – a critical issue in the development of effective cancer therapies. Rosenthal et al. reported using serotonin-linked QDs to target the neurotransmitter receptor on the cell surface (Rosenthal et al., 2002). The QDs probes not only recognized and labelled serotonin-specific neurotransmitters on cell membranes, but also inhibited the serotonin transportation in a dose-dependent manner. Although one to two orders of magnitude less potent at inhibiting the receptor than free serotonin, the behaviour of QDs conjugates was similar to that of free serotonin, making QDs a valuable probe for exploring the serotonin transportation mechanism.

Simon and coworkers have taken advantages of QDs and the high resolution of fluorescence after they reported using QDs to simultaneously track different populations of cells in lung tissue (Voura et al., 2004). They combined QDs and emission spectrum scanning multiphoton microscopy to develop a means to study extravasations *in vivo*. The mixture cell culture of two populations of B16F10 cells staining with different QDs (510nm or 570nm emission) did not result in the cells labelled with two colors because of cell division. To examine the cell metastasis in a natural tissue environment, Simon and coworkers injected this mixed population into the tail vein of mouse, extracted and fixed lung tissues, and then used emission-scanning microscopy to distinguish both populations of cells in the whole tissue sample. This elegant example indicates that the use of emission spectrum scanning microscopy may enable simultaneously tracking several different QDs-tagged populations of cells in the same animal.

Other signalling pathways, such as erbB/HER receptor-mediated signal transduction, have also been examined using QDs (Lidke et al., 2004). Epidermal growth factor (EGF) conjugated to QDs is still capable of binding to and activating its receptor, the erbB1 receptor, which triggers internalization of both EGF-QDs and its receptor via endocytosis. In this case, examination of single QDs enabled discovery of a retrograde transport process in which the EGF-QDs, after binding to the filopodium of the cell, moves toward the cell body at a velocity of 10nm/s. Owing to the photostability of QDs, EGF-QDs binding and internalization kinetics were obtained, the latter being the rate-limiting process. Such quantitative

understanding of the transduction mechanism is essential for receptor-targeted therapeutics. QDs will be a valuable reagent for this kind of investigation.

### ***Suitability for long-term imaging and multicolor in vivo imaging***

Organic fluorophores are susceptible to photodamage and to metabolic and chemical degradation, making it difficult to tag cells for long periods. One substitution to surmount this problem is to use genetically encoded organic fluorophores, for example, the fluorescent proteins, which are continuously made and replenished in the cell. However, these fluorophores require up to one day or longer periods for expression after their introduction into cells, which give rise to several pitfalls in field of biology. In addition, the phenomena of photobleaching happened during continuous imaging for fluorescent proteins can cause the similar delays in long-term imaging.

Such limitations can be overcome by the use of QDs, which are resistant to photodamage (Jaiswal et al., 2003; Wu et al., 2003), degradation by enzymes in live cells (Jaiswal et al., 2003) and chemical damage (Voura et al., 2004). Thus, QDs have facilitated the monitoring of molecules in live cells for several hours (Dahan et al., 2003; Lidke et al., 2004), and monitoring cell fate during either a week of growth (Hoshino et al., 2004) or the whole developmental period of an organism (Dubertret et al., 2002; Jaiswal et al., 2003). Colloidal semiconductor nanocrystals have a two-photon cross-section that is two to three orders of magnitude greater than organic dyes (Larson et al., 2003). Therefore, multiphoton microscopy enables the imaging of structures deep within biological tissues with minimum photobleaching and photodamage. The ability to read out many signals simultaneously through the use of multiple, non-overlapping, emission spectra, with a single excitation wavelength is enabling cellular interactions to be examined during development, metastasis, and non-invasive surgeries to be carried out in a way that has not been feasible without QDs.

Larson et al., in 2003 (Larson et al., 2003) has achieved the live animal imaging using QDs fluorescence with multiphoton microscopy. The property of multiplexing for QDs makes them good candidates for biological applications. After being intravenously injected into mice, the QDs were detectable through intact skin at the base of the dermis (~100 micron) using an excitation wavelength of 900nm. To optimize the conditions of *in vivo* experiments, Ballou et al, tested QDs with different polymer coating *in vivo* using various imaging techniques, including light and electron microscopy on tissue sections, and non-invasive whole-body fluorescence imaging. These QDs maintained their fluorescence even after four

months *in vivo*. Therefore, using QDs as *in vivo* probes has a great potential for cancer studies, drug delivery, and non-invasive whole-body imaging.

Furthermore, QDs have facilitated the simultaneous imaging of at least five populations of live cells, each labelled with different colored QDs (Voura et al., 2004). If combinations of different QDs are used to tag cells, then an ability to resolve five colors will enable the resolution of 36 populations of cells. This potential has been recently realized to generate ten unique codes using five different-color QDs (Matteakis et al., 2004). Nowadays, use of QDs offers a significant advantage for studies requiring the simultaneous imaging of multiple fluorophores. This approach has facilitated *in vivo* imaging not only in mice (Larson et al., 2003), but also in big animals such as pigs (Kim et al., 2004).

In summary, colloidal QDs are robust and very stable light emitters and they can be broadly separated simply through size variation. Recently, there has been a development of a wide range of methods for bio-conjugating colloidal quantum dots in diverse areas of application: cell labelling, cell tracking, *in vivo* imaging, DNA detection and multiplexed beads. The use of QDs as biological probes has got significant advances. They will not replace the well-established fluorophores or fluorescent protein-fusion technologies, but will complement them for applications needing better photostability, near-infrared emission, or single-molecule sensitivity over long time scales. Before QDs can find wider use in biological research, several improvements must be made, including alterations of the surface properties that affect their stability in cellular environments, and developing methods for their delivery and efficient targeting in cells, without altering their properties. Although there is much that we still need to understand about these little wonders, it is likely that they will soon become a standard tool for biological applications.

## ***V.2 Multi-exponential Photoluminescence Decay of CdTe Quantum Dots upon One and Two Photon Excitation***

### ***V.2.1 INTRODUCTION***

In the coming decade, the ability to sense and detect the state of biological systems and living organisms optically, electrically and magnetically will be radically transformed by developments in materials physics and chemistry. The emerging ability to control the patterns of matter on the nanometer length scale can be expected to lead to entirely new types of biological sensors. These new systems will be capable of sensing at the single-molecule level in living cells, and capable of parallel integration for detection of multiple signals, enabling a diversity of simultaneous experiments, as well as better crosschecks and controls (Prasad, 2003). Semiconductor QDs with dimensions on the length scale of a few nanometers provide a nearly zero-dimensional system, where carrier confinement occurs in all spatial directions. Such quantum confinement results in the changes of the density of states for both electrons and photons and the mechanisms of electron-hole recombination. The QDs are expected to exhibit high luminescence yield and thermal stability in considering their optical properties, which are mainly due to their  $\delta$ -like density of states and strong quantum confinement (Lacowicz, 2006). Generally, the refractive index and nonlinear optical properties of semiconductor QDs change significantly compared to those of bulk. Compared with the traditional organic fluorophores, semiconductor QDs have the advantages of size and composition tunable photoluminescence (PL), higher quantum efficiency (QE), exceptional photostability and narrow emissions with a broad excitation band. Their novel optical properties make the QDs have considerable applications in photo-electronic devices such as optical switches and lasers (Prasad, 2003). For biological applications, QDs can be coupled to biological molecules such as proteins and DNA, which make the colloidal semiconductor water soluble and can be used as biomedical fluorescence labels for investigating biomolecular interactions and developing high-sensitivity detection and imaging. One important concern in these applications is the dynamic properties of luminescence from QDs, which not only help to gain fundamental insight into the charge carrier properties but also provide information to improve the luminescence yield. In addition, QDs display a cross section efficiency for two photon absorption and Gopper-Mayer coefficient are of two order of magnitude greater than common organic dye (West & Halas, 2003).

In this study, time-resolved photoluminescence decay and spectrometer measurements have been conducted on the mercaptopropionic acid (MPA) capped CdTe QDs, the

recombination dynamics of colloidal CdTe QDs have been studied. The principle of PL decay measurements is based on the technique of time-correlated single-photon counting (TCSPC). The time-resolved PL, using the kinetics of electron-hole recombination as a probe, gives direct information on the luminescence decay mechanism. Most of the previous studies of PL kinetics referred to average lifetime (Shu et al., 2007). The radiative lifetime of photoluminescence is generally supposed to be dominated by a biexponential distribution, consisting of a fast component ( $\sim$  several nanoseconds) and a slow component ( $\sim$  tens of nanoseconds) at room temperature (Sanz et al., 2008).

In our present study, we found that the PL decay detected at the maxima of the ground state transition, were fitted to a multiple exponential function. Maximum entropy data analyse method was adopted in present study, which is based on the principle that the probability distribution of components that maximizes the information entropy is the true probability distribution with respect to the testable information prescribed. The size dependence and temperature dependence of the time-resolved PL properties of the self-assembled CdTe QDs covered by MPA layers were investigated in present study. The influences of the environment in term of pH have also been studied. The absorption spectra were measured with a double-beam spectrometer with a resolution of 0.2nm. For PL measurements, the mode-locked Māitāi Ti:Sapphire tunable laser with 100fs pulse and the power of 80HZ was used to compare the PL decay under one-photon and two-photon excitation conditions. The origins of the fast and slow decays of PL in colloidal CdTe QDs were studied here, and the potential applications for this series of MPA-coated CdTe QDs in biological systems would be discussed.

## ***V.2.2 MATERIALS AND METHODS***

***Preparation of CdTe QDs-*** The quantum dots used in present study was synthesized by the group of Professor Ren Ji-cun at college of Chemistry and Chemical Engineering at Shanghai Jiaotong University at China. The chemicals used were of analytical grade or above. Milli-Q water (Millipore, USA) was used in the preparation of QDs. Cd precursor solutions were prepared by mixing a solution of CdCl<sub>2</sub> ( $1.25 \times 10^{-3}$  M) with mercaptopropionic acid (MPA) solution, and were adjusted to pH 8-9 with 1 M NaOH. This solution was deaerated with N<sub>2</sub>. Under vigorous stirring, oxygen-free NaHTe or NaHSe solution prepared according to the method proposed firstly by Klayman and Griffin (Klayman & Griffin, 1973; Zhang et al., 2003) was injected. The molar ratio of mixture solution was heated to 99-100 °C and refluxed to different time for controlling the size of QDs.

**Preparation of core/shell QDs-** The core/shell CdSe/CdS QDs were prepared using a microwave irradiation method similar to that reported by Li and his colleagues (Li et al., 2005). Water-soluble CdSe QDs were prepared according to the method elucidated in above and were served as the seeds. Then it was placed into a program-controlled microwave digestion furnace (WX-3000, Shanghai Yi-Yao Instruments, Shanghai, China) and heated by microwave irradiation for 60 min at 140 °C. With irradiation of microwave, MPA gradually released sulfide ions into aqueous solution, which leads to the formation of core/shell structure. The As-prepared products were precipitated with 2-propanol to remove free Cd<sup>2+</sup> and MPA as the approach described by Li et al. (Li et al., 2006). The quantum yield of CdTe QDs was up to 50%.

**Cary Eclipse Fluorescence Spectrophotometer-** The UV-vis absorption and emission spectra were recorded on Varian (Cary Eclipse) fluorescence spectrophotometers. The excitation and emission power was adjustable according to the intensity of fluorescence emitted by nanoparticles. When recording the emission spectra, the excitation and emission slits were 5nm and 2.5nm respectively, and changed to 2.5:5 when recording the excitation spectra. The 3x3-mm suprasil microcuvettes were adopted in present study. All the spectra were recorded at room temperature.

**Photoluminescence decay measurements-** The time-resolved emission was obtained using the time-correlated single photon counting technique. The excitation light pulse source was a Ti-sapphire subpicosecond laser (Mai Tai, Spectra Physics, Mountain View, CA) associated with a second harmonic generator tuned at 420 nm. The repetition of the laser was set down to 4 Mhz. Fluorescence emission was detected through a monochromator (SpectraPro 150, ARC,  $\Delta\lambda=15$  nm) by a microchannel plate photomultiplier (Hamamatsu R1564U-06) connected to an amplifier Phillips Scientific 6954 (gain 50). The excitation light pulse was triggered by a Hamamatsu photodiode (S4753). A time-correlated single-photon counting card SPC-430 (Becker-Hickl GmbH, Berlin, Germany) was used for the acquisition of both excitation and fluorescence emission light pulse. The profile of the instrumental response of the laser pulse (30 ps) was recorded by detecting the light scattered by a water solution. In case of two photon excitation, the photomultiplier sensitivity does not allow the detection of excitation profile at 840nm. A TAMRA solution was used as a reference assuming a lifetime of 1.75ns. The time scaling was 59.5ps per channel and 4096 channels were used. The fluorescence decay and the instrumental response profile were alternatively collected during 120 and 10s, respectively. Routinely the total count of the decay reached 10-25 millions. In order to insure a single-photon counting condition, the counting rate never exceeded 1% of the laser

excitation frequency to avoid pile-up effect, if necessary, a neutral density filter was used to attenuate the excitation intensity. The microcuvette (3x3-mm suprasil cuvettes) was thermostated with a Haake type-F3 circulating bath.

**Analysis and interpretation of data-** Analysis of the fluorescence intensity decay  $I(t)$  was performed using the PULSE5 program (MaxEnt Solutions Ltd, Cambridge, U.K.) based on the Quantified Maximum Entropy Method, QMEM (Livesey and Brochon, 1987; Brochon, 1994). Fluorescence decay data were fitted to a sum of discrete exponentials:

$$I(t) = \sum_{i=1}^N h_i(\tau_i) \exp(-t/\tau_i) \quad (1)$$

which approximates the continuous distribution of exponentials. The distribution of fluorescence lifetime probabilities  $h_i(\tau_i)$  is proportional to the number of fluorescing "centres". In case of single organic fluorophores in solution, it is proportional to  $\epsilon_i[M_i] / \tau_{n,i}$ , where  $\epsilon_i$ ,  $M_i$  and  $\tau_{n,i}$  are the molar absorption coefficient, the molar concentration and the natural lifetime of species  $i$  respectively. In case of multichromophore "centres" as in quantum dots, we assume that  $h_i(\tau_i)$  corresponds to the density of emitting atoms at a distance  $R_i$  of the surface.

**Maximum Entropy-** Maximum Entropy is an optimal criterion for reconstructing lifetime distribution  $h(\tau)$  from imperfect data. The general formulation of the entropy for a fluorescence kinetics is only dependent of  $h(\tau)$  :

$$S = \int_0^{\infty} h(\tau) - m(\tau) - h(\tau) \log \frac{h(\tau)}{m(\tau)} d\tau \quad (2)$$

In this expression,  $m$  is a measure, usually taken to be flat in logarithmic space, which quantifies the relative importance of the various "pixels".  $S$  measures the deviation of the distribution  $h(\tau)$  from this measure, attaining its global maximum of zero when  $h(\tau)$  is equal to  $m(\tau)$ . Because  $S$  is maximized by distributions which are as close as possible to the uniform and featureless (in log. space) measure  $m$ , maximum entropy uniquely gives the most probable reconstruction: there must be evidence in the data for any structure seen in a maximum entropy reconstruction. Suitably normalized,  $S$  is also minus the information content of  $h(\tau)$ , so that maximum entropy affords a uniquely comprehensible reconstruction, having only that minimum of information which is required to fit the data.

The program set up a statistic which measures the misfit between the actual (noisy) data  $D_k$  and the calculated data  $T_k$  which would be observed (in the absence of noise) if the actual distribution were correctly represented by the particular numbers  $h_i$ .

It is usual to use the normalized chi-squared value as a fit statistic.

$$\chi^2 = \frac{1}{M} \sum_{k=1}^M \frac{D_k - T_k}{\sigma_k^2} \quad (3)$$

where  $\sigma_k$  is the standard deviation of the  $k^{\text{th}}$  datum. On average, each datum should lie about one standard deviation from its calculated value, so that the normalized residuals should have unit variance and  $\chi^2$  should be close to unity. However, very many distributions remain which can fit an incomplete or noisy data set to the correct precision and very close value of  $\chi^2$ , each of which is consistent with the data, and most of which tend to be alarmingly irregular. The maximum entropy principle is appropriate to distinguish among these in a consistent way. One selects that single consistent distribution  $h(\tau)$  which has greatest entropy (or, more strictly, greatest generalized cross-entropy) leading to the best posterior probability distribution. Statistics from a Gaussian approximation around this optimum solution allows calculating error bars on some parameters of interest: peak surface, peak width and peak position (Gull, 1989; Skilling, 1991). In general, the distribution being sought is represented by set of "pixels" numbers  $h_i$  ( $i=1,2,\dots,N$ ) proportional to the numbers of fluorescing centres with decay time  $\tau_i$ . These numbers are to be inferred from the observed data  $D_k$  ( $k=1, 2, \dots, M$ ). It is clear that the digitalization of the fluorescence decay in  $M$  data points (in linear space) as well as the lifetime domain in  $N$  points may influence the final shape of the recovered lifetime distribution. Therefore we choose to use a large value of  $N$ , particularly if the lifetime domain to explore spans over several decades.

In the recovered distribution of discrete lifetime peaks, the centre  $\tau_j$  of a single resolved peak ranging from  $l^{\text{th}}$  lifetime to  $m^{\text{th}}$  lifetime is defined as:

$$\tau_j = \frac{\sum_{i=l}^{i=m} h_i(\tau_i) \tau_i}{\sum_{i=l}^{i=m} h_i(\tau_i)} \quad (4)$$

and its corresponding relative contribution  $c_j$  to the decay is:

$$c_j = \frac{\sum_{i=l}^{i=m} h_i(\tau_i)}{\sum_{i=1}^{i=n} h_i(\tau_i)} \quad (5)$$

On the contrary to the "historic" maximum entropy method (Livesey et al. 1987), the quantified method does not use anymore the  $\chi^2$  statistic criteria as a second selector to select the "best distribution" of a family of solutions but the most probable of a complete family of possible solutions. It ends with a complete probability distribution of solutions surrounding the maximum entropy possible value taking into account a Gaussian noise on data. This allows error bars to be calculated (Gull, 1989; Skilling, 1991).

In practice, 300 equally spaced values on the  $\tau$  logscale, between 0.05ns and 200ns were used. Since we have no prior information about the number, positions and relative importance of lifetimes before running the data analysis, all 300 lifetimes have the same prior probability and the program starts with a flat distribution. After a data noise estimate, the program iterates down the entropy trajectory in optimizing the posterior inference. A termination criteria is in action when the computed probability family of solution appears to be sufficiently close to correct i.e. the optimal probability is reached indicating that the algorithm should be stopped (Skilling, 1989; Gull, 1989).

### ***V.2.3 RESULTS***

The hydrodynamic diameters of MPA-coated CdTe QDs have been measured using Fluorescence Correlation Spectroscopy (Dong et al., 2006) and ranges from 2.0 to 5.5 nm. Individual CdTe QDs display non-blinking behavior and rather good stability in aqueous solution (He et al., 2006).

#### ***Displacement of emission spectra depends on the quantum dots size***

Cary Eclipse fluorescence spectrophotometer was used in present study to measure the emission spectra of QDs in a varied size. Our emission spectra exhibit a dependence on the QDs size: the intensity maxima of emission bands are shifted toward longer wavelengths when the QDs size is increased. As an example, Figure 1A,B presented the absorption and emission spectra for 2.4 and 4.9nm size QDs respectively. It was clearly noticed that the excitonic absorption peaks were centered at 527 and 627 nm for 2.4 and 4.9 nm diameter nanoparticles, respectively. The emission peaks were also shifted from 550 to 650 nm to the direction of longer wavelength. The result is a consequence of quantum size confinement. In addition, for QDs with a diameter of 2.1 nm, two observable emission peaks were found in present study with the primary one at 526nm and the minus one at 612 nm. PL decay analysis was carried out afterward to better understand such abnormal emission spectra. In combination the emission and absorption spectra for all the QDs, a significant size-dependence for the spectra displacement was observed (Figure 4).

#### ***Photoluminescence decay depends on the quantum dots size***

The PL decays of CdTe quantum dots in water at 20°C upon 2PE do not correspond to single or double exponential kinetics but can be fitted by a sum of five exponentials. There is no evidence for a broad continuous distribution of lifetime in any sample. However the time-resolved PL is clearly changing with the size of the nanoparticle, as shown in Figure 2 the decay becomes faster as the size of the particle decreases. Similar result was already obtained

by research group of Rogach (Rogach et al., 2007) without detailed analyses of the PL decays. The corresponding parameters of our data analysis are given in Table 1. Except the shortest lifetime ( $\tau_1$ ) all other four lifetimes and their corresponding relative contributions are changing with the size, notably the long component. The two longest components  $\tau_4$  and  $\tau_5$  and their relative amplitudes increase with size. On the contrary, the intermediate lifetime  $\tau_2$  and  $\tau_3$  decrease. On the whole, the average lifetime increases linearly with the size of the nanocrystal as show in Figure 3. However there is no good linearity between size and increase of long lifetime  $\tau_4$  and  $\tau_5$ . Since there is a relationship between the size and the corresponding fluorescence emission of QDs, PL decays were measured through the emission band. For the four largest particles under study there is no difference, within the present measurement and analysis accuracies, in PL decay through their emission peak band (data not shown). Nevertheless emission spectrum of small QDs, either CdSe or CdTe, displays a small shoulder at longer wavelength. For example, the small particle of 2.1 nm displays such a shoulder (Figure 4). The measurements of PL decay at 515 nm and 612nm corresponding to the “blue” part in the main emission peak and to the shoulder respectively, evidently displayed different decays (Figure5 and Table 2). Again except  $\tau_1$ , all lifetimes are larger at longer wavelength. We may reasonably assume that the shoulder corresponds to a very small amount of larger particles or aggregates.

Obviously, the origin of multiexponential PL decays in colloidal CdTe QDs remains an open question. First, people do not know clearly whether the recombines supposed to obey to a first order kinetics. Second, migration of charge toward the surface corresponding to a non radiative process is not well understood. Third, heterogeneity of the particle surface and symmetry in the particle shape (even without the size heterogeneity itself) are supposed to play a role in the complexity of the PL decay. It is already known that surface defects play an important role in the de-excitation, which may partly explained results in our study for small QDs. In previous studies, related PL decay measurement of QDs suffered from technical limitations. If the decay span is limited, the long lifetime correspond are not enough taken into account and therefore the average lifetime was estimated at a shorter value. Otherwise, the lack of accuracy in measuring PL decay (either low counting statistics or poor time resolutions) results in missing the detection of short lifetime and therefore in overestimation of the average lifetime. Taking advantage of the accuracy of TCSPC measurement over a large time domain and the powerful capability of the MEM of data analysis we detect a rather complex kinetics of CdTe quantum dots.

### ***PL decays upon one and two photon excitation***

Next, we conducted the PL decay measurements for the series of MPA-capped CdTe QDs (diameters varied from 2.1 to 5.5) under both one-photon and two-photon excitations. Results indicated that there is no marked difference in PL decays of CdTe QDs coated with mercaptopropionic acid in water upon one or two photon excitation as illustrated in Figure 6A. Only a slight difference appears on the smallest particle of 2.1nm in diameter (Figure 6B), with the PL decay profile under two-photon excitation displaying shorter lifetime in comparison with that under one-photon excitation. This small PL decay difference for QDs in diameter of 2.1 nm could be attributed to the abnormal emission spectra obtained through fluorescence spectrophotometer. Altogether these data, we can conclude the excitation mode (one-photon and two-photon excitation) had no significant influence on particle lifetime distribution during the PL decay measurements.

### ***Influence of the environment on the PL decay***

PL lifetime is a key parameter for fluorescent QDs in use for FRET measurement in aqueous medium, particularly in biology. Because of the large surface-to-volume ratio of QDs, their quantum efficiency is sensitive to surface states, especially in the case of colloidal QDs passivated with organic ligands. It was reported (Zhang et al., 2008a) that the acidic environment would cause the detachment of surface ligands from the semiconductor core, which would destroy the passivation of QDs and cause the formation of surface defects. These surface defects would enhance the nonradiative decay, thus leading to the reduction of PL quantum efficiency and shortening of PL lifetimes. Recently, the PL lifetimes have been measured of thiol-capped CdTe QDs in some water solution at different pH (Zhang et al 2008b) and in biological medium (Zhang et al., 2009) but only average lifetimes were reported. The authors demonstrated the strong influence of the environment on quantum efficiency, and a lifetime was found to be 80 ns at pH 7 and 18ns at pH 3. Addition of Lysine at neutral pH causes a drop in the lifetime to 63ns. As reported previously (Diaz et al. 1999; Susa et al. 2006), electronic couplings of ions with the electrons in the conduction band of excited semiconductor QDs would create nonradiative pathways for the recombination of photoexcited charge carriers.

For comparison, the PL lifetimes of the largest QD (4.9nm) in aqueous solutions with different pH (from 2.85-9.2) were measured at 20°C in our study. Data were illustrated in Table 3. Surprisingly, the PL decays of CdTe QDs in aqueous solution containing 50mM Tris can be satisfactorily fitted by only a sum of three exponential at pH 7 and 9 and by a sum of 4 and 5 exponentials at acidic pH, 5.5 and 2.85 respectively. At all pH measurement groups,

the relative contribution of a long lifetime, close to 60ns, remains almost constant as well as the contribution of lifetimes smaller than 0.6 ns. At acidic pH the short component was split into two lifetimes of lower value indicating an increase of the role of non radiative processes. We notice that the long lifetime  $\tau_5$  is close to the single lifetime value previously obtained by Zhang et al. but we did not detect a decrease of the average lifetime with pH.

#### ***Influence of temperature on PL decay***

The temperature adopted in present study to evaluate its influence on PL decay of CdTe quantum dots in aqueous solution was limited to those used commonly in use for biological studies. An example of variation of PL decay parameters is shown in Figure 7 and Table 4. The temperature has a limited effect on the average lifetime. The shortest lifetimes and their relative contributions are not markedly affected by temperature only the long components play a major role in the change of the decay profile. Similar results have been obtained for larger particles (data not shown).

### ***V.2.4 DISCUSSION AND CONCLUSION***

In this study, we reported the time-resolved photoluminescence transients of MPA-capped CdTe nanoparticles in aqueous solutions. According to the results, there is no sensible difference in PL emission in water upon one or two photon excitation, which confirmed the feasibility in our present study using two-photon excited measurement.

The size-dependent emission spectra displacement was observed in present study. Similar phenomenon has been observed in previous report where the dynamics of thioglycolic acid-capped CdTe nanoparticles were studied (Sanz et al., 2008). The spectra properties for 3.1nm and 3.6nm thioglycolic acid-capped CdTe QDs were studied by Sanz and others, they found that the intensity maxima of absorption and emission bands are shifted toward shorter wavelengths when the QD size is decreased. This finding is consistent with our present study in considering of MPA-capped CdTe nanoparticles. These global Stokes shifts could be explained either in terms of strong electron-photon interaction or by the presence of localized states (surface and/or defect) involved in the band-edge emission.

It has been confirmed that the PL decay are also dependent on the size of QDs. Previous report on luminescence properties of thiol-capped CdTe QDs in water shows that an increase in particle size drastically reduces the short component and a single-exponential decay yielding a fluorescence lifetime of 145ns has been recorded for MPA-capped CdTe QDs (diameter ~6nm) (Rogach et al., 2007). This observation is explained in terms of stabilized Te-related traps relative to the valence band position of the CdTe nanoparticles. Here we

observed multi-exponential decays for the MPA-capped CdTe QDs with a diameter varied from 2.1nm to 5.5nm. We observed that except the shortest lifetime ( $\tau_1$ ) all other four lifetimes and their corresponding relative contributions are changing with the size, notably the long component. On the whole, the average lifetime increases linearly with the size of the nanocrystal as show in Figure 3. The shortest component is assigned to radiative depopulation due to band-edge recombination of to e-h recombination at the surface (El-Sayed, 2004). The two longest components  $\tau_4$  and  $\tau_5$  and their relative amplitudes increase with size. On the contrary, the intermediate lifetime  $\tau_2$  and  $\tau_3$  decrease. This result agrees with that observed using different capping agents, such as thiol-capped CdTe (Sanz et al., 2008). However, it does not agree with the report by Rogach and his colleague, which shows an increase in the ns lifetime with the size of the particle, and where longer lifetimes, up to 145ns, have been observed (Rogach et al., 2007). These differences reflect the effect of a small experimental-condition change in the preparation of larger nanoparticles, and which controls thermodynamics and kinetics of growth. In our case, rate constants of non-radiative processes due to deep traps increase with the size of the QDs.

In practice, the long average lifetime displayed in water soluble CdTe QDs made them a proper candidate for FRET experiment in biology. Nevertheless reducing particle size to make it comparable to protein dimension, leads to low average lifetime. Whatever the size, the PL kinetics remains complex making the interpretation of FRET data difficult as it has already shown with CdSe QDs involved as energy transfer donor to an organic dye (Fernandez-Agüelles et al., 2007). The PL kinetics is strongly dependent of the solvent molecules which interact with the surface of the QDs. Our results also show that amine salt make the PL decay much slower and less complex than in pure water whatever the pH is between 3 and 9. Leitao and his colleagues have studied the influence of environmental pH on the multiway chemometric decomposition of excitation emission matrices for fluorescence of CdTe QDs (Leitao et al., 2008). They described the pH-induced fluorescent intensity variations of QDs and clarified the pH of the media where the QDs are dispersed affects critically their fluorescence properties. Such pH-induced influence was confirmed in our present study by measuring the PL decay. Under practical applications where quenching or enhancement of fluorescence is being measured, the pH-induced variations can be observed by PL decay assays concerning lifetime changes with pH, which is more reliable for measurements concerning fluorescence intensity.

Furthermore, we proposed that the PL decays of CdTe QDs are not sensitive to temperature commonly used in biological studies in this study. Existed studies related with

temperature effects were most focused on the extreme temperature. For example, Lee and his group member have reported the decay of PL intensity for colloidal CdSe/ZnS QDs. They declare that at 9K, PL decay curve can be best fitted by a biexponential function, indicating a fast component (~1ns) and a slow component (~6.3ns). As the increase of temperature, from 9K to 300K, the slow component remains constant, however, the fast component decreased as the increase of temperature (Lee et al., 2005). In combination our present study with that have been reported, we suggest that the different components consisting in PL decay process involve the recombination of the delocalized carriers and the localized carriers respectively.

### ***V.2.5 PROSPECTIVE***

Present study only generally characterized the fluorescence properties of MPA-capped QDs nanoparticles. The improved synthesis of water-stable QDs, the biological applications of biocompatible QDs, and the mathematic model are still need to be progressed. In detail, the following aspects would be taken more attention:

- Further chemical studies to test different passivation molecules and surface treatments in order to improve PL kinetics.
- Establishing the model for recombination kinetics in nanoparticle where thousands of atoms are involved in the charge migration and the shape smoothness.
- Setting up new theoretical kinetics models which can fit the data as well as a sum of many exponentials.
- Improving the conjugation of QDs to specific biomolecules
- Introducing the QDs into the research in biological domain

### ***V.2.6 FIGURES AND LEGENDS***

**Figure 1: Illustration of size-dependent absorption and emission spectra of MPA-capped CdTe QDs** – Room temperature UV-vis absorption and Eclips emission spectra of a neutral aqueous solution of CdTe nanoparticles was observed. **(A)** QDs with a diameter of 2.4nm; **(B)** QDs with a diameter of 4.9nm. The red line stands for absorption spectra; Black line stands for emission spectra

**Figure 2: Illustration of MPA-capped CdTe QDs size-dependent Photoluminescence decay**– **(A)** The PL decay profiles of colloidal CdTe/MPA QDs with the size of diameter varied from 2.1nm to 5.5nm was monitored at room temperature under two-photon excitation. **(B)** two-

photon excited lifetime distribution for the same QDs. Corresponding data analysis was carried out by Maximum Entropy Method.

**Figure 3: Illustration of size-dependent average lifetime for MPA-capped CdTe QDs with a diameter of 2.1nm-** Measurements were carried out under two-photon excitation at room temperature.

**Figure 4: Emission spectra for MPA-capped CdTe QDs with a diameter of 2.1nm-** This small particle displays two shoulders with the big one at 526nm and the small one at 612 nm.

**Figure 5: Photoluminescence decay measurements for MPA-capped CdTe QDs with a diameter of 2.1nm** – The measurement was carried out under two-photon excitation with the emission wavelength at 515nm and 612nm respectively. The PL decay profile was totally different under 1-PE and 2-PE for the same QDs.

**Figure 6: Illustration of PL decay profile for MPA-capped CdTe QDs under 1-PE and 2-PE conditions-** (A) QDs with a diameter of 3.0nm; (B) QDs with a diameter of 2.1nm.

**Figure 7: Illustration of temperature-dependent effects for MPA-capped CdTe QDs with a diameter of 2.1nm-** The measurements were carried out under two-photon excitation at the temperatures 5°C, 20°C and 33°C respectively. (A) The PL decay profiles of colloidal CdTe/MPA QDs. (B) two-photon excited lifetime distribution for the same QDs. Corresponding data analysis was carried out by Maximum Entropy Method.

**Table 1: ps-ns emission decays of MPA-capped CdTe nanoparticles in water at different wavelength of observation-** Values of time constants ( $\tau_j$ ) and normalized (to 100) relative contribution to the decay ( $c_j$ ) were illustrated by fitting from the Equ.4 and Equ.5 respectively. Multi-exponential fitting was processed here.

**Table 2: ps-ns emission decays of MPA-capped CdTe nanoparticles in diameter of 2.1nm under 2-PE-** Values of time constants ( $\tau_j$ ) and normalized (to 100) relative contribution to the decay ( $c_j$ ) were illustrated by fitting from the Equ.4 and Equ.5 respectively. Multi-exponential fitting was processed here.

**Table 3: *Environment influences on the ps-ns emission decays of MPA-capped CdTe nanoparticles in water***– Values of time constants ( $\tau_j$ ) and normalized (to 100) relative contribution to the decay ( $c_j$ ) was illustrated by fitting from the Equ.4 and Equ.5 respectively. Multi-exponential fitting was processed here. The QDs with the size of 2.7nm was used here.

**Table 4: *Temperature-dependent effects on the ps-ns emission decays of MPA-capped CdTe nanoparticles in water***– Values of time constants ( $\tau_j$ ) and normalized (to 100) relative contribution to the decay ( $c_j$ ) was illustrated by fitting from the Equ.4 and Equ.5 respectively. Multi-exponential fitting was processed here. The QDs with a size of 2.1nm was used here.

**Figure 1**

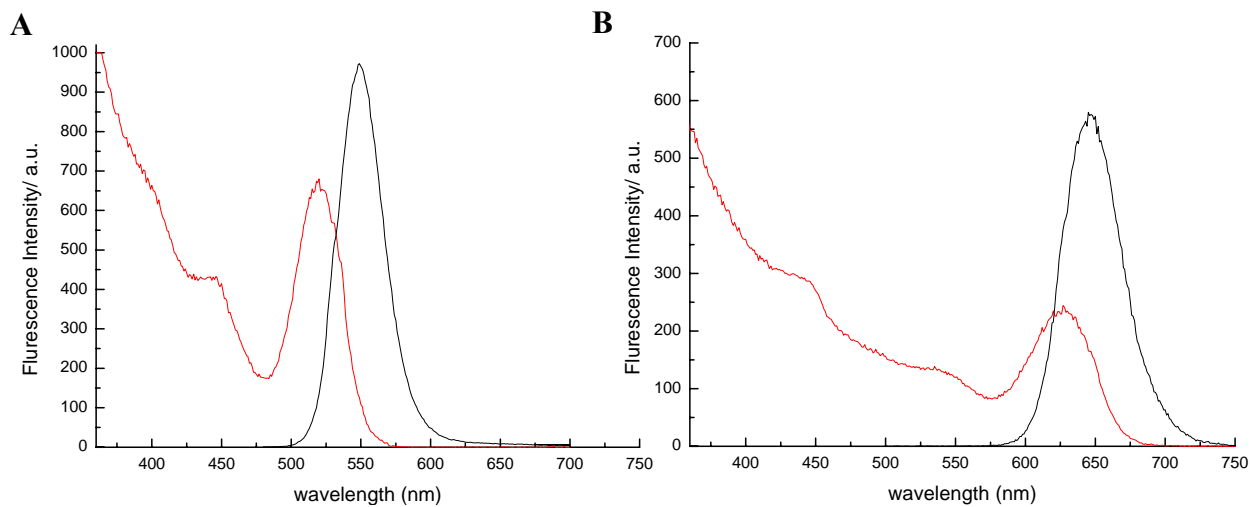


**Figure 2**

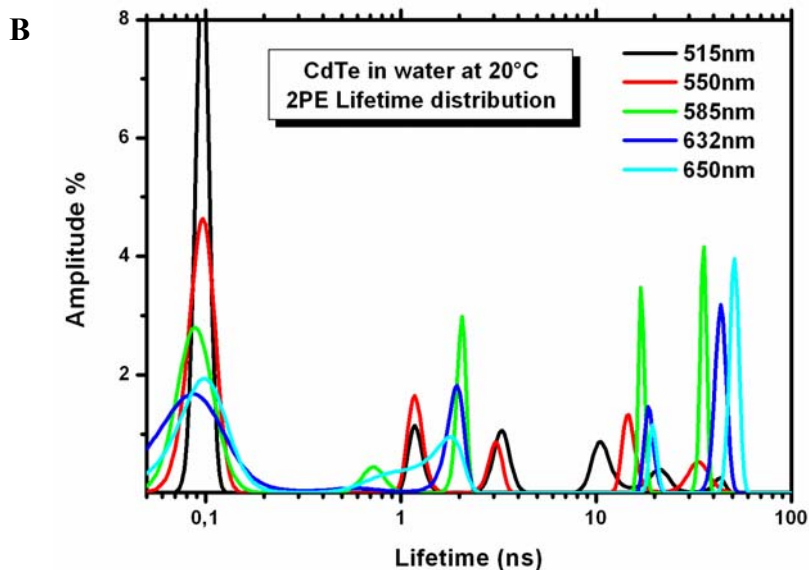
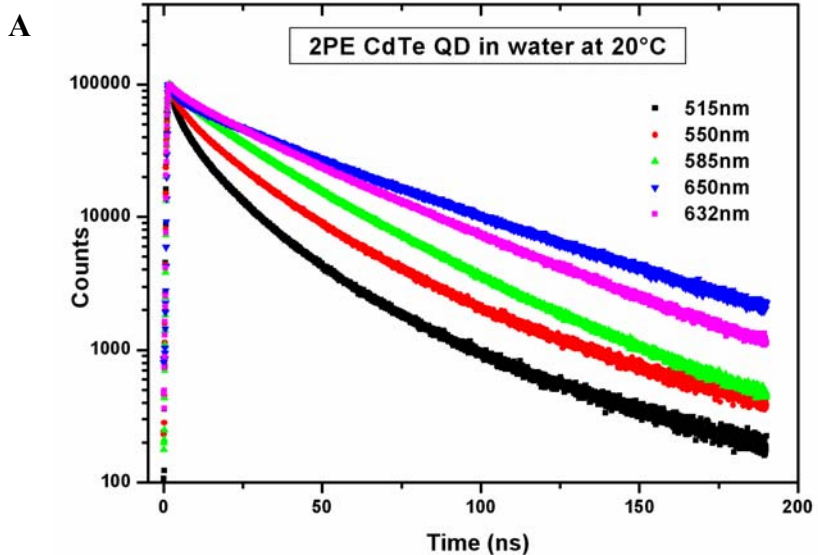


Figure 3

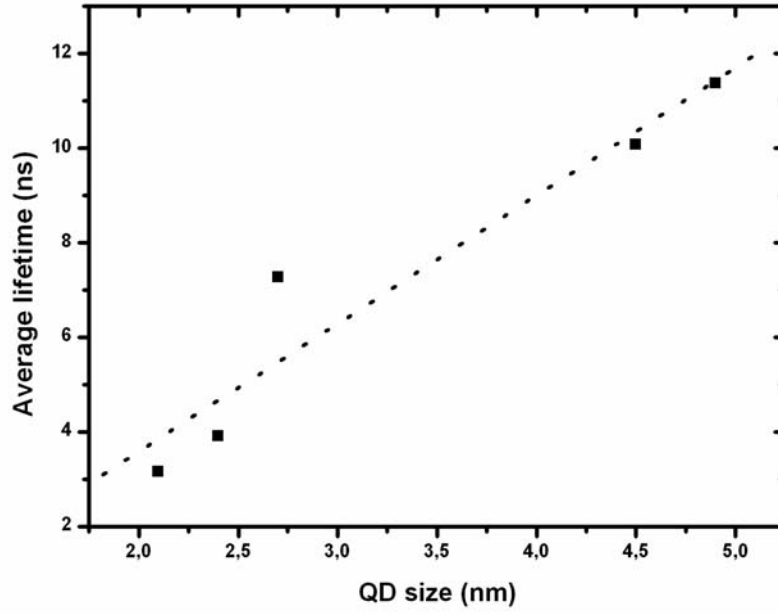


Figure 4

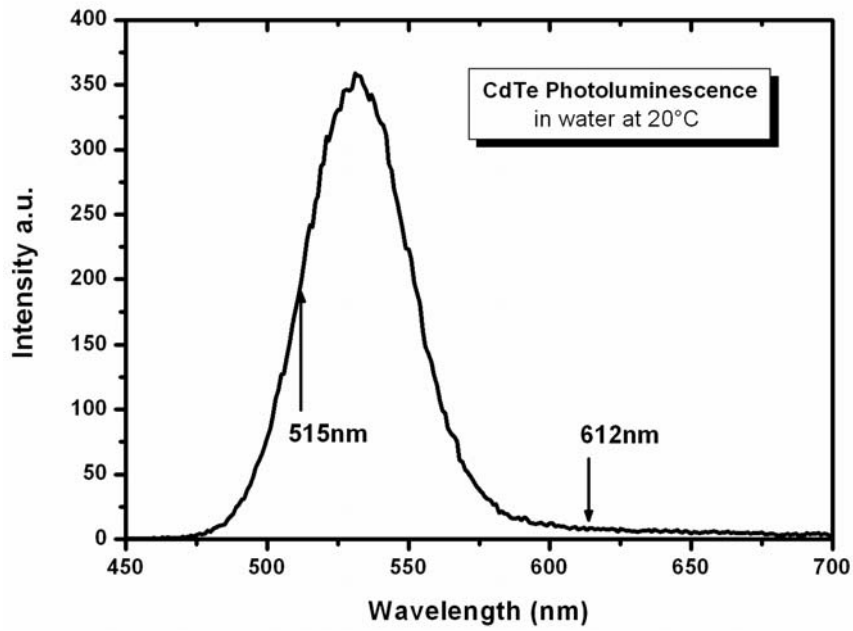


Figure 5

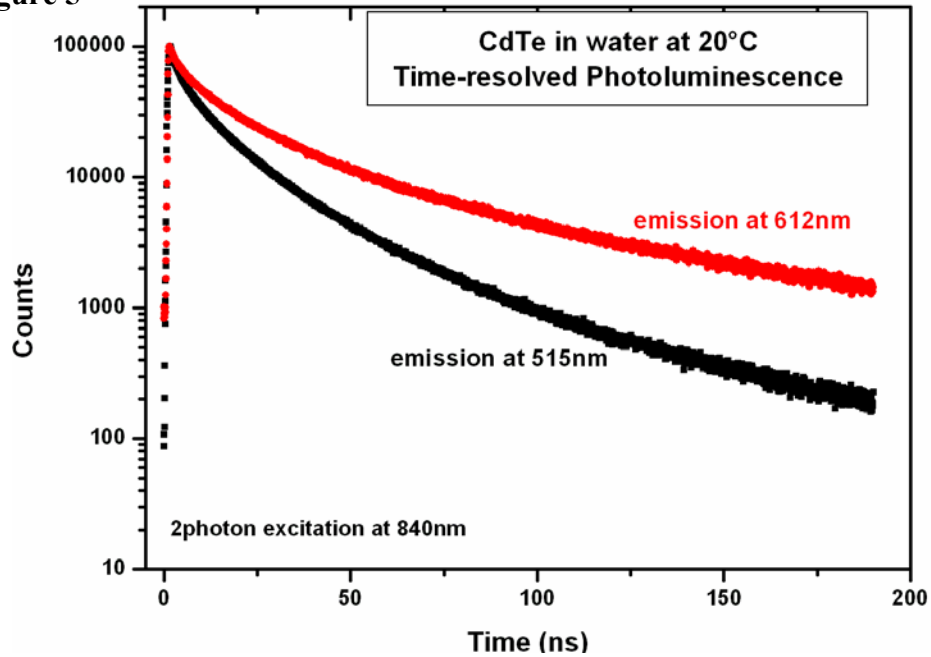
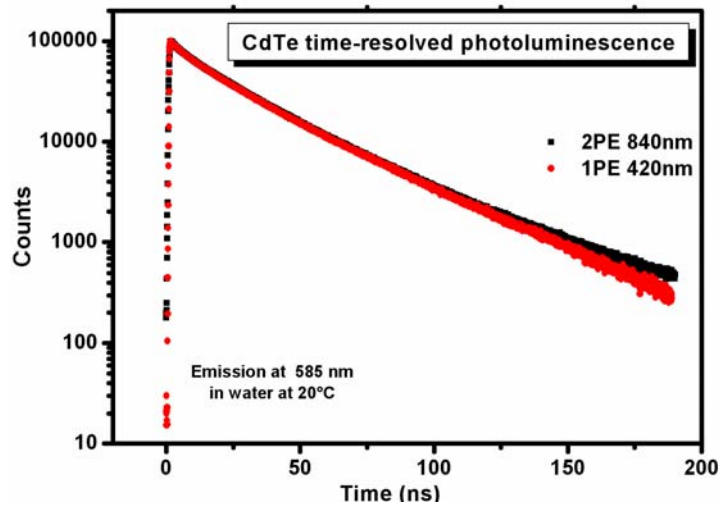


Figure 6

A



B

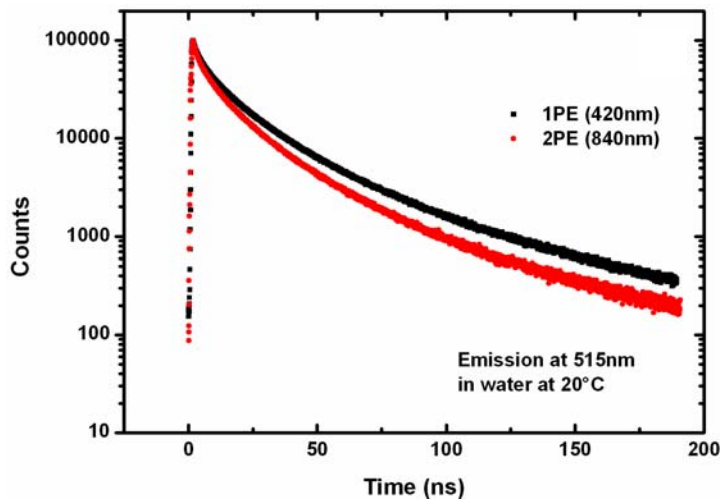
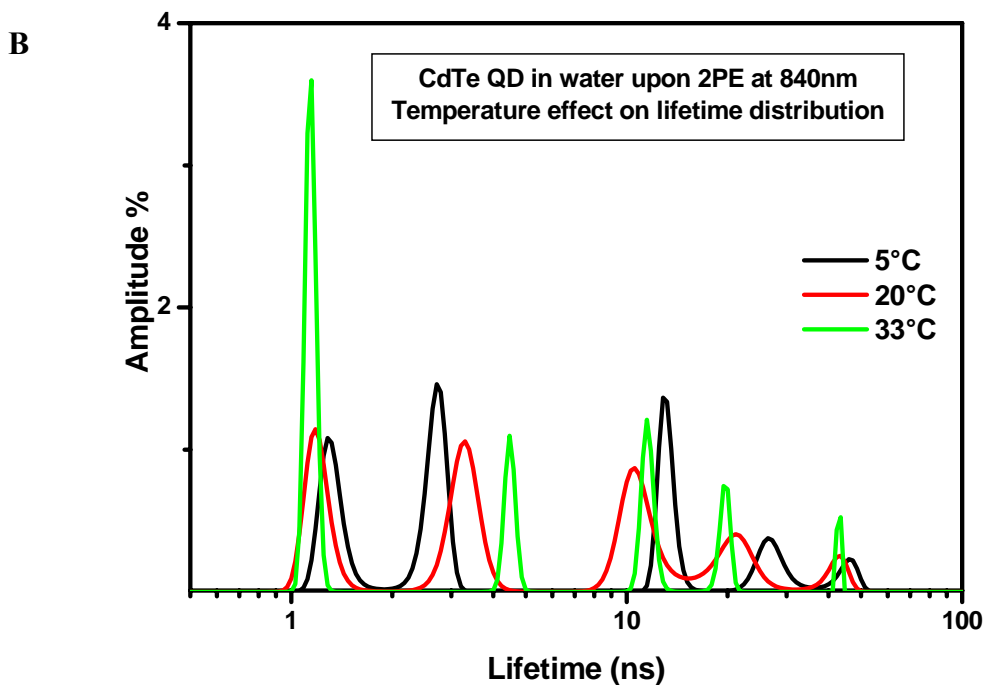
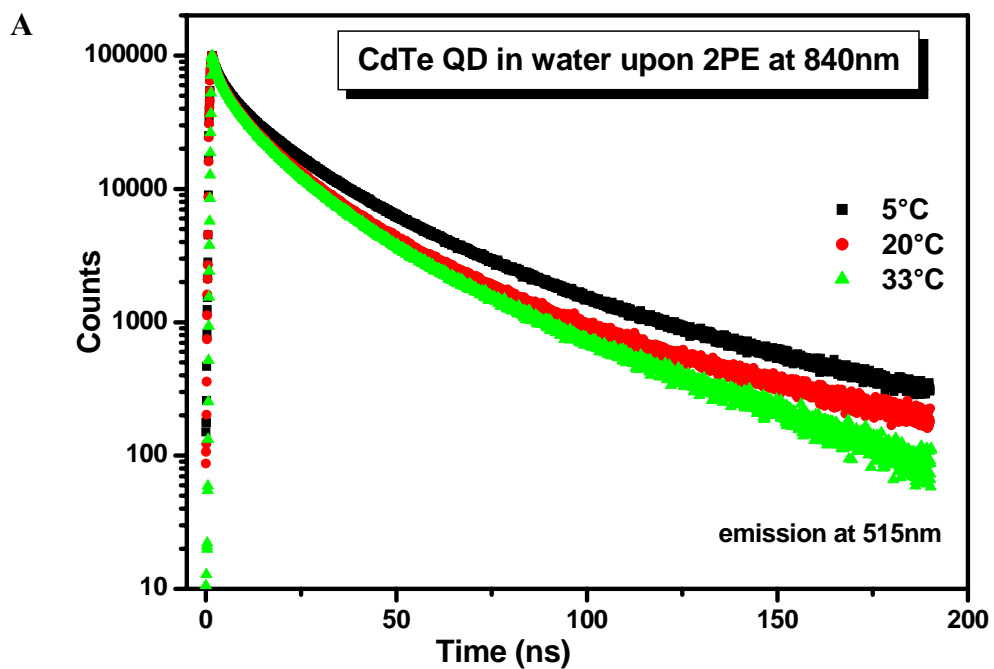


Figure 7



**TABLE 1:**

<b>QD Diameter (nm)</b>	<b><math>\lambda_{Emi}</math> (nm)</b>	<b><math>\tau_1</math> (ns)</b>	<b><math>c_1</math> (%)</b>	<b><math>\tau_2</math> (ns)</b>	<b><math>c_2</math> (%)</b>	<b><math>\tau_3</math> (ns)</b>	<b><math>c_3</math> (%)</b>
2.1	515	0.096	66.4	1.203	8.6	3.282	9.5
2.4	550	0.096	64.9	1.199	13.2	3.029	6.4
2.7	585	0.091	54.6	0.725	5.5	2.034	14.9
4.5	632	0.097	54.3	0.600	2.4	1.868	16.8
4.9	650	0.100	50.8	---	---	1.399	24.8
<b>QD Diameter (nm)</b>	<b><math>\lambda_{Emi}</math> (nm)</b>	<b><math>\tau_4</math> (ns)</b>	<b><math>c_4</math> (%)</b>	<b><math>\tau_5</math> (ns)</b>	<b><math>c_5</math> (%)</b>	<b><math>\langle\tau\rangle</math> (ns)</b>	<b>chi2</b>
2.1	515	10.890	9.0	21.090	4.8	3.160	1.355
2.4	550	14.940	9.3	33.860	6.2	3.910	1.185
2.7	585	17.120	10.8	35.410	14.2	7.280	1.212
4.5	632	18.790	7.3	43.370	19.2	10.070	1.026
4.9	650	19.620	4.7	50.930	---	11.370	1.053

**TABLE 2:**

<b><math>\lambda_{Emi}</math> (nm)</b>	<b><math>\tau_1</math> (ns)</b>	<b><math>c_1</math> (%)</b>	<b><math>\tau_2</math> (ns)</b>	<b><math>c_2</math> (%)</b>	<b><math>\tau_3</math> (ns)</b>	<b><math>c_3</math> (%)</b>
515	0.096	66.4	1.203	8.6	3.282	9.5
612	0.101	57.1	1.428	21.5	4.209	4.8
<b><math>\lambda_{Emi}</math> (nm)</b>	<b><math>\tau_4</math> (ns)</b>	<b><math>c_4</math> (%)</b>	<b><math>\tau_5</math> (ns)</b>	<b><math>c_5</math> (%)</b>	<b><math>\langle\tau\rangle</math> (ns)</b>	<b>chi2</b>
515	10.890	9.0	21.090	4.8	3.160	1.355
612	15.250	10.3	42.880	6.4	4.870	1.053

**TABLE 3:**

<b>pH</b>	<b><math>\tau_1</math> (ns)</b>	<b><math>c_1</math> (%)</b>	<b><math>\tau_2</math> (ns)</b>	<b><math>c_2</math> (%)</b>	<b><math>\tau_3</math> (ns)</b>	<b><math>c_3</math> (%)</b>
2.85	0.06	31.4	0.216	6.0	3.036	5.4
5.53	---	---	0.469	5.1	6.155	11.0
7.00	---	---	0.504	4.9	---	---
9.20	---	---	0.549	4.6	---	---
<b>pH</b>	<b><math>\tau_4</math> (ns)</b>	<b><math>c_4</math> (%)</b>	<b><math>\tau_5</math> (ns)</b>	<b><math>c_5</math> (%)</b>	<b><math>\langle\tau\rangle</math> (ns)</b>	<b>chi2</b>
2.85	20.080	10.7	60.340	46.4	30.390	1.104
5.53	21.250	6.4	59.290	42.1	26.610	1.241
7.00	18.880	6.8	59.720	44.6	28.190	1.359
9.20	15.580	5.6	58.670	48.7	29.680	1.233

**TABLE 4:**

<b>Temperature (°C)</b>	<b><math>\tau_1</math> (ns)</b>	<b><math>c_1</math> (%)</b>	<b><math>\tau_2</math> (ns)</b>	<b><math>c_2</math> (%)</b>	<b><math>\tau_3</math> (ns)</b>	<b><math>c_3</math> (%)</b>
5.0	0.128	71.8	1.326	7.6	2.693	9.4
20.0	0.096	66.4	1.203	8.6	3.282	9.5
33.0	0.050	75.6	1.143	12.6	4.484	3.7
<b>Temperature (°C)</b>	<b><math>\tau_4</math> (ns)</b>	<b><math>c_4</math> (%)</b>	<b><math>\tau_5</math> (ns)</b>	<b><math>c_5</math> (%)</b>	<b><math>\langle\tau\rangle</math> (ns)</b>	<b>chi2</b>
5.0	13.140	6.7	27.020	3.2	2.840	1.814
20.0	10.890	9.0	21.090	4.8	3.160	1.355
33.0	11.560	4.6	19.650	2.5	1.790	1.869

---

# **GENERAL CONCLUSION**

---

In present study, a variety of fluorescence detection approaches, including steady-state fluorescence anisotropy; fluorescence cross-correlation spectroscopy (FCCS); time-resolved fluorescence measurements, have been adopted to understand the fundamental principles of the light activation of biomolecules, bioassemblies, and the subsequent photoinduced processes. This thesis encompasses the fundamentals and various applications involving the integration of light, photonics and biology into biophotonics.

In the first part, the FCCS technique has been applied to monitor the enzymatic kinetics of RecQ helicase. The principle was based on the sensitivity of FCCS technique to the concomitant diffusion of the two fluorescently labelled DNA strands, with high cross-correlation amplitude characterizing the duplex molecule and a significant decrease in this amplitude upon physical separation of the two strands, without any limitation due to the size of the DNA strands that initially constitute the DNA substrate. Under the guidance of FCCS approach, the *E. Coli* RecQ helicase DNA unwinding activity and human RecQ5 $\beta$  helicase strand annealing activity have been studied.

- We found that the DNA-binding of *E. coli* RecQ helicase is characterized by a cooperative DNA-binding mode at 37°C, but essentially non-cooperative at 25°C. Our results highlight a different DNA-binding mode of *E. coli* RecQ helicase depending on the temperature, suggesting a specific protein conformation compatible with cooperative assembly that occurs at 37°C but not at 25°C. The thermodynamic DNA binding behaviour of RecQ helicase is compared with that of ATP concentration. Moreover, the extent of cooperativity for *E. coli* RecQ protein to DNA substrates is strongly related to the DNA size and there is the absence of cooperativity for the short DNA substrate (13-mer), even at 37°C, which is in total agreement with the binding size of 9-10 nt – for a monomeric unit – as previously determined (Zhang et al., 2006). We also revealed a synergistic effect of the presence of the two 3'-OH ss tails for all DNA lengths above 13-mer, and the cooperativity increases when the size of the duplex DNA region increases which indicate that the duplex region, not only the ss/ds DNA junction, plays a key role in the cooperative DNA-binding mode. We further examined the influences of the spontaneous DNA re-hybridization- following helicase translocation- and the single-stranded DNA binding property of helicase on the unwinding activity. To address these questions, the effects of complementary ssDNA and that of SSB protein were studied. Results indicate the influence for ssDNA and SSB protein on *E. coli* RecQ helicase is quite comparable. The stimulation effect of SSB on helicase activity via inhibition of the spontaneous re-annealing of unwound

strands is probably common to both single- and multiple- turnover catalytic modes. And at higher SSB concentrations, the helicase may be displaced from the DNA substrate ss3'-tails, which further explained the inhibition effects of SSB above the 150nM ( $K_{d,app} = 94\text{nM}$ ) should be attributed to the helicase/SSB interaction. Similarly, short complementary single strand oligonucleotides (typically 7- or 10-mer) display comparable stimulation effects on helicase activity with that of SSB was observed in present study. Such stimulation effects of SSB and as short oligonucleotides can be qualified as modest and only partially increase the apparent unwinding rate.

- When concerning about the RecQ5 $\beta$  helicase DNA-binding and strand annealing activities, the influence of temperature on the annealing efficiency on the same DNA substrate with and without enzyme was compared. The DNA substrate binding activity of RecQ5 $\beta$  was also conducted to further evaluate the enzyme annealing activity. We have characterized RecQ5 $\beta$  strand annealing efficiency had no dependence on oligonucleotide length, which is different with that in other human RecQ family members. Moreover, we found that RecQ5 $\beta$  possesses higher strand annealing activity at higher incubation temperatures, however, the related ssDNA binding affinity for RecQ5 $\beta$  decreases as the increase of the temperature (Figure 2, III.2). Furthermore, the strand annealing activity of RecQ5 $\beta$  is quite comparable on the 22-bp dsDNA and the 66-bp ssDNA, which confirmed that there is no DNA length and polarity dependence for RecQ5 $\beta$  helicase in case of strand annealing activity. In addition, the temperature dependence for RecQ5 $\beta$  annealing activity may suggests that the mechanism by which RecQ5 $\beta$  promotes ssDNA annealing is not for non-specifically binding of enzyme to the two ssDNA molecules and hence increase the proximity via protein-to-protein interactions. It reflects the innate RecQ5 $\beta$ -mediated annealing. No  $\text{Mg}^{2+}$  requirement was observed to perform RecQ5 $\beta$ -mediated strand annealing activity, which is consistent with that of BLM helicase when performing annealing activities (Cheek et al., 2005) and that of T4 phage UvsW helicase (Scott & Stephen, 2007). Results in our present study would definitely provide more knowledge on understanding the intrinsic DNA-strand annealing function for DNA helicases.

Therefore, the FCCS approach is particularly well-suited for monitoring the RecQ helicase enzymatic activity.

In the second part, steady-state fluorescence anisotropy was recorded by Beacon 2000 instrument to analyse impact of the two main raltegravir resistance pathways (N155H and

G140S/Q148H) on HIV viral replication and the catalytic properties of recombinant INs. In particular, the effect of the G140S/Q148H double mutation was investigated by constructing both the Q148H and G140S single mutants as well as the double mutant. We also studied the effect of IN background (laboratory strain or patient) on the properties of the enzymes.

- Present study has successfully monitored the DNA-binding and 3'-processing activities of wild-type and mutants of HIV-INs in real-time. Results indicated that each mutation described conferred resistance, but the extent of that resistance differed between mutations. The Q148H mutation caused strong resistance to RAL when present alone, while the G140S displays weak resistance. Importantly, the G140S/Q148H double mutation confers strong resistance to the drug and viral replication levels similar to that of wild-type virus. However, this mutation of Q148H severely impaired viral replication kinetic in addition to the catalytic activity of the recombinant IN. The G140S mutation did not confer strong resistance but restored the replication capability of the Q148H mutant. Accordingly, *in vitro*, the activity of the G140S/Q148H mutant is able to reach a wild-type level of activity but not the single mutant Q148H. Our kinetic study also reveals that Q148H is a catalytic mutant blocked in an inactive conformation. The G140S mutation induces a conformational transition compatible with activity. Thus, the combination of these two mutations results in a virus that is both able to replicate and highly resistant to RAL. Taken together, we hypothesized that the Q148H mutation primarily confers resistance to RAL, however, this mutation severely impaired viral replication. It is most likely that the G140S mutation counteracted this detrimental effect for the virus and increased viral fitness. Such compensation of the Q148H replication efficiency by G140S explains why rapidly after the administration of RAL, the G140S/Q148H mutant is detected. Finally, our data demonstrate that the Q148H mutant is more resistant to RAL in comparison to the N155H mutant, which explains why the N155 pathway often switched to the Q148 pathway.

In the third part, time-resolved photoluminescence decay and spectrometer measurements have been conducted on the MPA capped CdTe QDs. The size dependence and temperature dependence of the time-resolved PL properties of the self-assembled CdTe QDs covered by MPA layers were investigated. The principle of PL decay measurements is based on the technique of TCSPC. The time-resolved PL, using the kinetics of electron-hole recombination as a probe, gives direct information on the luminescence decay mechanism. The radiative lifetime of photoluminescence is generally dominated by a biexponential

distribution, consisting of a fast component (~ several nanoseconds) and a slow component (~ tens of nanoseconds) at room temperature. The PL decay detected at the maxima of the ground state transition, and the PL decay profiles of QDs were fitted to a multiple exponential function. Maximum entropy data analyse method was used in data processing.

- The hydrodynamic diameters of MPA-coated CdTe QDs has been measured using FCS technique (Dong et al., 2006) and ranges from 2.0 to 5.5 nm. Individual CdTe Qds display non-blinking behaviour and rather good stability in aqueous solutin (He et al., 2006). Spectrometer measurements indicate that the emission spectra of the smallest CdTe quantum dots displays a shoulder at long wavelength where the PL decay is slower than in the main peak. The PL decay of CdTe QDs analyses yields lifetime distribution with peaks arising around 0.1ns, 1-3ns, 10-20ns and 40-50 ns. Similar results have been obtained with coated CdSe QDs in use for FRET measurements (Fernandez-Aguëlles et al., 2007). Moreover, we found that the larger is the size of QDs, the slower is the PL decay. In small particles the relative contribution of fast component is greater than in large QD. The decays of CdTe QDs are very similar upon one or two photon excitation. Only a minor difference has been detected in the smallest particle. In addition, the PL decay of QDs was faster at higher temperature, which would be attributed to the increasing contribution of the smallest lifetime peak. Therefore, the QDs emission kinetics is rather complex and it is clearly depending on the particle size. The use of QDs for FRET experiment is therefore complicated by the multiple lifetime behaviour. The influence of surface charge of QDs on PL kinetics will be further investigated.

In conclusion, the applications of fluorescence-based techniques in biological fields have broadened our knowledge on biological macromolecules and their interactions. Present thesis has successfully realized the use of several fluorescence-based detection techniques in monitoring enzymatic kinetics and characterizing the fluorescence properties of nanoparticles. We convinced the fact that the fluorescence detection is highly sensitive and has more advantages (eg. low expense and less difficulty) when comparing with the traditional radioactive tracers presently used in most biochemical measurements. In the future, the need for better, minimally invasive diagnostic tools and more specialized instrumentation to answer highly specific biological questions would definitely trigger an avalanche in the fluorescence-based technique development.

---

# REFERENCES

---

- Akerman M.E., Chan W.C.W., Laakkonen P., Bhatia S.N., Ruoslahti E. (2002) Nanocrystal targeting *in vivo*. *Proc. Natl. Acad. Sci.* 99: 12617-12621
- Alberts B., Johnson A., Lewis J., Raff M., Roberts K. (2008) Molecular biology of the cell (5<sup>th</sup>. Edition). Garland Science Taylor&Francis press group. New York, USA 195-262
- Alivisatos A.P. (1996) Semiconductor cluster, nanocrystals, and quantum dots. *Science* 271: 933-937
- Alivisatos A.P. (2004) The use of nanocrystals in biological detection. *Nature Biotechnol* 22: 47-52
- Bacia K., Majoul I.V., Schwille P. (2002). Probing the endocytic pathway in live cells using dual-color fluorescence cross-correlation analysis. *Biophys. J.* 83:1184-1193
- Bacia K., Sally A.K., Schwille P. (2006) Fluorescence cross-correlation spectroscopy in living cells. *Nature Method.* 3:83-89
- Ballou B., Lagerholm B.C., Ernst L.A., Bruchez M.P., Waggoner A.S. (2004) Non-invasive imaging of quantum dots in mice. *Bioconju. Chem.* 15:79-86
- Bennett R.J., Keck J.L., Wang J.C. (1999) Binding specificity determines polarity of DNA unwinding by the Sgs1 protein of *S.cerevisiae*. *J Mol Biol.* 289(2): 235-248
- Berg J.M., Tymoczko J.L., Stryer L. (2006) Biochemistry (6<sup>th</sup> Edition). W.H. Freeman and Company, USA. 797-814
- Berland K.M., So P.T.C., Gratton E., (1995) Two-photon fluorescence correlation spectroscopy: method and application to the intracellular environment. *Biophys. J.* 68(2): 694–701
- Bernstein D.A., Keck J.L. (2003) Domain mapping of Escherichia coli RecQ defines the roles of conserved amino- and carboxyl-terminal regions in the RecQ family. *Nucleic Acids Res.*, 31, 2778-2785
- Bernstein D.A., Zittel M.C., Keck J.L. (2003) High-resolution structure of the E.Coli RecQ helicase catalytic core. *EMBO J.* 22, 4910-4921
- Bieschke J., Schwille P. (1998) Aggregation of prion protein investigated by dual-color fluorescence cross-correlation spectroscopy. *Fluorescence microscopy and fluorescent probes.* 2: 81-86
- Bjornson K.P., Amaratunga M., Moore K.J., Lohman T.M. (1994) Single-turnover kinetics of helicase-catalyzed DNA unwinding monitored continuously by fuorescence energy transfer. *Biochemistry.* 33: 14306-14316
- Borsch M., Turina P., Eggeling C., Fries J.R., Seidel C.A., Labahn A., Graber P. (1998) Conformational changes of the H<sup>+</sup>-ATPase from *Escherichia coli* upon nucleotide binding detected by single molecule fluorescence. *FEBS Lett.* 437: 251-254

- Brochon J.C., Tauc P., Merola F., Schoot B.M. (1993) Analysis of a recombinant protein preparation on physical homogeneity and state of aggregation. *Anal. Chem.* 65: 1028-1034
- Brosh R.M.Jr., Waheed J., Sommers J.A. (2002) Biochemical Characterization of the DNA substrate specificity of werner syndrome helicase. *J. Biol. Chem.* 277(26): 23236–23245
- Bruchez M.Jr., Moronne M., Gin P., Weiss S., Alivisatos A.P. (1998) Semiconductor Nanocrystals as Fluorescent Biological Labels. *Science* 281(5385): 2013-2016
- Chan W.C.W., Nie S.M. (1998) Quantum dot bioconjugates for ultrasensitive nonisotopic detection. *Science* 281:2016-2018
- Chang L.J., Pryciak P., Ganem D., Varmus H. E. (1989) Biosynthesis of the reverse transcriptase of hepatitis B viruses involves *de novo* translational initiation not ribosomal frameshifting. *Nature* 337: 364–368
- Chen Y., Müller J.D., Eid J.S. (2001) Two-photon fluorescence fluctuation spectroscopy, in: Valeur B. and Brochon J.C. [Ed.] *New trends in fluorescence spectroscopy. Applications to chemical and life sciences*, Springer-Verlag, Berlin, 275-296
- Cherepanov P., Sun Z.Y., Rahman S., Maertens G., Wagner G., Engelman A. (2005) Solution structure of the HIV-1 integrase-binding domain in LEDGF/p75. *Nature Struct. Mol. Biol.* 12: 526–532
- Cheok C.F., Bachrati C.Z., Chan K.L., Ralf C., Wu L., Hickson I.D. (2005) Roles of the bloom's syndrome helicase in the maintenance of genome stability. *Biochem Soc Trans.* 33(6) 1456-1459
- Choudhary S., Sommers J.A., Brosh Jr. R.M. (2004) Biochemical and kinetic characterization of the DNA helicase and exonuclease activities of werner syndrome protein. *J. Biol. Chem.* 279(33): 34603–34613
- Coffin J., In « Virology », [3rd Ed.] (1996) (B.N.Fields, D.M.Knipe, and P.M.Howley, Ed.) 2: 1767-1848. Lippincott-Raven, Philadelphia
- Dabbousi B.O., Rodriguez-Viejo J., Mikulec F.V., Heine J.R., Mattoussi R., Ober R., Jensen K.F., Bawendi M.G. (1997) (CdSe)ZnS core-shell quantum dots: synthesis and characterization of a size series of highly luminescent nanocrystallites. *J. Phys. Chem.* 101: 9463–9475
- Dahan M., Laurence T., Pinaud F., Chemla D.S., Alivisatos A.P., Sauer M., Weiss S. (2001) Time-gated biological imaging by use of colloidal quantum dots. *Opt. Lett.* 26(11): 825-827
- Dahan M., Lévi S., Luccardini C., Rostaing P., Riveau B., Triller A. (2003) Diffusion dynamics of glycine receptors revealed by single-quantum dot tracking. *Science* 302: 442–445
- Dauty E., Verkman A.S. (2005) Actin cytoskeleton as the principal determinant of size-dependent DNA mobility in cytoplasm. *J. Biol. Chem.* 280:7823-7828
- DeJesus E., Berger D., Markowitz M., Cohen C., Hawkins T., Ruane P., Elion R., Farthing

- C., Zhong L.J., Cheng A.K., McColl D., Kearney B. (2006) Antiviral activity, pharmacokinetics, and dose response of the HIV-1 integrase inhibitor GS-9137 (JTK-303) in treatment-naïve and treatment-experienced patients *J. Acquir. Immune. Defic. Syndr.* 43: 1-5
- Delelis O., Carayon K., Guiot E., Leh H., Tauc P., Brochon J. C., Mouscadet J. F., Deprez E. (2008) Insight to the integrase-DNA recognition mechanism: a specific DNA binding mode revealed by an enzymatically labelled integrase. *J. Biol. Chem.* 283, 27838-27849
- Delelis O., Malet I., Li N., Tchertanov L., Calvez V., Marcelin A.-G., Subra F., Deprez E., Mouscadet J.-F.. (2009) The G140S Mutation in HIV Integrases from Raltegravir-Resistant Patients Rescues Catalytic Defect due to the Resistance Q148H Mutation. *Nucleic Acids Research* 37: 1193–1201
- Deprez E., Tauc P., Leh H., Mouscadet J.F., Auclair C., Brochon J.C. (2000) Oligomeric states of the HIV-1 integrase as measured by time-resolved fluorescence anisotropy. *Biochemistry* 39: 9275-9284
- Deprez E., Barbe S., Kolaski M., Leh H., Zouhiri F., Auclair C., Brochon J.C., Le Bret M., Mouscadet J.F. (2004) Mechanism of HIV-1 integrase inhibition by Styrylquinoline Derivatives in Vitro. *Proc. Natl. Acad. Sci. USA.* 65(1): 85-98
- Diaz D., Robles J., Ni T., Blum S.E.C., Nagesha D., Fregoso J.A., Kotov N.A. (1999) Surface modification of CdS nanoparticles with Mos42- : a case study of nanoparticles-modifier electronic interaction. *J. Phys. Chem. B* 103: 9859-9866
- Dick D.C., Morley M.N., Watson J.T. (1982) Rothmund-Thomson syndrome and osteogenic sarcoma. *Clin. Exp. Dermatol.* 7: 119–123
- Diez M., Borsch M., Zimmermann B., Turina P., Dunn S.S., Graber P. (2004) Binding of the b-subunit in the ATP synthase from *Escherichia coli*. *Biochemistry.* 43: 1054-1064
- Dong C.Q., Qian H.F., Fang N.H., Ren J.C. (2006) Study of fluorescence quenching and dialysis process of CdTe quantum dots, using ensemble techniques and fluorescence correlation spectroscopy. *J. Phys. Chem. B* 110(23): 11069-11075
- Dou S.X, Wang P.Y., Xu H.Q., Xi X.G. (2004) The DNA binding properties of the *Escherichia coli* RecQ helicase. *J Biol Chem.* 279(8): 6354-6363
- Drouin C.A., Mongrain E., Sasseville D., Bouchard H.L., Drouin M. (1993) Rothmund-Thomson syndrome with osteosarcoma, *J. Am. Acad. Dermatol.* 28: 301–305
- Dubertret B., Skourides P., Norris D.J., Noireaux V., Brivanlou A.H., Libchaber A. (2002) *In vivo* imaging of quantum dots encapsulated in phospholipids micelles. *Science* 298: 1759–1762
- Eggleston A.K., Rahim N.A., Kowalczykowski S.C. (1996) A helicase assay based on the displacement of fluorescent, nucleic acid-binding ligands. *Nucleic Acids Res.* 24: 1179-1186

- Eigen M., Rigler R. (1994) Sorting single molecules: application to diagnostics and evolutionar biotechnology. *Proc Natl Acad Sci USA*. 91: 5740-5747
- El-Sayed M.A. (2004) Small is different: shape-, size-, and composition- dependent properties of some colloidal semiconductor nanocrystals. *Acc. Chem. Res.* 37(5): 326-333
- Ellis N.A., Groden J., Ye T.Z., Straughen J., Lennon D.J., Ciocci S., Proytcheva M., German J. (1995) The Bloom's syndrome gene product is homologous to RecQ helicases. *Cell*, 83: 655–666
- Elson E., Magde D. (1974) Fluorescence correlation spectroscopy. I. Conceptual basis and Theory. *Biopolymers*. 13:1-27
- Emiliani S., Mousnier A., Busschots K., Maroun M., Van Maele B., Tempe D., Vandekerckhove L., Moisant F., Ben-Slama L., Witvrouw M. (2005) Integrase mutants defective for interaction with LEDGF/p75 are impaired in chromosome tethering and HIV-1 replication. *J. Biol. Chem.* 280: 25517–25523
- Engelman A., Mizuuchi K., Craigie R. (1991) HIV-1 DNA integration: mechanism of viral DNA cleavage and DNA strand transfer. *Cell* 67: 1211-1221
- Engelman A., Craigie R. (1992) Identification of conserved amino acid residues critical for human immunodeficiency virus type 1 integrase function *in vitro*. *Journal of Virology* 66: 6361-6369
- Engelman A., Bushman F. D., Craigie R. (1993) Identification of discrete functional domains of HIV-1 integrase and their organization within an active multimeric complex. *EMBO Journal* 12: 3269-3275
- Enssle J., Jordan I., Mauer B., Rethwilm A. (1996) Foamy virus reverse transcriptase is expressed independently from the Gag protein *Proc. Natl. Acad. Sci. USA* 93: 4137–4141
- Erlwein O., Bieniasz P.D., McClure M.O. (1998) Sequences in *pol* Are required for transfer of human foamy virus-based vectors. *J. Virol.* 72: 5510-5516
- Fernandez-Arguelles M.T., Yakovlev A., Sperling R.A., Luccardini C., Gaillard S., Medel A.S., Mallet J.M., Brochon J.C., Feltz A., Oheim M., Parak W.J. (2007) Synthesis and characterization of polymer-coated quantum dots with integrated acceptor dyes as FRET-based nanoprobes. *Nano lett.* 7(9): 2613-2617
- Fradin C., Abu-Arish A., Granek R., Elbaum M. (2003) Fluorescence correlation spectroscopy close to a fluctuating membrane. *Biophys J.* 84: 2005-2020
- Fukuchi K., Martin G.M., Monnat Jr. R.J. (1989) Mutator phenotype of Werner syndrome is characterized by extensive deletions. *Proc. Natl. Acad. Sci USA* 86: 5893-5897

- Gao X., Chan W.C.W., Nie S. (2002) Quantum-dot nanocrystals for ultrasensitive biological labelling and multicolour optical encoding. *J. Biomed. Opt.* 7: 532
- Gao X., Cui Y., Levenson R.M., Chung L.W.K., Nie S. (2004) *In vivo* cancer targeting and imaging with semiconductor quantum dots. *Nature Biotechnol.* 22: 969-976
- Gaponik N., Talapin D.V., Rogach A.L., Hoppe K., Shevchenko E.V., Kornowski A., Eychmiiler A., Weller H. (2002) Thiol-capping of CdTe nanocrystals: an alternative to organometallic synthetic routes. *J Phys Chem B* 106: 7177-7185
- Garcia P.L., Liu Y.L., Jiricny J., West S.C., Janscak P. (2004) Human RecQ5beta, a protein with DNA helicase and strand-annealing activities in a single polypeptide. *EMBO J.* 23(14): 2882-2891
- Gerion D., Pinaud F., Williams S.C., Parak W.J., Zanchet D., Weiss S., Alivisatos A.P. (2001) Synthesis and properties of biocompatible water-soluble silica-coated CdSe/ZnS semiconductor quantum dots. *J Phys Chem B* 105: 8861-8871
- Gerion D., Chen F., Kannan B., Fu A., Parak W.J., Chen D.J., Majumdar A., Alivisatos A.P. (2003) Room-temperature single-nucleotide polymorphism and multiallele DAN detection using fluorescent nanocrystals and microarrays. *Anal. Chem.* 75: 4766-4772
- Goethals O., Clayton R., Wagemans E., Van Ginderen M., Vos A., Geluykens P., Dockx K., Smits V., Meersseman G., Jochmans D., Hallenberger S., Hertogs K. (2008) Resistance mutations in HIV-1 integrase selected with raltegravir or elvitegravir confer reduced susceptibility to a diverse panel of integrase inhibitors. *Antivir. Ther.* 13(suppl.3)
- Goldman E.R., Balighian E.D., mattoussi H., Kuno M.K., Mauro J.M., Tran P.T., Anderson G.P. (2002) Avidin: a natural bridge for quantum dot – antibody conjugates. *J. Am. Chem. Soc.* 124: 6378–6382
- Goldman E.R., Clapp A.R., Anderson G.P., Uyeda H.T., Mauro J.M., Medintz I.L., Mattoussi H. (2004) Multiplexed toxin analysis using four colors of quantum dot fluororeagents. *Anal. Chem.* 76: 684–688
- Gorbalenya A.E., Koonin,E.V. (1993) Helicases: amino acid sequence comparisons and structure-function relationships. *Curr. Opin. Struct. Biol.* 3: 419-429
- Grinsztejn B., Nguyen B., Katlama C., Gatell J., Lazzarin A., Vittecoq D., Gonzalez C., Chen J., Harvey C., Isaacs R. (2007) Safety and efficacy of the HIV-1 integrase inhibitor raltegravir (MK-0518) in treatment-experienced patients with multidrug-resistant virus: a phase II randomised controlled trial. *Lancet* 369: 1261-1269
- Guiot E., Carayon K., Delelis O., Simon F., Tauc P., Zubin E., Gottikh M., Mouscadet J.F., Brochon J.C., Deprez E. (2006) Relationship between the Oligomeric Status of HIV-1 Integrase on DNA and Enzymatic Activity. *J. Bio. Chem.* 281(32): 22707–22719
- Gull S.F. (1989) in “Maximum entropy and Bayesian methods”. Kluwer Academic Publishers, Dordrecht, the Netherlands. 53-71

- Guo W.Z., Li J.J., Wang Y.A., Peng X.G. (2003) Conjugation chemistry and bioapplications of semiconductor box nanocrystals prepared via dendrimer bridging. *Chem. Mater.* 15:3125-3133
- Gwack Y., Yoo H., Song I., Choe J., Han J.H. (1999) RNA-stimulated ATPase and RNA helicase activities and RNA binding domain of hepatitis G virus non-structural protein 3. *J. Virol.* 73(4): 2909-2915
- Harmon F.G., Kowalczykowski S.C. (2001) Biochemical characterization of the DNA helicase activity of the *Escherichia coli* RecQ helicase. *J. Biol. Chem.* 276, 232-243
- Hauer J.A., Taylor S.S., Johnson D.A. (1999) Binding-dependent disorder-order transition in PKI alpha: a fluorescence anisotropy study. *Biochemistry* 38: 6774-6780
- Hazuda D.J., Felock P., Witmer M., Wolfe A., Stillmock K., Grobler J.A., Espeseth A., Gabryelski L., Schleif W., Blau C., Miller M.D. (2000) Inhibitors of strand transfer that prevent integration and inhibit HIV-1 replication in cells. *Science* 287: 646-650
- Hazuda D.J., Young S.D., Guare J.P., Anthony N.J., Gomez R.P., Wai J.S., Vacca J.P., Handt L., Motzel S.L., Klein H.J., Dornadula G., Danovich R.M., Witmer M.V., Wilson K.A.A., Tussey L., Schleif W.A., Gabryelski L.S., Jin L.X., Miller M.D., Casimiro D.R., Emini E.A., Shiver J.W. (2004) Integrase inhibitors and cellular immunity suppress retroviral replication in rhesus macaques. *Science* 305: 528-532
- He H., Qian H.F., Dong C.Q., Wang K.L., Ren J.C. (2006) Single nonblinking CdTe quantum dots synthesized in aqueous thiopropionic acid. *Angew. Chem. Int. Ed.* 45: 7588-7591
- Heinze K.G., Koltermann A., Schwille P. (2000). Simultaneous two-photon excitation of distinct labels for dual-color fluorescence cross-correlation analysis. *Proc Natl Acad Sci USA.* 97: 10377-10382
- Hindmarsh P., Leis J. (1999) Retrovirus DNA integration. *Microbiology and Molecular Biology Reviews* 63(4): 836-843
- Hooks J.J., Gibbs, C.J., Jr. (1975) The foamy viruses. *Microbiol. Mol. Biol. Rev.* 39:169-185
- Hoshino A., Hanaki K.I., Suzuki K., Yamamoto K. (2004) Applications of T-lymphoma labeled with fluorescent quantum dots to cell tracing markers in mouse body. *Biochem. Biophys. Res. Commun.* 314: 46-53
- Housten P., Kodadek T. (1994) Spectrophotometric assay for enzyme-mediated unwinding of double-stranded DNA. *Proc. Natl Acad. Sci. U.S.A.* 91: 5471-5474
- Jaiswal J.K., Mattoussi H., Mauro J.M., Simon S.M. (2003) Long-term multiple color imaging of live cells using quantum dot bioconjugates. *Nat. Biotechnol.* 21: 47-51
- Jill P.S., Carrie L.M., Jennifer L.T., Sue V. Melody R., Kerry S., Christiaan W., Hanlie W., Stephen J.O. (2008) Genomic organization, sequence divergence, and recombination of feline immunodeficiency virus from lions in the wild. *BMC Genomics* 9:66

- Jones B.E., Beechem J.M., Mathews C.R. (1995) Local and global dynamics during the folding of *Escherichia coli* dihydrofolate reductase by time-resolved fluorescence spectroscopy. *Biochemistry* 34: 1867-1877
- Jordan A., Defechereux P., Verdin E. (2001) The site of HIV-1 integration in the human genome determines basal transcriptional activity and response to Tat transactivation. *EMBO J.* 20: 1726–1738
- Jordan, A., Bisgrove D., Verdin E. (2003) HIV reproducibly establishes a latent infection after acute infection of T cells *in vitro*. *EMBO J.* 22: 1868–1877
- Jyoti K.J., Sanford M.S. (2004) Potentials and pitfalls of fluorescent quantum dots for biological imaging. *Trends in cell biology.* 14(9): 497-504
- Kanagaraj R., Saydam N., Garcia P.L., Zheng L., Janscak P. (2006) Human RecQ5 $\beta$  helicase promotes strand exchange on synthetic DNA structures resembling a stalled replication fork. *Nucleic Acids Res.* 34(18): 5217-5231
- Kasha M. (1950) Characterization of electronic transitions in complex molecules. *Disc. Faraday. Soc.* 9: 14-19
- Kaul Z., Yaguchi T., Kaul S.C., Hirano T., Wadhwa R., Taira K. (2003). Mortalin imaging in normal and cancer cells with quantum dot immuno-conjugates. *Cell Res.* 13:503–507
- Kelly C.K., George J.W., Kreuzer K.N. (1997) Bacteriophage T4 UvsW protein is a helicase involved in recombination, repair and the regulation of DNA replication origins. *EMBO J.* 16(13): 4142-4151
- Ketting U., Koltermann A., Schwille P., Eigen M. (1998) Real-time enzyme kinetics monitored by dual-color fluorescence cross-correlation spectroscopy. *Proc. Natl. Acad. Sci. USA.* 95: 1416-1420
- Kim S., Bawendi M.G. (2003). Oligomeric ligands for luminescent and stable nanocrystal quantum dots. *J. Am. Chem. Soc.* 125:14652-14653
- Kim S., Lim Y.T., Soltész E.G., De Grand A.M., Lee J., Nakayama A., Parker J.A., Mihaljevic T., Laurence R.G., Dor D.M., Cohn L.H., Bawendi M.G., Frangioni J.V. (2004) Near-infrared fluorescent type II quantum dots for sentinel lymph node mapping. *Nat. Biotechnol.* 22: 93–97
- Kim S.A., Heinze K.G., Waxham M.N., Schwille P. (2004) Intracellular calmodulin availability accessed with two-photon cross-correlation. *Proc. Natl. Acad. Sci. USA.* 101:105-110
- Kim S.A., Heinze K.G., Bacia K., Waxham M.N., Schwille P. (2005) Two-photon cross-correlation analysis of intracellular reactions with variable stoichiometry. *Biophys J.* 88: 4319-4336
- Kinjo M., Nishimura G., Koyama T., Mets Ü., Rigler R. (1998) Single molecule analysis of restriction DNA fragments using fluorescence correlation spectroscopy. *Anal Biochem* 260: 166-172

Kitao S., Shimamoto A., Goto M., Miller R.W., Smithson W.A., Lindor N.M., Furuichi Y. (1999) Mutations in RECQ4 cause a subset of cases of Rothmund-Thomson syndrome. *Nat. Genet.* 22: 82–84

Klayman D.L., Griffin T.S. (1973) Reaction of selenium with sodium borohydride in protic solvents. A facile method for the introduction of selenium into organic molecule. *J. Am. Chem. Soc.* 95: 197-199

Kloepfer J.A., Mielke R.E., Wong M.S., Neelson K.H., Stucky G., Nadeau J.L. (2003) Quantum dots as strain and metabolism-specific microbiological labels. *Appl. Environ. Microbiol.* 69: 4205-4213

Kohl T., Heinze K.G., Kuhlemann R., Koltermann A., Schwille P.A. (2002) A protease assay for two-photon crosscorrelation and FRET analysis based solely on fluorescent proteins. *Proc. Natl. Acad. Sci. USA.* 99: 12161-12166

Kolterman A., Ketting U., Bieschke J., Winkler T., Eigen M. (1998) Rapid assay processing by integration of dual-color fluorescence crosscorrelation spectroscopy: high throughput screening for enzyme activity. *Proc. Natl. Acad. Sci. U.S.A.* 95: 1421–1426

Koppel D. E., Morgan F., Cowan A.E., Carson J.H. (1994) Scanning concentration correlation spectroscopy using the confocal laser microscope. *Biophys. J.* 66(2): 502-507

Korolev S., Hsieh J., Gauss G.H., Lohman T.M., Waksman G. (1997) Major domain swivelling revealed by the crystal structures of complexes of *E.coli* Rep helicase bound to single-stranded DNA and ADP. *Cell* 90: 635–647

Kuczynski J.P., Milosavljevic B.H., Thomas J.K. (1983) Effect of the synthetic preparation on the photochemical behaviour of colloidal CdS. *J. Phys. Chem.* 87:3368-3370

Lacowicz, J.R. [Ed.] (1983) Principle of fluorescence. 1<sup>st</sup> edition. Plenum Press, New York.

Lacowicz, J.R. [Ed.] (2006) Principle of fluorescence. 3<sup>rd</sup> edition. Plenum Press, New York. 3-15

Larson D.R., Zipfel W.R., Williams R.M., Clark S.W., Bruchez M.P., Wise F.W., Webb W.W. (2003). Water soluble quantum dots for multiphoton fluorescence imaging *in vivo*. *Science* 300: 1434-1436

Lee W.Z., Shu G.W., Wang J.S., Shen J.L., Lin C.A., Chang W.H., Ruaan R.C., Chou W.C., Lu C.H., Lee Y.C. (2005) Recombination dynamics of luminescence in colloidal CdSe/ZnS quantum dots. *Nanotechnol.* 16: 1517-1521

Leh H., Brodin P., Bischerour J., Deprez E., Tauc P., Brochon J.C., LeCam E., Coulaud D., Auclair C., Mouscadet J.F. (2000) Determinants of Mg<sup>2+</sup>-Dependent Activities of Recombinant Human Immunodeficiency Virus Type 1 Integrase. *Biochemistry* 39: 9285–9294

Lehninger A.L., Nelson D.L., Cox M.M. (1993) Principles of biochemistry (2<sup>nd</sup> edition).

Worth publishers Inc. New York, USA. 182-196

Leitão J.M.M., Gonçalves H., Mendonça C., Esteves da Silva J.C.G. (2008) Multiway chemometric decomposition of EEM of fluorescence of CdTe quantum dots obtained as function of pH. *Analytica Chimica Acta*. 628: 143-154

Lewinski, M.K., Bisgrove D., Shinn P., Chen H., Hoffmann C., Hannehalli S., Verdin E., Berry C.C., Ecker J.R., Bushman F.D. (2005) Genome-wide analysis of chromosomal features repressing human immunodeficiency virus transcription. *J. Virol.* 79: 6610–6619

Li L., Qian H.F., Ren J.C. (2005) Rapid synthesis of highly luminescent CdTe nanocrystals in the aqueous phase by microwave irradiation with controllable temperature. *Chem. Commun.* 528-530

Li L., Qian H.F., Fang N.H., Ren J.C. (2006) Significant enhancement of the quantum yield of CdTe nanocrystals synthesized in aqueous phase by controlling the pH and concentration of precursor. *J. Luminesc.* 116: 59-66

Li M, Mizuuchi M, Burke T, Jr, Craigie R. (2006) Retroviral DNA integration: reaction pathway and critical intermediates. *EMBO J.* 25: 1295-1304

Li N., Henry E., Guiot E., Rigolet P., Brochon J.C., Xi X.G., Deprez E. (2009) Multiple *Escherichia coli* RecQ helicase monomers cooperate to unwind long DNA substrates: a fluorescence cross-correlation study. under review.

Lidke D.S., Nagy P., Heintzmann R., Arndt-Jovin D.J., Post J.N., Grecco H.E., Jares-Erijman E.A., Jovin T.M. (2004) Quantum dot ligands provide new insights into erbB/HER receptor-mediated signal transduction. *Nat. Biotechnol.* 22: 198–203

Lim, Y.T., Kim S., Nakayama A., Stott N.E., Bawendi M.G., Frangioni J.V. (2003) Selection of quantum dot wavelengths for biomedical assays and imaging. *Mol. Imaging* 2: 50–64

Lindor N.M., Furuichi Y., Kitao S., Shimamoto A., Arndt C., Jalal S. (2000) Rothmund-Thomson syndrome due to RECQ4 helicase mutations: report and clinical and molecular comparisons with Bloom syndrome and Werner syndrome. *Am. J. Med. Genet.* 90: 223–228

Livesey A.K., Brochon J.C. (1987) Recovering the distribution of decay constants in pulse-fluorimetry using maximum entropy. *Biophysic. J.* 52: 693-706

Lochelt M., Muranyi W., Flugel, R.M. (1993) Human foamy virus genome possesses an internal, Bel-1-dependent and functional promoter. *Proc, Natl, Acad. Sci. USA* 90: 7317-7321

Lochelt M., Flugel R.M. (1996) The human foamy virus pol gene is expressed as a Pro-Pol polyprotein and not as a Gag-Pol fusion protein. *J. Virol.* 70: 1033–1040

Lohman T.M., Bjornson K.P. (1996) Mechanisms of helicase-catalyzed DNA unwinding. *Annu. Rev. Biochem.* 65:169-214

Lukas T.J., Burgess W.H., Prendergast F.G., Lau W., Watterson D.M. (1986) Calmodulin binding domains: characterization of a phosphorylation and calmodulin binding site from myosin light chain kinase. *Biochemistry.* 25: 1458-1464

Machwe A., Xiao L., Groden J., Matson S.W., Orren D.K. (2005) RecQ family members combine strand pairing and unwinding activities to catalyze strand exchange. *J. Biol. Chem.* 280: 23397–23407

Machwe A., Lozad E.M., Xiao L., Orren D.K. (2006) Competition between the DNA unwinding and strand pairing activities of the Werner and Bloom syndrome proteins. *BMC Mol. Biol.*, 7:1

Machwe A., Xiao L., Lloyd R.G., Bolt E., Orren D.K. (2007) Replication fork regression *in vitro* by the Werner syndrome protein (WRN): Holliday junction formation, the effect of leading arm structure and a potential role for WRN exonuclease activity. *Nucleic Acids Research.* 35(17): 5729–5747

Macris M.A., Krejci L., Bussen W., Shimamoto A., Sung P. (2006) Biochemical characterization of the RECQ4 protein, mutated in Rothmund-Thomson syndrome. *DNA Repair (Amst.)*. 5:172–180

Magde D., Elson E., Webb W.W. (1972) Thermodynamic fluctuations in a reacting system-measurement by fluorescence correlation spectroscopy. *Phys. Rev. Lett.* 29: 705-708

Maiti S., Haupts U., Webb W.W. (1997) Fluorescence correlation spectroscopy: diagnostics for sparse molecules. *Proc Natl Acad Sci USA* 94: 11753-11757

Malet I., Delelis O., Valantin M.A., Montes B., Soulie C., Wirden M., Tchertanov L., Peytavin G., Reynes J., Mouscadet J.F., Katlama C., Calvez V., Marcelin A.G. (2008) Mutations associated with failure of raltegravir treatment affect integrase sensitivity to the inhibitor *in vitro*. *Antimicrob. Agents Chemother.* 52: 1351-1358

Malicka J., Ganzynkowicz R., Groth M., Czaplewski C., Karolczak J., Liwo A., Wiczak W. (2001) Fluorescence decay time distribution analysis of cyclic enkephalin analogues; influence of solvent and Leu configuration in position 5 on conformation. *Acta Biochimica Polonica* 48: 95-102

Martin G.M. (1978) Genetic syndromes in man with potential relevance to pathobiology of aging. *Birth Defects Orig. Artic. Ser.* 14: 5–39

Matson S.W., Bean D.W., George J.W. (1994) DNA helicases enzymes with essential roles in all aspects of DNA metabolism. *Bioessays.* 16: 13-22

Mattheakis L.C., Dias J.M., Choi Y.J., Gong J., Bruchez M.P., Liu J.Q., Wang E. (2004) Optical coding of mammalian cells using semiconductor quantum dots. *Anal. Biochem.* 327: 200–208

Mattoussi H., Maum J.M., Goldman E.R., Anderson G.P., Sundar V.C., Mikulec F.V., Bawendi M.G. (2000) Self-assembly of CdSe-ZnS quantum dots bioconjugates using an engineered recombinant protein. *J. Am. Chem. Soc.* 122:12142

- Mayor S., Presley J.F., Maxfield F.R. (1993) Sorting of membrane-components from endosomes and subsequent recycling to the cell-surface occurs by a bulk flow process. *J. Cell Biol.* 121: 1257–1269
- Merck & Co. Inc. ISENTRESS™ (raltegravir) 400mg for treatment of HIV (NDA 22-145) FDA antiviral drugs advisory committee meeting, September 2007. Silver Spring MD
- Michalet X., Pinaud F.F., Bentolila L.A., Tsay J.M., Doose S., Li J.J., Sundaresan G., Wu M.A., Gambhir S.S., Weiss S. (2005) Quantum dots for live cells, *in vivo* imaging, and diagnostics. *Science.* 307: 538-544
- Miller M., Danovich R.M., Ke Y., Witmer M.V., Zhao J., Harvey C., Nguyen B.Y., Hazuda D.J. (2008) Longitudinal analysis of resistance to the HTV-1 integrase inhibitor raltegravir: results from P005 a Phase II study in treatment-experienced patients *Antiviral Therapy* 13: A8
- Minet O., Dressler C., Beuthan J. (2004) Heat stress induced redistribution of fluorescent quantum dots in breast tumor cells. *J. Fluoresc.* 14: 241–47
- Moebes A., Enssle J., Bieniasz P.D., Heinkelein M., Lindemann D., Bock M., McClure M.O., Rethwilm A. (1997) Human foamy virus reverse transcription that occurs late in the viral replication cycle. *J. Virol.* 71: 7305-7311
- Mouscadet J.F., Arora R., Andre J., Lambry J.C., Delelis O., Malet I., Marcelin A.G., Calvez V., Tchertanov L. (2009) HIV-1 IN alternative molecular recognition of DNA induced by raltegravir resistance mutations. *J. Mol. Recognit.* (published online)
- Murphy F.A., Fauquet C.M., Bishop D.H.L, Ghabrial S.A., Jarvis A.W., Martelli G.P., Mayo M.A., Summers M.D.[Ed.] (1994) Virus taxonomy: The classification and nomenclature of viruses, Retroviridae, Springer-Verlag, Vienna.
- Opresko P.L., von Kobbe C., Laine J.P., Harrigan J., Hickson I.D., Bohr V.A. (2002) Telomere-binding protein TRF2 binds to and stimulates the Werner and Bloom syndrome helicases. *J Biol Chem.* 277(43): 41110-41119
- Osaki F., Kanamori T., Sando S., Sera T., Aoyama Y. (2004) A quantum dot conjugated sugar ball and its cellular uptake on the size effects of endocytosis *in vivo*. *J. Am. Chem. Soc.* 126: 6520
- Otsuki M., Seki M., Inoue E., Abe T., Narita Y., Yoshimura A., Tada S., Ishii Y., Enomoto T. (2008) Analyses of functional interaction between RecQL1, RecQL5, and BLM which physically interact with DNA topoisomerase III alpha. *Biochim Biophys Acta.* 1782(2): 75-81
- Pathak S., Choi S.K., Arnheim N., Thompson M.E. (2001) Hydroxylated quantum dots as luminescent probes for in situ hybridization. *J. Am. Chem. Soc.* 123: 4103
- Pellegrino T, Manna L., Kudera S., Liedl T., Koktysh D., Rogach A.L., Keller S., Radler J., Natile G., Parak W.J. (2004) Hydrophobic nanocrystals coated with an amphiphilic polymer shell: a general route to water soluble nanocrystals. *Nano. Lett.* 4: 703-707

- Pinaud F., King D., Moore H.P., Weiss S. (2004) Bioactivation and cell targeting of semiconductor CdSe/ZnS nanocrystals with phytochelatin-related peptides. *J. Am. Chem. Soc.* 126: 6115-6123
- Pommier Y., Johnson A., Marchand C. (2005) Integrase inhibitors to treat HIV/AIDS Nat. purified preintegration complexes from virus-infected cells. *J. Virol.* 79: 8208-8216
- Prasad P.N. [Ed.] (2003) Introduction to biophotonics. John Wiley & Sons, Hoboken, New Jersey. 1-10
- Qian H., Elson E. L. (1991) Analysis of confocal laser-microscope optics for 3-D quantifying integrated HIV-1 DNA *Methods Mol. Biol.* 304: 139-154
- Rahman S., Lu R., Vandegraaff N., Cherepanov P., Engelman A. (2007) Structure-based mutagenesis of the integrase-LEDGF/p75 interface uncouples a strict correlation between *in vitro* protein binding and HIV-1 fitness. *Virology.* 357: 79-90
- Ramsden J.J., Gratzel M. (1984) Photoluminescence of small cadmium sulphide particles. *J. Chem. Soc. Faraday. Trans.* 80: 919-933
- Raney K.D., Sowers L.C., Millar D.P., Benkovic S.J. (1994) A fluorescence-based assay for monitoring helicase activity. *Proc. Natl Acad. Sci. U.S.A.* 91: 6644-6648
- Reiss P., Bleuse J., Pron A. (2002) Highly luminescent CdSe/ZnSe Core/Shell nanocrystals of low size dispersion. *Nano. Lett.* 2: 781-784
- Ren H., Dou S.X., Zhang X.D., Wang P.Y., Kanagaraj R., Liu J.L., Janscak P., Hu J.S., Xi X.G. (2008) The zinc-binding motif of human RecQ5beta suppresses the intrinsic strand-annealing activity of its DExH helicase domain and is essential for the helicase activity of the enzyme. *Biochem J.* 412(3): 425-433
- Rethwilm, A. (1995) Regulation of foamy virus gene expression. *Curr. Top. Microbiol. Immunol.* 193: 1-24
- Rigler R., Elson E.S. [Ed.] (2001) Fluorescence correlation spectroscopy: theory and applications. Springer, New York, 486
- Rogach A.L., Franzl T., Klar T.A., Feldmann J., Gaponik N., Lesnyak V., Shavel A., Eychmuller A., Rakovich Y.P., Donegan J.F. (2007) Aqueous synthesis of thiol-capped CdTe nanocrystals: State-of-the-art. *J. Phys. Chem. C* 111: 14628-14637
- Roman L.J., Kowalczykowski S.C. (1989) Characterization of the helicase activity of the *E. coli* RecBCD enzyme using a novel helicase assay. *Biochemistry.* 28: 2863-2873
- Roman L.J., Dixon D.A., Kowalczykowski S.C. (1991) Genetic control of recombination exchange frequency in *Escherichia coli* K-12 proteins. *Proc Natl Acad Sci.* 88, 3367-3371
- Rosenthal S.J., Tomlinson A., Adkins E.M., Schroeter S., Adams S., Swafford L., McBride J., Wang Y.Q., DeFelice L.J., Blakely R.D. (2002) Targeting cell surface receptors with ligandconjugated nanocrystals. *J. Am. Chem. Soc.* 124: 4586-4594

- Ross J.A., Schmidt C.J., Brand L. (1981) Time-resolved fluorescence of the two tryptophans in horse liver alcohol dehydrogenase. *Biochemistry*. 20: 4369-4377
- Rowland S. J., Dyke K. G. (1990) Tn522, a novel transposable element from *Staphylococcus aureus*. *Molecular Microbiology* 4: 961-975
- Rusu L., Gambhir A., McLaughlin S., Radler J. (2004) Fluorescence correlation spectroscopy studies of peptide and protein binding to phospholipids vesicles. *Biophys. J.* 87: 1044-1053
- Salk D., Au K., Hoehn H., Martin G.M. (1981) Cytogenetic of Werner's syndrome cultured skin fibroblasts: variegated translocation mosaicism. *Cytogenet. Cell Genet.* 30: 92-107
- Salk D., Bryant E., Hoehn H., Johnston P., Martin G.M. (1985) Growth characteristics of Werner's syndrome Cells *in vitro*. *Adv.Exp. Med. Biol.* 190: 305-311
- Sanz M., Correa-Duarte M.A., Liz-Marzan L.M., Douhal A. (2008) Femtosecond dynamics of CdTe quantum dots in water. *J. Photochem. Photobiol. A: Chemistry* 196: 51-58
- Schlicht H.J., Radziwill G., Schaller H. (1989) Synthesis and encapsidation of duck hepatitis B virus reverse transcriptase do not require formation of core-polymerase fusion proteins. *Cell* 56: 85-92
- Schliephake A.W., Rethwilm A. (1994) Nuclear localization of foamy virus Gag precursor protein. *J. Virol.* 68: 4946-4954
- Schweizer M., Neumann-Haefelin, D. (1995) Phylogenetic analysis of primate foamy viruses by comparison of *pol* sequences. *Virology* 207: 577-582
- Schwille P., Meyer-Almes F.J., Rigler R. (1997) Dual-color fluorescence cross-correlation spectroscopy for multicomponent diffusional analysis in solution. *Biophys J.* 72:1878-1886
- Schwille P. (2001) Cross-correlation analysis in FCS. *In fluorescence correlation spectroscopy: theory and applications* [Ed.] Rigler R., Elson E.S. Springer, New York. 360-378
- Schwille P., Hanstein E. (2003) Fluorescence correlation spectroscopy: an introduction to its concepts and applications. [Ed.] Printed in Germany
- Scott W.N., Stephen J.B. (2007) The T4 phage UvsW protein contains both DNA unwinding and strand annealing activities. *J. Biol.Chem.* 282(1): 407-416
- Sekelsky J.J., Brodsky M.H., Rubin G.M., Hawley R.S. (1999) Drosophila and human RecQ5 exist in different isoforms generated by alternative splicing. *Nucleic Acids Res.* 27(18): 3762-3769
- Sharma S., Sommers J.A., Gary R.K., Friedrich-Heineken E., Hubscher U., Brosh R.M. Jr. (2005) The interaction site of Flap endonuclease-1 with WRN helicase suggests a coordination of WRN and PCNA. *Nucleic Acids Res.* 33(21): 6769-6781

Shereda R.D., Bernstein D.A., Keck J.L. (2007) A central role for SSB in *Escherichia coli* RecQ DNA helicase function. *J.Biol.Chem.* 282: 19247-19258

Shereda R.D., Reiter N.J., Butcher S.E., Keck J.L. (2009) Identification of the SSB binding site on *E.Coli* RecQ reveals a conserved surface for binding SSB's C terminus. *J.Mol.Biol.* 386: 612-625

Shimamoto A., Nishikawa K., Kitao S., Furuichi Y. (2000) Human RecQ5 $\beta$ , a large isomer of RecQ5 DNA helicase, localizes in the nucleoplasm and interacts with topoisomerases 3 $\alpha$  and 3 $\beta$ . *Nucleic Acids Res.* 28(7): 1647–1655

Shu G.W., Wang C.K., Wang J.S., Shen J.L., Hsial R.S., Chou W.C., Chen J.F., Lin T.Y., Ko C.H., Lai C.M. (2007) The photoluminescence decay time of self-assembled InAs quantum dots covered by InGaAs layers. *Nanotechnology.* 17: 5722-5725

Shusterman R., Alon S., Gavrinyov T., Krichevsky O. (2004) Monomer dynamics in double- and single-strand DNA polymers. *Phys Rev Lett.* 92: 048303

Skilling J. (1989) in “Maximum entropy and Bayesian methods”. Kluwer Academic Publishers, Dordrecht, the Netherlands. 45-52

Skilling J. (1991) in “Maximum entropy in action” (Buck B. and Macaulay V.A. Eds) Oxford University Press (Clarendon) Oxford

Smolov M., Gottikh M., Tashlitskii V., Korolev S., Demidyuk I., Brochon J.C., Mouscadet J.F., Deprez E. (2006) Kinetic study of the HIV-1 DNA 3'-end processing: single-turnover property of integrase. *FEBS J.* 273: 1137-1151

So P.T.C., Köenig K., Berland K., Dong C.Y., French T., Büehler C., Ragan T., Gratton E. (1998) New time-resolved techniques in two-photon microscopy. *Cellular and Molecular Biology.* 44: 771-793

Soultanas P., Wigley D.B. (2000) DNA helicases: ‘inching forward’. *Curr. Opin. Struct. Biol.* 10: 124–128

Stephen C.D.R., Leonard A.H., Leonore A.H., Mario R. (2001) 11-color, 13-parameter flow cytometry: identification of human naive Tcells by phenotype, function and T-cell receptor diversity. *Nat. Med.* 7: 245–248

Stokes G.G. (1852) On the change of refrangibility of light. *Phil. Trans. Royal Society of London* 142: 463-562

Subramanya H.S., Bird L.E., Brannigan J.A., Wigley D.B. (1996) Crystal structure of a DExx box DNA helicase. *Nature.* 384: 379–383

Sukhanova A., Devy J., Venteo L., Kaplan H., Artemyev M., Oleinikov V., Klinov D., Pluot M., Cohen J.H.M., Nabiev I. (2004) Biocompatible fluorescent nanocrystals for immunolabeling of membrane proteins and cells. *Anal. Biochem.* 324: 60-67

- Susha A.S., Javier A.M., Parak W.J., Rogach A.L. (2006) Luminescent CdTe nanocrystals as ion probes and pH sensors in aqueous solutions. *Colloid Surf. A. Physicochem. Eng. Aspects*. 281: 40-43
- Svarovskaia E.S., Barr R., Zhang X.C., Pais G.C.G., Marchand C., Pommier Y., Burke T.R.Jr., Pathak V.K. (2004) Azido-containing diketo acid derivatives inhibit human immunodeficiency virus type 1 integrase in vivo and influence the frequency of deletions at two-long-terminal-repeat-circle junctions. *J. Virol.* 78: 3210-3222
- Thompson N.L. (1991) Fluorescence correlation spectroscopy, in: LAKOWICZ J.R. [Ed.] Topics in fluorescence spectroscopy, vol.1: Techniques, *Plenum Press*, New York, pp337-378.
- Tokumasu F., Dvorak J. (2003) Development and application of quantum dots for immunocytochemistry of human erythrocytes. *J. Microsc.* 211: 256–261
- Tsay J.M., Pflughoefft M., Bentolia L.A., Weiss S. (2004) Hybrid approach to the synthesis of highly luminescent CdTe/ZnS and CdHgTe/ZnS nanocrystals. *J. Am. Chem. Soc.* 126: 1926-1927
- Uhring M., Poterszman A. (2006) DNA helicases and human diseases. *Med. Sci. (Paris)*. 22(12): 1087-1094
- Ulrich K., Andre K., Petra S., Manfred E. (1998) Real-time enzyme kinetics monitored by dual-color fluorescence cross-correlation spectroscopy. *Proc. Natl. Acad. Sci. USA*. 95: 1416–1420
- Umez K., Nakayama K., Nakayama H. (1990) *Escherichia coli* RecQ is a DNA helicase. *Proc. Natl. Acad. Sci. U.S.A.* 87: 5363-5367
- Valeur B. [Ed.] (1993) Fluorescent probes for evaluation of local physical structural parameters. Wiley-Interscience, New York. 25-84
- Varma R., Mayor S. (1998) GPI-anchored proteins are organized in submicron domains at the cell surface. *Nature* 394: 798-801
- Varughese M., Leavey P., Smith P., Sneath R., Breatnach F., O’Meara A. (1992) Osteogenic sarcoma and Rothmund Thomson syndrome. *J. Cancer Res. Clin. Oncol.* 118: 389–390
- Velankar S.S., Soutlanas P., Dillingham M.S., Subramanya H.S., Wigley D.B. (1999) Crystal structures of complexes of PcrA DNA helicase with a DNA substrate indicate an inchworm mechanism. *Cell*. 97: 75–84
- Venkatech L.K., Theodorakis P.A., Chinnadurai G. (1991) Distinct *cis*-acting regions in U3 regulate *trans*-activation of the human supumaretrovirus long terminal repeat by the viral *bel1* gene product. *Nucleic Acids Res.* 19: 3661-3666
- Voura E.B., Jaiswal J.K., Mattoussi H., Simon S.M. (2004) Tracking metastatic tumor cell extravasation with quantum dot nanocrystals and fluorescence emission scanning microscopy. *Nat. Med.* 10: 993-998

- Wang L.L., Gannavarapu A., Kozinetz C.A., Levy M.L., Lewis R.A., Chintagumpala M.M., Ruiz-Maldonado R., Contreras-Ruiz J., Cunniff C., Erickson R.P., Lev D., Rogers M., Zackai E.H., Plon S.E. (2003) Association between osteosarcoma and deleterious mutations in the RECQL4 gene in Rothmund-Thomson syndrome, *J. Natl. Cancer Inst.* 95: 669–674
- Webb W.W. (2001) Fluorescence correlation spectroscopy: inception, biophysical experimentations, and prospectus. *Appl. Opt.* 40: 3969-3983
- Weiss R.A. (2007) Lessons from naked apes and their infections. *J. Med. Primatol.* 36: 172-179
- Weller H., Koch U., Gutierrez M., Henglein A. (1984) Photochemistry of colloidal metal sulfides: absorption and fluorescence of extremely small ZnS particles (the world of the neglected dimensions). *Ber. Bunsenges. Phys. Chem.* 88: 649-656
- West J.L., Halas N.J. (2003) Engineered nanomaterials for biophotonics applications: improving sensing, imaging, and therapeutics. *Annu. Rev. Biomed. Eng.* 5: 285-292
- Whaley S.R., English D.S., Hu E.L., Barbara P.F., Belcher A.M. (2000) Selection of peptides with semiconductor binding specificity for directed nanocrystal assembly. *Nature.* 405: 665-668
- Winkler T., Kettling U., Koltermann A., Eigen, M. (1999) Confocal fluorescence coincidence analysis: an approach to ultra high-throughput screening. *Proc. Natl Acad. Sci. U.S.A.* 96: 1375–1378
- Wiskerchen M., Muesing M.A. (1995) Human immunodeficiency virus type 1 integrase: effects of mutations on viral ability to integrate, direct viral gene expression from unintegrated viral DNA templates, and sustain viral propagation in primary cells. *J. Virol.* 69: 376-386
- Wong I., Lohman T.M. (1992) Allosteric effects of nucleotide cofactors on *Escherichia coli* Rep helicase-DNA binding. *Science.* 256: 350–355
- Wu M., Chari S., Yanchis T., Mergia A. (1998) *cis*-acting sequences required for simian foamy virus type 1 vectors. *J. Virol.* 72: 3451-3454
- Wu X., Maizels N. (2001) Substrate-specific inhibition of RecQ helicase. *Nucleic Acids Res.* 29: 1765-1771
- Wu X.Y., Liu H.J., Liu J.Q., Haley K.N., Treadway J.A., Larson J.P., Ge N.F., Peale F., Bruchez M.P. (2003) Immunofluorescent labelling of cancer marker Her2 and other cellular targets with semiconductor quantum dots. *Nature Biotechnol.* 21: 41-46
- Xu H.Q., Deprez E., Zhang A.H., Tauc P., Ladjimi M.M., Brochon J.C., Auclair C., Xi X.G. (2003) The *Escherichia coli* RecQ helicase functions as a monomer. *J. Biol. Chem.* 278: 34925-34933

Xu H.Q., Zhang A.H., Auclair C., Xi X.G. (2003) Simultaneously monitoring DNA binding and helicase-catalyzed DNA unwinding by fluorescence polarization. *Nucleic Acids Res.* 31(14): e70

Yarranton G.T., Geftter M.L. (1979) Enzyme-catalyzed DNA unwinding: studies on *Escherichia coli rep* protein. *Proc. Natl. Acad. Sci. U.S.A.* 76: 1658-1662

Yu C.E., Oshima J., Fu Y.H., Wijsman E.M., Hisama F., Alisch R., Matthews S., Nakura J., Miki T., Ouais S., Martin G.M., Mulligan J., Schellenberg G.D. (1996) Positional cloning of the Werner's syndrome gene. *Science* 272: 258-262

Yu W.W., Falkner J.C., Shih B.S., Colvin V.L. (2004) Preparation and characterization of monodisperse PbSe semiconductor nanocrystals in a noncoordinating solvent. *Chem. Mater.* 16: 3318-3322

Zhang Y., Mi L., Wang P.N., Ma J., Chen J.Y. (2008a) pH-dependent aggregation and photoluminescence behavior of thiol-capped CdTe quantum dots in aqueous solutions. *J. Lumin.* 128: 1948-1951

Zhang Y., Mi L., Wang P.N., Lu S.J., Chen J.Y., Guo J., Yang W.L., Wang C.C. (2008b) Photoluminescence decay dynamics of thiol-capped CdTe quantum dots in living cells under micro-excitation. *Small* 4: 777-780





## RESUME

Ce mémoire présente la mise en place des techniques de fluorescence en milieu biologique pour mieux comprendre le principe des interactions entre macromolécules biologiques ainsi que leurs mécanismes catalytiques. Dans ce contexte, nous avons appliqué trois méthodes d'analyse de la fluorescence.

Une première technique d'analyse dynamique, la spectroscopie de cross-corrélation de fluorescence, basée sur des mesures en micro-volume et sur une faible concentration moléculaire, a essentiellement été appliquée à étudier l'activité hélicase en mesurant la corrélation croisée des fluctuations de fluorescence entre deux molécules d'ADN complémentaires. En particulier, l'activité d'hélicase de la protéine *E.Coli* RecQ et l'activité d'annealing pour la protéine RecQ5 $\beta$  humaine ont été étudiées. Les performances de la technique FCCS pour appréhender l'étude des activités enzymatiques de la famille des hélicases RecQ ont été validées par nos résultats.

Une deuxième technique d'analyse dynamique qui nous permet de mesurer l'anisotropie de fluorescence statique a été appliquée pour comprendre l'effet de deux voies de résistances au Raltégravir (N155H et G140S/Q148H) sur la réplication virale du virus VIH-1 et sur les propriétés enzymatiques de l'intégrase du VIH (INs). Les applications de cette technique nous ont permis de démontrer la mutation Q148H joue un rôle prépondérant pour la résistance au Raltegravir, tandis que la mutation G140S augmente la fitness virale dans le contexte de la double mutation G140S/Q148H.

Une troisième technique d'analyse dynamique, le déclin de la photo luminosité résolue en temps de la fluorescence, a été appliquée à caractériser les propriétés de fluorescence de nanocristaux de CdTe couronnés par MPA. Cette approche a confirmé les avantages des nanocristaux et leurs applications pour le marquage de fluorescence.

En conclusion, ce mémoire inclus les principes et les applications variées des techniques de fluorescence qui sont engagées à intégrer la domaine différente (lumière, photoniques et biologie) dans la même domaine biophotonique.

## ABSTRACT

This thesis presents the applications of fluorescence detection approaches in understanding the fundamental principles of the light activation of biomolecules, bioassemblies, and their catalytic mechanisms. In this context, three frequently used fluorescent methods have been discussed.

The first technique, the fluorescence cross-correlation spectroscopy, based on measurements in micro-volumes with weak molecular concentration, has been essentially applied to monitor the cross-correlation of the fluorescence fluctuations of the two complementary DNA strands. In particular, the helicase activity of *E.Coli* RecQ enzyme and the strand annealing activity of human RecQ5 $\beta$  helicase have been monitored. Results proved that the FCCS approach is particularly well-suited for monitoring the RecQ helicase enzymatic activity.

The second technique, the fluorescence steady-state anisotropy measurements, has been adopted to analyse impact of the two main Raltegravir resistance pathways (N155H and G140S/Q148H) on HIV viral replication and the catalytic properties of recombinant integrase (INs). Results demonstrated the Q148H mutation is responsible for predominant resistance to Raltegravir whereas the G140S mutation increases viral fitness in the context of double mutant G140S/Q148H.

The third technique, the time-resolved photoluminescence decay measurement, has been conducted to characterise the fluorescent properties of MPA capped CdTe quantum dots (QDs). Results confirmed the advantages of QDs and their promising applications in fluorescent labelling.

In conclusion, this thesis encompasses the fundamentals and various applications involving the integration of light, photonics and biology into biophotonics.